Institut für Theoretische Physik
Fakultät für Mathematik und Naturwissenschaften
Technische Universität Dresden

Chemotaxis of Sperm Cells

Dissertation

zur Erlangung des akademischen Grades

Doctor rerum naturalium

vorgelegt von

Benjamin M. Friedrich
Geboren am 22. Juli 1979 in Rostock

Max-Planck-Institut für
Physik komplexer Systeme

Dresden, 2008

Zusammenfassung der Arbeit

Spermien werden vom Ei mit Chemoattraktant-Botenstoffen angelockt. Molekulare Motoren in der Spermien-Geißel erzeugen eine regelmäßige Wellenbewegung der Geißel welche das Spermium in einer Flüssigkeit antreibt. Spermien können aktiv einen Konzentrationsgradienten eines Chemoattraktants hinaufschwimmen, d.h. Spermien zeigen Chemotaxis. Ein Großteil der Experimente zur Spermien-Chemotaxis wurde mit Seeigel-Spermien durchgeführt. Die Membran der Spermien-Geißel enthält beim Seeigel spezielle Rezeptoren, welche Chemoattraktant-Moleküle binden und daraufhin ein Signalsystem in der Geißel anregen. Dieses Signalsystem steuert die Aktivität der molekularen Motoren und bedingt eine chemotaktische Schwimmantwort.

Seeigel-Spermien schwimmen im Kreis und entlang von Schraubenlinien. Beim Seeigel, sowie vielen weiteren Arten, schwimmen Spermien entlang helikaler Bahnen sofern weder Chemoattraktants noch Grenzflächen das Schwimmen beeinflußen. In der Nähe einer ebenen Grenzfläche schwimmen diese Spermien parallel zu dieser Fläche auf einer Kreisbahn. Die Krümmung ihrer Schwimmbahnen ist eine direkte Folge des asymmetrischen Schlagmusters der Spermien-Geißel. In einem Konzentrationsgefälle eines Chemoattraktants werden in zwei Dimensionen driftende Kreise als Schwimmbahnen und in drei Dimensionen gebogene Helices beobachtet.

Wie funktioniert Spermien-Chemotaxis? Wir entwickeln in dieser Doktorarbeit eine theoretische Beschreibung dieser Chemotaxis; kurzgefaßt beruht diese auf folgendem Mechanismus: Schwimmt ein Spermium in einem Konzentrationsgefälle entlang einer annährend kreisförmigen Schwimmbahn, so nimmt dies Spermium ein zeitlich periodisches Konzentrations-Signal wahr. Sein chemotaktisches Signalsystem verarbeitet dieses Signal und verursacht eine periodische Änderung der Krümmung der Schwimmbahn. Dies bedeutet, dass das Spermium entlang eines Trochoids schwimmt, d.h. seine Schwimmbahn ist ein driftender Kreis. Die Richtung des chemotaktischen Drifts relativ zu der des Konzentrationsgradienten wird bestimmt von der Phasenverschiebung zwischen dem Signal und den Oszillationen der Krümmung. Unsere theoretische Beschreibung stimmt mit experimentellen Daten gut überein. Der vorgestellte Mechanismus beschreibt zudem die Chemotaxis entlang helikaler Schwimmbahnen.

Unser Ergebnis. Unsere theoretische Beschreibung der Spermien-Chemotaxis erklärt deren Funktionsmechanismus und charakterisiert eine Navigations-Strategie welche sich grundsätzlich von der bekannten Bakterien-Chemotaxis unterscheidet. Insbesondere zeigen wir, dass das Auslesen eines Konzentrationsfeldes entlang kreisförmiger und helikaler Bahnen eine robuste Navigations-Strategie darstellt welche in einem großen Parameterbereich erfolgreich funktioniert und auch beim Auftreten von Fluktuation zuverlässig arbeitet. Im letzten Kapitel der Arbeit diskutieren wir Spermien-Chemotaxis in einem allgemeineren Rahmen und betrachten ein beispielhaftes Suchproblem.

Abstract

Sperm cells are guided to the egg by chemoattractants in many species.
Sperm cells are propelled in a liquid by the regular beat of their flagellum. In the
presence of a concentration gradient of a chemoattractant, they can steer upwards the
concentration gradient, a process called chemotaxis. Eggs release chemoattractants to
guide the sperm cells to the egg. Sperm chemotaxis is best studied experimentally in
the sea urchin. There, specific receptors in the flagellar membrane of the sperm cells are
activated upon binding of chemoattractant molecules and trigger a signaling cascade
which ultimately changes the activity of the molecular motors which drive the flagellar
beat and result in a swimming response.

Sea urchin sperm cells swim along circular and helical paths. Sperm cells of the
sea urchin and several other species swim along helical paths far from boundary surfaces
in the absence of chemoattractant. In a two-dimensional experimental geometry, sperm
swimming paths are planar circles. The non-zero curvature of their swimming paths is a
direct consequence of an asymmetry of their flagellar beat. In a concentration gradient
of chemoattractant, sperm swimming path are drifting circles in two dimensions and
bend helices in three dimensions.

What is the working mechanism of sperm chemotaxis? In this thesis, we
develop a theoretical description of sperm chemotaxis which can be subsumed as follows:
While swimming along an approximately circular path in a concentration gradient a
sperm cell traces a periodic concentration stimulus from the concentration field that has
the frequency of circular swimming. The chemotactic signaling system processes this
stimulus and causes a periodic modulation of the curvature of the swimming path which
then gives rise to a swimming path which is a drifting circle. The relative direction of
the drift with respect to the gradient direction is determined by the phase shift between
the stimulus and the curvature oscillations. This picture is in perfect agreement with
recent experimental findings. The mechanism is more general and also works in three
dimensions for swimming along helical paths.

Our results. Our theoretical description of sperm chemotaxis clarifies the concepts
underlying sperm chemotaxis. In particular, we derive the role of internal timing of
the chemotactic signaling system for sperm chemotaxis. We conclude that sampling a
concentration field along circular and helical paths is a robust strategy for chemotaxis
that does not require fine-tuning of parameters and which works reliable also in the
presence of fluctuations. In a last chapter of this thesis, we discuss sperm chemotaxis
in the more general context of an abstract search problem.

Acknowledgments

I want to thank

Contents

viii

x

Chapter 1
Introduction

The first step in fertilization is the fusion of a sperm cell and the egg. Even before physical contact is established, sperm cells communicate with the egg by responding to chemical factors released by the egg, so-called chemoattractants [78,99,100].

Animal sperm cells are active swimmers: Molecular motors in the flagellum of the sperm generate a regular bending wave of the $50\,\mu$m-long flagellum with a frequency of about $50\,$Hz; this flagellar beat propels the sperm cell in water at speeds of $100 - 200\,\mu$m/s [61,127]. The sperm flagellum serves a double purpose: It generates the thrust for forward propulsion and also harbors a chemotactic signaling system: Specific receptors in the flagellar membrane of the sperm cells are activated upon binding of chemoattractant molecules and trigger a signaling cascade which ultimately changes the activity of the molecular motors and results in a swimming response [22,77–79,108,148,162]. The interplay of motility and sensation allows sperm cells to steer upward a concentration gradient of chemoattractant. This navigation in a concentration field is called chemotaxis and its implementation in sperm cells is the central theme of this thesis. Besides playing an important role in fertilization, sperm chemotaxis also provides a key example of a feedback circuit of motility and sensation. Sperm chemotaxis is well established in marine invertebrates with external fertilization (e.g. sea urchins [100]) and has been demonstrated in mammals (e.g. humans [48]).

1.1 Morphology of sperm cells: Head and flagellum

A typical animal sperm cell (spermatozoon) consists of [4]

- a head of length $\approx 5\,\mu$m which contains the tightly packed haploid genome, and

- a single eukaryotic flagellum: a whip-like appendage of length $30 - 60\,\mu$m which can beat regularly and propel the sperm cell in a liquid.

Head and flagellum are connected by a midpiece of length $\approx 7\,\mu$m. The midpiece accommodates several mitochondria which serve as the power house of the sperm cell and generate the chemical fuel ATP which is required for example to power the flagellar beat. The head contains at its proximal tip the acrosome which initiates the fusion with the egg upon contact with the egg surface.

The typical sperm cell is a minimal cell: It is only equipped with what is necessary to deliver the DNA to the egg, but lacks cell organelles such as ribosomes, endoplasmatic
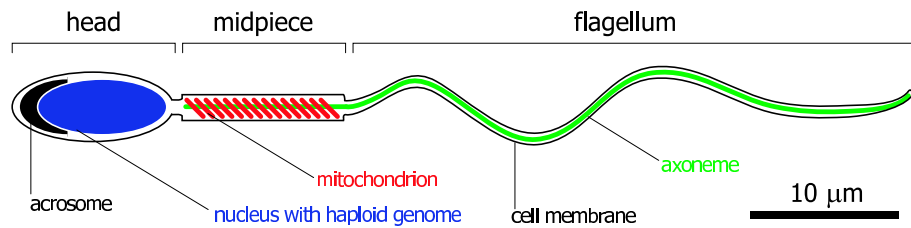
Figure 1.1: An animal sperm cell consists of head, midpiece and flagellum: The head contains the nucleus and an acrosome which initiates fusion with the egg. Several mitochondria are located in the midpiece. Midpiece and flagellum contain an axoneme: a rod-like cytoskeletal structure which can bend actively and propel the sperm cell in a liquid.
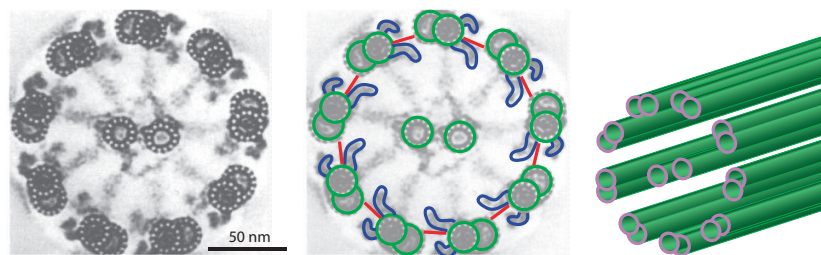
Figure 1.2: The axoneme is a cytoskeletal structure built out of nine microtubule doublets in a cylindrical arrangement. On the left, an electron micrograph of a cross-section through an "9+2"-axoneme is shown (taken from [3] with permission). The schematic drawing in the middle indicates the positions of the microtubules (green), dynein motors (blue) and nexin links (red); the chirality of the axoneme is apparent. A three-dimensional impression of the axoneme is given on the right.

reticulum or Golgi apparatus usually found in eukaryotic cells [5]. In mature sperm cells, transcription of DNA and synthesis of proteins is not possible.

Morphology of the flagellum. The flagellum has a length of $30 - 60 \,\mu$m and a diameter of $0.25 \,\mu$m [4]. It is membrane-sheathed and contains at its inner core an axoneme: The axoneme is an evolutionary highly-conserved cytoskeletal structure which is built out of nine microtubule doublets aligned parally to form a cylindrical arrangement. This structure is called "9+0"-axoneme. In sperm flagella, usually another pair of microtubules is found in the center of the cylindrical arrangement, forming in total a so-called "9+2" axoneme.

Microtubules are rigid filaments with a persistence length of several millimeters that have a structural polarity with a distinguished plus and minus end [69]. In the sperm flagellum, the minus ends of the microtubule doublets are anchored to the rest of the cell by another prominent cytoskeletal structure, the basal body. The basal body is built out of nine microtubule triplets arranged in a cylindrical fashion and is derived from the centrioles involved in organizing cell division [43].

In the axoneme, neighboring microtubule doublets are connected along their whole length by flexible nexin links which provide stability and dynein molecular motors which generate forces. Besides nexin and dynein, numerous other proteins are present in the axoneme [70]. What is remarkable about the axoneme is its chirality (i.e. the axoneme has a handedness): The dynein motors are rigidly attached to one microtubule doublet and reach with their motile arm for the neighboring doublet in a counter-clockwise sense (when viewed from the distal end) [2]. The ATP-driven dynein motors generate the forces which drive the flagellar beat underlying sperm motility. This chirality in the architecture of the axoneme is the origin of the asymmetric flagellar beat patterns observed [67].

The word 'flagellum' is also used in the literature to describe long appendages of *Escherichia coli* and other bacteria. These prokaryotic flagella differ significantly from the eukaryotic flagella of sperm cells from an evolutionary, morphological and functional point of view [8,55,105].

1.2 The flagellum as propeller and antenna

The flagellum of a sperm cell serves both for propulsion and as a sensor: The flagellum bends actively and propels the sperm cell in a liquid, while numerous chemoattractant receptors in the flagellar membrane detect chemoattractant molecules and activate a chemotactic signaling system within the flagellum. In the case of sea urchin sperm, about one million receptors are embedded in the flagellar membrane covering roughly half of its area [78].

1.2.1 Sperm cells swim by flagellar propulsion

The regular beat of the flagellum propels a sperm cell in a liquid [23,29,127]. The hydrodynamics of flagellar propulsion is governed by low Reynolds numbers, i.e. the motion is highly overdamped and viscous effects dominate over inertia [122,144]. The flagellar beat is driven by molecular motors in the axoneme which convert the chemical fuel ATP into forces.

Molecular motors shape the flagellar beat. The microtubule doublets in the flagellar axoneme are connected by dynein motors which are rigidly connected on one doublet and reach with their free arm for the neighboring one [4]. The density of dynein is about 70 /μm along one microtubule [136]. Each dynein motor cyclically binds and hydrolyzes ATP molecules and runs through concomitant cycles of conformational changes. By doing so, its free arm can step along the neighboring microtubule doublet towards the minus end and transmit forces [4]. This leads to relative sliding motion between neighboring microtubule doublets. Since the microtubule doublets are clamped at their proximal end of the axoneme in the basal body, sliding is restricted and will
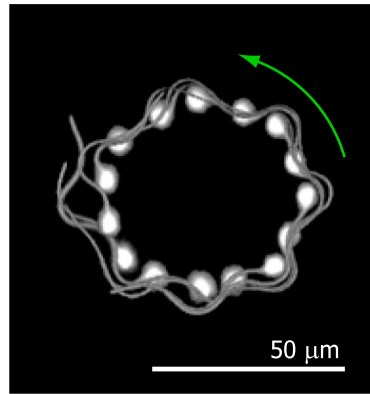
Figure 1.3: A sea urchin sperm cell swimming in a circle near a boundary surface. Shown is a superposition of subsequent positions taken at time intervals of 80 ms. Modified from [79] with permission.

lead to a bending of the axoneme [29,30,66]. The stall force of a single arm of flagellar dynein was estimated as 10 pN [136].

It has been proposed that a dynamic instability leads to an oscillatory motion of the molecular motors resulting in a periodic beat pattern of the axoneme. In the flagellum, an ensemble of molecular motors is working against an elastic element: It has been shown theoretically that these two components are sufficient to generate spontaneous oscillations [75] not only in the flagellum [29,30,66], but also in other biological systems such as in mitotic spindle oscillations [62].

The flagellar beat pattern of sperm cells is often nearly planar resembling a sinusoidal traveling wave propagating from the proximal to the distal end of the flagellum. Typical beat frequencies are in the range of $30 - 60 \,\mu$m/s [61,127]. Often, the flagellar beat pattern possesses an asymmetry which will result in a swimming path that is not straight but has non-zero curvature. As a consequence, sperm cells of many species swim along circular and helical swimming paths [22,33,37,61,100]. The origin of the asymmetry of the flagellar beat pattern is the broken chiral symmetry of the flagellum which is exemplified by the chiral arrangement of molecular motors in the axoneme. It is compelling to see how chirality at a microscopic scale gives rise to swimming paths with broken chiral symmetry on a macroscopic scale. In addition to planar flagellar beat patterns, helical beat patterns have been reported as well [71].

Many sperm swim along circular and helical paths.   Circular and helical swimming of sperm cells has been reported for many species [100] including sea urchin [61] and bull [127]; possible exceptions include abalone [128] and human sperm cells [57].

Swimming of sperm cells is usually observed under experimental conditions where sperm cells swim in a small observation chamber under the microscope. In this situation, sperm cells become localized near the surfaces of the chamber where they swim on circular paths, see figure 1.3. The curvature of their swimming path is a consequence of
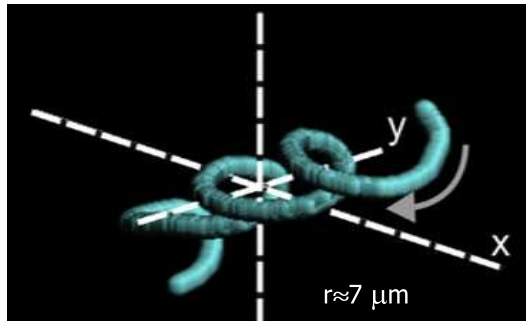
Figure 1.4: Helical swimming path of a sea urchin sperm cell swimming far from any boundary surfaces. The trajectory was obtained by acquiring image z-stacks at a high rate and localizing the sperm cell in each z-stack. The radius of the helix is about $7\,\mu$m. From [33] with permission.

the asymmetry of the flagellar beat [49,79]. In a concentration gradient of a chemoattractant, the circular swimming path drifts toward positions with higher concentration [22,100,165]. It has also been possible to track sperm swimming far from surfaces in three dimensional space. In this case, sperm swim on helical paths [33,37,38], see figure 1.4. Helical swimming paths had been proposed already in [25,61]. In the presence of a chemoattractant concentration gradient, the helices bend, eventually leading to alignment of the helix axis with the gradient [25,37].

1.2.2   The sperm flagellum harbors a chemotactic signaling system

Chemotaxis is mediated by a signaling system which is located in the sperm flagellum [22]. In the case of the sea urchin sperm *Arbacia punctulata*, it has been possible to unravel the key elements of this signaling system [22,78,79,148]. It is likely that the chemotactic signaling system of other external fertilizers has similar biochemistry; the chemotactic signaling of mammalian sperm, however, may differ significantly [47].

Specific receptors in the flagellar membrane of sea urchin sperm cells are activated upon binding of chemoattractant molecules and start the production of cyclic guanine monophosphate (cGMP) [78]. A rise in cGMP gates the opening of potassium channels (KCN) and causes a hyperpolarization of the flagellar membrane, see figure 1.5. This hyperpolarization triggers the opening of voltage gated sodium channels as well as calcium channels and the membrane depolarizes again [148]. The time trace of the membrane potential resembles action potentials in neurons. The overall effect of the signaling cascade is the generation of a transient increase of the internal calcium concentration along the flagellar length [148]. This calcium signal is thought to regulate the activity of dynein motor proteins in the flagellum thus affecting the geometry of the swimming path [22,100,162]. In an experiment with demembranated flagella, asymmetry of the flagellar beat was directly determined by the calcium concentration imposed externally [27].
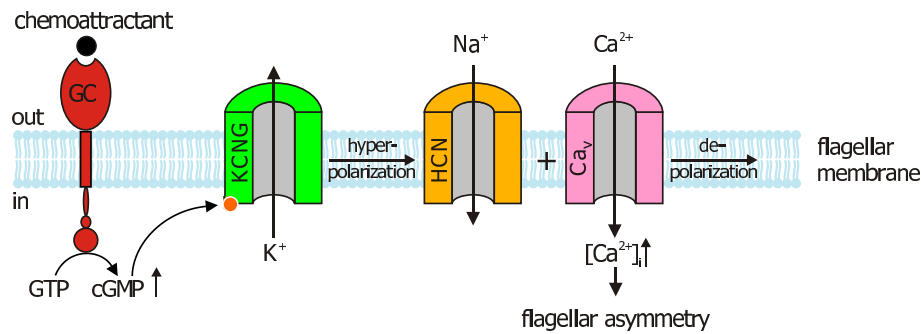
Figure 1.5: The chemotactic signaling cascade in sea urchin sperm: Chemoattractant molecules bind to receptors (GC) within the flagellar membrane which commence the production of cGMP after binding. The second messenger cGMP opens K^+-selective cyclic-nucleotide-gated ion channels (KCNG) which induces a potassium efflux that hyperpolarizes the flagellar membrane. As a response to the hyperpolarization, voltage-sensitive HCN and Ca^{2+}channels open and depolarize the membrane again. The rise of intra-flagellar calcium concentration $[Ca^{2+}]_i$ induces an increased asymmetry of the flagellar beat pattern. Adapted from [148] with permission.

Interestingly, this signaling system operates over a vast range of chemoattractant concentrations ranging from pico-molar to micro-molar concentrations [148], and probably can respond to single chemoattractant molecules [77]. This suggests that adaptation plays an important role in sperm chemotactic signaling. Adaptation is well established in bacterial chemotaxis [17].

1.2.3 The flagellum is a universal structure

The flagellum is a universal structure which is expressed not only in sperm cells, but also in many other eukaryotic cells [115,158,160]. Note that short flagella are often called cilia. Cilia and flagella can be motile and generate flows, or they can serve like an antenna as sensory structures to probe the environment [145].

Motile flagella generate flow.   The prime example for a motile flagellum is of course the flagellum of a sperm cell which propels the cell in a liquid by its regular flagellar beat. The unicellular alga *Chlamydomonas* swims with a breast-stroke swim pattern of its two flagella [132] and the unicellular protozoon *Paramecium* is covered by an array of cilia which beat in synchrony as a metachronal wave and locomote the cell [95]. Besides their role in cell locomotion, motile cilia generate flows resulting in transport: Ciliar arrays in the fallopian tubes of female mammals transport the ovum from the ovary to the uterus, while cilia of epithelial cells in the respiratory tract transport mucus away from the lungs [5]. In the multicellular green alga *Volvox* outward pointing flagella generate a flow to enhance nutrient uptake [146]. Finally, during embryonic development, nodal cilia generate a flow which transports morphogens resulting in the establishment of left-right asymmetry [109,110].

Flagella as sensory organelles.   Many eukaryotic cells express primary cilia with an "9+0"-axoneme which apparently have some sensory function [143]; for example kidney primary cilia can act as mechanoreceptors [116]. In several sensory organs of mammals, the actual task of sensation is performed by specialized cilia: Olfactory sensory neurons project cilia to detect air-borne odor molecules, and photoreceptor rod cells have a modified cilium containing the photosensitive pigment rhodopsin [116,145]. In the vertebrate ear, specialized cilia, the kinocilia, are intimately related to the hairbundles that detect sound waves [115]. In all these examples, the flagellum harbors a signaling system [78]. The high surface-to-volume ratio of a flagellum makes it an ideal antenna to detect and amplify weak stimuli. The sensitivity is striking in the above examples: Photoreceptor rod cells, for example, can detect single photons [63].

1.3   Sperm chemotaxis

1.3.1   Fertilization strategies

External fertilization, e.g. in marine species.   In external fertilizers, sperm cells are directly spawned into the sea where the sperm plume becomes rapidly diluted. Dilution is a prerequisite to activate sperm motility [153]. The eggs are either also spawned directly into the sea (egg-broadcaster) or kept within the female (egg-brooders). Some egg brooders can filter dilute sperm out of the water column [167]. In many species with external fertilization, eggs release chemical factors which are sensed by the sperm cells and provide the sperm with information about the position of the egg. Sperm cells can show enhanced motility and respiration as a response (chemokinesis), or they are able to detect a concentration gradient of such an egg-derived factor and steer upwards the gradient towards the source (chemotaxis) [100,159]. Sperm chemotaxis has been reported for example in the sea urchin [79,107], the star fish [22], the abalone [129], and in *Xenopus*, the African clawed frog [114]. A review of sperm chemotaxis in the animal kingdom can be found in [100]. Sperm chemotaxis has been also demonstrated in plants for bracken fern spermatozoids [25]. In several species, the chemoattractants have been identified [22,79,107,114,129,165]; the chemoattractants are usually short peptides or amino-acids. In the best studied example, the sea urchin *Arbacia punctulata*, the chemoattractant is the oligopeptide resact with a length of 14 amino-acids [79].

Sperm chemotaxis increases sperm-egg encounter rates and is important in ecological conditions of sperm limitation where eggs run the risk of remaining unfertilized due to low sperm concentration [91,167]. Sperm chemotaxis is one of several counter-measures that are found in external fertilizers to overcome sperm limitation: For example, in each spawning event of external fertilizers approximately $10^9 - 10^{10}$ sperm cells are spawned [147] as compared to only $10^7 - 10^9$ sperm cells ejaculated in mammalian mating [46]. Eggs are often enlarged with supplementary jelly layers to increase their diameter [52]. Spawning of eggs and sperm cells are synchronized, possibly triggered by temperature changes or chemical communication [117]. Also, individuals aggregate

in dense colonies, even at the cost of social stress to increase sperm-egg encounter rates [117].

Sperm cells not only swim actively; maybe even more importantly they are moved passively: They are convected by currents and complex hydrodynamic flows [53,112,130] and fertilization can occur several meters downstream from the spawning site [9]. It has been shown recently that a weak shear flow may enhance fertilization success as compared to conditions of still water [130]. We speculate that active swimming of sperm cells might be relevant only in the vicinity of the egg. Likewise, chemoattractant concentrations may be high enough to facilitate sperm chemotaxis only at distances of a few millimeter away from the egg.

The benefit of sperm chemotaxis for external fertilizers is twofold: First of all, sperm-egg encounter rates are enhanced. Secondly, sperm chemotaxis helps to main species barriers [128]: Chemoattractants differ strongly among species and chemotactic responsiveness to chemoattractants of different species is low [100]. In internal fertilizers, species specifity is ensured by alternative measures and sperm cells are often responsive to chemoattractants of a different species [150].

Mammals with internal fertilization. In internal fertilizers, the situation differs significantly. Sperm cells are directly deposited into the female genital tract; sperm concentration are usually sufficiently high to ensure reliable fertilization of the egg. Sperm cells are transported passively by uterine muscle contractions and they swim actively [149]. Chemotaxis of mammalian sperm cells to follicular factors has been demonstrated in humans [46,124], in mice [60,113] and in rabbits [50]. Additionally, it has been implied that mammalian sperm cells probably can orient in temperature gradients by thermotaxis [10]. Mammalian sperm cells undergo a ripening process within the female genital tract, the so-called capacitation. Only capacitated sperm cells are chemotactily responsive which makes chemotaxis assays for mammalian sperm difficult [48,57]. In fact, mammalian sperm chemotaxis is much less understood than in external fertilizers.

Sperm numbers are often surprisingly low in the vicinity of the egg, despite the high number of sperm cells deposited [48]. It has been proposed that the way through the uterus and the fallopian tubes towards the egg serves as a steeplechase to select healthy sperm cells with vigorous motility and full chemotactic ability [149].

1.3.2   Chemotaxis via spatial or temporal comparison

Chemotaxis requires the detection of a concentration gradient of a chemoattractant. Two principle mechanism can be thought of for this task:

- An organism can detect a concentration gradient by **spatial comparison**, i.e. by comparing concentrations at different parts of its body.

– Alternatively, an organism can employ **temporal comparison**, that is measure the local concentration at its position and respond to temporal changes of this concentration which arise from its own active motion in a concentration gradient.

Both mechanisms can be found in nature: The bacterium *E. coli* uses temporal comparison for its chemotaxis [138] and there is strong evidence that sperm chemotaxis is based on temporal comparison as well [22,57]. Chemotaxis of neutrophils [65] and the slime mold *Dictyostelium* [169], for example, relies on spatial comparison. A general mechanism for chemotaxis by spatial comparison has been proposed by Levine [88]. Berg and Purcell gave an estimate for the precision a cell can possibly achieve in measuring a concentration based on the number of molecules that will diffuse towards the cell in a given time interval. This number is proportional to the linear dimension of the cell as well as the time interval of measurement. If the cell is moving, the measuring time is limited if the concentration measured should correspond to a particular position. Berg and Purcell conclude that detecting a concentration gradient by spatial comparison requires a high precision of concentration measurements and is only feasible for large or slowly moving cells [19,20].

The best studied case of chemotaxis, both experimentally and theoretically, is the chemotaxis of the bacterium *E. coli*: It has been shown that these bacteria undergo a biased random walk toward the source of a chemoattractant. This is achieved by stochastic switching between running and tumbling modes of motion which is controlled by a chemotactic signaling system in a way that depends on the history of the chemotactic stimulus [17,18,138]. This chemotactic system provides a general mechanism for chemotaxis of microorganisms [17,18]. The swimming of sperm cells is very different from bacterial swimming: Sperm cells swim along circular and helical paths. The differences of the swimming motion of sperm cells as compared to bacteria suggest that fundamentally different principles of chemotaxis are at work in sperm.

1.3.3   Sperm chemotaxis in the sea urchin

We will focus on the chemotaxis of sea urchin sperm because of the large amount of experimental data available for this system. Sea urchins spawn both sperm and egg cells into the open sea.

In a two-dimensional experimental geometry, sea urchin sperm cells swim in circles in the absence of chemoattractant [22,61,100]. In a concentration gradient of chemoattractant, they swim along drifting circles, see figure 1.7(a). The curvature of the swimming path is periodically modulated with the frequency of circular swimming, see figure 1.7(b). The local chemoattractant concentration at the position of the sperm head changes in time due to the active motion of the sperm cell in the concentration gradient. This chemotactic stimulus is periodically modulated and strongly correlated with the curvature of the swimming path, see figure 1.7(b). In this experiment, also the fluorescence of a calcium-sensitive dye was recorded, which had been loaded into the
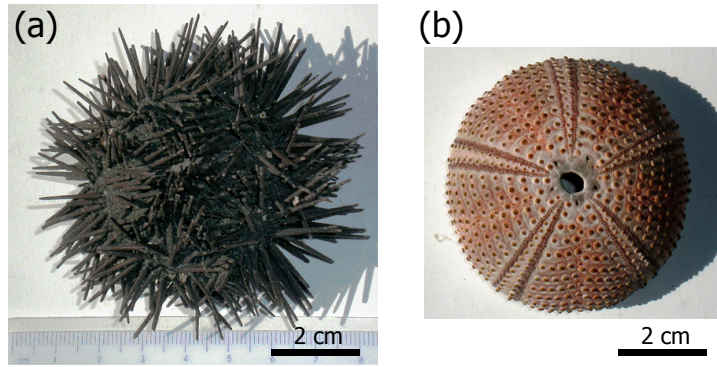
Figure 1.6: Sea urchin shell. Sea urchins are members of the phylum *Echinodermata*; they are external fertilizers which spawn their sperm cells directly into the open sea. Their inner organs are located in the inner cavity of the test, a hard shell covered with spines. Shown is a specimen of *Arbacia lixula* which is commonly found in the Mediterranean: (a) Test covered with spines, (b) test with spines removed, the five-fold symmetry of the sea urchin is apparent.

sperm flagellum before the experiments and which serves as an indicator for intraflagellar calcium concentration. Again, strong correlation between the chemotactic stimulus and the fluorescence trace was found (data not shown). Single-sperm experiments of this kind consolidate our picture of chemotactic signaling in which chemoattractant stimulates a chemotactic signaling network within the sperm flagellum which modulates the intraflagellar calcium concentration and the geometry of the sperm swimming path.

Other experimental techniques include stimulation of single sperm cells not with chemoattractants but with second messengers such as cGMP which is involved in downstream chemotactic signaling. A stimulation with cGMP elicits a chemotactic response [22] similar to stimulation with chemoattractant. Also stopped-flow experiments on the level of a whole population of sperm cells have been performed where a suspension of sperm cells loaded with specialized dyes is rapidly mixed with chemoattractant solution and the fluorescence signal of from the dye is recorded. With these experiments it is possible to record for example the flagellar membrane potential during a chemotactic response [148].

Sperm swimming paths have been also observed far from boundary surfaces in three dimensional space: There sperm cells swim along helical paths with net motion along the centerline of the helix [25,33,37,38,61]. In a concentration gradient of chemoattractant, these helices bent and align with the concentration gradient [25,37].

1.4   Overview of this thesis

In the next chapter, we review fundamental aspects of self-propulsion at low Reynolds numbers relevant for sperm swimming and discuss how an asymmetric flagellar beat
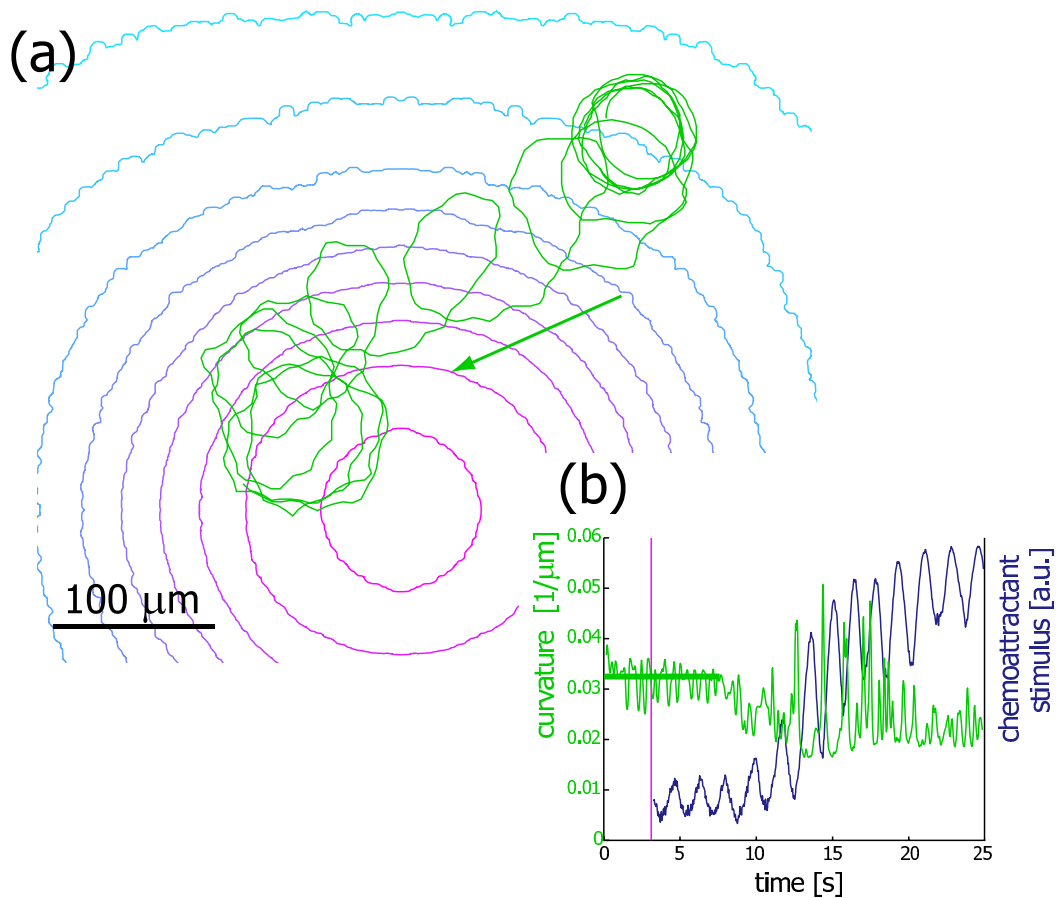
Figure 1.7: A sea urchin sperm cell swimming in a radial concentration field of chemoat-
tractant near a boundary surface. The concentration field was established by exposing
a homogenous solution of an inactive form of the chemoattractant to a short flash of
UV light at time = 2.9 s of the experiment to activate the chemoattractant.
(a) The trajectory of the sperm head is shown in green: At the beginning of the experi-
ment, before the UV-flash, the swimming path is a circle. After the UV-flash, the sperm
cell swims in a concentration gradient of chemoattractant along a swimming path that
resembles a drifting circle. Finally, the sperm cells resumes circular swimming again,
possibly due to over-stimulation. Iso-concentration lines of the initial chemoattrac-
tant concentration field are shown in shades of red (high) and blue (low). Since this
experimental method is difficult to calibrate, absolute concentrations are not known.
(b) Curvature of the sperm swimming path shown in panel (a): One can distinguish a
phase of constant curvature corresponding to a circular swimming path ($t = 0 \ldots 10 \, \mathrm{s}$),
followed by a phase characterized by a sequence of curvature spikes occurring approx-
imately with the frequency of circular swimming ($t = 10 \ldots 20 \, \mathrm{s}$). The second phase
corresponds to a swimming path resembling a drifting circle. Also shown is the local
chemoattractant concentration at the position of the sperm head. This chemotac-
tic stimulus is periodically modulated with the frequency of circular swimming and
is strongly correlated with the curvature of the sperm swimming path. The time of
the UV-flash is indicated (magenta). The rawdata was generously provided by Luis
Alvarez, Luru Dai and Benjamin Kaupp.

gives rise to circular and helical swimming paths.

In the third chapter, we develop a theoretical description of sperm chemotaxis along circular and helical paths. In our theoretical description of sperm chemotaxis in two and three dimensions, sperm cells probe a concentration field of chemoattractant along their swimming path. The chemotactic stimulus thus traced from the concentration field serves as the input of a chemotactic signaling system. Chemotactic signaling is described by a generic signaling module that regulates the curvature and torsion of the swimming path.
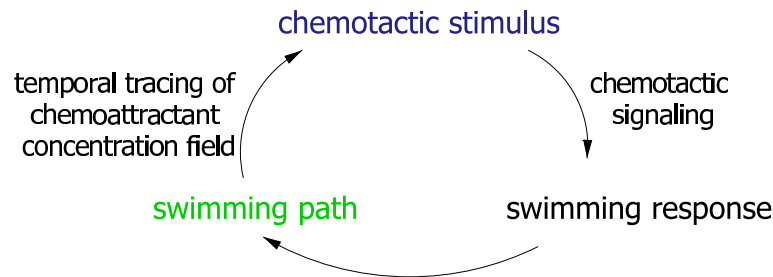
In the presence of a chemoattractant, swimming paths are drifting circles in two dimensions and deformed helices in three dimensions. The swimming paths can be described by a dynamical system that exhibits different dynamic regimes, which correspond to different chemotactic behaviors. We conclude that sampling a concentration field of chemoattractant along circular and helical swimming paths is a robust strategy for chemotaxis which works reliably for a vast range of parameters.

In the fourth and fifth chapter, we extend the deterministic theoretical description of chapter three to account for fluctuations inherent in sperm chemotaxis. Such fluctuations are given by the stochasticity in the counting of chemoattractant molecules, intrinsic fluctuations of the chemotactic signaling system and fluctuations of flagellar propulsion. The fourth chapter deals with the two dimensional case using complex notation; whereas in the fifth chapter the three-dimensional case is treated using the formalism of rigid body transformations. We derive stochastic effective equations of motion for sperm swimming paths in a concentration field which generalize the effective equations obtained in the deterministic description.

In the last chapter, we place the search of sperm cells for the egg in a more general context of an abstract search problem. In this search problem target distance and search time are specified; we find that search success is maximal if the level of fluctuations attains a finite value.

Chapter 2
Swimming of sperm cells

*Sperm cells are propelled in a liquid by the regular beat of their flagellum. The hydrody-
namics of flagellar propulsion is characterized by low Reynolds numbers. In this chapter
we first review swimming at low Reynolds numbers and then discuss sperm swimming
paths. In particular, we show how an asymmetric planar flagellar beat pattern gives
rise to circular swimming paths.*

2.1   Self-propulsion at low Reynolds numbers

The Stokes equation.   The swimming of sperm cells and of microorganisms is char-
acterized by low Reynolds numbers [86,122]. The Reynolds number of a swimmer is
defined as the dimensionless quantity

$$\mathrm{Re} = \frac{\rho \, v \, l}{\eta} \tag{2.1}$$

where l is a typical length scale of the swimmer, v a typical speed, η and ρ are the
viscosity and density of the surrounding liquid, respectively. The Reynolds number is
an estimate for the ratio of inertial and viscous terms in the Navier-Stokes equation
(for incompressible Newtonian fluids)

$$\rho \left(\dot{\mathbf{u}} + (\mathbf{u} \cdot \boldsymbol{\nabla})\mathbf{u} \right) = -\boldsymbol{\nabla} p + \eta \Delta \mathbf{u} \tag{2.2}$$

where $\mathbf{u}$ and p are the velocity and pressure fields of the fluid. Approximately, the
inertial terms on the left-hand side of (2.2) scale as $\rho \, \mathbf{u} \cdot \boldsymbol{\nabla}\mathbf{u} \sim \rho \, v^2/l$; whereas the
viscous terms on the right-hand side scale as $\eta \Delta \mathbf{u} \sim \eta \, v/l^2$.

For a swimming sperm cell, the Reynolds number is very small: We estimate $\mathrm{Re} \sim 10^{-3}$
using the diameter of the flagellum $l = 0.2 \, \mu\mathrm{m}$ as the relevant lengthscale and a maximal
speed $v \lesssim 1 \, \mathrm{cm/s}$ of the flagellum during flagellar beating [125], as well as the density
and viscosity of water, $\rho = 10^3 \, \mathrm{kg/m^3}$ and $\eta = 10^{-3} \, \mathrm{kg \, m^{-1} \, s^{-1}}$, respectively. Note that
it is the diameter rather than the length of the flagellum which is relevant in evaluating
the stress set up in the fluid by the motion of the flagellum [145].

In the limit of zero Reynolds number, the Navier-Stokes equation (2.2) becomes the
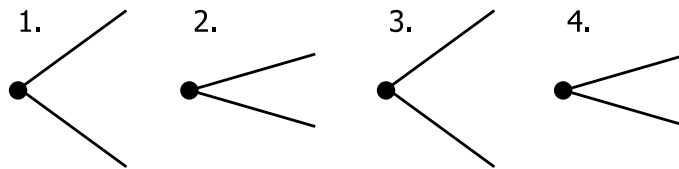
Figure 2.1: The swimming stroke of Purcell's scallop: This microswimmer consists of two legs connected by a joint and is immersed in a viscous liquid. As the angle between the two legs changes periodically, the swimmer will move back and forth. Its net displacement, however, will be zero in the zero Reynolds number limit, since the swimming stroke is reciprocal.

Stokes equation for creeping flows[1]

$$0 = -\nabla p + \eta \Delta \mathbf{u}. \tag{2.3}$$

The Stokes equation (2.3) is linear, thus the velocity field $\mathbf{u}$ scales linearly with the rate of shape change of a swimmer immersed in the liquid. As a consequence the path of the swimmer is determined solely by the sequence of shapes the swimmer assumes and does not depend on the rate of shape change.

The scallop theorem. The motion of a swimmer is called reciprocal if the sequence of shapes which the swimmer assumes is invariant under time-reversal. Since the Stokes equation is linear, it follows that such a swimmer has zero net displacement. A classical example illustrating this fact is Purcell's scallop [122]: a one-hinged swimmer consisting of two straight legs connected by a joint. A periodic change in the angle between the two legs is necessarily a reciprocal motion, and Purcell's scallop cannot swim. This example gave the name 'scallop theorem' to the fact that a swimmer must have at least two degrees of freedom to achieve net propulsion.

The quadratic law. For the following, see Shapere and Wilczek [84,142]. Consider a low-Reynonld's number swimmer, that changes its shape periodically. The quadratic law states that in the limit of small shape deformations of size ε, the net displacement of this swimmer after one swimming stroke scales as ε^2. For the proof, note that a cyclic shape change of small size can be expressed as a superposition of reciprocal shape changes. By the scallop theorem, none of these reciprocal modes of shape change gives rise to a net displacement of the swimmer. Due to the nonlinearity of the problem, however, there will be coupling terms between different reciprocal modes which cause a net displacement. The coupling terms are quadratic in ε. Numerous examples illustrating the quadratic law have been worked out, including the three sphere swimmer [104], the Purcell rotator [42], the Purcell three-link swimmer [12] and last but not

---

[1]The solutions of equation (2.3) provide suitable approximations for the flow-field near a low-Reynolds number swimmer and in particular allows the computation of its swimming path. However these solutions may provide wrong answers for the far-field of such a flow since at large distances from the swimmer inertial and viscous terms can become comparable [86].
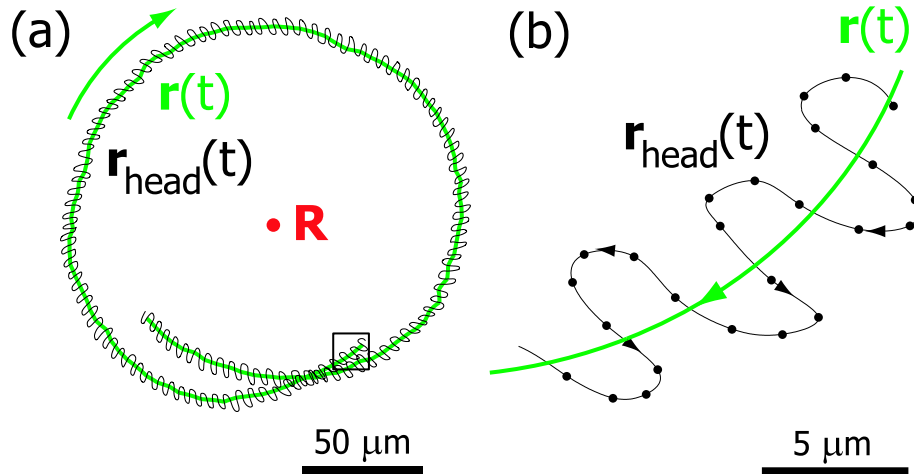
Figure 2.2: Trajectory $\mathbf{r}_{\text{head}}(t)$ of the head of a swimming bull sperm cell (black) and averaged swimming path $\mathbf{r}(t)$ (green). (a) The motion of the head is the superposition of a uniform motion and a periodic movement with the frequency of the flagellar beat. Averaging over the period of the flagellar beat yields the averaged swimming path. In the present case, the averaged swimming path is a circular trajectory with center $\mathbf{R}$ (red dot). (b) Magnified view of a portion of panel (a). Black dots indicated the measured positions of the sperm head; the sampling rate was 250 frames per second. The black line interpolates the data points. The experimental data was kindly provided by Ingmar Riedel-Kruse; methods and materials are described in [125].

least the swimming of sperm cells by beating their flagellum [61,81,141,144].

2.2   How to define sperm swimming paths?

Swimming paths. The swimming path of a swimming sperm cell allows for different definitions depending on the level of coarse-graining: In experiments, the *trajectory of the head* $\mathbf{r}_{\text{head}}(t)$ was seen to be a superposition of a uniform motion and a periodic movement of the head with the angular frequency ω_f of the flagellar beat [57,61], see figure 2.2. On intermediate time and length scales, one may average over the period of flagellar beat to define the *averaged swimming path* $\mathbf{r}(t)$. For sperm cells of many species, the averaged swimming path is circular near surfaces [22,61,100] and helical in three-dimensional space far from boundaries [25,33,37,38,61]. In these cases, an effective swimming path $\mathbf{R}(t)$ can be defined as the trajectory of the centerpoint of the swimming circle or as the *centerline* of the helical swimming path, respectively.

Swimming velocities. Let $\mathcal{G} = (\mathbf{e}_1, \mathbf{e}_2, \mathbf{e}_3, \mathbf{r}_{\text{head}})$ be a material frame of the sperm head with an orthonormal set of vectors $\mathbf{e}_j$ such that $\mathbf{e} = \mathbf{e}_1$ is parallel to the long axis of the head, see figure 2.3. We define the instantaneous translational velocity $\mathbf{v}(t)$ as

$$\dot{\mathbf{r}}_{\text{head}} = \mathbf{v} = v_j\, \mathbf{e}_j \qquad (2.4)$$
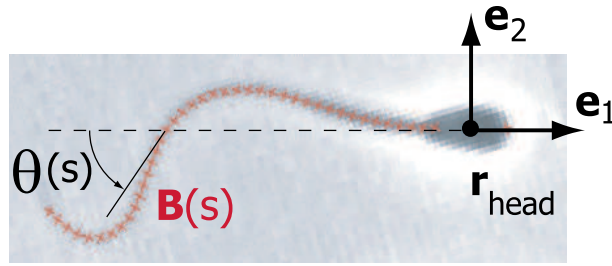
Figure 2.3: We choose a material frame $\mathcal{G} = (\mathbf{e}_1, \mathbf{e}_2, \mathbf{e}_3, \mathbf{r}_{\text{head}})$ for the sperm head: Here $\mathbf{r}_{\text{head}}$ is the center of the head and $\mathbf{e}_j$ is an orthonormal set of vectors with $\mathbf{e}_1$ parallel to the long axis of the head. The shape of the sperm's flagellum is characterized by the shear angle θ as a function of arclength s: $\theta(s)$ is the angle enclosed by the long axis of the head and the local tangent of the centerline $\mathbf{B}(s)$ of the flagellum.

and the instantaneous rotational velocity $\mathbf{\Omega}(t)$ such that

$$\dot{\mathbf{e}}_j = \mathbf{\Omega} \times \mathbf{e}_j = \epsilon_{kjl}\,\Omega_k\,\mathbf{e}_l \tag{2.5}$$

where Einstein summation convention is assumed and ϵ_{kjl} denotes the Levi-Civita symbol.

For a perfectly periodic flagellar beat, the velocity components $v_j(t)$ and $\Omega_j(t)$ will be periodic functions. The net motion after a time t is characterized by a translation vector $V \in \mathbb{R}^3$ and a rotation matrix $W \in SO(3)$

$$V(t)_j = [\mathbf{r}_{\text{head}}(t) - \mathbf{r}_{\text{head}}(0)] \cdot \mathbf{e}_j(0), \quad W(t)_{kl} = \mathbf{e}_k(0) \cdot \mathbf{e}_l(t). \tag{2.6}$$

Together, V and W describe a rigid body transformation $G = (V, W)$ which can be represented by a 4×4-matrix that reads in block matrix notation

$$G(t) = \begin{bmatrix} W(t) & V(t) \\ 0\ 0\ 0 & 1 \end{bmatrix} \in SE(3) \tag{2.7}$$

where $SE(3)$ denotes the Lie group of rigid body transformation, see appendix D. Rigid body transformations will be also used extensively in chapter 5. The dynamics of $G(t)$ is given by the matrix-valued differential equation

$$\dot{G} = G \cdot g \tag{2.8}$$

where g is an infinitesimal rigid body transformation that unites the instantaneous

rotational velocity $\boldsymbol{\Omega}$ and the instantaneous rotational velocity $\mathbf{v}$

$$
\mathrm{g} = \begin{bmatrix} 0 & -\Omega_3 & \Omega_2 & v_1 \\ \Omega_3 & 0 & -\Omega_1 & v_2 \\ -\Omega_2 & \Omega_1 & 0 & v_3 \\ 0 & 0 & 0 & 0 \end{bmatrix} \in \mathfrak{se}(3). \tag{2.9}
$$

In fact, equation (2.8) is just a reformulation of equations (2.4), (2.5). The solution of the differential equation (2.8) with initial condition $\mathrm{G}(0) = \mathbb{1}$ can be given as a (reverse) time-ordered exponential integral, see appendix D

$$
\begin{aligned}
\mathrm{G}(t) &= \mathbf{T}\exp \int_0^t dt_0\, \mathrm{g}(t_0) \\
&= \sum_{n=0}^{\infty} \int_{0<t_1<...<t_n<t} dt_1 \cdots dt_n\, \mathrm{g}(t_1) \cdots \mathrm{g}(t_n).
\end{aligned} \tag{2.10}
$$

For a time-independent $\mathrm{g}(t) = \mathrm{g}_0$, the time-ordered exponential integral equation (2.10) is just the ordinary matrix exponential $\mathrm{G}(t) = \exp t\mathrm{g}_0$. In appendix D, we show that the matrix logarithm of $\mathrm{G}(T_f)$ represents averaged swimming velocities, where $T_f = 2\pi/\omega_f$ is the period of the flagellar beat

$$
\log \mathrm{G}(T_f) = T_f \bar{\mathrm{g}} = T_f \begin{bmatrix} 0 & -\bar{\Omega}_3 & \bar{\Omega}_2 & \bar{v}_1 \\ \bar{\Omega}_3 & 0 & -\bar{\Omega}_1 & \bar{v}_2 \\ -\bar{\Omega}_2 & \bar{\Omega}_1 & 0 & \bar{v}_3 \\ 0 & 0 & 0 & 0 \end{bmatrix}. \tag{2.11}
$$

The averaged translational velocity

$$
\bar{\mathbf{v}} = \bar{v}_j\, \mathbf{e}_j \tag{2.12}
$$

and the averaged rotational velocity

$$
\bar{\boldsymbol{\Omega}} = \bar{\Omega}_j\, \mathbf{e}_j \tag{2.13}
$$

are the velocities by which the sperm cells travels along the averaged swimming path $\mathbf{r}(t)$: A swimmer that moves with the constant velocities $\bar{\mathbf{v}}$ and $\bar{\boldsymbol{\Omega}}$ will have changed its position and orientation by the rigid body transformation G after time T_f. We define the averaged speed v_0 as $v_0 = |\bar{\mathbf{v}}|$ and the angular frequency ω_0 of the averaged motion as $\omega_0 = |\bar{\boldsymbol{\Omega}}|$.

Helical swimming paths. For a sperm cell with perfectly periodic flagellar beat pattern, the instantaneous velocities $v_j(t)$ and $\Omega_j(t)$ are periodic functions of time t and the averaged velocities $\bar{v}_j$ and $\bar{\Omega}_j$ are constant. In this case, the resulting (averaged) swimming path is a perfect helix with radius r_0 and pitch $2\pi h_0$ that depend on the averaged velocities $\bar{v}_j$ and $\bar{\Omega}_j$. Note that the helix may be degenerated and actually be

a circle if $h_0 = 0$. The rotational velocity $\boldsymbol{\Omega}$ is the sum of two components

(i) a component $\boldsymbol{\Omega}_\parallel = \Omega_\parallel \, \bar{\mathbf{v}}$ parallel to $\bar{\mathbf{v}}$ of length $\Omega_\parallel = (\bar{\boldsymbol{\Omega}} \cdot \bar{\mathbf{v}})/v_0$, and

(ii) a component $\boldsymbol{\Omega}_\perp = \bar{\boldsymbol{\Omega}} - \boldsymbol{\Omega}_\parallel$ perpendicular to $\bar{\mathbf{v}}$ of length $\Omega_\perp = |\boldsymbol{\Omega}_\perp|$.

In general $\Omega_\parallel \neq 0$, $\Omega_\perp \neq 0$ and the averaged swimming path $\mathbf{r}(t)$ is a helix with radius r_0, pitch $2\pi h_0$ and angular frequency ω_0 where

$$r_0 = \frac{v_0}{\omega_0^2}\,\Omega_\perp, \quad \text{and} \quad h_0 = \frac{v_0}{\omega_0^2}\,\Omega_\parallel. \tag{2.14}$$

The helix is right-handed for $\Omega_\parallel > 0$ and left-handed for $\Omega_\parallel < 0$. If $\Omega_\parallel = 0$, the averaged swimming path is a planar circle with radius $r_0 = v_0/\omega_0$, and if both $\Omega_\parallel = \Omega_\perp = 0$ then the averaged swimming path $\mathbf{r}(t)$ is a straight line.

2.3   Sperm swimming paths in a plane

Swimming of sperm cells is usually observed in a shallow observation chamber; in such a setup sperm cells localize at the boundary surface where they swim with a planar flagellar beat pattern along planar paths. For sperm cells from many species, these planar swimming paths are circles [22,77,79,100,162,165]. The non-zero curvature of the swimming path is a consequence of the asymmetry of the flagellar beat of the sperm cell.

The shape of the flagellum is characterized by its centerline $\mathbf{B}(s,t)$ which is a function of arclength s and time t. In the material frame of the head $\mathcal{G} = (\mathbf{e}_1, \mathbf{e}_2, \mathbf{e}_3, \mathbf{r}_{\text{head}})$, we can express $\mathbf{B}(s,t)$ as

$$\mathbf{B}(s,t) = \mathbf{r}_{\text{head}}(t) + b_j(s,t)\,\mathbf{e}_j(t). \tag{2.15}$$

We may assume that $\mathbf{e}_3$ is constant and perpendicular to the plane of swimming; we then have $b_3 = 0$. Instead of b_1, b_2, we can use the shear angle θ to characterize the flagellar beat: $\theta(s,t)$ is the angle enclosed by the long axis of the head $\mathbf{e}_1$ and the local tangent of the flagellum $\mathbf{t}(s,t) = \partial_s \mathbf{B}(s,t)$ and satisfies $\cos\theta = \partial_s b_1$, $\sin\theta = -\partial_s b_2$. See figure 2.3.

Resistive force theory.   We want to compute swimming velocities from the flagellar beat pattern. For this we use resistive force theory as introduced by Gray and Hancock [61]. The central idea of resistive force theory is to compute the hydrodynamic drag force $\mathbf{f}$ of a bent rod by decomposing the rod into a sequence of infinitesimal cylinders and sum up the drag forces of all cylinders. The drag force acting on a moving cylinder of length ds is linear in the components of its velocity $\mathbf{v}$ where $\mathbf{v}_\perp$, $\mathbf{v}_\parallel$ are the
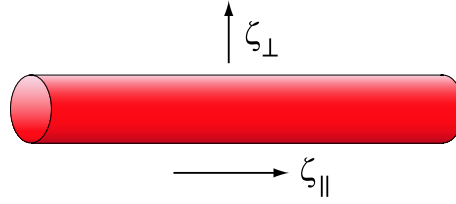
Figure 2.4: The hydrodynamic drag force of a moving cylinder is characterized by drag coefficients $\zeta_\perp$ and $\zeta_\parallel$ for motion perpendicular and parallel to the long axis of the cylinder, respectively. See equation (2.16). The hydrodynamic drag force of a sperm flagellum can be approximated by decomposing it into a sequence of cylinders.

components of $\mathbf{v}$ perpendicular and parallel to the cylinder's long axis, respectively [2]

$$\mathbf{f} = -\zeta_\perp \mathbf{v}_\perp ds - \zeta_\parallel \mathbf{v}_\parallel ds. \tag{2.16}$$

The drag coefficients $\zeta_\perp$ and $\zeta_\parallel$ are given in appendix J.3. In the limit of an infinitely slender cylinder, the ratio $\zeta_\perp/\zeta_\parallel$ approaches 2.

Let $\mathbf{t}(s,t) = \partial_s \mathbf{B}(s,t)$ be the tangent vector along the flagellum. On each infinitesimal segment of the flagellum $\mathbf{t}\, ds$ acts a hydrodynamic drag force density

$$\mathbf{f}(s,t) = -\zeta_\perp \dot{\mathbf{B}}(s,t) - (\zeta_\parallel - \zeta_\perp)\left(\dot{\mathbf{B}}(s,t)\cdot\mathbf{t}(s,t)\right)\mathbf{t}(s,t) \tag{2.17}$$

The total force and the total torque acting on the flagellum are

$$\mathbf{F}(t) = \int_0^L ds\, \mathbf{f}(s,t), \quad \mathbf{M}(t) = \int_0^L ds\, \mathbf{f}(s,t) \times \mathbf{B}(s,t) \tag{2.18}$$

where L is the length of the flagellum. Since no external forces or torques act on the sperm cell, force and torque balance must hold

$$\mathbf{F}(t) \stackrel{!}{=} 0, \quad \mathbf{M}(t) \stackrel{!}{=} 0. \tag{2.19}$$

Equation (2.19) provides a linear equation for the velocities $\mathbf{v}(t)$ and $\mathbf{\Omega}(t)$ [3]

$$\Gamma \begin{bmatrix} \mathbf{v} \\ \mathbf{\Omega} \end{bmatrix} = - \begin{bmatrix} \mathbf{F}_1 \\ \mathbf{M}_1 \end{bmatrix}. \tag{2.20}$$

Here Γ is a 6×6-matrix, the so-called resistance matrix, with block structure

$$\Gamma = \begin{bmatrix} \Gamma_{\mathbf{F},\mathbf{v}} & \Gamma_{\mathbf{F},\mathbf{\Omega}} \\ \Gamma_{\mathbf{M},\mathbf{v}} & \Gamma_{\mathbf{M},\mathbf{\Omega}} \end{bmatrix}. \tag{2.21}$$

The precise form of the vectors $\mathbf{F}_1(t)$ and $\mathbf{M}_1(t)$, as well as of the resistance matrix $\Gamma(t)$

---

[2]This approach is feasible if the local radius of curvature of the bent rod is much larger than the diameter of the rod.

[3]For ease of notation, we identify vectors with their coordinate representations with respect to the material frame $\mathcal{G}$, i.e. $\mathbf{v} = (v_1, v_2, v_3)$, etc.

is given in appendix J.1. The linear equation (2.20) has a simple physical interpretation: The left-hand side gives the force $\mathbf{F}_2 = \Gamma_{\mathbf{F},\mathbf{v}}\mathbf{v} + \Gamma_{\mathbf{F},\mathbf{\Omega}}\mathbf{\Omega}$ and the torque $\mathbf{M}_2 = \Gamma_{\mathbf{M},\mathbf{v}}\mathbf{v} + \Gamma_{\mathbf{M},\mathbf{\Omega}}\mathbf{\Omega}$ exerted by the swimmer on the fluid when it moves with translational velocity $\mathbf{v}$ and rotational velocity $\mathbf{\Omega}$ without changing its shape. The vectors $\mathbf{F}_1$ and $\mathbf{M}_1$ on the right-hand side of equation (2.20) represent the force and the torque, respectively, exerted by the swimmer on the fluid if it changes its shape according to (2.15), but the frame $\mathcal{G} = (\mathbf{e}_1, \mathbf{e}_2, \mathbf{e}_3, \mathbf{r}_{\text{head}})$ does not move with respect to the lab frame. In solving equation (2.20), we determine an (infinitesimal) change of the co-moving frame $\mathcal{G} = (\mathbf{e}_1, \mathbf{e}_2, \mathbf{e}_3, \mathbf{r}_{\text{head}})$, such that the drag force $\mathbf{F}_2$ and torque $\mathbf{M}_2$ due to this motion cancel the force $\mathbf{F}_1$ and the torque $\mathbf{M}_1$ due to the (infinitesimal) shape change of the flagellum. As a consequence, force and torque balance (2.19) holds.

Drag anisotropy. If the drag coefficients $\zeta_\perp$ and $\zeta_\parallel$ were equal, a bending rod could not move forward. For a one-line proof, let $\overline{\mathbf{B}}(t)$ be the center of mass of a homogenous bending rod. Force balance implies [12]

$$
\frac{d}{dt}\overline{\mathbf{B}} = \frac{1}{L}\frac{d}{dt}\int_0^L \mathbf{B}(s,t)\,ds = \frac{1}{L}\int_0^L \frac{\partial \mathbf{B}}{\partial t}\,ds =
$$
$$
\frac{1}{L}\int_0^L \mathbf{v}(s,t)\,ds \sim \frac{1}{L}\int_0^L \mathbf{f}(s,t)\,ds = \mathbf{F}(t) = 0. \tag{2.22}
$$

Thus drag anisotropy is crucial for forward propulsion. Net rotation, however, is still possible if $\zeta_\perp = \zeta_\parallel$.

Drag force of the head. To describe sperm swimming accurately, the hydrodynamic drag force of the head must be considered [73]. For this aim, the resistance matrix of the head Γ_{head} has to be added to the resistance matrix $\Gamma(t)$ of the flagellum and equation (2.20) be used with $\Gamma_{\text{sperm}} = \Gamma + \Gamma_{\text{head}}$. In our numerical example given in figure 2.6, we approximate the shape of the sperm head as a spheroid and use the formulas for the hydrodynamic drag force and torque of a spheroid, see appendix J.3.

2.3.1 Limit of small flagellar beat amplitude

To illustrate typical effects of flagellar propulsion, we study the limit of small beat amplitudes for an example beat pattern with a shear angle $\theta(s,t)$ that is a function of time t and arclength s

$$
\theta(s,t) = \theta_0 s + \theta_1[\cos(\omega_f t - 2\pi n s/L) - \cos(\omega_f t)]. \tag{2.23}
$$

This beat pattern is a superposition of a curved mean shape and a traveling wave: The zeroth Fourier mode $\theta_0 s$ accounts for an asymmetric mean shape of the flagellum of constant curvature θ_0. The first Fourier mode $\theta_1[\cos(\omega_f - 2\pi n s/L) - \cos(\omega_f t)]$ describes a travelling sine wave of wavelength L/n and constant beat amplitude $2\pi n\theta_1/n$ traveling with speed

$$
v_f = L/nT_f. \tag{2.24}
$$

Note that $\theta(0, t) = 0$; the tangent of the flagellum at its base is always parallel to the long axis of the head $\mathbf{e}_1$. For simplicity, we neglect the drag force of the sperm head. We also assume that the wave number n is an integer. To leading order in θ_0 and θ_1, the average translation speed $\overline{v}$ and the average rotational speed $\overline{\Omega}_3$ read

$$\overline{v} = \Theta_v \left(\frac{\zeta_\perp}{\zeta_\parallel} - 1 \right) \theta_1^2 \, v_f \quad + \mathcal{O}(\theta_0 \theta_1^2, \theta_1^3) \tag{2.25}$$

and

$$\overline{\Omega}_3 = \Theta_\Omega \, \theta_0 \, \theta_1^2 \, v_f \quad + \mathcal{O}(\theta_0^2 \theta_1^2, \theta_0 \theta_1^3) \tag{2.26}$$

with prefactors Θ_v, Θ_Ω that depend on the wave number n and the ratio $\zeta_\perp / \zeta_\parallel$ of drag coefficients[4]

$$\Theta_v = \frac{1}{2} - \frac{6}{(2\pi n)^2},$$
$$\Theta_\Omega = \frac{36[(2\pi n)^2 - 32]\zeta_\parallel^2 - [(2\pi n)^4 - 576]\zeta_\parallel \zeta_\perp + [(2\pi n)^2 - 12](2\pi n)^2 \zeta_\perp^2}{2(2\pi n)^4 \zeta_\parallel \zeta_\perp}. \tag{2.27}$$

We remark on some properties of the expressions (2.25) and (2.26) for the averaged velocities

- Microswimming is a second-order effect: The translational and rotational speed scale with the square of the beat amplitude θ_1^2 in accordance with the quadratic law, see section 2.1. The instantaneous speeds $v_j(t)$ and $\Omega_j(t)$, however, scale linearly with θ_1

$$v_j(t) \sim \theta_1, \quad \Omega_j(t) \sim \theta_1. \tag{2.28}$$

- In the case of isotropic drag coefficients $\zeta_\parallel = \zeta_\perp$, the translational speed $\overline{v}$ vanishes, see the paragraph on drag anisotropy on page 20.

- Provided $\overline{\Omega}_3 \neq 0$, the sperm cell will swim along a circular swimming path with radius $r_0 = \overline{v}/\overline{\Omega}_3$. Hence the curvature of the swimming path $\kappa_0 = 1/r_0$ is proportional to the curvature θ_0 of the mean shape of the flagellum. A similar result was found in [81].

- The direction of forward propulsion is opposite to the propagation direction of the flagellar traveling wave, provided $\zeta_\perp > \zeta_\parallel$. For most flagella $\zeta_\perp \approx 2\zeta_\parallel$ holds, but exceptions exist [23]

Even for a symmetric beat pattern with $\theta_0 = 0$, the instantaneous rotational speed $\Omega_3(t)$ oscillates with the frequency ω_f of the flagellar beat. Of course, the averaged rotational speed $\overline{\Omega}_3$ vanishes in this case, $\overline{\Omega}_3 = 0$, as is required by symmetry. The case of a symmetric flagellar beat with $\theta_0 = 0$ was first addressed in [61,144] and reexamined in [141]. Note that the authors in [61,144] imposed the constraint $\Omega_3(t) = 0$ for their

---

[4]The computation of these prefactors was done according to equations (2.20), (2.4), (2.5), and (2.11) using a computer algebra system and a user-defined term simplification scheme.

calculation. With this constraint, the expressions for the translational speeds $v_j(t)$ look completely different; for the averaged translational speed $\overline{v}$ they find (2.25) with prefactor $\Theta_{\overline{v}} = 1/2$. These differences in the results for $\overline{v}$ highlight the role of constraints in microswimming problems.

2.4   Relation to experiments: Bull sperm swimming in circles

Figure 2.5(a) shows an example of the planar flagellar beat pattern of a bull sperm cell swimming in a plane parallel to the boundary surface of the observation chamber. The period of the flagellar beat is $T_f \approx 32\,\text{ms}$. The beat pattern shown has a pronounced asymmetry. This asymmetry gives rise to a curved (averaged) swimming path: The sperm cell swims in a circle with a radius of $r_0 \approx 30\,\mu\text{m}$, see figure 2.5(b).

Planar swimming is characterized by three velocities : Translational velocities v_1 and v_2 parallel and perpendicular to the long axis of the sperm head, and a rotational velocity Ω_3 describing rotations in the plane of swimming. Figure 2.6 shows the (instantaneous) swimming velocities for the motion of the sperm head along the trajectory shown in figure 2.5. The swimming velocities are periodic with the frequency of the flagellar beat. For the averaged speeds, we have $\overline{v} \approx 110\,\mu\text{m s}^{-1}$ and $\overline{\Omega}_3 \approx -3.8\,\text{s}^{-1}$. Thus the period of circular swimming is $T \approx 1.6\,\text{s}$ in the present example. We can use the measured beat pattern to predict the swimming velocities using resistive force theory. We find good agreement between the measured velocities and the velocities computed from the beat pattern for the translational velocity v_2 perpendicular to the long axis of the head and the rotational velocity Ω_3, see figure 2.6. Resistive force theory was already used in [168] to numerically compute sperm swimming paths from observed flagellar beat pattern of mammalian sperm.

The experimental data analyzed in this section was kindly provided by Ingmar Riedel-Kruse. Materials and methods of his experiments are detailed in [125].

(a)

(b)

10 μm

20 μm
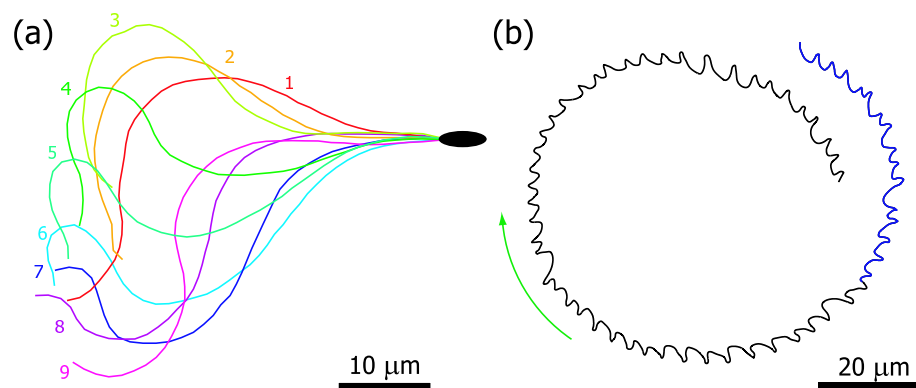
Figure 2.5: Bull sperm swimming with asymmetric flagellar beat along a circular path. (a) Flagellar beat pattern of a swimming bull sperm cell. Subsequent shapes of the flagellum are 4 ms apart and are numbered accordingly. The flagellar beat pattern has a pronounced asymmetry. (b) Shown is the trajectory of the sperm head for an observation period of 2 s. From the trajectory and the orientation of the head, we can obtain instantaneous velocities, see figure 2.6. The part of the trajectory corresponding to the velocity data depicted in figure 2.6 is marked blue. The experimental data was kindly provided by Ingmar Riedel-Kruse.
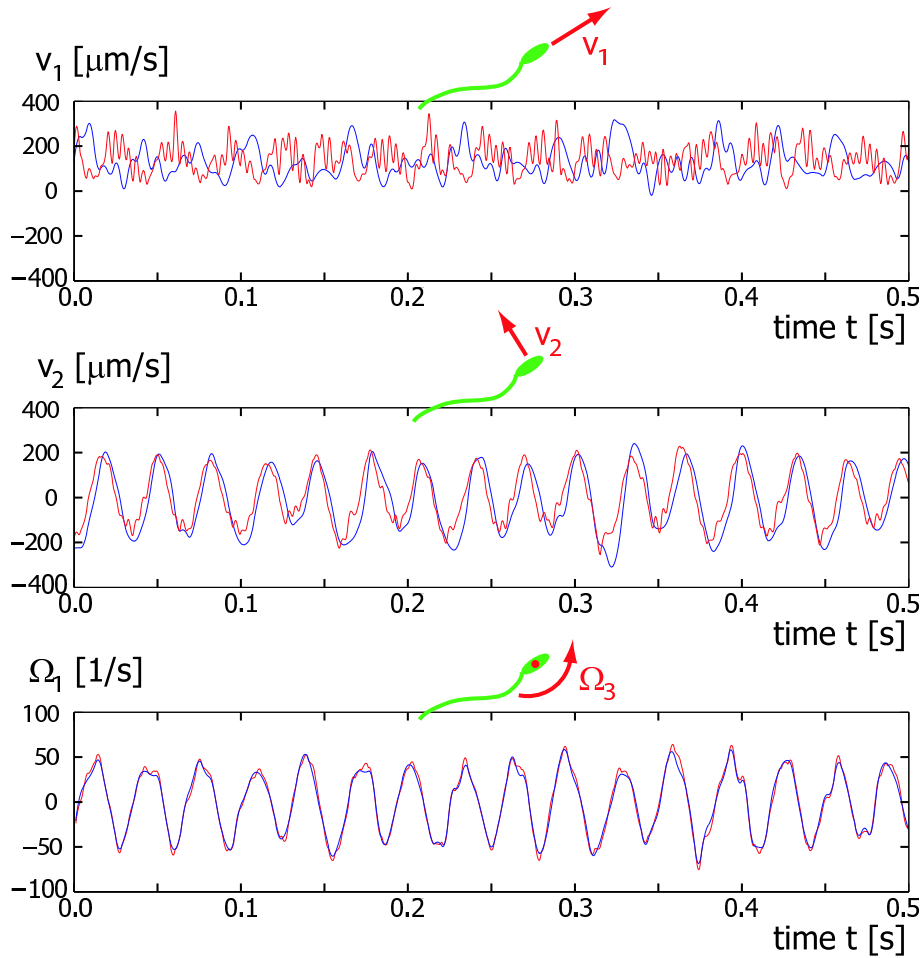
Figure 2.6: instantaneous swimming velocities of a bull sperm cell swimming in a plane (blue graphs). Planar swimming is characterized by three velocities: Translational velocities v_1 and v_2 parallel and perpendicular to the long axis of the sperm head, and a rotational velocity Ω_3 describing rotations in the plane of swimming. The swimming velocities are periodic with the frequency of the flagellar beat. Together with the position and orientation of the head, the shape of the flagellum was measured. We can use the measured beat pattern to predict the swimming velocities using resistive force theory (red graphs). We find good agreement between the measured velocities and the velocities computed from the beat pattern for the translational velocity v_2 perpendicular to the long axis of the head and the rotational velocity Ω_3. For the computation of the velocities, resistive force theory was used with drag coefficients as specified in equation (2.16). Parameters: For the radius of the flagellum, we used $r_f = 0.1\,\mu$m; the hydrodynamic drag of the sperm head was estimated by approximating the head as a spheroid with long axis $r_1 = 5\,\mu$m and short axis $r_2 = 2.5\,\mu$m and using the formulas of Perrin [119]. The experimental raw data was kindly provided by Ingmar Riedel-Kruse.

Chapter 3
Theoretical description
of sperm chemotaxis

In this chapter, we develop a theoretical description of sperm chemotaxis. We characterize a simple and general mechanism for chemotaxis in two dimensions which is motivated by recent experiments [22,79,148,162]. Sperm cells swimming on circular paths in a concentration gradient of a chemoattractant sample a periodic concentration stimulus. Their chemotactic signaling system transfers this stimulus into a periodic modulation of the curvature of the swimming path. As a result the circular path drifts in a direction which depends on the dynamical properties of the signaling system. We show that this principle is more general and also works for helical trajectories in three dimensions. We discuss conditions under which a swimming sperm reaches the egg, both in two and three dimensions. Our work characterizes a novel principle for the chemotaxis of microorganisms along circular and helical paths.

3.1   Chemotaxis along circular paths in a plane

3.1.1   Dynamic equations of sperm motion

Chemotaxis can be studied in two dimensions for sperm swimming near a surface along a path $\mathbf{r}(t)$. The swimming path is defined as the position of the head averaged over one cycle of the flagellar beat as a function of time. This average eliminates rapid periodic movements of the head at the frequency of the flagellar beat. The swimming velocity is characterized by the speed $v = |\dot{\mathbf{r}}|$ and the tangent vector $\mathbf{t} = \dot{\mathbf{r}}/v$ of the swimming path. Dots denote time derivatives. The normal vector $\mathbf{n}$ of the swimming path $\mathbf{r}(t)$ is given by tangent vector $\mathbf{t}$ rotated by $\pi/2$ in a counterclockwise sense.[5] The geometry of the swimming path is described by the Frenet-Serret equations in two dimensions

$$\dot{\mathbf{r}} = v\,\mathbf{t}, \quad \dot{\mathbf{t}} = v\kappa\,\mathbf{n}, \quad \dot{\mathbf{n}} = -v\kappa\,\mathbf{t}, \tag{3.1}$$

where κ is the (signed) curvature of the swimming path $\mathbf{r}(t)$. The absolute value of the (signed) curvature satisfies the familiar relation $|\kappa| = |\dot{\mathbf{t}}|/v$. If the curvature is constant, $\kappa = \kappa_0 > 0$, the swimming path is a circle with radius $r_0 = 1/\kappa_0$. The angular frequency of swimming in circles is $\omega_0 = v_0\kappa_0$ if speed $v(t) = v_0$ is constant. In

---

[5]We assume that a sense of orientation has been chosen for the plane. In an experimental setup, the plane of sperm swimming would be parallel to a boundary surface: In this situation, the inward normal of the boundary surfaces determines a sense of orientation for the plane.

the following, we consider the case where sperm cells swim in a counterclockwise sense along their circular swimming paths $\mathbf{r}(t)$ such that $\kappa_0 > 0$. Our results also apply for swimming in a clockwise sense, however, r_0 and ω_0 will attain negative values in this case.

We consider a swimming path in a concentration field $c(\mathbf{x})$ of chemoattractant, where $\mathbf{x} = (x, y)$ denotes a position in two dimensional space. The swimming sperm perceives a temporal concentration stimulus $s(t)$

$$s(t) = c(\mathbf{r}(t)). \tag{3.2}$$

This stimulus $s(t)$ triggers a response of the chemotactic signaling network. In general the signaling network is a dynamic system which generates a time-dependent output which depends on the history of the stimulus. Due to its complexity and our incomplete knowledge, it is not feasible to model the chemotactic signaling network in detail. Instead, we will consider a generic signaling system which captures the essential properties of chemotactic signaling. We characterize the response of the chemotactic signaling system by a dimensionless output variable $a(t)$ with $a = 1$ in steady state. We assume that this output variable directly affects the curvature κ of the swimming path by

$$\kappa(t) = \kappa_0 + \kappa_1 \left(a(t) - 1 \right). \tag{3.3}$$

The variable $a(t)$ plays a similar role as the internal calcium concentration within the flagellum. The calcium concentration is controlled by the chemotactic signaling network and influences the activity of dynein motors, thereby modulating the flagellar beat pattern and the curvature of the swimming path. For simplicity we assume that the swimming speed is constant $v(t) = v_0$ and not affected by chemotactic signaling.

We can capture the essential properties of the chemotactic signaling network, namely its ability to adapt and its relaxation dynamics by a simple dynamical system [6,11,56]

$$\begin{aligned}
\sigma \, \dot{a} &= p \left(s_b + s \right) - a, \\
\mu \, \dot{p} &= p \left(1 - a \right).
\end{aligned} \tag{3.4}$$

Here $p(t)$ is an internal variable which governs adaptation and represents a dynamic sensitivity; σ is a relaxation time and μ is a time-scale of adaptation. The parameter s_b has units of a concentration and stabilizes (3.4) in the absence of a stimulus. This parameter sets a detection limit for low stimuli and could result from a background activity of the chemoattractant receptors in the absence of any stimulus.

For a time-independent stimulus $s(t) = s_0$ the system reaches a steady state with $a = 1$ and $p = 1/(s_b + s_0)$. The system is adaptive since the steady state output is independent of the stimulus level s_0. The set of equations (3.1-3.4) determine a unique swimming path $\mathbf{r}(t)$ in a self-consistent manner for given initial conditions and the concentration field. Examples of swimming paths for linear and radial concentration fields are shown

in figures 3.1 and 3.2. These paths can be described as circles whose centers drift along well defined trajectories.

Small periodic variations of the stimulus $s(t) = s_0 + s_1 \cos \omega_0 t$ evoke a periodic response of the curvature $\kappa(t) = \kappa_0 + \rho_\kappa s_1 \cos(\omega_0 t + \varphi_\kappa) + \mathcal{O}(s_1^2)$ with amplitude gain ρ_κ and phase shift φ_κ. For the signaling system (3.4), the linear response coefficient $\widetilde{\chi}_\kappa(\omega_0) = \rho_\kappa \exp(i\varphi_\kappa)$ reads

$$\widetilde{\chi}_\kappa(\omega_0) = \frac{\kappa_1}{s_b + s_0} \frac{i\omega_0 \mu}{1 + \mu\omega_0 - \sigma\mu\omega_0^2}, \tag{3.5}$$

see appendix B. The amplitude gain $\rho_\kappa = |\widetilde{\chi}(\omega_0)|$ scales inversely with the stimulus strength $s_b + s_0$ due to the adaptation property of the chemotactic signaling system and can be written as $\rho_\kappa = \overline{\rho}_\kappa/(s_b + s_0)$ with a constant $\overline{\rho}_\kappa$ that represents an amplification strength. The linear response coefficient $\widetilde{\chi}_\kappa(\omega_0) = \rho_\kappa \exp(i\varphi_\kappa)$ will play a key role to characterize swimming paths.

3.1.2   Sperm swimming paths are drifting circles

The set of equations (3.1-3.4) for the swimming path $\mathbf{r}(t)$ can be solved numerically. For a linear concentration field $c(\mathbf{x}) = c_0 + \mathbf{c}_1 \cdot \mathbf{x}$ the swimming paths are drifting circles. The overall motion of these circling paths is captured by the trajectory of the circle centers which defines the centerline $\mathbf{R}(t)$. The centerline $\mathbf{R}(t)$ is oriented approximately at constant angle α with respect to the direction of the concentration gradient $\mathbf{c}_1$, see figure 3.1.

In a radial concentration field with $c(\mathbf{x}) = c_0/|\mathbf{x}|$ the centerline $\mathbf{R}(t)$ is a spiral that circles toward the origin at $\mathbf{x} = (0,0)$, see figure 3.2. This choice of the radial decay is motivated by the steady state concentration field established in three dimensions by diffusion from a source, see section 3.2.4. Note, that the spiral shape of the centerline does not depend on the precise form of the radial decay.

In order to understand these results, we will consider the limit of weak gradients in the next section.

3.1.3   The limit of weak concentration gradients

We study the chemotactic feedback loop for planar swimming given in equations (3.1-3.4) in the limit of weak chemoattractant gradients. The relative strength of the gradient $|\boldsymbol{\nabla} c|/c$ is an inverse length that should be compared to a characteristic length scale of circular swimming. We are thus led to consider the dimensionless parameter

$$\nu = r_0 |\boldsymbol{\nabla} c|/c; \tag{3.6}$$

this parameter will be small for weak concentration gradients. We determine the swimming path in a linear concentration field $c(x,y) = c_0 + c_1 x$ by a perturbation calculation in ν. We anticipate that the swimming path $\mathbf{r}(t) = (x(t), y(t))$ is a perfect circle whose
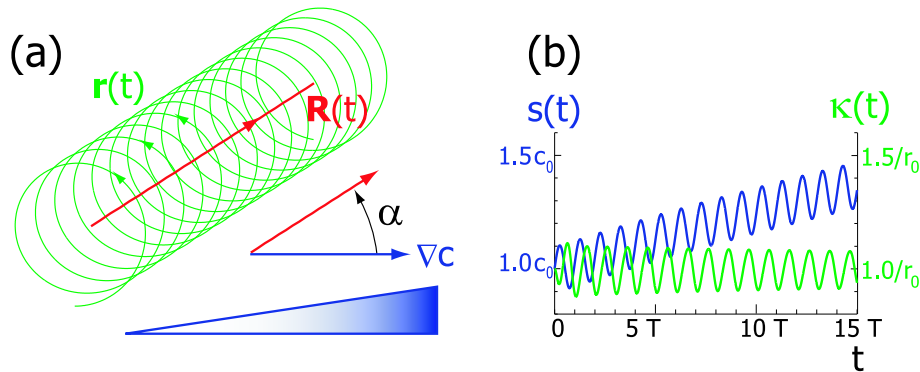
Figure 3.1: Swimming path $\mathbf{r}(t)$ in two dimensions in a linear concentration field. (a) In a linear concentration field $c(\mathbf{x}) = c_0 + \mathbf{c}_1 \cdot \mathbf{x}$ with constant gradient vector (blue arrow), the swimming path $\mathbf{r}(t)$ (green line) is a drifting circle. This drift can be described by the motion of the center of the circle $\mathbf{R}(t)$ (red line). This centerline encloses an approximately constant angle of $\alpha \approx 0.57$ with the gradient direction $\boldsymbol{\nabla} c = \mathbf{c}_1$. (b) Chemotactic stimulus $s(t) = c(\mathbf{r}(t))$ (blue) and curvature $\kappa(t)$ of the swimming path $\mathbf{r}(t)$ (green). The stimulus comprises (i) a periodic modulation with the frequency ω_0 of circular swimming which results from the fact that the sperm cell traces the concentration gradient along a circular swimming path, and (ii) and a monotonic increase of its average value which results from the fact that the swimming circles drift upwards the concentration gradient. The chemotactic signaling system (3.4) processes the chemotactic stimulus and causes a periodic modulation of the curvature. Due to the adaptation property of the signaling system, there is no increase of the average curvature. We find a phase shift of $\varphi_\kappa \approx 4.14$ between the stimulus and the curvature oscillations, which is close to the value $\arg \widetilde{\chi}_\kappa(\omega_0) \approx 4.12$ predicted by our analytic theory, see equation (3.5). Note that $\alpha + \varphi_\kappa \approx 3\pi/2$, see equation (3.13). The path shown is a numerical solution to the equations of sperm motion (3.1-3.4) with parameters $v_0 = r_0/\sigma$, $|\mathbf{c}_1| = 0.1\,c_0/r_0$, $s_b = 0$, $\kappa_1 = -2/r_0$, $\mu = 0.4\,\sigma$, where c_0, r_0, σ set the concentration, length and time scales of the problem, respectively. Initial conditions were $\mathbf{r}(0) = (0, -1)r_0$, $a(0) = 1$, and $p(0) = 1/c(\mathbf{r}(0))$.
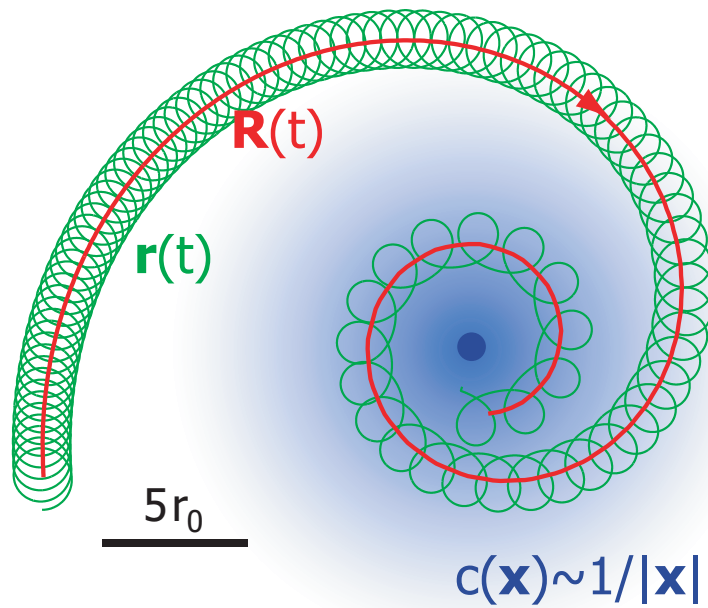
Figure 3.2: Swimming path $\mathbf{r}(t)$ in two dimensions in a radial concentration field $c(\mathbf{x}) = C(|\mathbf{x}|) = C_0/|\mathbf{x}|$. The swimming path is a circle which drifts along a spiral to the origin of the radial distribution (blue dot). The path shown is a numerical solution to the equations of sperm motion (3.1-3.4) with parameters $\kappa_1 = -2/r_0$, $\mu = 0.8\,\sigma$, $v_0 = r_0/\sigma$, $s_b = 0$ where r_0, σ set the concentration, length and time scale, respectively. The initial conditions were $\mathbf{r}(0) = (-10, -10)r_0$, $a(0) = 1$, and $p(0) = 1/c(\mathbf{r}(0))$.

shape is perturbed to first order in ν

$$\mathbf{r}(t) = r_0(\cos \omega_0 t, \sin \omega_0 t) + \mathcal{O}(\nu). \tag{3.7}$$

The chemoattractant concentration field is linear with the gradient chosen to point in x-direction for simplicity

$$c(x, y) = c_0 + c_1 x. \tag{3.8}$$

According to equation (3.2), a sperm moving along $\mathbf{r}(t)$ samples a time-dependent stimulus

$$s(t) = c_0 + r_0 \, c_1 \cos \omega_0 t + \mathcal{O}(\nu^2). \tag{3.9}$$

The stimulus contains a monotonically increasing (or decreasing) contribution $\sim c_1 v_d \cos(\alpha) t$ which is of second order in ν and thus is neglected in our perturbation calculation. The chemotactic signaling network responds to the chemotactic stimulus with an output that to linear order in ν evokes curvature oscillations

$$\kappa(t) = \kappa_0 + \rho_\kappa c_1 r_0 \, \cos(\omega_0 t + \varphi_\kappa) + \mathcal{O}(\nu^2). \tag{3.10}$$

Integrating equation (3.1) with this time dependence of the curvature gives the swimming path

$$\mathbf{r}(t) = r_0 \left(\cos \varphi(t), \sin \varphi(t) \right) + v_d \left(\cos \alpha, \sin \alpha \right) t + \mathcal{O}(\nu^2), \tag{3.11}$$

with rotation rate $\dot{\varphi} = \Omega_3 = \omega_0 + v_d \kappa_0 \cos(\omega_0 t + \varphi_\kappa)$. The resulting swimming path $\mathbf{r}(t)$ is thus a drifting circle with drift speed v_d and a drift direction with respect to the gradient which is characterized by the angle α. From the perturbation calculation, we find

$$v_d = \delta_\kappa \, \rho_\kappa \, c_1 + \mathcal{O}(\nu^2) \tag{3.12}$$

where $\delta_\kappa = \frac{1}{2} v_0 r_0^2$ and

$$\alpha = 3\pi/2 - \varphi_\kappa + \mathcal{O}(\nu), \tag{3.13}$$

where φ_κ is the phase of the linear response coefficient $\widetilde{\chi}_\kappa(\omega_0) = \rho_\kappa e^{i\varphi_\kappa}$ at the angular frequency ω_0.[6] The upper and lower turning points of the drifting circle correspond to the minima and maxima of the oscillating curvature (3.10).

The centerline $\mathbf{R}(t)$ of this drifting circle $\mathbf{r}(t)$ is given by

$$\mathbf{R}(t) = v_d \left(\cos \alpha, \sin \alpha \right) t + \mathcal{O}(\nu^2). \tag{3.14}$$

Remark: Higher order perturbation. It is possible to compute the sperm swimming path $\mathbf{r}(t)$ to second order in ν; we then find that the frequency ω of circular

---

[6]Equation (3.13) also holds in the case of clockwise circular swimming provided κ denotes signed curvature with $\kappa_0 < 0$. If we had defined the normal vector $\mathbf{n}$ as the tangent vector rotated by $\pi/2$ in **clockwise** sense, then the case of clockwise circular swimming would correspond to positive values of the signed curvature and instead of equation (3.13) we would have $\alpha = \pi + \varphi_\kappa$.

swimming and the radius r of the circular path are perturbed to second order in ν

$$\omega = \omega_0 + \mathcal{O}(\nu^2), \quad r = r_0 + \mathcal{O}(\nu^2). \tag{3.15}$$

For the particular signaling system (3.4), we find $\omega = \omega_0 - \mu v_d \sin \varphi_\kappa |\boldsymbol{\nabla} c|/c$ and $r = v_0/\omega$. The expressions (3.12) and (3.13) found above for the drift speed v_d and the drift angle α hold true also to second order in ν.

Remark: Nonlinear concentration field. In principle, the calculation of the sperm swimming path $\mathbf{r}(t)$ could be repeated for a nonlinear concentration field $c(\mathbf{x}) = c(x_1, x_2)$. If we locally Taylor-expand $c(x_1, x_2)$ around $\mathbf{R}(0) = 0$ as

$$c(x_1, x_2) = c_0 + c_j x_j + c_{kl} x_k x_l + \ldots, \tag{3.16}$$

we find that to linear order the second derivative of the concentration field $\boldsymbol{\nabla}^2 c = (c_{kl})$ does not contribute to the drift $\mathbf{R}(t)$ of the swimming circles $\mathbf{r}(t)$. This result can also be deduced from symmetry considerations, since $\boldsymbol{\nabla}^2 c$ is invariant with respect to reflection at its principal axes, but any drift vector $\dot{\mathbf{R}}$ is not.

3.1.4   Effective equation of motion

The equation (3.14) for the centerline in a linear concentration field can be generalized to the case of a nonlinear concentration field provided that the gradient is weak, $\nu \ll 1$, and the nonlinearities are small on the length-scale r_0, $|\boldsymbol{\nabla}^2 c| \ll |\boldsymbol{\nabla} c|/r_0$. Equation (3.14) for the centerline can then be generalized as

$$\boxed{\dot{\mathbf{R}} = v_d \, \mathcal{M}(\alpha) \, \boldsymbol{\nabla} c/|\boldsymbol{\nabla} c| + \mathcal{O}(\nu^2)} \tag{3.17}$$

where the operator $\mathcal{M}(\alpha)$ rotates the vector $\boldsymbol{\nabla} c$ in the plane in a counterclockwise sense by the angle α given by equation (3.13). Equation (3.17) represents a differential equation for the centerline $\mathbf{R}(t)$ if the gradient $\boldsymbol{\nabla} c$ of the concentration field is evaluated at any time at position $\mathbf{R}(t)$.

Note that the calculation above is general and applies to any signaling system which shows adaptation and is characterized by a linear response coefficient χ_κ for the curvature.

3.1.5   Criterion for chemotactic success

In a concentration field of chemoattractant, $c = c(\mathbf{x})$, the sperm swimming path $\mathbf{r}(t)$ are drifting circles whose center move along the centerline $\mathbf{R}(t)$. The angle α enclosed by the concentration gradient $\boldsymbol{\nabla} c$ and the drift direction $\dot{\mathbf{R}}$ is $\alpha = 3\pi/2 - \varphi_\kappa + \mathcal{O}(\nu)$ with $\nu = r_0 |\boldsymbol{\nabla} c|/c_0$, see section 3.1.4. Here φ_κ is the argument of the linear response coefficient $\widetilde{\chi}_\kappa(\omega_0)$ of the chemotactic signaling system (3.4). We thus find that the swimming circles of the sperm cells move upwards the concentration gradient of chemoattractant,

whenever

$$\pi < \varphi_\kappa < 2\pi. \tag{3.18}$$

We conclude that chemotactic success only depends on the dynamic properties of the chemotactic signaling system characterized by the phase shift φ_κ between the stimulus and the induced curvature response. The drift upwards the concentration gradient is maximal for $\varphi_\kappa = 3\pi/2$.

Logarithmic spirals in a radial concentration field.   The criterion for chemotactic success (3.18) can be illustrated for the case of a radial concentration field $c(\mathbf{x}) = C(|\mathbf{x}|)$. According to equation (3.17), the centerline $\mathbf{R}(t)$ winds around the origin in a logarithmic spiral

$$R(\theta) = R_0 \exp(-\cot(\alpha)\theta) \tag{3.19}$$

where θ is the polar angle and $R = |\mathbf{R}|$, see figure 3.3. It spirals inwards for $-\pi/2 < \alpha < \pi/2$, which corresponds to a phase shift of the signaling system of $\pi < \varphi < 2\pi$. Otherwise it spirals outwards.
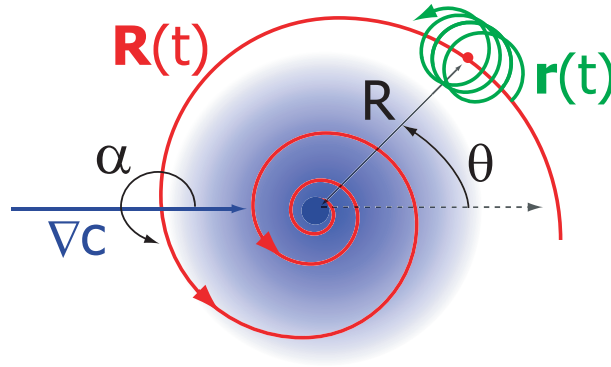
Figure 3.3: Schematic representation of a swimming path in two dimensions in a radial concentration field of chemoattractant. The swimming path $\mathbf{r}(t)$ (green line) is a drifting circle whose center moves along the centerline $\mathbf{R}(t)$ (red line). In the limit of weak concentration gradients with the parameter ν small, see text, this centerline is a logarithmic spiral whose tangent encloses a constant angle of α with the gradient direction at every point. The distance $R = |\mathbf{R}|$ of the centerline to the source and the polar angle θ are used in the formula of the logarithmic spiral, see text.

An example of a swimming path in a radial concentration field is given in figure 3.2: The spiral shape of the centerline $\mathbf{R}$ can be seen clearly.

Comparison with numerical solutions.   We have compared solutions to the dynamic equations (3.1-3.4) for the swimming path to solutions of equation (3.17) for the center line in our perturbation calculation and found good quantitative agreement for $\nu \lesssim 0.1$. Furthermore, the criterion for chemotactic success (3.18) could predict perfectly whether the path reached the egg or not.

3.2   Chemotaxis along helical paths
in three-dimensional space

3.2.1   Dynamic equations of sperm motion

Far from any surface, sperm cells swim along helical paths if no chemoattractant is present [37]. The geometry of the swimming path $\mathbf{r}(t)$ is characterized by the tangent vector $\mathbf{t} = \dot{\mathbf{r}}/v$, the normal vector $\mathbf{n} = \dot{\mathbf{t}}/|\dot{\mathbf{t}}|$ and the binormal vector $\mathbf{b} = \mathbf{t} \times \mathbf{n}$. The time evolution of these vectors $\mathbf{r}$, $\mathbf{t}$, $\mathbf{n}$ and $\mathbf{b}$ is given by the Frenet-Serret equations in three dimensions

$$\dot{\mathbf{r}} = v\,\mathbf{t}, \quad \dot{\mathbf{t}} = v\kappa\,\mathbf{n}, \quad \dot{\mathbf{n}} = -v\kappa\,\mathbf{t} + v\tau\,\mathbf{b}, \quad \dot{\mathbf{b}} = -v\tau\,\mathbf{n}. \tag{3.20}$$

For constant curvature $\kappa(t) = \kappa_0$ and torsion $\tau(t) = \tau_0$ the swimming path is a perfect helix with radius $r_0 = \kappa_0/(\kappa_0^2 + \tau_0^2)$ and pitch $2\pi h_0 = 2\pi\,\tau_0/(\kappa_0^2 + \tau_0^2)$. The angular frequency of helical swimming is $\omega_0 = v_0\,(\kappa_0^2 + \tau_0^2)^{1/2}$. The helix can be right- or left-handed, depending on the sign of τ_0: For $\tau_0 > 0$, the helix is right-handed, and for $\tau_0 < 0$ it is left-handed. For the particular case $\tau_0 = 0$, the helix degenerates to a circle. In the following, we will consider the case where sperm cells swim along right-handed helical paths with $\tau_0 > 0$. Our results also apply for the case of swimming along a left-handed helix, however, h_0 will attain a negative value in this case.

Swimming along such a helical path in a chemoattractant concentration field leads again to a time-dependent stimulus $s(t)$ of the signaling system as in the two dimensional case. In our three dimensional description, we assume that the output variable $a(t)$ of this system modulates both the curvature $\kappa(t)$ and the torsion $\tau(t)$ of the swimming path

$$\begin{aligned}
\kappa(t) &= \kappa_0 + \kappa_1\,(a(t) - 1), \\
\tau(t) &= \tau_0 + \tau_1\,(a(t) - 1).
\end{aligned} \tag{3.21}$$

The system of equations (3.2), (3.4), (3.20) and (3.21) uniquely determines the swimming path $\mathbf{r}(t)$ for given concentration field and initial conditions. Figure 3.5(a) shows an example of a swimming path in a radial concentration field which leads toward the origin of the concentration field. The swimming path $\mathbf{r}(t)$ is super-helical: It is a perturbed helix that winds around a curved centerline $\mathbf{R}(t)$, see figure 3.5(b).

The response of the torsion to weak stimuli is characterized by a linear response coefficient $\widetilde{\chi}_\tau(\omega_0) = \rho_\tau \exp(i\varphi_\tau)$ which is defined analogously to the linear response coefficient $\widetilde{\chi}_\kappa$ of the curvature, see equation (3.5).

3.2.2   Sperm swimming paths are bent helices

Our numerical solutions for swimming paths in three dimensions shown in figure 3.4 demonstrate that the modulation of curvature and torsion of the path by the signaling
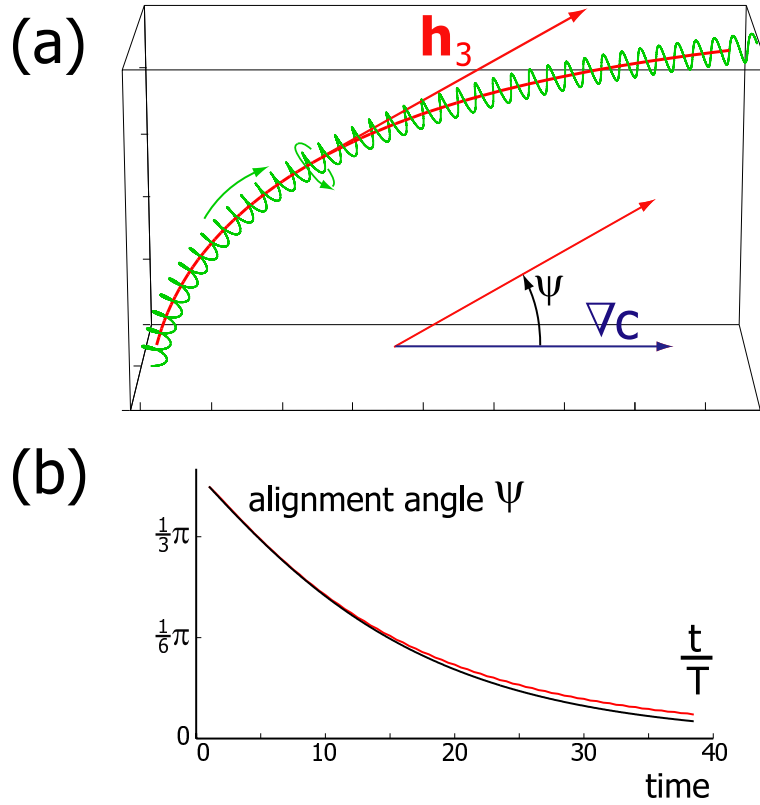
Figure 3.4: Helical sperm swimming path in a linear concentration field. (a) In a linear concentration field $c(\mathbf{x}) = c_0 + \mathbf{c}_1 \cdot \mathbf{x}$ with constant gradient vector (blue arrow), the swimming path $\mathbf{r}$ is a deformed helix (green line), which bends and eventually aligns with the gradient: The angle ψ between the the gradient direction ∇c and the helix vector $\mathbf{h}$ decreases monotonically. The centerline $\mathbf{R}$ of the helical path $\mathbf{r}$ is shown in red. (b) Time evolution of the angle ψ (red). For comparison, the analytical solution for ψ given by the effective equation of motion (3.26) is also shown (black). The value β for the bending rate was determined with the relative strength $|\nabla c|/c_0$ of the concentration gradient evaluated at $\mathbf{r}(0)$. Time t is specified relative to the period T of a helical turn. The path shown in panel (a) is a numerical solution to the set of equations (3.2), (3.4), (3.20) and (3.21) with parameters $\kappa_1 = -2/r_0$, $\tau_0 = 0.2/r_0$, $\tau_1 = 2/r_0$, $\mu = \sigma$, $v_0 = r_0/\sigma$, $s_b = 0$, and initial conditions $\mathbf{r}(0) = (0,0,0)r_0$, $\mathbf{t}(0) = (1,0,0)$, $\mathbf{n}(0) = (0,1,0)$, $\mathbf{b}(0) = (0,0,1)$, $a(0) = 1$, and $p(0) = 1/c(\mathbf{r}(0))$. The concentration gradient is $\mathbf{c}_1 = 0.01\,(1,0,0)\,c_0$. For the period of a helical turn, we have $T \approx 2\pi\sigma$. The size of the box is about $45r_0 \times 20r_0 \times 25r_0$. The centerline $\mathbf{R}$ and the helix vector $\mathbf{h}$ were obtained by fitting short segments of a perfect helix to $\mathbf{r}$.
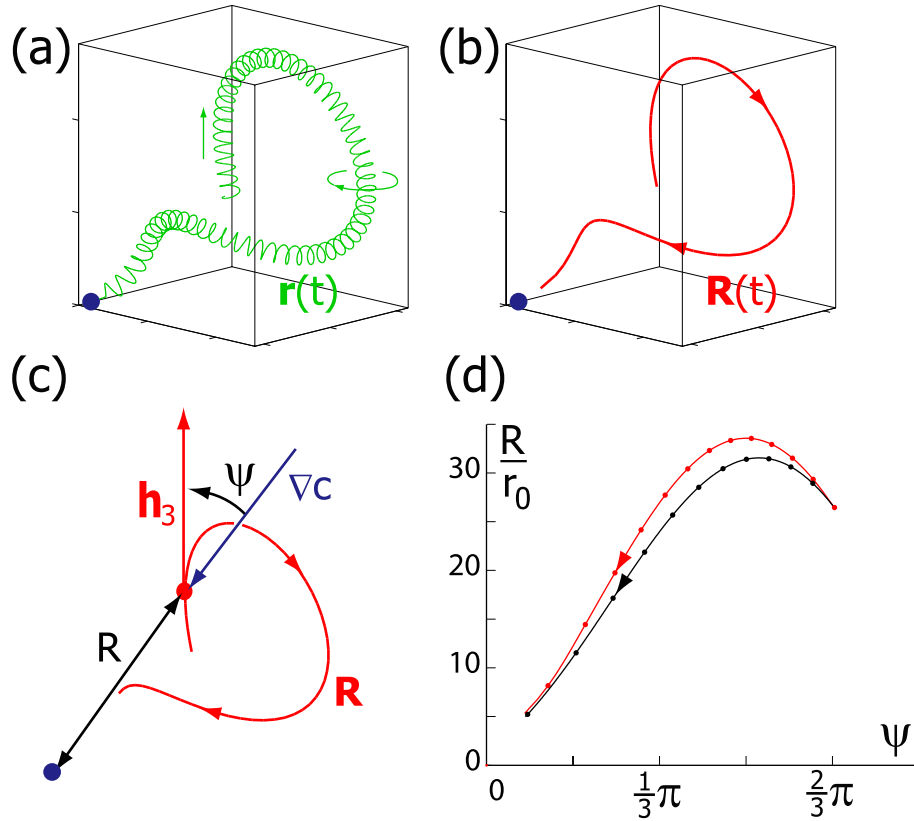
Figure 3.5: Helical swimming path of a sperm cell in a radial concentration field $c(\mathbf{x}) = C_0/|\mathbf{x}|$. (a) The swimming path $\mathbf{r}(t)$ is super-helical and leads to the chemoattractant source (blue dot). (b) The centerline $\mathbf{R}(t)$ of the full swimming path. (c) We can characterize the centerline $\mathbf{R}(t)$ by two coarse-grained variables: the distance $R = |\mathbf{R}|$ to the center of the radial concentration field and the alignment angle ψ between helix vector and gradient direction (red curve). (d) Dynamics of the coarse-grained variables $R = |\mathbf{R}|$ and alignment angle ψ (red curve). Temporal information is provided by dot marks along the (R, ψ)-trajectory, which are separated by a time interval of $5\,T$ where T is the period of a helical turn. For comparison, the (R, ψ)-trajectory as obtained by our perturbation calculation for the small perturbation parameter ν, see Eq. (3.30), is shown in black. We find reasonable agreement between both trajectories, the value of the perturbation parameter ν rises form 0.04 to 0.2 along the trajectories, Numerical integration of the set of equations (3.2), (3.4), (3.20) and (3.21) was done for $\kappa_1 = -2/r_0$, $\tau_0 = 0.2/r_0$, $\tau_1 = 2/r_0$, $\mu = 0.4\,\sigma$, $v_0 = r_0/\sigma$, $s_b = 0$, and initial conditions $\mathbf{r}(0) = (0, 20, 15)\,r_0$, $\mathbf{t}(0) = (1, 0, 0)$, $\mathbf{n}(0) = (0, 1, 0)$, $\mathbf{b}(0) = (0, 0, 1)$, $a(0) = 1$, and $p(0) = 1/c(\mathbf{r}(0))$. The size of the box in (a) and (b) is about $20\,r_0 \times 25\,r_0 \times 30 r_0$.

system lead to chemotactic behavior. In the absence of a concentration gradient, the swimming path is a perfect helix with a straight centerline. If this trajectory encounters a linear concentration field, the helix bends until its axis is parallel or anti-parallel to the concentration gradient. In a radial concentration field, swimming paths are deformed helices which wind toward the origin of the concentration field. In order to understand these numerical observations, we generalize the ideas developed in the previous section to three dimensions.

The net motion resulting from swimming along a deformed helical path $\mathbf{r}(t)$ is captured by the trajectory of the centerline $\mathbf{R}(t)$. For given centerline, the helical path can be described by tracing the trajectory of a point on the circumference of an imagined solid disk with radius r_0, rotating in its plane with a rotation rate Ω_3 and with its center moving along $\mathbf{R}(t)$. The orientation of the disk is characterized by the unit vector $\mathbf{h}_3$ normal to the disk, which we call the helix vector, see figure 3.6. Note that $\mathbf{h}_3$ is not necessarily tangential to the centerline $\mathbf{R}$ since the disk can also move transversally. For a comparison of the full swimming path $\mathbf{r}(t)$ and its centerline $\mathbf{R}(t)$, see figures 3.4 and 3.5.

3.2.3   The limit of weak concentration gradients

As in the planar case, the chemotactic feedback loop for three space dimensions (3.2), (3.4), (3.20) and (3.21) can be studied in the limit of weak gradients by a perturbation calculation in the small parameter $\nu = r_0|\boldsymbol{\nabla} c|/c$.

Again we assume that the nonlinearities of the concentration field $c(\mathbf{x})$ are small on the length-scale r_0, $|\boldsymbol{\nabla}^2 c| \ll |\boldsymbol{\nabla} c|/r_0$, which implies that during a few helical turns of the swimming path we approximate the concentration field linearly. In the presence of a chemoattractant stimulus, the swimming path will be a deformed helix that winds around a centerline $\mathbf{R}(t)$. Recall that such a helical swimming path can be described as the trajectory of a point on the circumference of an imagined solid disk of radius r_0 that rotates in its plane with rotation rate Ω_3 and whose center moves along the centerline $\mathbf{R}(t)$. The orientation of the disk is characterized by the unit vector $\mathbf{h}_3$ normal to the disk, which we call the helix vector, see figure 3.6.

We introduce the material frame of the imagined disk consisting of orthogonal unit vectors $\mathbf{h}_1$ and $\mathbf{h}_2$, in the plane of the disk and $\mathbf{h}_3 = \mathbf{h}_1 \times \mathbf{h}_2$. The deformed helical swimming path can now be written as

$$\mathbf{r}(t) = \mathbf{R}(t) + r\,\mathbf{h}_1(t), \tag{3.22}$$

where the radius $r = r_0 + \mathcal{O}(\nu)$ may change only on a slow time-scale. The time dependence of the frame $\mathbf{h}_j$ is given by pure rotations $\dot{\mathbf{h}}_j = \epsilon_{kjl}\,\Omega_k\,\mathbf{h}_l$, where the Ω_k denote rotation rates. In the absence of a chemotactic stimulus, the swimming path is a perfect helix with $\dot{\mathbf{R}} = \omega_0 h_0 \mathbf{h}_3$, $r = r_0$, $\Omega_1 = \Omega_2 = 0$ and $\Omega_3 = \omega_0$. In the presence of a weak concentration gradient $\boldsymbol{\nabla} c$, the swimming path $\mathbf{r}(t)$ is a perturbed helix. The
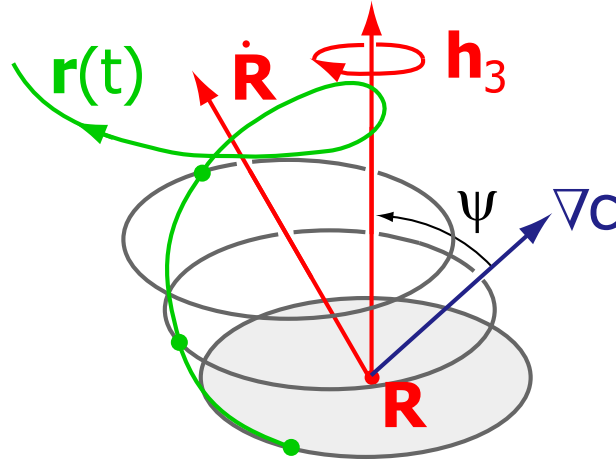
Figure 3.6: A deformed helical path $\mathbf{r}(t)$ can be generated by the motion of a point on an imagined solid disk which spins around the helix axis given by the vector $\mathbf{h}_3$ normal to the disk. The center of the disk moves along a curved centerline $\mathbf{R}(t)$ with tangent $\dot{\mathbf{R}}$. The gradient direction $\boldsymbol{\nabla}c$ and the helix vector $\mathbf{h}_3$ enclose an angle ψ.

concentration gradient $\boldsymbol{\nabla}c$ can be expressed as the sum of (i) a component $\mathbf{c}_{\parallel} = c_{\parallel}\mathbf{h}_3$ with $c_{\parallel} = \boldsymbol{\nabla}c\cdot\mathbf{h}_3$ parallel to $\mathbf{h}_3$, and (ii) a component $\mathbf{c}_{\perp} = \boldsymbol{\nabla}c - \mathbf{c}_{\parallel}$ perpendicular to $\mathbf{h}_3$ of length $\mathbf{c}_{\perp} = |\mathbf{c}_{\perp}|$. The helical swimming path samples a time dependent chemotactic stimulus which has a periodic component that is governed by $\mathbf{c}_{\perp}$

$$s(t) = c(\mathbf{R}(t)) + r_0 c_{\perp}\cos\varphi(t). \tag{3.23}$$

Here $\varphi(t) = \varphi_0 + \omega_0 t + \mathcal{O}(\nu)$ is the angle enclosed by $\mathbf{c}_{\perp}$ and $\mathbf{h}_1$. This periodic component of the stimulus generates an output signal $a(t)$ which periodically modulates both curvature and torsion of the path with phase shifts φ_κ and φ_τ, respectively. This fast modulations result in slow variations of $\dot{\mathbf{R}}$ and $\mathbf{h}_3$. The details of the calculation can be found in appendix K. To present results in a concise form, we define the complex gradient vector

$$\mathbf{c} = \mathbf{c}_{\perp} + i\,\mathbf{h}_3 \times \mathbf{c}_{\perp}. \tag{3.24}$$

We now have the following equation of motion for the center $\mathbf{R}$ and the body frame $(\mathbf{h}_1, \mathbf{h}_2, \mathbf{h})$ of the rotating disk which characterizes the helical swimming path $\mathbf{r}(t)$

$$\begin{aligned}
\dot{\mathbf{R}} &= \omega h\,\mathbf{h}_3 - \delta_\kappa \operatorname{Im}\left(\widetilde{\chi}_\kappa\,\mathbf{c}\right) + \delta_\tau \operatorname{Im}\left(\widetilde{\chi}_\tau\,\mathbf{c}\right) + \mathcal{O}(\nu^2),\\
\dot{\mathbf{h}}_3 &= \qquad - \varepsilon_\kappa \operatorname{Re}\left(\widetilde{\chi}_\kappa\,\mathbf{c}\right) + \varepsilon_\tau \operatorname{Re}\left(\widetilde{\chi}_\tau\,\mathbf{c}\right) + \mathcal{O}(\nu^2),\\
\dot{\mathbf{h}}_1 &= \quad \Omega_3\,\mathbf{h}_2 - (\dot{\mathbf{h}}_3 \cdot \mathbf{h}_1)\,\mathbf{h}_3,\\
\dot{\mathbf{h}}_2 &= -\,\Omega_3\,\mathbf{h}_1 - (\dot{\mathbf{h}}_3 \cdot \mathbf{h}_2)\,\mathbf{h}_3.
\end{aligned} \tag{3.25}$$

Here the coefficients read $\delta_\kappa = \omega_0 r_0(2r_0^2 + 3h_0^2)/4$, $\delta_\tau = \omega_0 r_0^2 h_0/4$, $\varepsilon_\kappa = \omega_0 r_0 h_0/2$, and $\varepsilon_\tau = \omega_0 r_0^2/2$. The helix frequency $\omega = \omega_0 + \mathcal{O}(\nu)$, the helix radius $r = r_0 + \mathcal{O}(\nu)$, and the helix pitch $2\pi h = 2\pi h_0 + \mathcal{O}(\nu)$ are perturbed to first order in ν. The rotation rate Ω_3 is given by the helix frequency ω plus a periodic modulation of order $\mathcal{O}(\nu)$, see

appendix K for details.

In the limit of $\tau_0 = \tau_1 = 0$ with $\delta_\tau = 0$, $\varepsilon_\kappa = \varepsilon_\tau = 0$ and $h_0 = 0$, we recover chemotaxis in a plane as discussed above.

Note that this calculation is general and applies to any signaling system which shows adaptation and is characterized by linear response coefficients χ_κ and χ_τ for curvature and torsion.

The case of a linear concentration field. Alignment of the helical path $\mathbf{r}$ with the concentration gradient is characterized by the alignment angle ψ enclosed by the helix vector $\mathbf{h}$ and the gradient vector $\boldsymbol{\nabla} c$, see figure 3.4. In a linear concentration field $c(\mathbf{x}) = c_0 + \mathbf{c}_1 \cdot \mathbf{x}$, we can derive a dynamic equation for ψ: From $\dot{\mathbf{h}} \cdot \mathbf{c}_\perp = -c_\perp \dot{\psi}$ and equation (3.25), we conclude

$$\boxed{\dot{\psi} = -\beta \sin \psi + \mathcal{O}(\nu^2),} \qquad (3.26)$$

where the bending rate β reads

$$\beta = |\boldsymbol{\nabla} c| \, \mathrm{Re}\left[\varepsilon_\tau \widetilde{\chi}_\tau(\omega_0) - \varepsilon_\kappa \widetilde{\chi}_\kappa(\omega_0)\right] \qquad (3.27)$$

with $\varepsilon_\kappa = \omega_0 r_0 h_0/2$, $\varepsilon_\tau = \omega_0 r_0^2/2$. This equation has two fixed points at $\psi = 0$ and $\psi = \pi$ which correspond to helical paths whose helix vectors are parallel and anti-parallel to the gradient vector, respectively. The sign of β determines which of the fixed points is stable. The rate at which the helix aligns with the gradient direction is $|\beta|$. Therefore, for almost all initial conditions, the system exhibits chemotaxis upwards the gradient if $\beta > 0$. A sufficient condition for $\beta > 0$ can be given in terms of the phase shifts φ_κ and φ_τ

$$\boxed{\pi < \varphi_\kappa < 2\pi, \quad 0 < \varphi_\tau < \pi.} \qquad (3.28)$$

This behavior is therefore robust and does not depend on fine-tuning of parameters.

The case of a radial concentration field. In a radial concentration field $c(\mathbf{x}) = C(|\mathbf{x}|)$, we can simplify equation (3.25) by exploiting rotational symmetry. We can express the centerline position $\mathbf{R}$ and the helix vector $\mathbf{h}_3$ by five parameters, the distance to the origin $R = |\mathbf{R}|$, the angle ψ between the helix vector $\mathbf{h}_3$ vector and the radial direction of the gradient $\boldsymbol{\nabla} c$, as well as three Euler angles θ, ξ, η, as

$$\begin{aligned} \mathbf{R} &= R\,\mathbf{e}_R, \\ \mathbf{h}_3 &= -\cos\psi\,\mathbf{e}_R - \sin\psi\,(\cos\eta\,\mathbf{e}_\theta + \sin\eta\,\mathbf{e}_\xi) \end{aligned} \qquad (3.29)$$

where $\mathbf{e}_R = (\cos\theta, \cos\xi \sin\theta, \sin\xi \sin\theta)$, $\mathbf{e}_\theta = \frac{\partial}{\partial\theta}\mathbf{e}_R$, $\mathbf{e}_\xi = \mathbf{e}_R \times \mathbf{e}_\theta$. Inserting equation (3.29) into equation (3.25) yields dynamic equations for R, ψ, θ, ξ, η, see appendix C Because of rotational symmetry, the variables R and ψ decouple from the other three

variables and obey the dynamic equations

$$
\boxed{
\begin{aligned}
\dot{R} &= -\omega h \cos\psi - \gamma \sin^2\psi, \quad \text{and} \\
\dot{\psi} &= -\sin\psi \left(\beta - \tfrac{1}{R}\left(\omega h - \gamma \cos\psi \right) \right)
\end{aligned}
}
\tag{3.30}
$$

where the bending rate β is given by equation (3.27) and the tilt rate γ reads

$$
\gamma = |\boldsymbol{\nabla} c| \operatorname{Im}\left[\delta_\tau \widetilde{\chi}_\tau(\omega_0) - \delta_\kappa \widetilde{\chi}_\kappa(\omega_0) \right]
\tag{3.31}
$$

with $\delta_\kappa = \omega_0 r_0 (2r_0^2 + 3h_0^2)/4$, $\delta_\tau = \omega_0 r_0^2 h_0 /4$, The dynamic equation for θ, ξ, η can be found in appendix C. Helix frequency $\omega = \omega_0 + \mathcal{O}(\nu)$, and helix pitch $2\pi h = 2\pi h_0 + \mathcal{O}(\nu)$ are perturbed to first order in ν, see appendix K.

In the next section 3.2.4, we will analyze the dynamical system (3.30) to predict whether a sperm cell will find a target such as an egg located at the center of a radial concentration field.

3.2.4   Will the sperm cell find the egg?

Equation (3.30) provides an effective equation of motion for the centerline $\mathbf{R}$ of a helical sperm swimming path $\mathbf{r}$ in a radial concentration field of chemoattractant. We can analyze under what conditions sperm swimming paths find an egg of radius R_{egg} located at the center of the radial concentration field $c(\mathbf{x}) = C(|\mathbf{x}|)$ by discussing phase space trajectories of this dynamical system (3.30). We find a 'criterion for chemotactic success' which depends on the bending rate β and the tilt rate γ. These rates β and γ depend on the local concentration field and hence will be a function of R, the distance to the egg, in a radial concentration field. Below, we discuss the chemoattractant concentration field established by diffusion from a single source such as an egg and derive a 'criterion for chemotactic success' for a particular scenario for the R-dependence of β and γ.

Chemoattractant concentration field around an egg.   Chemoattractant is released by the egg at some rate $Q(t)$ and then diffuses away according to the diffusion equation in three-dimensional space

$$
\dot{c} = D \, \Delta c
\tag{3.32}
$$

with boundary condition (at the surface of the egg)

$$
-D \oint \nabla c \cdot dS = Q
\tag{3.33}
$$

where $\mathbf{c}(\mathbf{x}, t)$ is the time-dependent concentration profile of chemoattractant and D is the diffusion constant of the chemoattractant. The integral in (3.33) integrates over the surface of the egg. For a spherical egg located at the origin, the concentration field

will be radial $c(\mathbf{x}) = C(|\mathbf{x}|)$ with a radial profile that satisfies

$$\dot{C} = D\, R^{-1}\, \partial_R^2\, (RC) \tag{3.34}$$

and with boundary condition at the surface of the egg

$$4\pi R_{\text{egg}}^2 D\, \partial_R C = Q. \tag{3.35}$$

If the chemoattractant release rate is constant in time, $Q(t) = Q_0$, we find for the steady-state concentration profile

$$C(R) = \frac{Q_0}{4\pi D}\, \frac{1}{R}. \tag{3.36}$$

If the chemoattractant is not chemically stable but degraded with a rate k_{deg}, then the concentration field $c(\mathbf{x}, t)$ satisfies the dynamic equation $\dot{c} = D\Delta c - k_{\text{deg}}c$. In this case, the steady-state concentration field is[19]

$$C(R) \sim \exp(-\lambda R)/R \tag{3.37}$$

with $\lambda^2 = k_{\text{deg}}/D$. Hence $|\boldsymbol{\nabla}c|/c \approx \lambda$ for $R \gg \lambda^{-1}$. It should be noted, that in the case of the sea urchin *Arbacia punctulata* degradation of the respective chemoattractant resact is very slow and can probably be neglected for the time scales relevant for the establishment of the concentration gradient in the vicinity of the egg [76].

In the open sea, released chemoattractant will be dispersed not only by simple diffusion, but also by complex hydrodynamic flows. In general, this will result in an irregular concentration field [101]. There is evidence that hydrodynamic flows in the vicinity of the egg enhance the release of chemoattractant from the egg [163]. However, we will not consider these effects.

Criterion for chemotactic success.   We analyze under what conditions swimming paths find an egg of radius R_{egg} at the origin by discussing phase space trajectories of the dynamical system (3.30). In general, the bending rate β and the tilt rate γ depend on the distance R to the target; we assume that β and γ scale inversely with distance R to the origin

$$\beta = \frac{B_0}{R}, \quad \gamma = \frac{\Gamma_0}{R}. \tag{3.38}$$

This scenario arises in a situation with

  (i) a concentration field of the form (3.36) where the relative strength of the gradient is $|\boldsymbol{\nabla}c|/c = 1/R$, and

  (ii) linear response coefficients $\widetilde{\chi}_\kappa$ and $\widetilde{\chi}_\tau$ which scale inversely with local concentration.

---

[19]The original version of this thesis contained an error in equation (3.37).

Such a concentration field corresponds to the steady state concentration field established by diffusion from a single chemoattractant source with constant chemoattractant release rate. The second condition on the response coefficients is satisfied for the particular signaling system given by equation (3.4) if $s_b = 0$, see equation (3.5). For simplicity, we assume $\omega = \omega_0$, $h = h_0$.

As a warm-up case, let us assume $\Gamma_0 = 0$; in this case, the dynamical system (3.30) has no isolated fixed points. Depending on the parameter B_0, the flow of the dynamical system (3.30) can exhibit different regimes: For $B_0 > \omega_0 h_0$, we have $\dot{\psi} < 0$ and all trajectories approach $(\psi_\infty, R_\infty) = (0, 0)$. These trajectories correspond to sperm swimming paths which align to the concentration gradient and then move towards the origin. For $B_0 > \omega_0 h_0$, we have $\dot{\psi} > 0$ and all trajectories escape to infinity. These trajectories correspond to sperm swimming paths which fail to align with the concentration gradient and move away from the origin.

Now we study the general case with $\Gamma_0 \neq 0$. Again, we can distinguish different regimes for the flow of the dynamical system (3.30)

- regime **A**: $B_0 > \omega_0 h_0$, $\Gamma_0 > 0$,

- regime **B**: $B_0 > \omega_0 h_0$, $\Gamma_0 < 0$,

- regime **C**: $B_0 < \omega_0 h_0$, $\Gamma_0 > 0$, and

- regime **D**: $B_0 < \omega_0 h_0$, $\Gamma_0 < 0$,

see figure 3.7. In regime **A** and **B** with $B_0 > 0$, there exists a fixed point (ψ_0, R_0), where

$$R_0 = \frac{|\Gamma_0|}{\sqrt{(B_0 - \omega_0 h_0)B_0}}, \quad \cos \psi_0 = -\frac{\Gamma_0}{B_0 R_0}. \tag{3.39}$$

This fixed point corresponds to sperm swimming paths for which the centerline circles around the origin and R is constant. A linear stability analysis of (3.30) shows that the fixed point (ψ_0, R_0) is repulsive in case **A** and attractive in case **B**, see appendix C.2. In both regimes, (ψ, R)-trajectories are spirals near the fixed point, see figure 3.7(a),(b). In regime **C**, no fixed points exist. A separatrix divides the phase space into two regions, see figure 3.7(c). The trajectories in either region differ by their ω-limit point (ψ_∞, R_∞). Trajectories in the region bounded on the left by the separatrix move towards $(\psi_\infty, R_\infty) = (0, 0)$. These trajectories correspond to swimming paths which lead to the origin. The trajectories in the second region bounded on the right by the separatrix move towards $(\psi_\infty, R_\infty) = (\pi, \infty)$ and correspond to swimming paths which move away from the origin. In regime **D**, no fixed points exist. All trajectories move towards $(\psi_\infty, R_\infty) = (\pi, \infty)$ and correspond to swimming paths which escape to infinity, see figure 3.7.

In the presence of an egg with radius R_{egg}, the centerline of swimming paths reaches the egg for almost all initial conditions in case **A**, see figure 3.8(a). For case **B**, (R, ψ)-trajectories starting in a finite neighborhood of the fixed points (R_0, ψ_0) correspond

to swimming paths that do not reach the egg. Further away from this neighborhood, trajectories can reach the egg before they spiral to the fixed point, see figure 3.8(b). In case **C** and **D** most swimming paths fail to reach the egg, see figure 3.8(c). We conclude that chemotaxis is most reliable in regime **A** for which a sufficient condition is given by

$$\pi < \varphi_\kappa < 3\pi/2, \quad 0 < \varphi_\tau < \pi/2, \tag{3.40}$$

provided $|\beta| > \omega_0 h_0 |\boldsymbol{\nabla} c|/c$.

In this section, we assumed a scenario where the bending rate β and the tilt rate γ scale inversely with distance R from the origin. Similar results can be found for a more general R-dependence of β and γ. In appendix C.3, we will consider a second scenario assuming constant β and γ. Such a scenario corresponds to a radial concentration field with $|\boldsymbol{\nabla} c|/c = \text{constant}$ which occurs if chemoattractant is degraded at a constant rate, see equation (3.37).

Remark: Detection limit of chemoattractant concentration. The scenario (3.38) studied above corresponds to a situation where the sensitivity threshold of chemotactic signaling vanishes, $s_b = 0$, i.e. a situation were sperm cells can respond to arbitrarily low chemoattractant concentrations. In a more realistic setting, the sensitivity threshold s_b would have a finite value. Then sperm swimming paths which are further away from the origin of a radial concentration field $c(\mathbf{x}) = C_0/|\mathbf{x}|$ than $R_{\text{limit}} = C_0/s_b$ will show almost no chemotaxis. Such a behavior corresponds to $\beta(R) \approx 0$, $\gamma(R) \approx 0$ for $R > R_{\text{limit}}$ in equation (3.25).

Remark: Life time of sperm cells. Note that we have assumed an arbitrarily long life time of the sperm cells in our discussion of chemotactic success. If life time t_s is finite, some sperm swimming path will not reach the egg even in regime **A**. Figure 3.9 shows initial conditions where the sperm cell does not find the egg for a particular example with finite life time.

3.3   Relation to experiments

Our theoretical results are consistent with experimental observations both in two and three dimensions. When sperm cells swim close to a surface, observed swimming paths in a concentration gradient of chemoattractant resemble drifting circles which drift upwards the concentration gradient [22,100,165]. Recent experiments have shown that upon periodic stimulation the signaling network generates calcium spikes which are phase-locked to the chemotactic stimulus with a phase shift of about $-0.4 \cdot 2\pi$ [22]. In these experiments, also the curvature of the swimming path is periodically modulated with a strong correlation with the chemotactic stimulus, see figure 1.7 from the introduction. The time-lag between the chemotactic stimulus and the curvature modulations is in the range where chemotaxis is successful in two dimensions with a chemotactic drift upwards the concentration gradient. Our theoretical description of
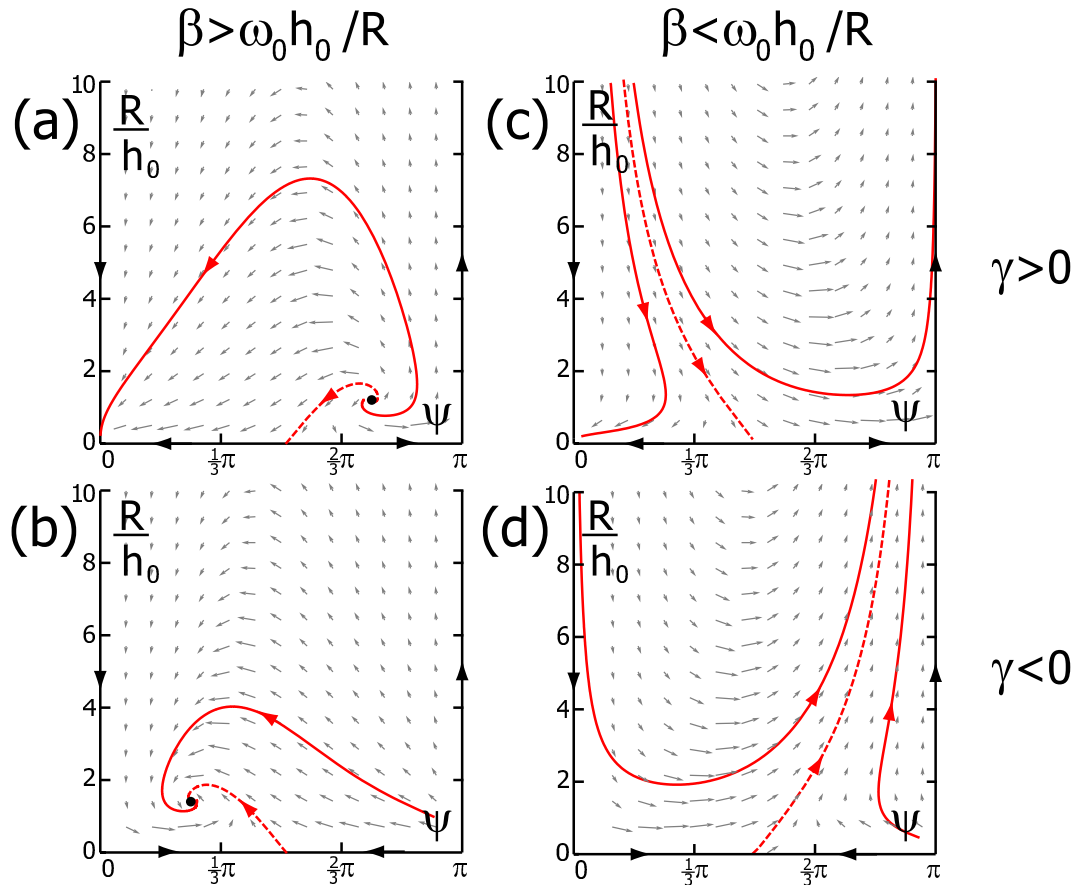
Figure 3.7: Sperm swimming paths in a radial concentration field are characterized by the distance $R = |\mathbf{R}|$ of the centerline position $\mathbf{R}$ to the origin of the concentration field and the alignment angle ψ enclosed by the helix vector and the gradient direction. The figure shows the flow field and typical trajectories in the (R, ψ)-phase space for the effective equation of motion (3.30) for sperm chemotaxis along helical paths. Distance R is shown relative to h_0 where $2\pi h_0$ is the pitch of the unperturbed helix. The three panels (a), (b), (c), and (d) are examples for the regimes **A**, **B**, **C**, and **D**, respectively: In regimes **A** and **B**, the chemotactic bending coefficient $\beta = B_0/R$ is positive, while β is negative in regimes **C** and **D**. The chemotactic tilt coefficient $\gamma = \Gamma_0/R$ is positive in regimes **A** and **C** and negative in regimes **B** and **D**, see text for details. Typical (R, ψ)-trajectories (red lines) as well as the gradient vector field (gray arrows) are shown. (a) In regime **A**, the system possesses a repulsive fixed point (black dot). The (R, ψ)-trajectories are spirals which spiral away from the fixed point. (b) In regime **B**, the fixed point is attractive and (R, ψ)-trajectories spiral toward the fixed point. (c) In regime **C**, no fixed points exist. A separatrix (dashed red line) divides the phase space into two regions; the trajectories in either region differ by their ω-limit point (ψ_∞, R_∞). Trajectories in the region bounded on the left by the separatrix move towards the chemoattractant source and have $(\psi_\infty, R_\infty) = (0, 0)$, while trajectories in the region bounded on the right by the separatrix move away from the chemoattractant source with $(\psi_\infty, R_\infty) = (\pi, \infty)$. (d) In regime **D**, no fixed points exist. A separatrix (dashed red line) divides phase space into two regions; the trajectories in either region differ by their α-limit point. Ultimately, all trajectories move away from the chemoattractant source. The flow field shown correspond to the parameter values (a) $B_0 = 2\,\omega_0 h_0$, $\Gamma_0 = 2\,\omega_0 h_0^2$, (b) $B_0 = 2\,\omega_0 h_0$, $\Gamma_0 = -2\,\omega_0 h_0^2$, (c) $B_0 = 0$, $\Gamma_0 = 2\,\omega_0 h_0^2$, (d) $B_0 = 0$, $\Gamma_0 = -2\,\omega_0 h_0^2$,
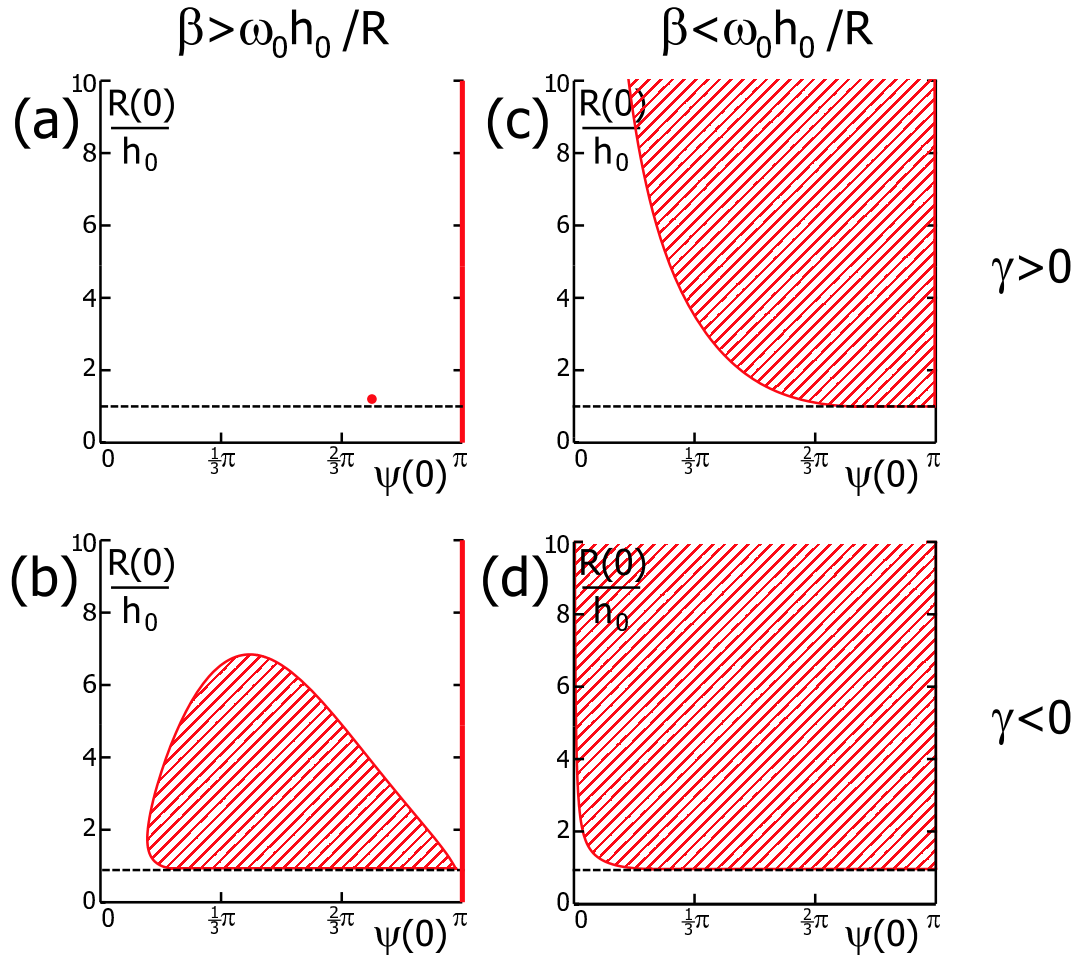
Figure 3.8: Chemotactic success as a function of initial conditions for sperm cells swimming along helical paths in a radial concentration field. The initial conditions of a path are characterized by the initial distance $R(0)$ of the centerline to the chemoattractant source and the initial angle $\psi(0)$ between the helix axis and the gradient direction. To determine chemotactic success, the effective equation of motion given by equation (3.30) was used. For a given initial condition, chemotaxis is unsuccessful if the correspondent swimming path has a distance $R(t)$ to the chemoattractant source which is always greater than an egg radius R_{egg}, $R(t) > R_{egg}$. Initial conditions with unsuccessful chemotaxis are shown as red dots, red lines and red hatched regions. Distance R is shown relative to h_0 where $2\pi h_0$ is the pitch of the unperturbed helix. The radius of the egg R_{egg} is indicated by a dashed line. The panels (a), (b), (c) and (d) are examples for the three regimes **A**, **B**, **C**, and **D**, respectively, see text for details. (a) In regime **A**, a repulsive fixed point exists, see figure 3.7(a), chemotaxis is robust and fails only at the fixed point and the marginal case $\psi(0) = \pi$. (b) In regime **B**, the fixed point is attractive (see figure 3.7(b)). Chemotaxis is successful in a large range of initial conditions and fails only in a neighborhood of the fixed points as well as in the marginal case $\psi(0) = \pi$. (c), (d) In regime **C** and **D**, no fixed points exist (see figure 3.7(c),(d)). Chemotaxis is unsuccessful except for those initial conditions where the initial distance to the source is already small and the helix axis is nearly aligned with the gradient direction. The parameter values used were $R_{egg} = h_0$ and (a) $B_0 = 2\,\omega_0 h_0$, $\Gamma_0 = 2\,\omega_0 h_0^2$, (b) $B_0 = 2\,\omega_0 h_0$, $\Gamma_0 = -2\,\omega_0 h_0^2$, (c) $B_0 = 0$, $\Gamma_0 = 2\,\omega_0 h_0^2$, (d) $B_0 = 0$, $\Gamma_0 = -2\,\omega_0 h_0^2$,
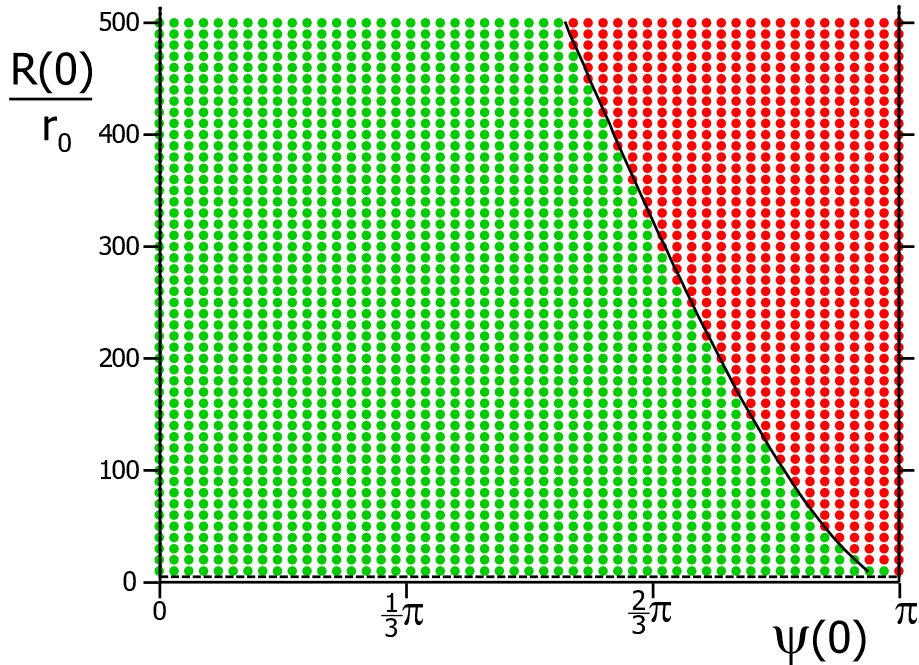
Figure 3.9: Chemotactic success as a function of initial conditions for sperm chemotaxis along helical paths in a radial concentration field with a finite search time. Initial conditions are marked depending on whether a sperm swimming path in a radial concentration field $c(\mathbf{x}) = C_0/|\mathbf{x}|$ starting with initial conditions characterized by $\psi(0)$ and $R(0)$ will reach a target at the origin in a finite time t_s (green dots) or fail to do so (red circles). Sperm swimming paths $\mathbf{r}(t)$ were computed numerically according to the equations of sperm motion (3.2), (3.4), (3.20) and (3.21). For comparison, we also determined which initial conditions are successful when we compute only coarse-grained swimming paths $\mathbf{R}(t)$ using the effective equation of motion (3.25) and the same parameter set; the boundary line separating the region of successful from the region of unsuccessful initial conditions obtained in this way is shown in black. The radius R_{egg} of the target is indicated as a dashed line. Numerical integration of the set of equations (3.2), (3.4), (3.20) and (3.21) was done for $\kappa_1 = -2/r_0$, $\tau_0 = 0.2/r_0$, $\tau_1 = 2/r_0$, $\mu = 0.4\,\sigma$, $v_0 = r_0/\sigma$, $s_b = 0$ and initial conditions of the signaling system $a(0) = 1$, and $p(0) = 1/c(\mathbf{r}(0))$. Initial conditions of the swimming paths were chosen in a way to ensure correct values of $R(0) = |\mathbf{R}(0)|$ and $\cos\psi(0) = \mathbf{R}(0) \cdot \mathbf{h}(0)/R(0)$: $\mathbf{r}(0) = (-R(0)\sin\psi(0), r_0, -R(0)\cos\psi(0))$, $\mathbf{t}(0) = (\cos\theta, 0, \sin\theta)$, $\mathbf{n}(0) = (0, -1, 0)$, and $\mathbf{b}(0) = (-\sin\theta, 0, \cos\theta)$, Here θ is the helix angle with $\tan\theta = \tau_0/\kappa_0$. Note that approximately $\mathbf{h} = \sin\theta\mathbf{t} + \cos\theta\mathbf{b}$ up to terms of order ν. The radius of the target was $R_{\text{egg}} = 5\,r_0$, the life time of the sperm cells was $t_s = 5000\,\sigma$. The parameter used correspond to regime **A** discussed in the text.

sperm chemotaxis developed in this thesis implies that the direction of drift of sperm swimming circles could be tuned arbitrarily by modifying the dynamic properties of the chemotactic signaling system. Indeed, the group of Wood et al. performed experiments with sperm cells that had been treated with the Ca^{2+} channel blocker Nimodipine which interferes with the chemotactic signaling system. They could observe significantly different drift directions of sperm swimming circles as a response to a pulse stimulus of the second messenger cGMP after Nimodipine treatment.[7] In three dimensions, tracking experiments showed that sperm swim along helices [33,37,38] as had been suggested earlier [25,61]. It was furthermore observed that in a concentration gradient the helix axis aligned with the gradient vector [25,26,37].

We used a simplified description of the signaling network which captures essential properties such as adaptation and a simple relaxation dynamics which generates a phase shift between stimulus and output. Experimental studies of the signaling system revealed that the flagellar membrane potential exhibits spikes on a 100 ms time scale with an amplitude that increases from 2 mV to 45mV when stimulus concentration is varied over 5 orders of magnitude from 250 fM to 25 nM. The spike amplitude saturates for stimulus concentrations as low as ~ 25 pM [148]. This non-linear response suggests a more complex dynamics than the simple system used in our theoretical description.

3.3.1   Estimates of relevant parameters

From experiments, we can estimate parameter values which are relevant to our description.

Sperm swimming. Typical values for the swimming speed, average curvature and torsion of sea urchin sperm swimming along helical paths are

$$v_0 \approx 100 - 200 \, \mu\mathrm{m\,s^{-1}}, \quad \kappa_0 \approx 0.05 \, \mu\mathrm{m^{-1}}, \quad \tau_0 \approx -0.025 \, \mu\mathrm{m^{-1}}, \tag{3.41}$$

respectively [37]. For planar circular swimming paths, $\kappa_0 \approx 0.025 - 0.050 \, \mu\mathrm{m^{-1}}$ was observed [22]. For comparison, the radius of the egg is $R_{\mathrm{egg}} \approx 100 \, \mu\mathrm{m}$ [52]. These values are typical also for other species, see [51,127].

Chemotactic signaling. From stopped-flow experiments, it is known that chemotactic signaling system operates on time-scales $100 - 500$ ms [148], we thus expect the phenomenological parameters σ, μ to fall in that range

$$\sigma, \mu \approx 100 - 500 \, \mathrm{ms}. \tag{3.42}$$

Sperm cells probably respond to single chemoattractant molecules [78], we therefore expect $s_b \lesssim 1/\sigma$.

---

[7]Note, however, that these experimental results have to be interpreted with care, since unphysiological high doses of Nimodipine were used [162]. Also these experiments were conducted with sperm cells of the sea urchin *S. purpuratus* for which chemotaxis has not yet been proven unequivocally.

Chemotactic swimming response. Drift speeds $v_d \approx 25 - 50\,\mu\mathrm{m\,s}^{-1}$ have been reported in [22]. In an early experiment with bracken fern spermatozoids, Brokaw measured the bending rate of the helix as a function of the concentration gradient. He suggested equation (3.26) as a phenomenological description of his observations and could estimate [25]

$$\beta c / |\boldsymbol{\nabla} c| \approx 150\,\mu\mathrm{m\,s}^{-1}. \tag{3.43}$$

Furthermore, he observed that bending of the helix occurred in the plane spanned by the helix vector and the gradient, which suggests that $\beta' = |\boldsymbol{\nabla} c|(\varepsilon_\kappa \mathrm{Im}\,\chi_\kappa - \varepsilon_\tau \mathrm{Im}\,\chi_\tau) \approx 0$.

Diffusion constant of the chemoattractant resact. We can estimate the diffusion constant of the chemoattractant resact as

$$D_{\mathrm{resact}} \approx 300\,\mu\mathrm{m}^2/\mathrm{s} \tag{3.44}$$

from the Einstein relation [45]

$$D = \frac{k_B T}{6\pi\eta\,a} = \frac{k_B T}{6\pi\eta}\left(\frac{m}{4\pi\rho}\right)^{1/3} \tag{3.45}$$

using a temperature of $T = 20°\mathrm{C}$, the molecular weight of resact $m = 1246\,\mathrm{Dalton}$ [58], and an average mass density $\rho = 1.5\,\mathrm{kg/dm}^3$ of proteins from the literature [54]. For simplicity, we have assumed a globular shape of this oligopeptide with radius a. Deviations from such a globular shape give rise to logarithmic corrections in (3.45), e.g. a rotationally symmetric ellipsoid with long semi-axis a and short semi-axis b moving at random will have a diffusion constant given by (3.45) multiplied by a factor of $\ln(2a/b)$ [16]. Since the density of the molecule enters only with the power $1/3$ in (3.45), the uncertainty about this quantity will have little effect on the result.

The above estimate is consistent with the value $D = 179\,\mu\mathrm{m}^2/\mathrm{s}$ found by fluorescence correlation spectroscopy measurements (FCS) with a fluorescently labeled resact: resact-Alexa647. Note that the molecular weight of the fluorescent dye Alexa647 is $1250\,\mathrm{Da}$, i.e. it is comparable to the weight of resact [41]. If we repeat the above calculation for resact-Alexa647, we find $D \approx 250\,\mu\mathrm{m}^2/\mathrm{s}$.

Chemoattractant release rate. It is not known how much of the chemoattractant resact is released by sea urchin eggs. In the African clawed frog *(Xenopus laevis)*, the sperm chemoattractant is the $21\,\mathrm{kDa}$-protein Allurin. The size of *Xenopus* eggs is $500\,\mu\mathrm{m}$. Chemoattractant is released from an outer jelly layer of thickness $200\,\mu\mathrm{m}$ surrounding the egg cell (and some inner jelly layers). The chemoattractant concentration within the outer jelly layer of freshly spawned eggs is $5\,\mu\mathrm{M}$. The half-time of chemoattractant release is $5\,\mathrm{min}$. Assuming that all of the chemoattractant is released at a constant rate Q_0 over a period of $5\,\mathrm{min}$, we estimate $Q_0 \approx 3\,\mathrm{fmol/s}$ [163].

In the red abalone *(Haliotis rufescens)*, the chemoattractant is the amino acid tryptophan. A chemoattractant release rate Q_0 of approximately $3\,\mathrm{amol/s}$ was measured by high-precision liquid chromatography (HPLC) [128]. The release rate was approx-

imately constant as long as the eggs remained viable. This value for the release rate
is surprisingly low and would correspond to a chemoattractant concentration on the
order of $10\,\mathrm{pM}$ in the vicinity of the egg according to equation (3.36).

Chapter summary

We have presented a theoretical description of sperm swimming paths, taking into
account chemotactic signaling. Our main assumptions are (i) that the curvature and
torsion of the swimming path are modulated by the signaling system, and (ii) that the
signaling system receives a temporal chemoattractant concentration stimulus implying
that concentration differences along the length of the flagellum are not relevant. We
study sperm swimming paths both in two and three dimensions and for linear and radial
concentration fields. In all cases, periodic components occur in the stimulus; one can
say, that the spatial information about the direction of the concentration gradient is
encoded in the temporal oscillations of the stimulus. These stimulus oscillations elicit
periodic variations of curvature and torsion of the path. Using both numerical and
analytical methods, we show that the resulting swimming paths are drifting circles in
two dimensions and helices that are bent and tilted in three dimensions. We discuss the
geometry of these paths and determine the conditions under which the system moves
to regions of high chemoattractant concentration. We find that key parameters for
chemotactic success are the phase shifts φ_κ and φ_τ between stimulus and modulations
of curvature and torsion, respectively. In both two and three dimensions there exist
large ranges of these parameters for which chemotaxis is reliable. There is an extensive
overlap of those ranges where chemotaxis works for the same parameters in two and
three dimensions. Therefore, chemotaxis is a robust property of the system which does
not require fine-tuning of parameters if the signaling system is adaptive.

Our work is related to earlier work by Crenshaw who suggested that chemotaxis could
be realized for helical paths by periodically modulating rates of translation and rotation
of swimming sperm [34,35,39]. Several works have studied chemotaxis for helical paths
using computer simulations [72,154] or by experiments with robots [82,93].

Chapter 4
The impact of noise in sperm chemotaxis: The planar case

Biological systems such as single cells must function in the presence of fluctuations. It has been shown in a two-dimensional experimental setup that sea urchin sperm cells move towards a source of chemoattractant along planar trochoidal swimming paths, i.e. drifting circles. In this chapter, we extend the theoretical description of sperm chemotaxis in the plane introduced in the previous chapter to take fluctuations into account. We derive a coarse-grained theory of stochastic sperm swimming paths in a concentration field of chemoattractant. We discuss the stochastic properties of sperm swimming paths and predict a concentration-dependence of the effective diffusion constant of perm swimming circles which could be tested in future experiments.

Introduction

Chemotaxis of sea urchin sperm is usually observed under experimental conditions where sperm cells swim in a shallow observation chamber under the microscope [22, 77,79,100,162,165]. In this situation, sperm cells become localized near the surfaces of the chamber where they swim along planar paths. In the absence of chemoattractant, the swimming paths are circular. The curvature of their swimming paths is a direct consequence of the chirality of their flagellar beat [79]. The rotational sense of circular swimming is mostly clockwise (when viewed in a direction parallel to the inward normal of the boundary surface).

In a concentration gradient of chemoattractant, the circular swimming paths drift towards regions of higher chemoattractant concentration, giving rise to trochoidal swimming paths, i.e. drifting circles [22,100,165]. Experiments indicate that while swimming in a concentration gradient of chemoattractant, both the intraflagellar calcium concentration and the curvature of the swimming path exhibit characteristic periodic modulations with the frequency of circular swimming [22].

Experiments on sperm chemotaxis reveal a pronounced variability of the observed sperm swimming paths. We argue that sperm chemotaxis is subject to fluctuations of various sources: The chemotactic stimulus received by a sperm cell exhibits fluctuations since the binding of chemoattractant molecules to their respective receptors is a discrete process. Additionally, intrinsic fluctuations of the chemotactic signaling system and fluctuations in the activity of the motor ensemble which drive the flagellar beat will be present.

Note on notation. Throughout this chapter, we will represent points in the plane (x_1, x_2) as complex numbers $\underline{x} = x_1 + i\,x_2$; an analogous convention applies for planar vectors. This notation will simplify the calculations.

4.1 Stochastic description of sperm chemotaxis in the plane

4.1.1 Dynamic equations of sperm motion

We extend the theoretical description of sperm chemotaxis in two dimensions developed in section 3.1.1 to account for fluctuations. We consider swimming paths for sperm cells swimming near a surface along a planar path $\underline{r}(t) = r_1(t) + i\,r_2(t)$ with x- and y-coordinates $r_1(t)$ and $r_2(t)$, respectively. The velocity of the swimming path $\underline{r}(t)$ is characterized by the speed $v = |\underline{\dot{r}}|$ and the tangent $\underline{t} = \underline{\dot{r}}/v$, where dots denote time derivatives. The normal vector reads $\underline{n} = i\,\underline{t}$. The Frenet-Serret equations in two dimensions can now be written as a complex-valued differential equation

$$\underline{\dot{r}} = v\,\underline{t}, \quad \underline{\dot{t}} = v\,\kappa\,\underline{n}, \quad \underline{\dot{n}} = -v\,\kappa\,\underline{t}, \tag{4.1}$$

where $\kappa = \underline{\dot{t}}\,\underline{n}^*/v$ is the (signed) curvature of the swimming path and the star denotes the complex conjugate. From equation (4.1), we find for the time evolution of the argument φ of the tangent $\underline{t} = e^{i\varphi}$

$$\dot{\varphi} = v\,\kappa. \tag{4.2}$$

For constant curvature $\kappa(t) = \kappa_0 > 0$, the swimming path $\underline{r}(t)$ is a circle with radius $r_0 = 1/\kappa_0$. The angular frequency of circular swimming is $\omega_0 = v_0\kappa_0$ if speed $v(t) = v_0$ is constant. In the following, we consider the case where sperm cells swim in a counterclockwise sense along their circular swimming paths $\underline{r}(t)$ such that $\kappa_0 > 0$. Our results also apply for swimming in a clockwise sense, however, r_0 and ω_0 will attain negative values in this case. Note that a change of sign $\kappa_0 \to -\kappa_0$ corresponds to using the complex-conjugate path $\underline{r} \to \underline{r}^*$.

We consider a sperm swimming path in a concentration field $c(\underline{x}) = c(x+iy)$ of chemoattractant. Due to the motion of the sperm cell, the local concentration $c(\underline{r}(t))$ at the position $\underline{r}(t)$ of the sperm cell changes with time t. Chemoattractant molecules bind to specific receptors on the flagellar membrane with a rate $q(t)$ which is defined by an ensemble average and which we assume to be proportional to the local concentration

$$q(t) = \lambda c(\underline{r}(t)). \tag{4.3}$$

We introduce the chemoattractant stimulus $s(t) = \sum \delta(t - t_j)$ which counts binding events of single chemoattractant molecules to the receptors which occur at times t_j. Since binding events are stochastic, the stimulus $s(t)$ is a stochastic flux with expectation value

$$\langle s(t) \rangle = q(t). \tag{4.4}$$

Note that the chemotactic stimulus $s(t)$ has units of a rate, whereas the stimulus $s(t)$ considered in chapter 3 has units of a concentration. We will use the same symbol for both variables since they play analogous roles in our description. As in section 3.1.1, the stimulus $s(t)$ triggers a response of the chemotactic signaling network whose response we characterize by a dimensionless output variable $a(t)$ with $a = 1$ for a constant stimulus in the absence of fluctuations. We assume that this output variable $a(t)$ directly affects the curvature $\kappa(t)$ of the swimming path

$$\kappa(t) = \kappa_0 + \kappa_1(a(t) - 1) + \xi_m. \tag{4.5}$$

We include a noise term ξ_m with zero mean in (4.5) to account for fluctuations of the flagellar beat due to fluctuation in the activity of the motor ensemble.

For simplicity, we assume that the swimming speed $v(t) = v_0$ is constant, unaffected by chemotactic signaling.

As in chapter 3, we capture the essential properties of the chemotactic signaling system by a simple dynamical system [6,11,56]

$$\sigma\, \dot{a} = p\,(s_b + s) - a + \xi_a,$$
$$\mu\, \dot{p} = p\,(1 - a). \tag{4.6}$$

Here $p(t)$ is an internal variable which governs adaptation, σ is a relaxation time and μ is a time-scale of adaptation. The parameter s_b has units of a rate and sets a detection limit for low stimuli and could result from a background activity of the chemoattractant receptors in the absence of any stimulus. The intrinsic fluctuations of the molecular network underlying chemotactic signaling are included in a generic fashion by the noise term ξ_a with zero mean. This particular form of the noise term represents a simple example case to demonstrate the influence of intrinsic noise.

For a time-independent stimulus $s(t) = s_0$, the stochastic system (4.6) reaches a stationary state with $\langle a \rangle \approx 1$ and $\langle p \rangle \approx 1/(s_b + s_0)$. Approximations of the expectation values of a and p are computed by using a cumulant expansion [155] and truncating at order ≥ 3. The system is adaptive since the expectation value (and also the full statistics) of the steady-state output is independent of the stimulus level s_0.

In the noise-free case, $\xi_a = 0$, $\xi_m = 0$, small periodic variations of the stimulus $s(t) = s_0 + s_1 \cos \omega_0 t$ evoke a periodic response of the curvature $\kappa(t) = \kappa_0 + \rho_\kappa s_1 \cos(\omega_0 t + \varphi_\kappa) + \mathcal{O}(s_1^2)$ with amplitude gain ρ_κ and phase shift φ_κ. The linear response coefficient $\widetilde{\chi}_\kappa(\omega_0) = \rho_\kappa e^{i\varphi_\kappa}$ is given in appendix B. The amplitude gain ρ_κ is a function of the stimulus level s_0 and can be written as

$$\rho_\kappa = \overline{\rho}_\kappa/(s_b + s_0) \tag{4.7}$$

with a constant $\overline{\rho}_\kappa$ that represent an amplification strength of the chemotactic signaling system.

4.1.2   Characterization of noise terms

Stochastic chemoattractant stimulus. Sperm cells "measure" the local chemoattractant concentration $c = c(\underline{r}(t))$ by "reading out" the number of their activated chemoattractant receptors. A chemoattractant receptor becomes activated upon binding a chemoattractant molecule and deactivates again on a time-scale of $300\,\mathrm{ms}$ [78]. Activation and deactivation of receptors is subsumed together with downstream signaling in the generic signaling system (4.6) whose input $s(t)$ is the stochastic flux of binding events of individual chemoattractant molecules. Let us consider first a homogenous concentration field of chemoattractant $c(\underline{x}) = c_0$. If fluctuations of the concentration field can be neglected, the binding events of individual chemoattractant molecules to the receptors can be treated as independent and the series of binding events is a Poissonian spike train $s(t) = \sum_j \delta(t - t_j)$ with expectation value equal to the rate $q_0 = \lambda c_0$ of binding events. Here t_j denotes the time of the jth binding event.

In an inhomogeneous concentration field, the local chemoattractant concentration $c(\underline{r}(t))$ changes with time; thus $q(t)$ changes as well. We describe the statistics of the event times t_j by a non-homogenous Poisson process, i.e. by a renewal process with conditional probability density

$$P(t_{j+1}|t_j) = q(t_{j+1}) \exp\left(-\int_{t_j}^{t_{j+1}} dt\, q(t)\right). \tag{4.8}$$

This choice gives $\langle s(t)\rangle = q(t)$ and a Poissonian statistics of binding times for slowly varying $q(t)$.

The generic signaling module (4.6) serves as a low-pass filter which averages the incoming stimulus over the relaxation time σ of the signaling module (4.6). Thus the relevant time-scale to which the rate q of binding events should be compared to is the relaxation time σ. When the rate q is large compared to σ^{-1} and $q(t)$ changes on a time-scale slow compared to the mean inter-event-interval $1/q$, then we can replace $s(t)$ by a coarse-grained version known as the diffusion limit

$$s(t) \approx q(t) + \sqrt{q(t)}\,\xi_s(t) \tag{4.9}$$

where $\xi_s(t)$ is Gaussian white noise with $\langle \xi_s(t_1)\xi_s(t_2)\rangle = \delta(t_1 - t_2)$. In this limit, the parameter $\eta = (q\sigma)^{-1/2}$ which characterizes the relative noise strength of $s(t)$ is small. Here the relative noise strength of $s(t)$ averaged over a time τ is defined as

$$\frac{\langle \delta s\rangle_\tau^2}{\langle s\rangle_\tau^2} = \frac{1}{q\tau} \tag{4.10}$$

with $\delta s = s - \langle s\rangle$, where $\langle \cdot \rangle_\tau$ denotes an average over a time interval of length τ. Hence η^2 equals the relative noise strength of s for an averaging time $\tau = \sigma$.

Intrinsic noise of chemotactic signaling. Chemotactic signaling of sperm cells refers to the chain of events within the sperm's flagellum relating the activation of

chemoattractant receptors to a motor response which changes the swimming path of the sperm cell. Early steps of the signaling cascade are likely to involve only low numbers of the messenger molecules cyclic GMP. Thus, we expect that the chemotactic signaling system is a source of fluctuations as well. We describe these fluctuations effectively by a noise term ξ_a with power spectrum $\widetilde{S}_a(\omega)$. The power spectrum $\widetilde{S}(\omega)$ of a process $\xi(t)$ is defined by $\langle \widetilde{\xi}(\omega_1)\widetilde{\xi}^*(\omega_2)\rangle = 2\pi\,\delta(\omega_1 - \omega_2)\,\widetilde{S}(\omega_1)$ with $\widetilde{\xi}(\omega) = \int_{-\infty}^{\infty} dt\,\xi(t)e^{-i\omega t}$ being the Fourier transform of $\xi(t)$. Note $\int_{-\infty}^{\infty} d\omega\,\widetilde{S}(\omega) = 2\pi\,\langle\xi^2\rangle$.

Fluctuations of flagellar propulsion. Sperm cells are propelled in a liquid by the periodic beat of their flagellum which is driven by an ensemble of dynein motors. We expect fluctuations in the propulsion generated by the flagellar beat due to noise in the activity of the motor ensemble. These fluctuations cause fluctuations ξ_m, in the curvature of the swimming path $\underline{r}(t)$, which we characterize by the power spectrum $\widetilde{S}_m(\omega)$ of ξ_m. In general, fluctuations in the activity of the motor ensemble will cause also fluctuations of the swimming speed $v(t)$. For simplicity, we neglect speed fluctuations here. Including speed fluctuations in our description is straightforward and does not change results significantly.

Hydrodynamic flows. In the open sea, complex hydrodynamic flows convect the sperm cell and perturb the concentration field of chemoattractant. Here, we do not take these effects into account.

We consider stochastic sperm swimming paths $\underline{r}(t)$ in a concentration field of chemoattractant $c(\underline{x})$ which obey equations (4.1-4.5). Note that all noise terms are additive. Figure 4.1 shows an example of a stochastic swimming path $\underline{r}(t)$ in a radial concentration field of chemoattractant. The swimming circle is both drifting and diffusion; finally, the sperm cell finds the center of the concentration field.

4.2   Statistical properties of sperm swimming paths

4.2.1   Homogenous concentration field: Diffusion of swimming circles

As an introductory example, we study planar sperm swimming paths $\underline{r}(t)$ in the absence of a concentration gradient of chemoattractant: Sperm cells then swim along circles of radius r_0 with a curvature $\kappa(t)$ that fluctuates around its mean $\kappa_0 = 1/r_0$

$$\kappa(t) = \kappa_0 + \xi_\kappa(t). \tag{4.11}$$

Here ξ_κ is a stationary stochastic process with mean zero and power spectrum $\widetilde{S}_\kappa(\omega)$ which represents the curvature fluctuations.

These curvature fluctuations result in an effective diffusion of the center $\underline{R}(t)$ of the swimming circle. In the following, we characterize the diffusion of $\underline{R}(t)$ in the limit of weak curvature fluctuations with the limit parameter ε small, where $\varepsilon^2 = r_0^2\langle\xi_\kappa^2\rangle$. We require the higher moments of ξ_κ to be of order at least ε^3, i.e. $r_0^n\langle\xi_\kappa^n\rangle = \mathcal{O}(\varepsilon^3)$, $n \geq 3$,
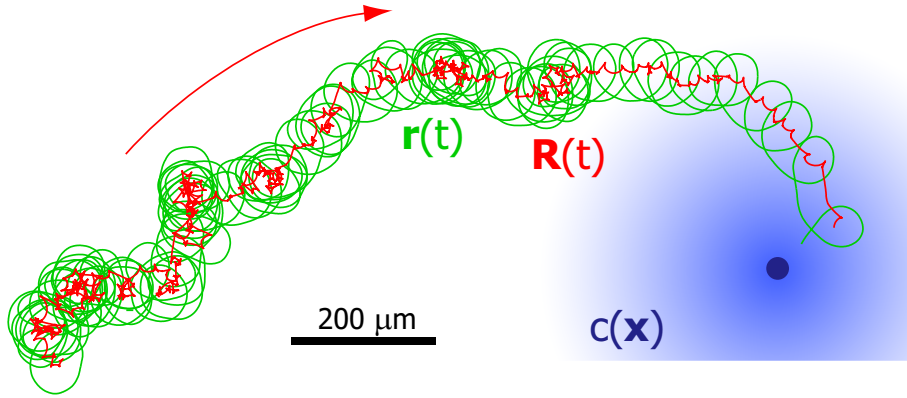
Figure 4.1: Noisy trochoidal swimming path $\underline{r}(t)$ (green) in a radial concentration field of chemoattractant. The center of the concentration field is indicated by a blue dot. The swimming path can be described as a circle which is both drifting and diffusing. The motion of the circle is characterized by the trajectory of its center $\underline{R}(t)$ (red). The path shown is a numerical solution to the set of stochastic equations (4.1-4.5) with parameters $\kappa_0 = 0.025\,\mu\mathrm{m}^{-1}$, $\kappa_1 = -2\kappa_0$, $v_0 = 100\,\mu\mathrm{m/s}$, $\sigma = 100\,\mathrm{ms}$, $\mu = 400\,\mathrm{ms}$, $s_b = 10\,\mathrm{s}^{-1}$, $\lambda = 10\,\mathrm{pM}^{-1}\mathrm{s}^{-1}$, $\widetilde{S}_a = 3 \cdot 10^{-3}\,\mathrm{s}$, $\widetilde{S}_m = 0$. These parameter values are consistent with experimental findings, see section 4.4. The radial concentration field is given by $c(\underline{x}) = C_0/|\underline{x}|$ with $C_0 = 10\,\mathrm{pM\,mm}$. The initial conditions were $a(0) = 1$, $p(0) = 1/(s_b + \lambda c_0)$, $\underline{R}(0) = 1\,\mathrm{mm}$. For the noise term ξ_a, representing the intrinsic noise of chemotactic signaling Gaussian white noise with $\langle \xi_a(t_1)\xi_a(t_2)\rangle = \widetilde{S}_a\delta(t_1 - t_2)$ was chosen.

which excludes the possibility of fat tails in the probability distribution function of ξ_κ.

We introduce the moving center $\underline{R}(t)$ of the swimming path $\underline{r}(t)$, see figure 4.2(a)

$$\underline{R} = \underline{r} + r_0\,\underline{n} = \underline{r} + r_0\,i\,\underline{t}. \tag{4.12}$$

In the noise-free case, $\varepsilon = 0$, this definition yields the centerpoint $\underline{R}$ of the perfect circle $\underline{r}(t)$. By differentiation, we obtain the following stochastic differential equation for $\underline{R}(t)$

$$\dot\varphi = v_0\kappa_0 + v_0\xi_\kappa,$$
$$\dot{\underline{R}} = -r_0 v_0\,\xi_\kappa\,e^{i\varphi}. \tag{4.13}$$

Note that the second equation contains multiplicative noise. These equations also hold for the case where ξ_κ is Gaussian white noise provided the Stratonovich interpretation is used. We assume that the argument φ_0 of the tangent $\underline{t}(0) = e^{i\varphi_0}$ at time $t = 0$ is uniformly distributed in $[0, 2\pi)$. Without loss of generality, we choose $\underline{R}(0) = 0$. Then the rotational symmetry of the problem implies

$$\langle \underline{R} \rangle = 0. \tag{4.14}$$

The expectation value $\langle \cdot \rangle$ averages over an ensemble of stochastic paths with $\underline{R}(0) = 0$ and random φ_0 (uniformly distributed). In the following, we compute the variance matrix $C_{kl} = \langle R_k R_l \rangle$ where $k, l = 1, 2$ and $\underline{R} = R_1 + iR_2$. The trace of the variance
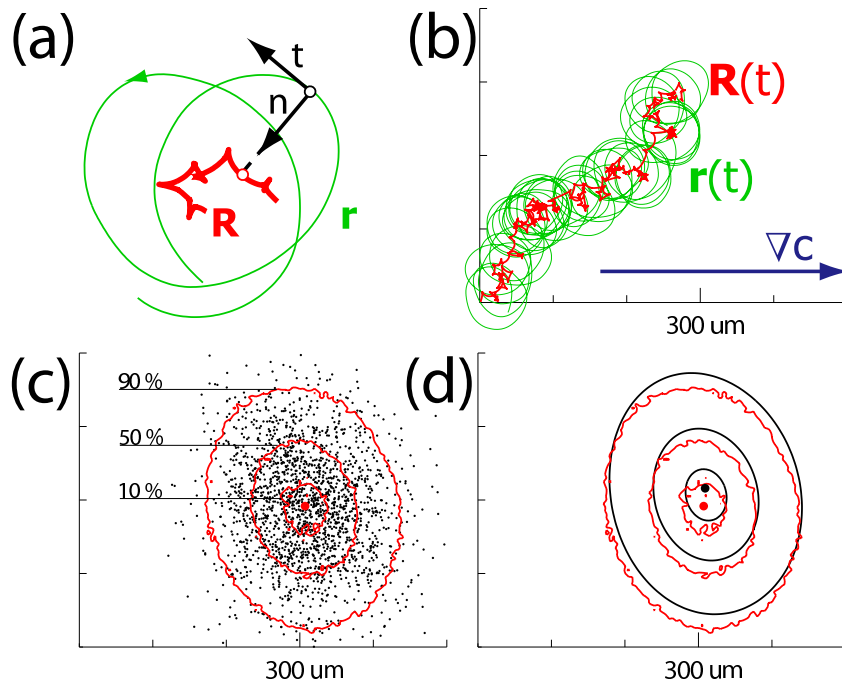
Figure 4.2: (a) Schematic depiction of a noisy circular swimming path $\underline{r}(t)$ (green) and its moving center $\underline{R}(t)$ (red). The centerline $\underline{R}(t)$ is defined as $\underline{R} = \underline{r} + r_0 i \underline{t}$ in terms of the path $\underline{r}(t)$ and its tangent $\underline{t} = \underline{\dot{r}}/v_0$, see equation (4.12). (b) Swimming path $\underline{r}(t)$ (black) in a linear concentration field of chemoattractant. The direction of the concentration gradient is indicated by a blue arrow. The swimming path is a drifting circle. The drift of the circle can be described by the motion of its center $\underline{R}(t)$ (red). The path shown is a numerical solution to equations (4.1-4.5) with parameters $\kappa_0 = 0.025\,\mu\text{m}^{-1}$, $\kappa_1 = -2\kappa_0$, $v_0 = 100\,\mu\text{m}/s$, $\sigma = \mu = 200\,\text{ms}$, $s_b = 10\,\text{s}^{-1}$, $\lambda = 10\,\text{pM}^{-1}\,\text{s}^{-1}$, $\widetilde{S}_a = 3 \cdot 10^{-3}\,\text{s}$, $\widetilde{S}_m = 0$. These parameter values are consistent with experimental findings, see appendix 3.3.1. The linear concentration field is given by $c(\underline{x}) = c_0 + c_1 \text{Re}\,\underline{x}$ with $c_0 = 10\,\text{pM}$, $c_1 = 0.1\,c_0/r_0$. Integration time was $t_{\text{end}} = 100\,\text{s}$. The initial conditions were $a(0) = 1$, $p(0) = 1/(s_b + \lambda c_0)$, $\underline{r}(0) = -r_0 i e^{i\varphi_0}$, and $\varphi_0 \in [0, 2\pi)$ drawn randomly from a uniform distribution. For the noise term ξ_a, representing the intrinsic noise of chemotactic signaling Gaussian white noise with $\langle \xi_a(t_1)\xi_a(t_2)\rangle = \widetilde{S}_a\delta(t_1 - t_2)$ was chosen. (c) Endpoints $\underline{R}(t_{\text{end}})$ of centerlines of swimming paths in a linear concentration field for $n = 10^4$ different realizations (black dots). All centerlines (not shown) start at the origin. The same parameters as for panel (b) were used. Also shown is the contour plot of a histogram of the centerline endpoints (red contour lines). The contour lines enclose regions which contain 10%, 50%, and 90% of the endpoints, respectively. The histogram was computed from $n = 10^6$ realizations. The expectation value $\langle \underline{R}(t_{\text{end}})\rangle$ is indicated by a red dot. (d) Contour plot of the spatial distribution function of the endpoints $\underline{\widehat{R}}(t_{\text{end}})$ of the coarse-grained centerline $\underline{\widehat{R}}(t)$ determined by the effective equation of motion (4.39) (black contour lines). As in panel (c), the contour lines enclose regions which contain 10%, 50%, and 90% of the endpoints, respectively. The distribution function of $\underline{\widehat{R}}(t_{\text{end}})$ was obtained by numerically integrating the Fokker-Planck equation associated to (4.39). The expectation value $\langle \underline{\widehat{R}}(t_{\text{end}})\rangle$ is indicated by a black dot. For comparison, the contour plot from panel (c) is shown again (red contour lines).

matrix $C_{kk} = \langle |\underline{\mathrm{R}}|^2 \rangle$ is computed as a double integral

$$
\begin{aligned}
\langle |\underline{\mathrm{R}}(t)|^2 \rangle &= \int_0^t dt_1 \int_0^t dt_2 \, \langle \dot{\underline{\mathrm{R}}}(t_1) \dot{\underline{\mathrm{R}}}(t_2)^* \rangle \\
&= (r_0 v_0)^2 \int_0^t dt_1 \int_0^t dt_2 \, S_\kappa(t_2 - t_1) e^{i\omega_0(t_1 - t_2)} + \mathcal{O}(\varepsilon^3).
\end{aligned}
\tag{4.15}
$$

Here the autocorrelation function $S_\kappa(t_1 - t_2) = \langle \xi_\kappa(t_1) \xi_\kappa(t_2) \rangle$ is the Fourier transform of $\widetilde{S}_\kappa(\omega)$.[8] For times t much larger than the correlation time of ξ_κ, we can approximate $\langle |\underline{\mathrm{R}}|^2 \rangle$ as

$$
\begin{aligned}
\langle |\underline{\mathrm{R}}(t)|^2 \rangle &\approx (r_0 v_0)^2 \int_0^t dt_1 \int_{-\infty}^{\infty} d\tau \, S_\kappa(\tau) e^{-i\omega_0 \tau} \\
&= (r_0 v_0)^2 \, \widetilde{S}_\kappa(\omega_0) \, t
\end{aligned}
\tag{4.16}
$$

Note that the variance $\langle |\underline{\mathrm{R}}|^2 \rangle$ grows linearly in time as is typical for a diffusion process. The complex number $\langle \underline{\mathrm{R}}^2 \rangle$ characterizes an anisotropy of the diffusion process

$$
\langle \underline{\mathrm{R}}^2 \rangle = \langle R_1^2 \rangle - \langle R_2^2 \rangle + 2i \langle R_1 R_2 \rangle.
\tag{4.17}
$$

To leading order in ε, we compute

$$
\langle \underline{\mathrm{R}}(t)^2 \rangle \approx (r_0 v_0)^2 \int_0^t dt_1 \, \langle e^{2i\omega_0 t_1 + 2i\varphi_0} \rangle \, \widetilde{S}_\kappa(\omega_0) = 0
\tag{4.18}
$$

for a uniform distribution of φ_0. Indeed, the rotational symmetry of the problem already implies $\langle \underline{\mathrm{R}}(t)^2 \rangle = 0$. We conclude, that curvature fluctuations result in effective isotropic diffusion of the center $\underline{\mathrm{R}}(t)$ of the swimming circles with an effective diffusion constant D that is proportional to the power spectrum of the curvature fluctuations evaluated at the circle frequency ω_0

$$
\boxed{4D \approx (v_0 r_0)^2 \widetilde{S}_\kappa(\omega_0).}
\tag{4.19}
$$

The approximation (4.19) is valid up to terms of order $\mathcal{O}(\varepsilon^3)$. For the particular model given in (4.1-4.5), $\widetilde{S}_\kappa(\omega)$ has contributions from (i) the stochastic stimulus, (ii) the intrinsic fluctuations of the chemotactic signaling system and (iii) from the fluctuations in the activity of the motor ensemble. Below we give an approximation for $\widetilde{S}_\kappa$ in the limit of weak noise, see equation (4.35). In general, $\widetilde{S}_\kappa$ and D are functions of the concentration c_0 of a homogenous concentration field of chemoattractant. Figure 4.3 displays the concentration dependence of D; a pronounced maximum of D can be observed close to $c^* = s_b/\lambda$.

It is interesting that the result (4.19) for the diffusion coefficient is proportional to the power spectrum $\widetilde{S}_\kappa$ of the curvature fluctuations evaluated at the frequency ω_0 of circular swimming. A similar result has been found in a different context of diffusing spirals in an excitable medium where effective diffusion was characterized by a noise

---

[8]This is the so-called Wiener-Khintchine theorem, see [131].
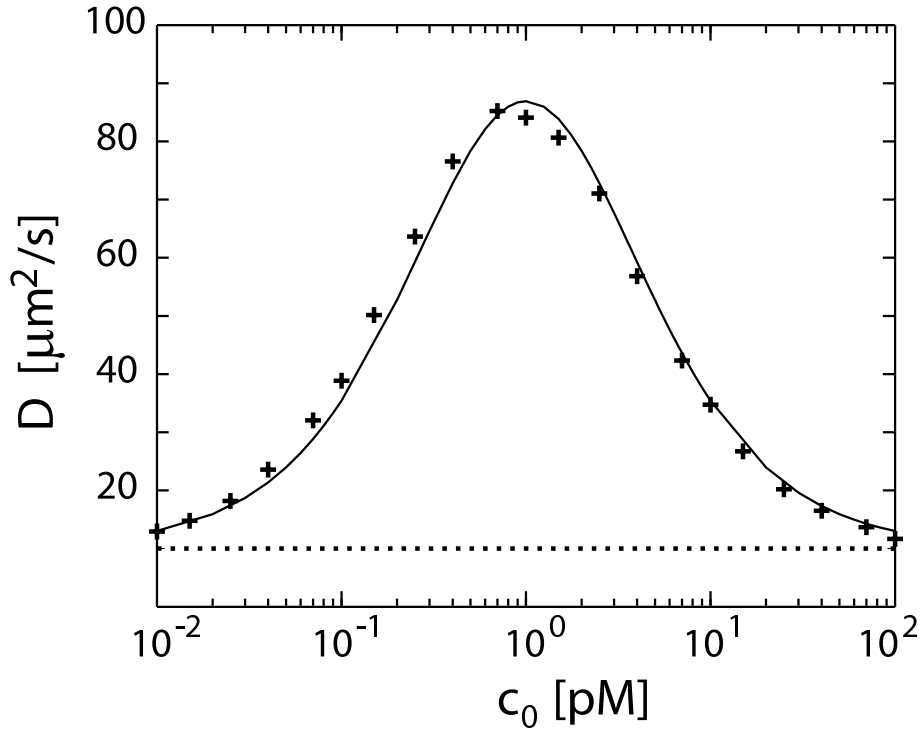
Figure 4.3: Effective diffusion constant D of swimming circles as a function of concentration c_0 for a homogenous concentration field of chemoattractant. Shown are simulation results (symbols) and our analytical result (solid line), see equations (4.19), (4.35). Error bars are of the size of the symbols. The dotted line represents the analytic value for the diffusion constant in the absence of chemoattractant, $D^{(0)} = (r_0 v_0)^2 \widetilde{S}_\kappa^{(0)}(\omega_0)/4$. The same parameter set as for figure 4.2 was used, these parameters are consistent with experimental findings.

spectrum evaluated at the frequency of spiral rotation [140].

Using the same reasoning as above, one can derive an exact expression for the diffusion constant D

$$4D = v_0^2 \, \widetilde{C}_\kappa(\omega_0). \tag{4.20}$$

Here $\widetilde{C}_\kappa(\omega)$ is the Fourier transform of the characteristic function $C_\kappa(t) = \langle \exp iv_0 \, \Phi_\kappa(t) \rangle$ of $\Phi_\kappa(t) = \int_0^t dt_0 \, \xi_\kappa(t_0)$. Expanding (4.20) in powers of ε reproduces (4.19) as leading order contribution. In the special case where the curvature fluctuations ξ_κ are modeled as Gaussian white noise with $\xi_\kappa(t_1) \, \xi_\kappa(t_2) \rangle = 2D_\kappa \delta(t_1 - t_2)$, we have $C_\kappa(t) = \exp(-v_0^2 D_\kappa |t|)$ and $4D = 2D_\kappa v_0^4/(\omega_0^2 + D_\kappa^2 v_0^4)$. This special case is treated in [156].

4.2.2   Chemoattractant gradient with low concentration

There is evidence, that sperm cells can detect single chemoattractant molecules, when chemoattractant concentration is sub-pico-molar [78]. To characterize sperm chemotaxis at very low chemoattractant concentrations, we study the set of equations (4.1-4.5) in the limit of a low chemoattractant concentration with a chemoattractant molecule

binding rate q small compared to σ^{-1}, where σ is the relaxation time scale of the signaling system in (4.6). For simplicity, we neglect the intrinsic noise of chemotactic signaling and the fluctuations in the activity of the motor ensemble, i.e. $\xi_a = 0$ and $\xi_m = 0$.

The swimming response. Every binding event evokes a stereotypic swimming response which can be effectively described as a translation of the center $\underline{R}$ of the swimming circle $\underline{r}(t)$ by a vector $\Delta\underline{R}$. The curvature response to a single stimulus spike $s(t) = \delta(t)$ is given by the linear response function χ_κ

$$\kappa(t) = \kappa_0 + \chi_\kappa(t). \tag{4.21}$$

The tangent $\underline{t} = \underline{\dot{r}}/v_0$ integrates as

$$\underline{t}(t) = \exp(i\omega_0 t + i\varphi_0) \cdot \exp\left(iv_0 \int_{-\infty}^{t} dt_0\, \chi_\kappa(t_0)\right). \tag{4.22}$$

We may assume $\underline{R}(t) = 0$ before the stimulus spike occurred; hence $\underline{r}(t) = -ir_0 \exp(i\omega_0 + i\phi_0)$ for $t < 0$. For times long after the stimulus spike, $t \gg \sigma$, the swimming path resumes a perfect circular trajectory again

$$\underline{r}(t) = \underline{u}\, e^{i\varphi_0} - ir_0 \exp(i\omega_0 t + i\varphi_0 + i\varphi_u). \tag{4.23}$$

with a phase shift $\varphi_u = v_0\widetilde{\chi}_\kappa(0)$ and a translation vector $\Delta\underline{R} = \underline{u}\, e^{i\varphi_0}$. By integrating equation (4.22), we find $\underline{u} \approx -r_0 v_0 \widetilde{\chi}_\kappa^*(\omega_0)$ to leading order in $v_0|\chi_\kappa|$. Here $\widetilde{\chi}_\kappa(\omega_0) = \rho_\kappa e^{i\varphi_\kappa}$ is the linear response coefficient at the circling frequency ω_0 of the generic signaling module given in (3.4), see (B.5). For an adapting signaling system such as (3.4), we have $\varphi_u = 0$.

Statistics of sperm swimming paths. We study (4.1-4.5) for a linear concentration field of chemoattractant,

$$c(\underline{x}) = c(x + iy) = c_0 + c_1 x, \tag{4.24}$$

where we assume for simplicity that the gradient is parallel to the x-axis. We consider the limit of (i) a shallow concentration gradient with $\nu = c_1 r_0/c_0 \ll 1$, and (ii) a binding rate $q(t)$ of chemoattractant molecules low compared with σ^{-1}. Between two binding events, $t_j \ll t < t_{j+1}$, the swimming path is circular once the jth swimming response relaxed

$$\underline{r}(t) = \underline{R}(t) - ir_0 e^{i\omega_0 t + i\varphi_0}. \tag{4.25}$$

This results in a periodic modulation of the binding rate

$$q(t) = \lambda c(\underline{r}(t)) = \lambda c(\underline{R}(t)) + \lambda c_1 r_0 \sin(\omega_0 t + \varphi_0). \tag{4.26}$$

For $q\sigma \ll 1$, we can treat individual binding events independently and find for the center $\underline{R}$ of the circular swimming path $\underline{r}$ for $t > 0$

$$\underline{R}(t) = \underline{u} \sum_{0 < t_j < t} e^{i\varphi_j}. \tag{4.27}$$

Here, the t_j denote the times of the individual binding events and $\varphi_j = \varphi(t_j)$. From the periodic modulation of the binding rate (4.26), we determine the probability density $P(\varphi)$ of the angles φ_j

$$2\pi P(\varphi) = 1 + \nu \sin\varphi + \mathcal{O}(\nu^2). \tag{4.28}$$

The number n of binding events in the time interval $0 < t_j < t$ satisfies $\langle n \rangle = \langle \delta n^2 \rangle = \lambda c_0 t + \mathcal{O}(\nu)$ where $\delta n = n - \langle n \rangle$. Thus we find using (4.27) and (4.28)

$$\langle \underline{R}(t) \rangle = \underline{u}\,\lambda c_0 t \int_0^{2\pi} d\varphi\, P(\varphi) e^{i\varphi} + \mathcal{O}(\nu^2)$$
$$= \underline{u}\,\lambda c_0 t\, i\,\nu + \mathcal{O}(\nu^2), \quad \text{and} \tag{4.29}$$
$$\langle |\delta\underline{R}(t)|^2 \rangle = |\underline{u}|^2\,\lambda c_0\,t + \mathcal{O}(\nu^2).$$

with $\delta\underline{R} = \underline{R} - \langle\underline{R}\rangle$. Thus, the circle center $\underline{R}$ is both (i) drifting with drift speed $v_d = \rho_\kappa \lambda c_1 r_0^2 v_0 / 2$ in a direction which encloses an angle $\alpha = 3\pi/2 - \varphi_\kappa$ with the concentration gradient and (ii) diffusing in both space dimensions with an effective diffusion coefficient $D = \langle |\delta\underline{R}|^2 \rangle / (4t) = (r_0 v_0)^2 \rho_\kappa^2 \lambda c_0 / 4 + \mathcal{O}(\nu^2)$. The average drift of the circle center is exactly the same as the one obtained for a deterministic description of sperm chemotaxis [56]. Thus the deterministic approach is providing a mean-field description. Diffusion is essentially isotropic; the quantity $\langle \delta\underline{R}^2 \rangle = \langle \delta R_1^2 \rangle - \langle \delta R_2^2 \rangle + 2i\langle \delta R_1\,\delta R_2 \rangle$ which characterizes anisotropy of diffusion vanishes to linear order in ν, $\langle \delta\underline{R}^2 \rangle = 0 + \mathcal{O}(\nu^2)$. The relative strength of the chemotactic drift compared to the undirected diffusive motion of the center of the swimming circle is characterized by a dimensionless Peclet number

$$\text{Pe} = \frac{v_d\, r_0}{4D} = \frac{s_b + \lambda c}{2\overline{\rho}_\kappa \omega_0} \frac{|\boldsymbol{\nabla} c|}{c} + \mathcal{O}(\nu^2). \tag{4.30}$$

This expression for the Peclet number only holds, if intrinsic fluctuations of chemotactic signaling and noise in the activity of the flagellar motor ensemble can be neglected. In the next section, we derive an expression for the effective diffusion coefficient D where these noise sources have been included, see equations (4.35) and (4.36). With these noise sources, we find that the Peclet number scales with the relative concentration gradient $|\nabla c|/c$ for high concentrations c.

4.2.3   Chemoattractant gradient with high concentration

To gain further insight into the stochastic description of sperm chemotaxis, we study the set of equations (4.1-4.5) in the weak noise limit for a linear concentration field of chemoattractant $c(\underline{x}) = c_0 + c_1 \text{Re}\,\underline{x}$. More precisely, we consider the limit of (i) a

shallow concentration gradient with $\nu = c_1 r_0/c_0 \ll 1$ and (ii) a high chemoattractant concentration c_0 with a binding rate $q(t) = \lambda c(\underline{r}(t))$ of chemoattractant molecules much higher than σ^{-1}, where σ sets the relaxation time scale of the chemotactic signaling system in (4.6). In this limit, the parameter $\eta = (q\sigma)^{-1/2}$ is small; η characterizes the relative noise strength of $s(t)$. For simplicity, we first neglect the intrinsic noise of chemotactic signaling and the fluctuations in the activity of the motor ensemble, i.e. $\xi_a = 0$ and $\xi_m = 0$. The general case will be studied in equation (4.35). In a systematic expansion of $\langle \underline{R} \rangle$, $\langle |\delta \underline{R}|^2 \rangle$ and $\langle \delta \underline{R}^2 \rangle$ in powers of ν and η, many terms vanish due to the symmetries of the problem; to leading order we find

$$
\begin{aligned}
\langle \underline{R}(t) \rangle &\sim \nu\, t &&+ \mathcal{O}(\nu\eta^2, \nu^3), \\
\langle |\delta \underline{R}(t)|^2 \rangle &\sim \eta^2\, t &&+ \mathcal{O}(\nu^2\eta^2, \eta^3), \\
\langle \delta \underline{R}(t)^2 \rangle &= 0 &&+ \mathcal{O}(\nu^2\eta^2).
\end{aligned}
\tag{4.31}
$$

The expansion of $\langle \underline{R} \rangle$ in powers of ν can only contain odd powers of ν since reversing the direction of the gradient changes the sign of both ν and $\langle \underline{R} \rangle$. Likewise the expansions of both $\langle |\underline{R}|^2 \rangle$ and $\langle \underline{R}^2 \rangle$ contain only even powers of ν. Terms proportional to η yield zero in the noise-average. Since $\langle \delta \underline{R}^2 \rangle$ measures anisotropy, this expression must vanish in the case $\nu = 0$ when the rotational symmetry is not broken. For the leading order coefficients of $\langle \underline{R} \rangle$ and $\langle |\underline{R}|^2 \rangle$ we recover essentially the results obtained for the case of low concentration

$$
\langle \underline{R}(t) \rangle = -i\, v_d\, e^{-i\varphi_\kappa}\, t + \mathcal{O}(\nu\eta^2, \nu^3),
\tag{4.32}
$$

$$
\langle |\delta \underline{R}(t)|^2 \rangle = (r_0 v_0)^2\, \widetilde{S}_\kappa(\omega_0)\, t + \mathcal{O}(\nu^2\eta^2, \eta^3)
\tag{4.33}
$$

with chemotactic drift speed

$$
v_d = \rho_\kappa \lambda c_1 r_0^2 v_0/2
\tag{4.34}
$$

and $\widetilde{S}_\kappa(\omega_0) = \rho_\kappa^2 \lambda c_0$. We sketch the derivation of (4.32), (4.33) in appendix L.

So far, we have neglected the intrinsic noise of chemotactic signaling and the fluctuations in the activity of the motor ensemble. Now we include these noise terms and consider the limit of weak noise with $\eta \ll 1$, $\langle \xi_a^2 \rangle \lesssim \eta^2$ and $r_0^2 \langle \xi_m^2 \rangle \lesssim \eta^2$. We also assume that the higher-order moments of ξ_a and ξ_m are of order at least $\mathcal{O}(\eta^3)$. In this limit, $\widetilde{S}_\kappa(\omega)$ is a sum of contributions from the different noise sources

$$
\widetilde{S}_\kappa(\omega_0) = \rho_\kappa^2 \lambda c_0 + \bar{\rho}_\kappa^2 \widetilde{S}_a(\omega_0) + \widetilde{S}_m(\omega_0) + \mathcal{O}(\nu^2, \eta^3)
\tag{4.35}
$$

where $\rho_\kappa = \bar{\rho}_\kappa/(s_b + \lambda c_0)$ is given in appendix B. The second summand of the right-hand side of equation (4.35) describes a contribution to $\widetilde{S}_\kappa$ stemming from the intrinsic noise of chemotactic signaling; while the third summand describes a contribution due to fluctuations in the activity of the motor ensemble. We define the concentration-independent part of $\widetilde{S}_\kappa(\omega_0)$ as $\widetilde{S}_\kappa(\omega_0)^{(0)} = \bar{\rho}_\kappa^2 \widetilde{S}_a(\omega_0) + \widetilde{S}_m(\omega_0)$. We can thus write $\widetilde{S}_\kappa(\omega_0)$ as the sum of a concentration-independent part $\widetilde{S}_\kappa(\omega_0)^{(0)}$ and a concentration-dependent part $\widetilde{S}_\kappa(\omega_0)^{(c)} = \rho_\kappa^2 \lambda c_0$. From $\rho_\kappa = \bar{\rho}_\kappa/(s_b + \lambda c_0)$, we see that $\widetilde{S}_\kappa(\omega_0)^{(c)}$

scales like $c_0/(s_b + \lambda c_0)^2$. As a consequence, $\widetilde{S}_\kappa(\omega_0)$ is a non-monotonous function of concentration c_0 with a maximum at $c^* = s_b/\lambda$. Hence, also the effective diffusion coefficient

$$D = \langle |\delta\underline{R}|^2 \rangle/(4t) = (r_0 v_0)^2 \widetilde{S}_\kappa(\omega_0)/4 + \mathcal{O}(\nu^2\eta^2, \eta^3) \qquad (4.36)$$

depends on concentration c_0 via $\widetilde{S}_\kappa(\omega_0)$, see figure 2. The consequences of a space-dependent diffusion coefficient have been discussed in the context of bacterial chemotaxis in reference [137].

Interestingly, (4.36) also provides a good approximation in the regime of low and intermediate concentrations c_0. This agreement suggests that our results are more general and hold not only in the particular limit case considered here. For example, similar results can be derived in the case of weak output noise with $\langle \delta a^2 \rangle \ll 1$ where $\delta a = a - \langle a \rangle$.

4.3 Effective equation for the centerline

We derive an effective equation of motion for a coarse-grained centerline $\widehat{\underline{R}}(t)$ in a linear concentration field (4.24). On short time scales $t < T = 2\pi/\omega_0$, the centerline $\underline{R}(t)$ is a stochastic trajectory that depends on the particular shape of the spectra $\widetilde{S}_a$ and $\widetilde{S}_m$ and therefore has non-generic properties. For longer time intervals $\Delta t = nT$, however, we find simple, general expressions for the drift $\langle \underline{R}(\Delta t) - \underline{R}(0) \rangle$ and for the variance $\langle |\underline{R}(\Delta t)|^2 \rangle$, see equations (4.32-4.33).

In order to derive a genuine coarse-grained description, we introduce a discrete centerline $\widehat{\underline{R}}(t_k)$ which is defined at the discrete times $t_k = k\,\Delta t$, $k = 0, 1, 2, \ldots$, and which reproduces (to leading order) the second-order statistics of $\underline{R}(t)$ at the discrete times t_k. The stochastic process generating $\widehat{\underline{R}}(t_k)$ is defined by the following stochastic difference equation

$$\widehat{\underline{R}}(t_{k+1}) = \widehat{\underline{R}}(t_k) + \langle \underline{R}(t_{k+1}) - \underline{R}(t_k) \rangle_k + \Xi_k. \qquad (4.37)$$

Here Ξ_k is a complex random variable with mean zero. The second moments of Ξ_k are given by

$$\langle |\Xi_k|^2 \rangle = \langle |\delta\underline{R}(t_{k+1})|^2 \rangle_k, \quad \text{and} \quad \langle \Xi_k^2 \rangle = \langle \delta\underline{R}(t_{k+1})^2 \rangle_k \qquad (4.38)$$

where $\delta\underline{R} = \underline{R} - \langle \underline{R} \rangle_k$. The expectation value $\langle \cdot \rangle_k$ averages over an ensemble of stochastic centerlines $\underline{R}(t)$ with initial condition $\underline{R}(t_k) = \widehat{\underline{R}}(t_k)$ and with uniformly distributed argument φ_k of the tangent $\underline{t}(t_k) = e^{i\varphi_k}$.

We restrict ourselves to the limit case of weak noise with $\eta \ll 1$ as specified in the previous section 4.2.3. This limit case is characterized by (i) a high chemoattractant concentration, (ii) weak intrinsic noise of chemotactic signaling, and (iii) small fluctuations of the activity of the flagellar motor ensemble. Additionally, we assume that the concentration gradient is shallow with $\nu = c_1 r_0/c_0 \ll 1$. From the perturbation calculation in the previous section, we know that $\langle \delta\underline{R}^2 \rangle_k = 0 + \mathcal{O}(\nu^2\eta^2)$. Therefore,

we can describe the components Ξ_1, Ξ_2 of $\underline{\Xi}_k = \Xi_1 + i\,\Xi_2$ by uncorrelated Gaussian random variables with $\langle \Xi_k \Xi_l \rangle = 2D\Delta t\,\delta_{kl}$ where $4D\Delta t = \langle |\delta\underline{R}(t_{k+1})|^2 \rangle_k$. If we choose Δt longer than the correlation time of total curvature fluctuations $\xi_\kappa(t)$, we may treat the stochastic increments $\underline{\Xi}_k$ in equation (4.37) for different k as mutually independent. Now equation (4.37) describes an Euler scheme for the numerical integration of a stochastic differential equation in Itō interpretation. We can perform the continuum limit of (4.37) and obtain the stochastic differential equation (4.39) for the continuous-time stochastic path $\underline{\widehat{R}}(t)$.

We obtain an effective equation of motion for the coarse-grained centerline $\underline{\widehat{R}}$ which is valid on time-scales large compared to Δt

$$\text{(I)} \quad \frac{d}{dt}\underline{\widehat{R}}(t) = v_d\,e^{i\alpha}\,\underline{\nabla}c/|\underline{\nabla}c| + \underline{\xi}. \tag{4.39}$$

Here $\underline{\xi} = \xi_1 + i\,\xi_2$ is a complex random variable whose components ξ_j are uncorrelated Gaussian random variables with $\langle \xi_k(t_1)\xi_l(t_2) \rangle = 2D\,\delta(t_1 - t_2)\,\delta_{kl}$ for $k,l = 1,2$. The concentration gradient $\underline{\nabla}c$ is the complex number $\underline{\nabla}c(x+iy) = \partial_x c(x+iy) + i\,\partial_y c(x+iy)$. The time-evolution of the coarse-grained centerline $\underline{\widehat{R}}$ described by equation (4.39) is the superposition of (i) a deterministic drift with drift velocity v_d in a direction that encloses an angle of α with the concentration gradient, and (ii) pure diffusion with an effective diffusion coefficient of D. Since the diffusion coefficient D depends on concentration, the noise term in equation (4.39) is effectively multiplicative. Equation (4.39) is defined by using the Itō interpretation; see [87, 111] for a discussion of Itō and Stratonovich stochastic differential equations. Note that the Itō and the Stratonovich version of (4.39) differ by a noise-induced drift term which is of order $\sim \nu\eta^2$.

We can generalize (4.39) for a nonlinear concentration field $c(\underline{x})$, provided the nonlinearities of the concentration field are small on the length-scale r_0, i.e. $|\boldsymbol{\nabla}^2 c| \ll |\boldsymbol{\nabla}c|/r_0$. Our equation of motion (4.39) can be regarded as a complex Keller-Segel equation [80].

Figure 4.2(d) compares (i) the distribution of centerline endpoints $\underline{R}(t_{\text{end}})$ obtained from the full dynamic equations of sperm motion (4.1-4.5), and (ii) the distribution of endpoints $\underline{\widehat{R}}(t_{\text{end}})$ of the coarse-grained centerline obtained from the effective equation of motion (4.39). We find good agreement between both endpoint distributions. In particular, both endpoint distributions are anisotropic. This is remarkable, since the distribution of endpoints $\underline{\widehat{R}}(t_{\text{end}})$ of coarse-grained centerlines is obtained from simulating equation (4.39) which has an isotropic noise term. The apparent anisotropy is a consequence of the position-dependence of the drift speed $v_d(\underline{R})$. Note that in the special case $\alpha = 0$, the stochastic equation of motion (4.39) of the coarse-grained centerline $\underline{\widehat{R}}$ describes the trajectory of a particle diffusing in an effective potential $E = \Theta\,\nabla\ln(s_b + \lambda c)$ which satisfies $-\nabla E(\underline{R}) = v_d\,\nabla c/|\nabla c|$. Here $\Theta = \bar{\rho}_\kappa r_0^2 v_0/2$ is a constant.

4.3.1   Example: Radial concentration field

We discuss the case of a radial concentration field $c(\underline{x}) = C(|\underline{x}|)$, which arises if chemoattractant diffuses away from a single source such as an egg. The chemotactic drift speed v_d and the effective diffusion coefficient D of sperm swimming circles depend on concentration c, see equations (4.34) and (4.36). In a radial concentration field, these quantities become functions $v_d = v_d(R)$ and $D = D(R)$ of the distance $R = |\underline{R}|$ from the source. We introduce polar coordinates (R, ψ) such that $\underline{R} = R\,e^{i\psi}$. Equation (4.39) describes the stochastic dynamics of R_1 and R_2 with $\underline{R} = R_1 + iR_2$. Using the Itō chain rule (E.6), we find for the dynamics of $R = \sqrt{R_1^2 + R_2^2}$ and $\psi = \arctan(R_2/R_1)$

$$(\text{I}) \quad \begin{aligned} \dot{R} &= -v_d \cos\alpha + \xi_1 \cos\psi + \xi_2 \sin\psi + D/R, \\ \dot{\psi} &= (-v_d \sin\alpha - \xi_1 \sin\psi + \xi_2 \cos\psi)/R. \end{aligned} \qquad (4.40)$$

The expression for $\dot{R}$ in equation (4.41) contains a noise-induced drift term D/R which results from the nonlinearity of the coordinate transformation $\underline{R} = R\,e^{i\psi} \mapsto (R, \psi)$. We introduce $\xi_1' = \xi_1 \cos\psi + \xi_2 \sin\psi$ and $\xi_2' = -\xi_1 \sin\psi + \xi_2 \cos\psi$. Since ξ_j and ψ are independent in the Itō calculus, we conclude that ξ_j' are again Gaussian white noise terms with $\langle \xi_k'(t_1)\xi_l'(t_2)\rangle = 2D\,\delta_{kl}\delta(t_1 - t_2)$. Hence the stochastic dynamics of R and ψ can equivalently be described by the following Itō stochastic differential equation

$$(\text{I}) \quad \begin{aligned} \dot{R} &= v_d \sin\varphi_\kappa + \xi_1 + D/R, \\ \dot{\psi} &= (v_d \cos\varphi_\kappa + \xi_2)/R. \end{aligned} \qquad (4.41)$$

Here $\varphi_\kappa = 3\pi/2 - \alpha$ and ξ_j, $j = 1, 2$, is uncorrelated Gaussian white noise with $\langle \xi_k(t_1)\,\xi_l(t_2)\rangle = 2D\,\delta(t_1 - t_2)\,\delta_{kl}$ for $k, l = 1, 2$. We introduce the probability density $S(\underline{R}, t)$ such that $S\,dA$ is the probability to find a sperm cell in the area element dA at time t. The total number of sperm cells in the system equals $\int dA\, S(\underline{R}, t)$. It is useful to introduce also the radial probability density $P(R, t) = R\int_0^{2\pi} d\psi\, S(Re^{i\psi}, t)$. Note that $P\,dR$ is the probability to find a sperm cell in a thin annulus of radius R and width dR. In our effective equation of motion (4.41), the dynamics of R decouples from ψ reflecting the symmetries of the problem. Therefore, the radial probability $P(R, t)$ obeys a Fokker-Planck equation which reads [131]

$$\frac{\partial}{\partial t} P = \mathcal{L}\, P \qquad (4.42)$$

with a Fokker-Planck operator $\mathcal{L}$ given by

$$\mathcal{L} = \frac{\partial}{\partial R}\left[-\left(v_d(R)\sin\varphi_\kappa + D(R)/R\right) + \frac{\partial}{\partial R} D(R)\right]. \qquad (4.43)$$

For completeness, we mention that the Fokker-Planck equation for the probability density $S(\underline{R}, t) = S(Re^{i\psi}, t)$ has the form $R\frac{\partial}{\partial t}S = \mathcal{L}(RS) + \frac{\partial}{\partial \psi}\left(-v_d \cos\varphi_\kappa RS + \frac{\partial}{\partial \psi} DS\right)$.

A simple scenario: We are interested in the rate at which sperm cells reach the egg and study in the following an idealized scenario where (i) we neglect the concentration dependence of the effective diffusion coefficient $D(R) = D_0$, (ii) the sensitivity threshold of chemotactic signaling vanishes, $s_b = 0$, and (iii) the radial chemoattractant concentration field decays as a power-law $c(\underline{x}) \sim 1/|\underline{x}|^\beta$ with exponent β. Note that the steady-state concentration field established by diffusion in three-dimensional space from a spherical chemoattractant source with constant release rate of chemoattractant corresponds to $\beta = 1$. For adaptive chemotactic signaling (without sensitivity threshold), the relevant input quantity is the relative concentration gradient $|\boldsymbol{\nabla} c|/c$ which for our choice of concentration field scales inversely with distance as $|\boldsymbol{\nabla} c|/c = \beta/R$. Hence, the drift speed in radial direction reads $v_d \sin \varphi_\kappa = -\Gamma_0/R$ where $\Gamma_0 = -\beta \overline{\rho}_\kappa r_0^2 v_0 \sin \varphi_\kappa$ is a constant. Likewise, the drift speed in azimuthal direction is given by $v_d \cos \varphi_\kappa = -\Gamma_0 \cot \varphi_\kappa/R$.

To mimic the egg, we consider a disk-shaped target of radius R_{target} located at the origin of the concentration field which absorbs any sperm cell hitting its boundary. The absorbing target gives rise to a boundary condition $P(R_{\text{target}}) = 0$. We first study the steady-state solution of equation (4.42) subject to this boundary condition and the condition $P_0(R) \approx 2\pi R\, S_\infty$ for large R where S_∞ is the sperm concentration far from the target. For positive chemotaxis with $\Gamma_0 > 0$, the stationary probability density reads $S_0(\underline{R}) = P_0(R)/(2\pi R)$

$$S_0(\underline{R}) = S_\infty \left[1 - \left(\frac{R_{\text{target}}}{|\underline{R}|} \right)^{\Gamma_0/D_0} \right]. \tag{4.44}$$

In steady-state, sperm cells arrive at the target with a constant rate $k_0 = 2\pi\, S_\infty\, \Gamma_0$. The stationary state is characterized by a net flux in azimuthal direction $J_\psi = v_d \cos \varphi_\kappa\, S_0(\underline{R})$, i.e. $k_\psi = J_\psi\, dR$ is the rate by which sperm cells pass through a section of length dR on a ray emanating from the origin. Thus there is a net circular current whirling around the origin. Such an azimuthal flux has been already discussed in the context of an alternative stochastic model of sperm chemotaxis in [7]. Note that if chemotaxis is absent or negative with $\Gamma_0 \leq 0$, then there exists no steady-state probability distribution $S_0(\underline{R})$ with fixed concentration S_∞ at infinity [32]. If we start in this case with a homogenous distribution of sperm cells $S(\underline{R}, 0) = S_\infty$ at time $t = 0$, a growing region around the target becomes depleted of sperm cells and the time-dependent rate $k(t)$ of sperm cells arriving at the target vanishes in the limit of long times. We thus find that the system undergoes a dynamic second-order phase transition as a function of chemotactic strength Γ_0 where $k_0 = \lim_{t \to \infty} k(t)$ plays the role of an order parameter.

Success probability. We now turn our focus to single sperm cells and calculate the probability $p_0(R_0)$ for a single sperm cell released at a distance R_0 at time $t = 0$ to find the target after sufficiently long time. Recall that for a freely diffusing particle in two dimensions, the probability to find a target equals 1, this is just the classical result of Pólya on the recurrence property of planar random walks [120]. However, the mean time for reaching the target diverges for a diffusing particle. In the case

of sperm cells swimming in the plane, the "success probability" $p_0(R_0)$ is obviously also 1 if chemotaxis is positive with $\Gamma_0 > 0$. In the case of negative chemotaxis with $\Gamma_0 < 0$ we obtain $p_0(R_0) < 1$, i.e. sperm cells may be repelled from the target with a finite probability. We also find that the mean time $u_0(R_0)$ to reach the target is finite provided the chemotactic drift is strong enough with Γ_0 exceeding a critical value of $\Gamma^* = 2D_0$. We can calculate $p_0(R_0)$ as the limit of a splitting probability: We introduce a cutoff radius R_{target} and consider solutions $P(R,t)$ to equation (4.42) for the time-dependent probability density with absorbing boundary conditions both at the target and the cutoff distance, $P(R_{\text{target}}, t) = P(R_{\text{cutoff}}, t) = 0$, as well as initial conditions $P(R, 0) = \delta(R - R_0)$. After an arbitrarily long time, all sperm cells will have left through either of the boundaries. We consider the fraction $p(R_0; R_{\text{cutoff}})$ of sperm cells which have left through the boundary $R = R_0$, i.e. which have found the target. This splitting probability $p(R_0; R_{\text{cutoff}})$ obeys the ordinary differential equation [131,155]

$$\mathcal{L}^\dagger p = 0 \tag{4.45}$$

with boundary conditions $p(R_0; R_{\text{cutoff}}) = 1$ and $p(R_{\text{cutoff}}; R_{\text{cutoff}}) = 0$. Here $\mathcal{L}^\dagger$ is formally given by the adjoint operator to $\mathcal{L}$ with each occurrence of R replaced by R_0 [131][9]

$$\mathcal{L}^\dagger = \left[\frac{D_0 - \Gamma_0}{R_0} + D_0 \frac{\partial}{\partial R_0} \right] \frac{\partial}{\partial R_0}. \tag{4.46}$$

Solving (4.45), we find $p(R_0; R_{\text{cutoff}}) = (R_{\text{cutoff}}^v - R_0^v)/(R_{\text{cutoff}}^v - R_{\text{target}}^v)$ with $v = |\Gamma_0|/D_0$ for $\Gamma_0 \neq 0$. In the absence of chemotaxis with $\Gamma_0 = 0$, we have $p(R_0; R_{\text{cutoff}}) = \ln(R/R_{\text{cutoff}})/\ln(R_{\text{target}}/R_{\text{cutoff}})$. In the limit of a large cutoff radius R_{cutoff}, we thus find

$$p_0(R_0) = \lim_{R_{\text{cutoff}} \to \infty} p(R_0; R_{\text{cutoff}}) = \left(\frac{R_{\text{target}}}{R_0} \right)^{|\Gamma_0|/D_0} \quad \text{for } \Gamma_0 < 0 \tag{4.47}$$

and $p_0(R_0) = 1$ for $\Gamma_0 \geq 0$. Thus in the case of negative chemotaxis with $\Gamma_0 < 0$ the target is reached with a finite probability $p_0(R_0) < 1$.

Mean time to reach the target. We now calculate the mean time $u_0(R_0)$ to reach the target as a function of initial distance R_0. Again, we first consider a bounded domain with absorbing boundary conditions both at the target and at the cutoff radius. Let $u(R_0; R_{\text{target}})$ be the mean first passage time for a sperm cell initially released at $R = R_0$ to reach either of the two boundaries. Then $u(R_0; R_{\text{target}})$ obeys an ordinary differential equation similar to equation (4.45) [131,155]

$$\mathcal{L}^\dagger u = -1 \tag{4.48}$$

with boundary conditions $u(R_{\text{target}}; R_{\text{cutoff}}) = u(R_{\text{cutoff}}; R_{\text{cutoff}}) = 0$. By solving (4.48),

---

[9]Recall that the operator $\mathcal{L}^\dagger$ is familiar from the backward Kolmogorov equation: We can write $P(R, t|R_0, 0)$ for $P(R, t)$ to emphasize the initial conditions. Then the probability density $P(R, t|R_0, 0)$ satisfies as well $\frac{\partial}{\partial t} P(R, t|R_0, 0) = \mathcal{L}^\dagger P(R, t|R_0, 0)$ in addition to (4.42).

we find in the limit of a large cutoff radius R_{cutoff}

$$u_0(R_0) = \lim_{R_{\text{target}} \to \infty} u(R_0; R_{\text{cutoff}}) = \frac{1}{2} \frac{R_0^2 - R_{\text{target}}^2}{\Gamma_0 - 2D_0} \quad \text{if } \Gamma_0 > \Gamma^* = 2D_0 \qquad (4.49)$$

as well as $u(R_0) = \infty$ if $\Gamma_0 \leq \Gamma^*$. We conclude that the mean time $u_0(R_0)$ to reach the target is finite if the chemotactic drift is strong enough and Γ_0 exceeds the critical value $\Gamma^* = 2D_0$. Note that (4.49) generalizes the result $u_0(R_0) = (R_0^2 - R_{\text{target}}^2)/(2\Gamma_0)$ for the time to reach the target in the deterministic case with $D_0 = 0$. The mean time u to reach the target exhibits different scaling regimes as a function of the initial distance $\Delta R_0 = R_0 - R_{\text{target}}$ from the target boundary: If ΔR_0 is small with $\Delta R_0 \ll R_{\text{target}}$, we find $u_0 \sim \Delta R_0$; whereas for large ΔR_0 with $\Delta R_0 \gg R_{\text{target}}$, we have $u_0 \sim \Delta R_0^2$.

The result (4.49) is independent of the absolute strength of the radial concentration field $c(\underline{x}) = C_0/|\underline{x}|^\beta$. Note that we assumed for simplicity that the sensitivity threshold s_b of chemotactic signaling vanishes. If s_b has a finite value, we expect a similar result for the mean time $u_0(R_0)$ to reach the target provided the sperm cell starts sufficiently close to the target such that the concentration C_0/R_0^β at its starting distance R_0 is much larger than $c^* = s_b/\lambda$.

4.4   Estimates of relevant parameters

Chemoattractant binding. Chemoattractant molecules bind to the respective receptors of the sperm cell at a rate $q(t)$ which depends on concentration c. For sufficiently low concentrations c_0, we expect a binding reaction that is diffusion limited, and thus a linear relationship between the mean binding rate $q(c)$ and c, $q(t) = \lambda c$. We estimate the factor of proportionality λ: We assume that the surface of the flagellum is fully absorbing. We approximate the geometry of the flagellum as an elongated spheroid with semi-axes a and b with $a \gg b$. The diffusion current to the flagellum-spheroid is then given as [16]

$$q_0 = \frac{4\pi D \, c_0 \, a}{\ln(2a/b)} \qquad (4.50)$$

where D is the diffusion constant of the chemoattractant and c_0 is the chemoattractant concentration far from the sperm cell. Note that this formula is dominated by the length a of the long semi-axis, while the length b of the short semi-axis enters only as a logarithmic correction. The fact that the diffusion current is not proportional to the area of the absorber but to its linear dimensions is typical for diffusion-to-capture problems, see appendix H. This scaling behavior is due to local depletion of the concentration field in the vicinity of the absorber. Because of the insensitivity of the diffusion current to the precise shape of the absorbing body, the error in using a simplified geometry for the flagellum is small. Using the values $a = 25\,\mu$m and $b = 0.1\,\mu$m for a flagellum of length $L = 50\,\mu$m as well as the estimate (3.44) for the

diffusion constant of the chemoattractant resact yields

$$\lambda \approx 1.5 \cdot 10^4 \, \mu\text{m}^3 \, \text{s}^{-1} \approx 20 \, \text{pM}^{-1} \, \text{s}^{-1}. \tag{4.51}$$

Now, not the whole of the flagellar surface will be absorbing for the chemoattractant molecules but only the area covered by the active domains of the respective receptors. Nevertheless, already a modest coverage of the flagellar surface by receptors is sufficient to ensure almost maximal molecule uptake [16,19]: Let us assume for a moment that each receptor is a perfect sink for the chemoattractant molecules. For a small number N of receptors which are widely separated, we may assume that the diffusion of molecules to the different receptors is mutually independent and we find the estimate $q(N) \approx 4\pi N D c_0 r_b$ for the total current to the N receptors. Here $2r_b$ is a typical size of a single receptor, we may take $r_b = 10 \, \text{\AA}$. As N increases, the receptors will interfere with each other: The presence of one receptor decreases the concentration of molecules in the vicinity of another. If N is so large, that the entire flagellar surface is completely covered by receptors, $q(N)$ approaches the maximal current q_0. Both the case of low and high number of receptors are reproduced by a simple saturation function $q(N) = q_0 N/(N^* + N)$ where $N^* = a/[r_b \log(2a/b)]$. With this approximation for $q(N)$, we find that the total current to the receptors $q(N)$ is comparable to q_0 if $N \gg N^*$. For the sperm flagellum, we estimate $N^* \approx 10^4$; thus a few percent coverage of the flagellar surface would be sufficient for ensure half-maximal uptake of chemoattractant molecules. For the sperm flagellum, the total number of receptors is $N \approx 10^6$ [78]. Our argument can be made more quantitative in the case of a sphere covered with absorbing patches [16,19], see also appendix H.2. As a side-remark, we note that the diffusive current of chemoattractant molecules to the receptors will not decline if the number of free receptors decreases due irreversible binding of chemoattractant molecules as long as a sufficient number of free receptors is still present.

The estimate (4.51) applies for the diffusive current to a quiescent flagellum. However, the flagellum is beating vigorously, thus stirring the surrounding fluid which contains the chemoattractant molecules. This local stirring is likely to increase the binding current q. The precise computation of q for a moving flagellum would be an interesting problem that requires the solution of a convection-diffusion equation

$$\dot{c} = D\Delta c + \mathbf{u}\nabla c \tag{4.52}$$

with absorbing (Dirichlet) boundary conditions at the moving flagellar membrane. Here $\mathbf{u}(t)$ is the flow field around the sperm cell. We will not solve equation (4.52), but give a qualitative argument instead: Let v_f be an upper bound for the instantaneous speed of any part of the beating flagellum; from the frequency and the amplitude of the flagellar beat, we estimate $v_f \lesssim 500 \, \mu\text{m/s}$. The diffusive current of molecules to the flagellum will be even higher if it does not beat periodically with maximal local speed v_f but instead keeps its shape and is towed with speed v_f uniformly through the fluid. For a spherical absorber of radius a, it is known that the uptake q of molecules is enhanced

by a factor $q/q_0 \approx 0.49 \, (v_f a/D)^{1/3}$ if this absorbing sphere moves with constant speed v_f where $q_0 = 4\pi a D c_0$ is the current to a stationary sphere [1]. This approximation is valid in the limit $v_f a/D \gg 1$ provided the Reynolds number Re $= \rho v_f a/\eta$ is still small, see equation (2.1). The number $v_f a/D$ is a Peclet number that compares the speed v_f of the absorber, its length-scale a and the diffusion constant D of the molecules to be absorbed. Due to the small exponent in the factor for the increase of the uptake, even considerably large speeds v_f result only in a moderate increase of the diffusive uptake. This is peculiar for the regime of low Reynolds numbers where a moving object drags a thick boundary layer of fluid with it which prevents effective mixing [19,123]. We expect a similar result to hold true also in the case of a beating flagellum. Using the half-length $a = 25\,\mu\text{m}$ of the flagellum and the diffusion constant $D = 300\,\mu\text{m}^2/\text{s}$ of the chemoattractant resact, we compute $v_f a/D \approx 40$ and $0.49\,(v_f a/D)^{1/3} \lesssim 2$. We conclude that the estimate (4.51) still provides the correct order of magnitude also in the case of a vigorously beating flagellum.

We predict a concentration-dependence of the diffusion coefficient $D(c_0)$ with a maximum at $c_0 = c^*$ from equations (4.35) and (4.36). With the estimate (4.51) and $s_b \lesssim 1/\sigma$ (section 3.3.1), we find $c^* = s_b/\lambda \approx 0.1 - 1\,\text{pM}$.

Curvature fluctuations. We give an estimate for the strength of curvature fluctuations of circular sperm swimming paths. In an experiment with sea urchin sperm in a shallow observation chamber in the absence of chemoattractant, sperm cells were observed to swim along circular paths $\underline{r}(t)$ with radius $r_0 = 40\,\mu\text{m}$ and a swimming speed $v_0 = 100\,\mu\text{m/s}$. The center $\underline{R}(t)$ of the swimming circle was diffusing with an effective diffusion constant $D = 9 \pm 2 \mu\text{m}^2/\text{s}$ [126]. Using equation (4.36), we find that the swimming noise stemming from the intrinsic fluctuations of chemotactic signaling and the fluctuations in the activity of the flagellar motor ensemble is characterized by $\widetilde{S}_\kappa^{(0)}(\omega_0) = \bar{\rho}_\kappa^2 \widetilde{S}_a(\omega_0) + \widetilde{S}_m(\omega_0) \approx 2.5 \cdot 10^{-6}\,\text{s}\,\mu\text{m}^{-2}$.

Sperm swimming and sperm chemotaxis. Typical values for the swimming speed and average curvature, as well as for the chemotactic response coefficient have been already presented in section 3.3.1.

The motion of sperm cells in a concentration gradient is characterized by a Peclet number which compares drift speed and the effective diffusion coefficient on the length scale of sperm swimming circles. For fixed relative strength $|\boldsymbol{\nabla}c|/c$ of the concentration gradient, this Peclet number increases with concentration c and saturates for high concentrations $c \gg c^*$ For a concentration gradient with $|\boldsymbol{\nabla}c|/c = 1/100\,\mu\text{m}$ as employed in [22], we estimate Pe ≈ 1 at $c \approx c^*$ and Pe $\approx 10 - 100$ for $c \gg c^*$.

We did not consider interactions between sperm cells; thus our study corresponds to the dilute limit. For high sperm concentrations, interesting phenomena such as vortex formation of entrained sperm cells can arise from sperm-sperm interactions [126]. Sea urchin sperm cells are spawned in high-density clouds with densities $\rho \sim 10^{10}$ sperm/ml [90] which are subsequently diluted. A certain dilution ($\rho \sim 10^5$ sperm/ml) is necessary to activate the motility of the initially quiescent sperm cells [153].

Chapter summary

In this chapter, we presented a stochastic description of sperm chemotaxis in the plane which takes into account sources of fluctuations such as (i) a finite precision of the cell's measurement of the local chemoattractant concentration, (ii) intrinsic noise of chemotactic signaling, and (iii) fluctuations in the activity of the propulsion mechanism. In the presence of fluctuations, the paths can be described as noisy trochoids, resulting from the superposition of a chemotactic drift and unbiased random motion. We find expressions for the chemotactic drift velocity and the effective diffusion coefficient. The mean-field behavior of the noisy trochoids is described by the noise-free theory, see chapter 3. We have shown that the chemotaxis mechanism of sperm cells displays a high degree of robustness in the presence of fluctuations and is operative even at very low chemoattractant concentrations.

In a homogenous concentration field of chemoattractant, our theory predicts a diffusion constant of the center of the swimming circle which depends on concentration in a non-monotonic way with a maximum at a finite concentration $c^* = s_b/\lambda$, see figure 4.3. This concentration dependence of the diffusion constant results from the fact that fluctuations of the chemotactic stimulus elicit a stochastic chemotactic response and contribute to the effective diffusion constant. For low concentrations $c_0 \ll c^*$, the chemotactic stimulus and its fluctuations are small, producing only a negligible contribution to the effective diffusion constant. For high concentrations $c_0 \gg c^*$, the chemotactic signaling system adapts its sensitivity to an averaged stimulus and thus generates an output with small fluctuations. The concentration-dependence of the effective diffusion constant of sperm swimming paths could be tested in future experiments. With the parameter estimates given above, we find a value for c^* in the sub-pico-molar range, $c^* = 0.1 - 1\,\mathrm{pM}$.

Our work is related to earlier work of Alt *et al.*, who studied a stochastic model of sperm chemotaxis in which chemotactic swimming responses are triggered at a rate that depends on the temporal change of the local chemoattractant concentration [7].

So far, we studied planar swimming path of sperm cells close to a surface, as they arise in most experimental setups, where sperm cells localize at the boundary of an observation chamber. Far from boundary surfaces, sperm cells swim along helical paths [33,37] as a consequence of the chirality of their flagellar beat [67,78]. The stochastic description of sperm chemotaxis for planar swimming paths can be extended to the three-dimensional case and will be studied in the next chapter.

Chapter 5

The impact of noise in sperm chemotaxis:
The three-dimensional case

The helical motion of sea urchin sperm cells is at the core of a chemotaxis mechanism which guides these sperm cells towards the egg, see chapter 3. In this chapter, we extend our theoretical description of sperm chemotaxis to account for fluctuations inherent in the chemotactic stimulus. We present a stochastic description of sperm chemotaxis along helical swimming paths and derive a coarse-grained theory of sperm swimming paths in a concentration field of chemoattractant. We find a formal kinship between (i) the dynamics of the helix vector which characterizes the direction of net motion of helical swimming and (ii) the rotational dynamics of a polar molecule in an electric field which is subject to rotational Brownian motion.

5.1   Stochastic description of sperm chemotaxis

Far from boundary surfaces, sperm cells swim along helical paths, if no chemoattractant is present [37]. The geometry of the swimming path $\mathbf{r}(t)$ is characterized by the tangent $\mathbf{t} = \dot{\mathbf{r}}/v$, the normal $\mathbf{n} = \dot{\mathbf{t}}/|\dot{\mathbf{t}}|$ and the binormal $\mathbf{b} = \mathbf{t} \times \mathbf{n}$, where $v = |\dot{\mathbf{r}}|$ is speed. The time evolution of these vectors $\mathbf{r}$, $\mathbf{t}$, $\mathbf{n}$ and $\mathbf{b}$ is given by the Frenet-Serret equations

$$\dot{\mathbf{r}} = v\,\mathbf{t}, \quad \dot{\mathbf{t}} = v\kappa\,\mathbf{n}, \quad \dot{\mathbf{n}} = -v\kappa\,\mathbf{t} + v\tau\,\mathbf{b}, \quad \dot{\mathbf{b}} = -v\tau\,\mathbf{n}. \qquad \text{cf. eqn. (3.20)}$$

For constant curvature $\kappa(t) = \kappa_0$ and torsion $\tau(t) = \tau_0$ the swimming path is a perfect helix with radius $r_0 = \kappa_0/(\kappa_0^2 + \tau_0^2)$ and pitch $2\pi h_0 = 2\pi\,\tau_0/(\kappa_0^2 + \tau_0^2)$. The angular frequency of helical swimming is $\omega_0 = v_0\,(\kappa_0^2 + \tau_0^2)^{1/2}$ if speed $v(t) = v_0$ is constant.

We consider a sperm cell swimming along a path $\mathbf{r}(t)$ in a concentration field $c(\mathbf{x})$ of chemoattractant. As detailed in chapter 4, chemoattractant molecules bind to specific receptors on the flagellar membrane with a rate $q(t)$ which we assume to be proportional to the local concentration at the position of the sperm cell

$$q(t) = \lambda c(\mathbf{r}(t)). \qquad \text{cf. eqn. (4.3)}$$

In chapter 4, we introduced the stochastic chemoattractant stimulus $s(t) = \sum_j \delta(t - t_j)$ which counts binding events of single chemoattractant molecules occurring at random times t_j. Since binding events are stochastic, the stimulus is a stochastic flux with

expectation value

$$\langle s(t) \rangle = q(t). \qquad \text{cf. eqn. (4.4)}$$

The stimulus $s(t)$ triggers a response of the chemotactic signaling network. We characterize this response by a dimensionless output variable $a(t)$ with $\langle a \rangle = 1$ for a constant stimulus in the absence of noise. We assume that this output variable $a(t)$ directly affects the curvature $\kappa(t)$ and torsion $\tau(t)$ of the swimming path

$$\kappa(t) = \kappa_0 + \kappa_1(a(t) - 1),$$
$$\tau(t) = \tau_0 + \tau_1(a(t) - 1). \qquad \text{cf. eqn. (3.21)}$$

It is straightforward to amend equations (3.21) with noise terms as in equation (4.5) to account for fluctuations in the activity of the ensemble of molecular motors which drive the flagellar beat. We will refrain from doing so in order to keep the exposition simple.

As in chapter 3, we capture the essential properties of the chemotactic signaling system by a simple dynamical system [6,11]

$$\sigma \dot{a} = p(s_b + s) - a,$$
$$\mu \dot{p} = p(1 - a). \qquad \text{cf. eqn. (3.4)}$$

Small periodic variations of the stimulus $s(t) = s_0 + s_1 \mathrm{Re}\, e^{i\omega t}$ evoke a periodic response of the output variable $a(t) = 1 + s_1 \mathrm{Re}\, \widetilde{\chi}_a(\omega) e^{i\omega t} + \mathcal{O}(s_1^2)$ with amplitude gain $|\widetilde{\chi}_a(\omega)|$ and phase shift $\arg \widetilde{\chi}_a(\omega)$. The linear response coefficient $\widetilde{\chi}_\kappa = \kappa_1 \widetilde{\chi}_a$ is given in appendix B.

We consider stochastic sperm swimming paths $\mathbf{r}(t)$ in a concentration field of chemoattractant $c(\mathbf{x})$ which obey the equations of sperm motion (3.4), (3.20), (3.21), (4.3), (4.4) above. Figure 5.1 shows an example of a stochastic swimming path $\mathbf{r}(t)$ in a linear concentration field of chemoattractant. The swimming path $\mathbf{r}(t)$ is a fluctuating helix with a helix axis that tends to align with the concentration gradient. An example of a swimming path in a radial concentration field of chemoattractant is shown in figure 5.2; the helical swimming path eventually finds a target at the origin of the concentration field.

We can ask for the probability that a sperm cell swimming in a radial concentration field of chemoattractant finds a spherical target at the origin of the concentration field. Figure 5.3 shows this probability as a function of initial conditions. The probability was computed by simulating (i) the full set of stochastic equations of sperm swimming (3.4), (3.20), (3.21), (4.3), (4.4) from section 5.1 as shown in panel (a) of this figure, and (ii) the deterministic equations of motion (3.2), (3.4), (3.20) and (3.21) from chapter 3 as shown in panel (b). We find that in the proximity of the egg, fluctuations may facilitate chemotactic success for initial conditions where sperm cells would not find the egg in the deterministic case. The reason for this beneficial role of noise is that fluctuations may help to correct an unfavorable initial direction of swimming. If, however, the initial
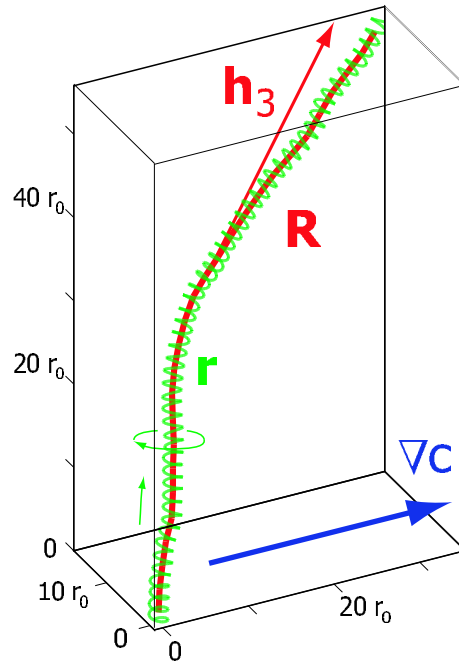
Figure 5.1: Noisy helical sperm swimming path $\mathbf{r}$ in a linear concentration field according to the stochastic dynamic equations of sperm motion (3.4), (3.20), (3.21), (4.3), (4.4) from section 5.1: The helix tends to align with the concentration gradient $\boldsymbol{\nabla}c$. Parameters were $v_0 = r_0/\sigma$, $\tau_0 = 0.2/r_0$, $-\kappa_1 = \tau_1 = 0.5/r_0$, $\mu = \sigma$, $s_b = 0$, $\lambda c_0 = 10^2/\sigma$, $|\mathbf{c}_1| = 10^{-2}c_0/r_0$.

distance of the sperm cell from the egg is too large, the success rate is reduced in the presence of fluctuations as compared to the deterministic case.

5.2   The helix disk of helical sperm swimming paths

The helix disk. In chapter 3, we introduced the concept of the helix disk: A helical path $\mathbf{r}$ can be described as the trajectory of a marker point on the circumference of an imagined solid disk of radius r_0 with center $\mathbf{R}$ and axis $\mathbf{h}_3$ that is both translating along $\mathbf{R}(t)$ and rotating. The centerline $\mathbf{R}(t)$ characterizes the path of net motion of the sperm cell. In the case of a perfect helix with constant curvature and torsion, $\kappa(t) = \kappa_0$ and $\tau(t) = \tau_0$, we have

$$\mathbf{R} = \mathbf{r} + r_0 \mathbf{n}, \quad \text{and}$$
$$\mathbf{h}_3 = \sin\theta\,\mathbf{t} + \cos\theta\,\mathbf{b} \tag{5.1}$$

where θ is the helix angle with $\tan\theta = \tau_0/\kappa_0$. The helix disk then translates along $\mathbf{R}(t)$ with velocity $\omega_0 h_0\,\mathbf{h}_3$ and rotates around $\mathbf{h}_3$ with rate ω_0. Let

$$\mathbf{h}_1 = -\mathbf{n}, \quad \mathbf{h}_2 = \mathbf{h}_3 \times \mathbf{h}_1 \tag{5.2}$$

such that $(\mathbf{h}_1, \mathbf{h}_2, \mathbf{h}_3)$ is a body frame of the solid disk with $\mathbf{h}_1$, $\mathbf{h}_2$ parallel to the plane
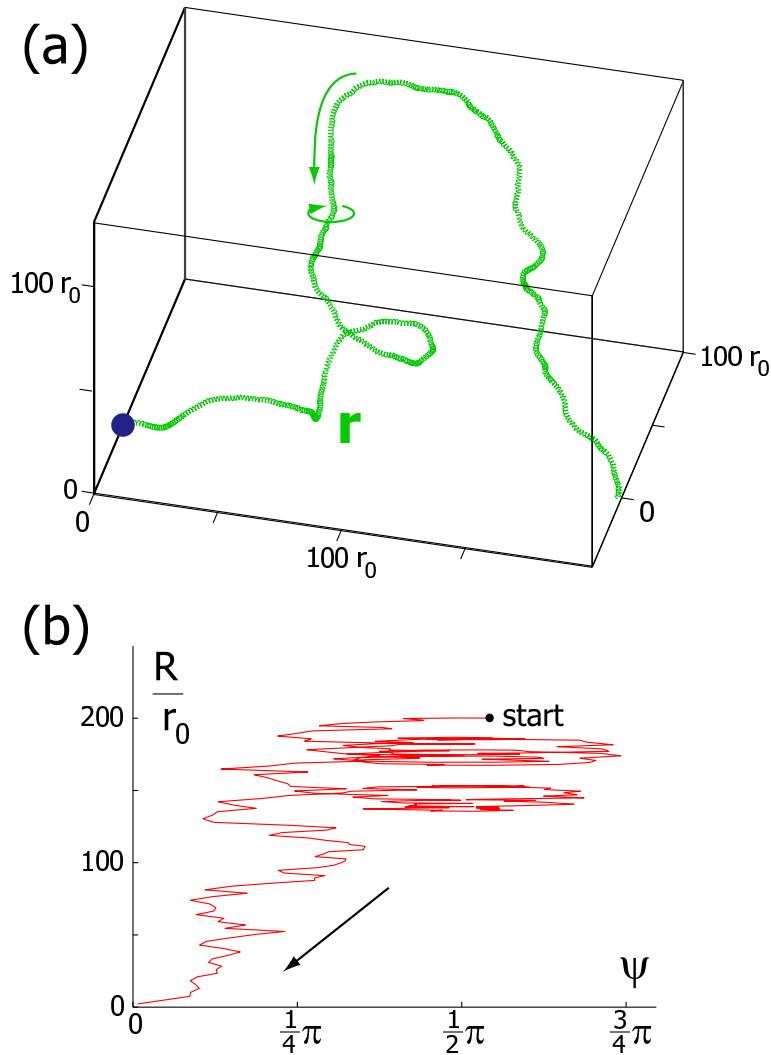
Figure 5.2: Noisy helical sperm swimming path in a radial concentration field according to the stochastic dynamic equations of sperm motion (3.4), (3.20), (3.21), (4.3), (4.4) from section 5.1. (a) The helical path $\mathbf{r}$ (green) eventually leads to the origin of the radial concentration field (blue dot). (b) In a coarse-grained description of helical swimming, the swimming path is characterized by (i) the distance $R = |\mathbf{R}|$ of the centerline $\mathbf{R}$ of the helical swimming path to the origin of the radial concentration field, and (ii) the angle ψ enclosed by the helix vector $\mathbf{h}_3$ and the direction of the local concentration gradient $\boldsymbol{\nabla} c(\mathbf{R})$. Panel (b) shows the (ψ, R)-plot corresponding to the swimming path shown in panel (a); the stochasticity of the swimming path is clearly visible. Parameters were $v_0 = r_0/\sigma$, $\tau_0 = 0.2/r_0$, $-\kappa_1 = \tau_1 = 2/r_0$, $\mu = 0.4\,\sigma$, $s_b = 0$, $\sigma\lambda c(\mathbf{x}) = 5 \cdot 10^4\, r_0/|\mathbf{x}|$. Initial conditions were chosen such that $R(0) = 200$, $\psi(0) = \pi/2$.
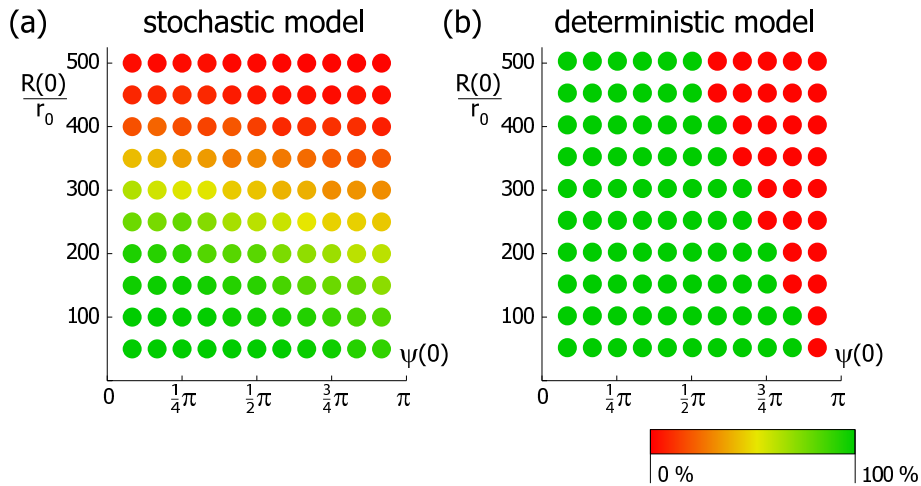
Figure 5.3: Chemotactic success as a function of initial conditions. (a) An ensemble of helical sperm swimming paths in a radial concentration field of chemoattractant was simulated according to the set of stochastic equations (3.4), (3.20), (3.21), (4.3), (4.4) from section 5.1 and the fraction of swimming paths which successfully found a spherical target of radius R_{egg} at the origin of the concentration field was computed. This simulation was repeated for different sets of initial conditions which are characterized by different values of the alignment angle $\psi(0)$ at time $t = 0$ and the initial distance $R(0)$ to the origin. The alignment angle ψ measures the angle enclosed by the gradient direction $\boldsymbol{\nabla} c$ and the helix vector $\mathbf{h}_3$ introduced in the text. The results of these simulations are presented as one colored dot for each simulation which is positioned in the $(\psi(0), R(0))$-plane according to the initial conditions used with a color coding that represents the fraction of successful sperm cells in the particular simulation according to the color bar on the right. (b) For comparison, we repeated the simulation from panel (a) also with the deterministic description of sperm chemotaxis given in equations (3.2), (3.4), (3.20) and (3.21) from chapter 3 using the same parameters. Naturally, the chemotactic success rate can only take the values 100% and 0% in the deterministic case. Parameter values used were as for figure 5.2, the radius of the target is $R_{\text{egg}} = 5\,r_0$. Sperm swimming path were simulated for a maximal time of $t_{\text{max}} = 5000\,\sigma$.
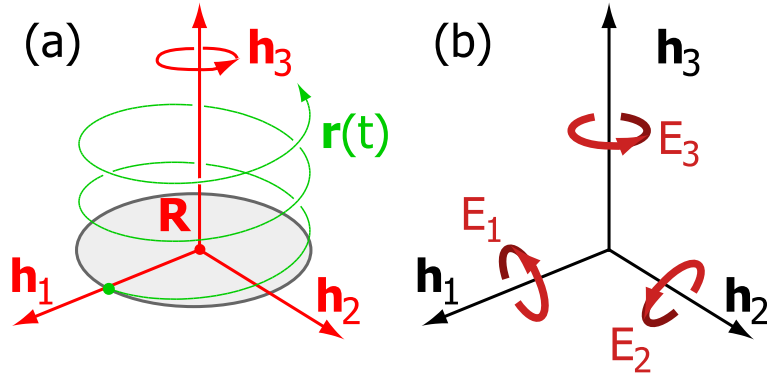
Figure 5.4: The helix frame $(\mathbf{h}_1, \mathbf{h}_2, \mathbf{h}_3)$. (a) A perfect helical path $\mathbf{r}(t)$ (green) can be described as the trajectory of a marker point (green dot) on the circumference of a solid disk (grey) which is both rotating around its axis $\mathbf{h}_3$ and translating. Let $\mathbf{h}_1$ be a unit vector pointing from the center $\mathbf{R}$ of the disk towards the marker point and $\mathbf{h}_2 = \mathbf{h}_3 \times \mathbf{h}_1$; then the helix frame $(\mathbf{h}_1, \mathbf{h}_2, \mathbf{h}_3)$ is a body frame of the solid disk with $\mathbf{h}_1$, $\mathbf{h}_2$ parallel to the plane of the disk. This picture generalizes to the case of perturbed helical paths. (b) The rotational velocity of the helix frame can be expressed in terms of the infinitesimal rotations $\mathrm{E}_j \in \mathfrak{so}(3)$.

of the helix disk, see figure 5.4(a). In the case of a perturbed helical path, we use the same definition (5.1) for the centerline $\mathbf{R}(t)$ and the helix frame $(\mathbf{h}_1, \mathbf{h}_2, \mathbf{h}_3)$.[10]

The Frenet matrix. For later use, we introduce the Frenet matrix $\mathrm{F}(t)$ with entries $F_{kl} = \mathbf{e}_k(0) \cdot \mathbf{e}_l(t)$ where $\mathbf{e}_1 = \mathbf{t}$, $\mathbf{e}_2 = \mathbf{n}$, $\mathbf{e}_3 = \mathbf{b}$. The Frenet matrix characterizes the change of the Frenet frame $(\mathbf{t}, \mathbf{n}, \mathbf{b})$ of a sperm swimming path $\mathbf{r}(t)$ with time. It is a rotation matrix, i.e. an element of the Lie group SO(3). The Lie algebra $\mathfrak{so}(3)$ of SO(3) is spanned by the infinitesimal rotations E_j with $(\mathrm{E}_j)_{kl} = \epsilon_{kjl}$, $j = 1, 2, 3$. The evolution of $\mathrm{F}(t)$ is given by a matrix-valued differential equation

$$\dot{\mathrm{F}} = \mathrm{F} \cdot \mathrm{f} \in \mathfrak{so}(3) \tag{5.3}$$

with an infinitesimal propagator f comprising curvature and torsion

$$\mathrm{f}(t) = v_0 \, (\tau(t)\,\mathrm{E}_1 + \kappa(t)\,\mathrm{E}_3) \; \in \mathfrak{so}(3). \tag{5.4}$$

Equation (5.3) is simply a reformulation of the Frenet-Serret equations (3.20) from page 71. The formal solution to (5.3) with initial condition $\mathrm{F}(0) = \mathbb{1}$ is given by a (reverse)

---

[10]Note that in chapter 3, we used a slightly different definition of the helix vector $\mathbf{h}_3$ in the analytic calculations: There we read off an appropriate form of $\mathbf{h}_3$ directly from the results of the perturbation calculation for the swimming path $\mathbf{r}$. The helix vector $\mathbf{h}_3$ as defined here simplifies some calculations but exhibits a small precession for helical swimming paths of sperm cells in a concentration gradient.

time-ordered exponential integral

$$
\begin{aligned}
\mathrm{F}(t) &= \mathbf{T}\exp \int_0^t dt\, \mathrm{f}(t) \\
&= \sum_{n=0}^{\infty} \int_{0<t_1<\ldots<t_n<t} dt_1 \cdots dt_n\, \mathrm{f}(t_1) \cdots \mathrm{f}(t_n).
\end{aligned}
\tag{5.5}
$$

The time-ordering is necessary since values $\mathrm{f}(t_1)$, $\mathrm{f}(t_2)$ of the infinitesimal propagator $\mathrm{f}(t)$ at different times $t = t_1, t_2$ do not necessarily commute.

The helix matrix. The Frenet matrix is closely related to the helix matrix which we define now: The helix matrix $\mathrm{H}(t)$ fully characterizes the orientation of the helix disk; its entries are defined by $H_{kl} = \mathbf{h}_k(0) \cdot \mathbf{h}_l(t)$. The helix matrix $\mathrm{H}(t)$ is again a rotation matrix. It is related to the Frenet matrix by the on-axis-transformation [13,14]

$$
\mathrm{H} = \mathrm{G}_{\mathrm{ax}}^{-1} \cdot \mathrm{F} \cdot \mathrm{G}_{\mathrm{ax}} \in \mathrm{SO}(3)
\tag{5.6}
$$

with

$$
\mathrm{G}_{\mathrm{ax}} = \begin{pmatrix} 0 & \cos\theta & \sin\theta \\ -1 & 0 & 0 \\ 0 & -\sin\theta & \cos\theta \end{pmatrix} \in \mathrm{SO}(3)
\tag{5.7}
$$

where θ is the helix angle with $\tan\theta = \tau_0/\kappa_0$. Note that $\sin\theta = \tau_0 v_0/\omega_0$ and $\cos\theta = \kappa_0 v_0/\omega_0$. The time evolution of $\mathrm{H}(t)$ is given by the matrix-valued differential equation

$$
\dot{\mathrm{H}} = \mathrm{H} \cdot \mathrm{h} \in \mathfrak{so}(3)
\tag{5.8}
$$

with infinitesimal propagator

$$
\mathrm{h} = \mathrm{G}_{\mathrm{ax}}^{-1} \cdot \mathrm{f} \cdot \mathrm{G}_{\mathrm{ax}} \in \mathfrak{so}(3).
\tag{5.9}
$$

In the case of a perfect helix with $\kappa(t) = \kappa_0$ and $\tau(t) = \tau_0$, we find $\mathrm{h} = \omega_0\, \mathrm{E}_3$, i.e. h is then just a rotation around the helix vector $\mathbf{h}_3$ with angular speed ω_0.

5.3   Rotational dynamics of the helix disk
in the limit of high chemoattractant concentrations

In this section, we study the rotational dynamics of the helix disk associated to helical sperm swimming paths for sperm cells swimming in a concentration field of chemoattractant. For pedagogical reasons, we postpone the treatment of translational motion to section 5.5. We derive an effective equation of motion in the limit of high chemoattractant concentrations. As detailed in chapter 4, the generic signaling module (3.4) from page 72 serves as a low-pass filter which averages the incoming stimulus $s(t)$ over its relaxation time σ. When the rate q is large compared to σ^{-1} and $q(t)$ changes on a time-scale slow compared to the mean inter-event-interval $1/q$, then we can replace

$s(t)$ by a coarse-grained version known as the diffusion limit

$$s(t) \approx q(t) + \sqrt{q(t)}\, \xi_s(t), \qquad \text{cf. eqn. (4.9)}$$

where $\xi_s(t)$ is Gaussian white noise with $\langle \xi_s(t_1)\xi_s(t_2)\rangle = \delta(t_1 - t_2)$. In this limit $\eta \ll 1$ where $\eta = (q\sigma)^{-1/2}$ characterizes the relative noise strength of $s(t)$ for an averaging time σ.

5.3.1 Statistical properties of helix disk motion

Statistics of the helix matrix for swimming in a homogenous concentration field. In a homogenous concentration field of chemoattractant, $c(\mathbf{x}) = c_0$, sperm cells swim along helical paths with curvature $\kappa(t)$ and torsion $\tau(t)$ that fluctuate around their mean values

$$\kappa(t) = \kappa_0 + \kappa_1 \xi_a(t), \quad \tau(t) = \tau_0 + \tau_1 \xi_a(t) \tag{5.10}$$

due to the fluctuations $\xi_a = a - 1$ in the output of the chemotactic signaling system (3.4) from page 72. In the limit of high chemoattractant concentration with $\eta \ll 1$, the power spectrum $\widetilde{S}_a$ of ξ_a is

$$\widetilde{S}_a(\omega) \approx |\widetilde{\chi}_a(\omega)|^2 \,\lambda c_0. \tag{5.11}$$

The helix frame $\mathrm{H}(t)$ which characterizes the orientation of the disk obeys the dynamic equation (5.8) with a stochastic propagator

$$\mathrm{h} = \omega_0 \mathrm{E}_3 + \xi_j \mathrm{E}_j \tag{5.12}$$

where we used Einstein summation convention for $j = 1, 2, 3$. The action of the infinitesimal rotations E_j on the helix frame $(\mathbf{h}_1, \mathbf{h}_2, \mathbf{h}_3)$ is visualized in figure 5.4(b). The stochastic processes ξ_j relate to the curvature and torsion fluctuations (5.10) by the on-axis-transform (5.9) and satisfy

$$\begin{aligned}
\xi_1 &= 0, \\
\xi_2 &= v_0 \left(\tau_1 \cos\theta - \kappa_1 \sin\theta \right) \xi_a = \Theta_{\mathrm{Y}}\, \xi_a, \\
\xi_3 &= v_0 \left(\tau_1 \sin\theta + \kappa_1 \cos\theta \right) \xi_a = \Theta_3\, \xi_3,
\end{aligned} \tag{5.13}$$

where the coefficients Θ_{Y} and Θ_3 are defined accordingly. The ξ_j have a concrete geometric meaning: Bending of the helix is characterized by ξ_1 and ξ_2; while ξ_3 characterizes excess twist of the helix. Future calculation are simplified by introducing complex notation: We write $\mathrm{Y} = \mathrm{X}_1 + i\mathrm{X}_2 \in \mathfrak{se}(3) \otimes \mathbb{C}$ for the complex generator of bending. We also write $\xi_{\mathrm{Y}} = \xi_1 - i\xi_2$ for the respective coefficient.

Exponential coordinates for the helix frame. After n helical turns, the disk is

rotated by $H(nT)$. We write

$$H(nT) = \exp(\Xi_j E_j). \tag{5.14}$$

with stochastic variables Ξ_j. The exponential coordinates Ξ_j are uniquely determined if we require $\sqrt{\Xi_j \Xi_j} < \pi$ [103]. The Ξ_j can be expressed in terms of the ξ_j; we find to leading order in η

$$\Xi_Y = \int_0^{nT} dt\, \xi_Y(t)\, e^{-i\omega_0 t} + \mathcal{O}(\eta^2),$$
$$\Xi_3 = \int_0^{nT} dt\, \xi_3(t) + \mathcal{O}(\eta^2). \tag{5.15}$$

How to derive these formulas? The Ξ_j are computed by evaluating time-ordered integrals, see equation (5.5). We formally expand these integrals to linear order in ξ_j, since we are only interested in leading order contributions. Special care has to be taken to deal with the non-commutativity of $\mathfrak{so}(3)$. Instead of giving the full derivation, we compute $\mathbf{T}\exp \int_0^{nT} dt\, (\omega_0 E_3 + \xi_Y(t)\, Y)$ as a simple example to convey the central idea of the calculation. The crux is to use a recursion relation

$$E_3^l \cdot Y = E_3^{l-1} \cdot (Y \cdot E_3 - i\, Y) = \ldots = Y \cdot (E_3 - i\, \mathbb{1})^l \tag{5.16}$$

at step $(*)$ of our example calculation:

$\mathbf{T}\exp \int_0^{nT} dt\, [\omega_0\, E_3 + \xi_Y(t)\, Y]$

$$= \sum_{k=-1}^{\infty} \int_{0 < t_1 < \cdots < t_{k+1} < nT} dt_1 \cdots dt_{k+1} \prod_{l=1}^{k+1} (\omega_0\, E_3 + \xi_Y(t_l)\, Y)$$

$$= \mathbb{1} + \sum_{k=0}^{\infty} \frac{\omega_0^k}{k!} \int_0^{nT} dt \sum_{l=0}^{k} \binom{k}{l} t^l\, (nT - t)^{k-l}\, \xi_Y(t)\, E_3^l \cdot Y \cdot E_3^{k-l} + \mathcal{O}(\eta^2)$$

$$\stackrel{(*)}{=} \mathbb{1} + \sum_{k=0}^{\infty} \frac{\omega_0^k}{k!} \int_0^{nT} dt \sum_{l=0}^{k} \binom{k}{l} t^l\, (nT - t)^{k-l}\, \xi_Y(t)\, Y \cdot (E_3 - i\,\mathbb{1})^l \cdot E_3^{k-l} + \mathcal{O}(\eta^2)$$

$$= \mathbb{1} + \sum_{k=0}^{\infty} \frac{1}{k!} \int_0^{nT} dt\, \xi_Y(t)\, Y \cdot (2\pi n\, E_3 - i\omega_0 t\,\mathbb{1})^k + \mathcal{O}(\eta^2)$$

$$= \left(\mathbb{1} + \Xi_Y^{(0)}\, Y\right) \cdot \exp(2\pi n\, E_3) + \mathcal{O}(\eta^2)$$

$$= \exp \Xi_Y^{(0)}\, Y + \mathcal{O}(\eta^2)$$

$$\tag{5.17}$$

with $\Xi_Y^{(0)} = \int_0^{nT} dt\, \xi_Y(t)\, e^{-i\omega_0 t}$. From (5.15), we see that the expectation values $\langle \Xi_j \rangle$ vanish to linear order in η

$$\langle \Xi_j \rangle = 0 + \mathcal{O}(\eta^2), \quad j = 1, 2, 3. \tag{5.18}$$

We introduce the correlation matrix C with entries $C_{kl} = \langle \Xi_k \Xi_l \rangle$. If n is chosen such

that nT is much longer than the correlation time σ of ξ_a, then most entries of C vanish to leading order and C has the form

$$
\mathrm{C} = \left(\langle \Xi_k \, \Xi_l \rangle \right)_{kl} = \begin{pmatrix} C_{11} & 0 & 0 \\ 0 & C_{11} & 0 \\ 0 & 0 & 0 \end{pmatrix} + \mathcal{O}(\eta^3). \tag{5.19}
$$

The entries C_{11} and C_{22} are equal and read

$$
C_{11} = C_{22} \approx \Theta_{\mathrm{Y}}^2 \, nT \, \widetilde{S}_a(\omega_0)/2, \tag{5.20}
$$

with $\Theta_{\mathrm{Y}} = v_0(\tau_1 \cos\theta - \kappa_1 \sin\theta)$. As an example for the type of calculations involved in computing C we consider

$$
\begin{aligned}
C_{11} + C_{22} &= \langle \Xi_1^2 + \Xi_2^2 \rangle = \langle |\Xi_{\mathrm{Y}}|^2 \rangle \\
&= \Theta_{\mathrm{Y}}^2 \int_0^{nT} dt_1 \int_0^{nT} dt_2 \, S_a(t_1 - t_2) \, e^{-i\omega_0(t_1 - t_2)} + \mathcal{O}(\eta^3) \\
&\approx \Theta_{\mathrm{Y}}^2 \, nT \, \widetilde{S}_a(\omega_0)
\end{aligned} \tag{5.21}
$$

where S_a is the autocorrelation function of ξ_a. Similarly, one can show $C_{33} \approx \Theta_3^2 \, nT \, \widetilde{S}_a(0)$ which is zero since $\widetilde{S}_a(0) = |\widetilde{\chi}_a(0)|^2 \lambda c_0 = 0$ due to the adaptation property of the chemotactic signaling system (3.4) from page 72. We conclude that on time-scales larger than nT, the stochastic dynamics of the helix vector can be described as rotational diffusion with an effective rotational diffusion constant $D_{\mathrm{rot}} = C_{11}/(2nT)$. Since $\mathbf{R}(t) = \omega_0 h_0 \, \mathbf{h}_3 + \mathcal{O}(\eta)$, we find that the centerline $\mathbf{R}(t)$ of the helical swimming path $\mathbf{r}(t)$ can be approximately considered as a persistent random walk on time-scales larger than nT with persistence time $t_P = nT/C_{11}$ and persistence length $l_P = \omega_0 h_0 t_P$, see also appendix F. From equations (5.11) and (5.20), we see that the persistence length l_P is a function of chemoattractant concentration c_0

$$
l_P = \frac{2 \, \omega_0 h_0}{|\Theta_{\mathrm{Y}} \, \widetilde{\chi}_a(\omega_0)|^2 \, \lambda c_0} \sim \frac{(c^* + c_0)^2}{c_0} \tag{5.22}
$$

with a minimum at $c^* = s_b/\lambda$. Recall that in chapter 4, we had found a similar concentration dependence of the effective diffusion constant of circular sperm swimming paths in a plane, see figure 4.3.

Statistics of the helix matrix for swimming in a concentration gradient. We study the set of equations from section 5.1 for a linear concentration field of chemoattractant

$$
c(\mathbf{x}) = c_0 + \mathbf{c}_1 \cdot \mathbf{x} \tag{5.23}
$$

in the limit of

(i) a weak concentration gradient with $\nu = c_1 r_0/c_0 \ll 1$, and

(ii) a high chemoattractant concentration c_0 with $\eta = (\lambda c_0 \sigma)^{-1/2} \ll 1$.

We assume $\mathbf{R}(0) = 0$ such that $c(\mathbf{R}(0)) = c_0$. The concentration gradient $\boldsymbol{\nabla} c$ is the sum of (i) a component $\mathbf{c}_\parallel = c_\parallel \mathbf{h}_3$ parallel to $\mathbf{h}_3$ with $c_\parallel = \boldsymbol{\nabla} c \cdot \mathbf{h}_3$, and (ii) a component $\mathbf{c}_\perp = \boldsymbol{\nabla} c - \mathbf{c}_\parallel$ perpendicular to $\mathbf{h}_3$ of length $c_\perp = |\mathbf{c}_\perp|$.

To leading order, we anticipate a helical swimming path

$$\mathbf{r}(t) = \omega_0 h_0 t \, \mathbf{h}_3(0) + r_0 \cos \omega_0 t \, \mathbf{h}_1(0) + r_0 \sin \omega_0 t \, \mathbf{h}_2(0) + \mathcal{O}(\nu, \eta) \tag{5.24}$$

which results in a temporal change of the binding rate $q(t)$ due to the presence of the concentration gradient

$$q(t)/\lambda = c_0 + c_\parallel \omega_0 h_0 t + c_\perp r_0 \cos(\omega_0 t + \varphi_0) + \mathcal{O}(\nu^2, \nu \eta) \tag{5.25}$$

where φ_0 is the angle enclosed by $\mathbf{c}_\perp$ and $\mathbf{h}_1$. The change of the binding rate comprises (i) a monotonic change proportional to $c_\parallel$, and (ii) a periodic modulation proportional to $c_\perp$. The stimulus (4.9) elicits by the signaling system (3.4) from page 72 a modulation of the output variable $a(t)$ as

$$a(t) = 1 + \mu \, \omega_0 h_0 \, c_\parallel / c_0 + \xi_a + \lambda c_\perp r_0 \, \mathrm{Re} \, \widetilde{\chi}_a(\omega_0) e^{i(\omega_0 t + \varphi_0)} + \mathcal{O}(\nu^2, \nu \eta, \eta^2). \tag{5.26}$$

Approximately, we can treat ξ_a as stationary with power spectrum $\widetilde{S}_a(\omega) \approx |\widetilde{\chi}_a(\omega)|^2 \lambda c_0$. From (5.15), we find for the expectation values to linear order

$$\begin{aligned} \langle \Xi_Y \rangle = \langle \Xi_1 - i\Xi_2 \rangle &= -nT \, c_\perp \, i\varepsilon_a \widetilde{\chi}_a(\omega_0) \, e^{-i\varphi_0} &+ \mathcal{O}(\nu^2, \nu\eta, \eta^2), \\ \langle \Xi_3 \rangle &= nT \, c_\parallel \, \bar{\varepsilon} &+ \mathcal{O}(\nu^2, \nu\eta, \eta^2) \end{aligned} \tag{5.27}$$

where $\varepsilon_a/\lambda = \varepsilon_\tau \tau_1 - \varepsilon_\kappa \kappa_1 = r_0 \Theta_Y/2$ and $\bar{\varepsilon} = \mu \omega_0 h_0 \Theta_3/c_0$. The expressions (5.27) for $\langle \Xi_j \rangle$ found here are equivalent to the results obtained already in the deterministic case, see equation (3.25). For the variances of $\delta \Xi_j = \Xi_j - \langle \Xi_j \rangle$ we find to leading order the same result as in the case of a homogenous concentration field

$$\langle \delta \Xi_k \, \delta \Xi_l \rangle = C_{kl} \quad + \mathcal{O}(\nu \eta^2, \eta^3), \quad k, l = 1, 2, 3. \tag{5.28}$$

5.3.2   Effective equation of motion

Continuum limit. We perform a continuum limit to derive an effective equation of motion for the helix matrix $\mathrm{H}(t)$ in a linear concentration field (5.23). On short time scales $t < \sigma$, the statistics of the stochastic helix matrix $\mathrm{H}(t)$ depends on the particular form of the signaling system (3.4) from page 72 and therefore has non-generic properties. For time intervals $\Delta t = nT$ which are much longer than the correlation time σ of the fluctuations ξ_a of the output variable a, however, we find simple, general expressions for the expectation value and the variance of $\mathrm{H}(\Delta t)$, see equations (5.27) and (5.28). In the following, we assume that the coarse-graining time-scale Δt is both much longer than σ and also much shorter than the time-scale T/ν on which $c(\mathbf{R}(t))$ changes. We design a stochastic trajectory $\widehat{\mathrm{H}}(t)$ in SO(3) which reproduces to leading order the second-order

statistics of H(t) at the discrete times $t_m = m \, \Delta t$. More formally, we write $\widehat{H}$ as

$$\widehat{H}(t_{m+1}) = \widehat{H}(t_m) \cdot \exp\left(\omega_0 \Delta t X_3 + \widehat{\Xi}_j E_j\right) \tag{5.29}$$

and require for the statistics of the $\widehat{\Xi}_j$

$$\begin{aligned}
\langle \widehat{\Xi}_j \rangle &= \langle \Xi_j \rangle + \mathcal{O}(\nu^2, \eta^2), \\
\langle \delta\widehat{\Xi}_k \, \delta\widehat{\Xi}_l \rangle &= \langle \delta\Xi_k \, \delta\Xi_l \rangle + \mathcal{O}(\nu\eta^2, \eta^3).
\end{aligned} \tag{5.30}$$

Here the expectation value $\langle \cdot \rangle$ averages over an ensemble of stochastic paths $\mathbf{r}(t)$ with initial condition $\mathbf{R}(t_m) = 0$ and $\mathbf{h}_l(t_m) = \widehat{H}_{kl}(t_m)\mathbf{h}_k(0)$. For the dynamics of $\widehat{H}$, we anticipate a Stratonovich stochastic differential equation of the form

$$\text{(S)} \quad \frac{d}{dt}\widehat{H} = \widehat{H} \cdot \widehat{h}. \tag{5.31}$$

To fulfill (5.30), we choose $\widehat{h}$ as

$$\widehat{h} = \omega_0 X_3 + \langle \Xi_j/\Delta t \rangle E_j + \widehat{\xi}_j E_j \tag{5.32}$$

where $\widehat{\xi}_j$ is Gaussian white noise with $\langle \widehat{\xi}_k(t_1)\widehat{\xi}_l(t_2) \rangle = \widehat{C}_{kl} \, \delta(t_1 - t_2)$. The variances read

$$\widehat{C}_{kl} = C_{kl}/\Delta t, \quad k, l = 1, 2, 3. \tag{5.33}$$

Rewriting (5.31) explictly yields a set of Stratonovich stochastic differential equations for the $\mathbf{h}_j(t)$

$$\text{(S)} \quad \begin{aligned}
\dot{\mathbf{h}}_3 &= \varepsilon_a \operatorname{Re} \widetilde{\chi}_a(\omega_0)\, \mathbf{c} &&+ \widehat{\xi}_2 \mathbf{h}_1 - \widehat{\xi}_1 \mathbf{h}_2, \\
\dot{\mathbf{h}}_1 &= -(\dot{\mathbf{h}}_3 \cdot \mathbf{h}_1)\, \mathbf{h}_3 &&+ \omega\, \mathbf{h}_2, \\
\dot{\mathbf{h}}_2 &= -(\dot{\mathbf{h}}_3 \cdot \mathbf{h}_2)\, \mathbf{h}_3 &&- \omega\, \mathbf{h}_1
\end{aligned} \tag{5.34}$$

where $\mathbf{c}$ is the complex gradient vector $\mathbf{c} = \mathbf{c}_\perp + i\, \mathbf{h}_3 \times \mathbf{c}_\perp$ and $\omega = \omega_0 + c_\parallel \bar{\varepsilon}$. Equation (5.34) provides a coarse-grained description of the time evolution of the helix matrix on time-scales larger than Δt. The description breaks down, however, for times $t \gtrsim T/\nu$ since then the change of $c(\mathbf{R}(t))$ has to be taken into account. This can be done by considering a coarse-grained dynamics of both $\mathbf{R}(t)$ and H(t), see section 5.5.

Effective dynamics of the alignment angle. In a linear concentration field $c(\mathbf{x}) = c_0 + \mathbf{c}_1 \cdot \mathbf{x}$, we can exploit symmetries and derive an effective equation for the alignment angle ψ enclosed by the helix vector $\mathbf{h}_3$ and the gradient direction $\mathbf{c}_1$ by rewriting equation (5.34) in spherical coordinates. The symmetries of the problem imply that the dynamics of ψ decouples from the other degrees of freedom. Using the rules of stochastic calculus, we derive in appendix E.2

$$\boxed{\dot{\psi} = -\beta \sin\psi + \xi + D_\psi \cot\psi.} \tag{5.35}$$

Here ξ denotes Gaussian white noise with $\langle \xi(t_1)\, \xi(t_2) \rangle = 2D_\psi\, \delta(t_1 - t_2)$, with $2D_\psi = \widehat{C}_{11}$, see equation (M.19). The alignment coefficient β reads $\beta = |\boldsymbol{\nabla} c|\varepsilon_a \operatorname{Re} \chi_a$. The effective

equation (5.35) is valid in the limit of (i) a weak concentration gradient with $\nu = |\nabla c| r_0 / c \ll 1$, and (ii) a high chemoattractant concentration c with $\eta^2 = \lambda c \sigma \ll 1$ on time-scales larger than σ. Using the effective potential $E(\psi) = -\beta \cos \psi - D_\psi \ln \sin \psi$, equation (5.35) can be rewritten as $\dot{\psi} = -dE/d\psi + \xi$.

The Fokker-Planck equation for the distribution $P(\psi, t)$ of alignment angles ψ associated to (5.35) reads

$$\frac{\partial}{\partial t} P(\psi, t) = -\frac{\partial}{\partial \psi} \left[-\left(\frac{d}{d\psi} E(\psi) \right) - D_\psi \frac{\partial}{\partial \psi} \right] P(\psi, t). \tag{5.36}$$

The boundary conditions for $P(\psi, t)$ are $P(0, t) = P(\pi, t) = 0$ since the volume element for spherical coordinates $\sin \psi \, d\psi$ vanishes for $\psi = 0$ and $\psi = \pi$. The steady-state solution $P_0(\psi)$ of (5.35) is found as

$$P_0(\psi) = N_0 \exp(-E(\psi)/D_\psi) = N_0 \sin \psi \exp(\mathrm{Pe} \cos \psi) \tag{5.37}$$

where we have defined the angular Peclet number

$$\mathrm{Pe} = \frac{\beta}{D_\psi}. \tag{5.38}$$

The normalization constant is $N_0 = \mathrm{Pe}/(2 \sinh \mathrm{Pe})$.

We can rephrase these results in terms of the probability distribution $Q(z, t)$ of the cosine $z = \cos \psi$ of the alignment angle ψ which is related to $P(\psi, t)$ by $Q(\cos \psi, t) = P(\psi, t)/\sin \psi$. The Fokker-Planck equation for $Q(z, t)$ reads $\dot{Q} = -\partial_z [(1 - z^2)(\beta - D_\psi \partial_z)] Q$. The steady-state distribution $Q_0(z)$ is exponential $Q_0(z) \sim \exp(\beta z / D_\psi)$ with maximum at $z^* = \mathrm{sign} \, \beta$. For the expectation value of z in steady-state, we find [40]

$$\langle z \rangle = \langle \cos \psi \rangle = \coth \mathrm{Pe} - \frac{1}{\mathrm{Pe}}. \tag{5.39}$$

Thus after a transient period of alignment of duration β^{-1}, the sperm cell moves up a concentration gradient with average speed $\omega_0 h_0 \langle z \rangle$, provided $\beta > 0$. We introduce the chemotaxis index defined as the average speed upwards the gradient divided by the swimming speed. This chemotaxis index reads $\omega_0 h_0 \langle z \rangle / v_0$ and is of order unity for $\mathrm{Pe} \gtrsim 1$, or equivalently for $\nu = |\nabla c| r_0 / c \gtrsim |\Theta_Y \widetilde{\chi}_a(\omega_0)|$. This condition can be rephrased as $|\nabla c|$ being larger than a threshold gradient strength $|\Theta_Y \widetilde{\chi}_a(\omega_0)| \, c/r_0$ which becomes independent of concentration c provided $c \gg c^*$. This result is in contrast to the case of bacterial chemotaxis which is characterized by a chemotaxis index roughly linear in the relative concentration gradient $|\nabla c|/c$.

The dependence (5.39) of the mean orientation $\langle z \rangle$ on the Peclet number is compared to experimental data in section 5.3.4.

In figure 5.5, we compare a solution to the Fokker-Planck equation (5.36) to simulation results for the full set of dynamic equations of sperm motion (3.4), (3.20), (3.21), (4.3), (4.4) from section 5.1 and find excellent agreement.
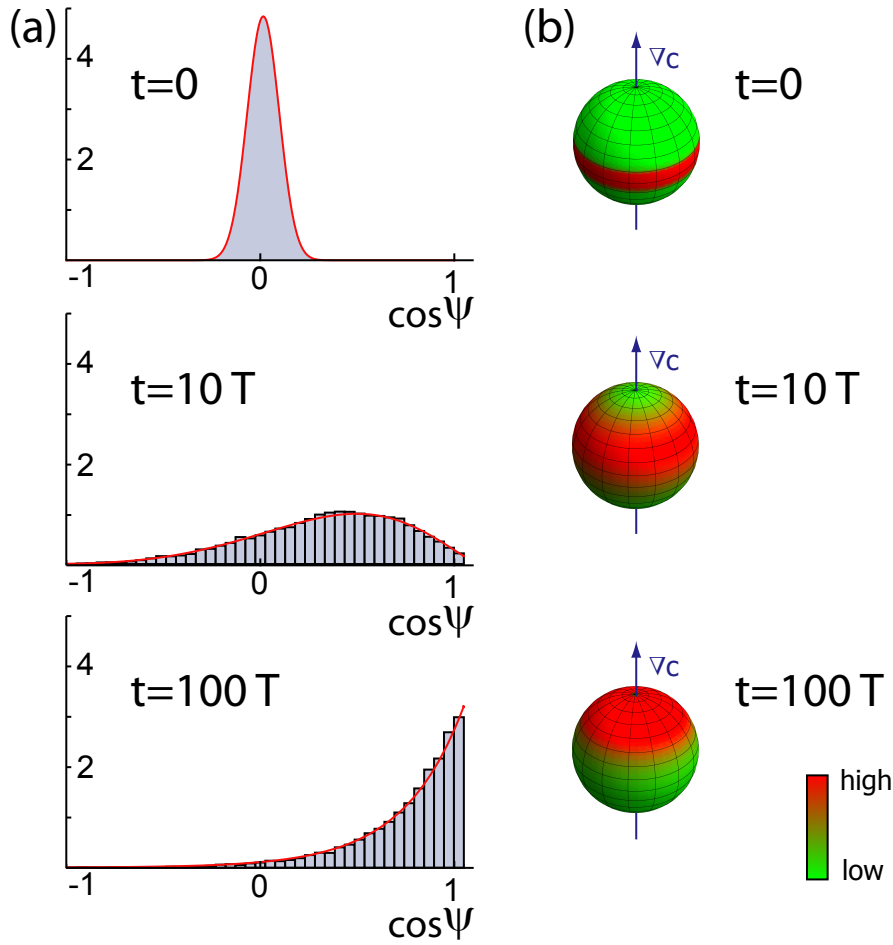
Figure 5.5: Alignment of helical swimming paths with a concentration gradient ∇c. The simulation from figure 5.1 was repeated for a whole ensemble of helical sperm swimming paths in a linear concentration field. Panel (a) shows the histograms of $z = \cos\psi$ from this simulation, where ψ equals the angle enclosed by the helix axis $\mathbf{h}_3$ and the gradient direction ∇c at times $t = 10\,T$ and $t = 100\,T$ as well as the initial distribution at $t = 0$. Also shown is the analytical solution $Q(z, t)$ (red line) which was computed according to equation (5.36). As time progresses, the helix axes $\mathbf{h}_3$ of the helical sperm swimming paths $\mathbf{r}$ tends to align with the concentration gradient which is manifested by $z = \cos\psi$ taking values close to 1. The distribution $Q(z, 100\,T)$ at time $t = 100\,T$ approximately equals the steady-state distribution $Q_0(z)$. (b) Schematic depiction of the distribution of the helix vector at different times of the simulation: Directions correspond to a point on the unit sphere; the direction of the concentration gradient is indicated. High and low probability densities are shown in red and green, respectively.

5.3.3   Polar molecules in an electric field

The effective equation of motion (5.35) for the helix vector is familiar from a different context: Consider a (rigid) polar molecule with electric dipole moment $\mathbf{m}$ in an electric field $\mathbf{E}$ subject to rotational Brownian motion [40]. We introduce the alignment angle ψ enclosed by $\mathbf{m}$ and $\mathbf{E}$. The free energy $A(\psi)$ of the molecule as a function of ψ reads

$$A(\psi) = -|\mathbf{m}||\mathbf{E}|\cos\psi - k_B T \ln\sin\psi. \tag{5.40}$$

The free energy A is the sum of the internal energy $U = -|\mathbf{m}||\mathbf{E}|\cos\psi$ and an entropy term $-ST$ with entropy $S = k_B \ln\sin\psi$. Note that each value of ψ corresponds to a whole set of different orientation vectors $\mathbf{m}$ with $\mathbf{m}\cdot\mathbf{E} = |\mathbf{m}||\mathbf{E}|\cos\psi$ and hence to a multiplicity of $\sin\psi$.[11] Let us assume that the individual molecule is rotationally symmetric around the axis $\mathbf{m}$ and has a rotational drag coefficient ζ_{rot} for rotations with an axis perpendicular to $\mathbf{m}$. In the limit of overdamped dynamics, the dynamics of ψ is governed by

$$\zeta_{\mathrm{rot}}\dot{\psi} = -\frac{d}{d\psi}A(\psi) + \xi \tag{5.41}$$

where ξ is Gaussian white noise with $\langle\xi(t_1)\xi(t_2)\rangle = 2k_B T\,\zeta_{\mathrm{rot}}\,\delta(t_1 - t_2)$. This is precisely equation (5.35) with $\beta = |\mathbf{m}||\mathbf{E}|/\zeta_{\mathrm{rot}}$ and an Einstein relation $D_\psi = k_B T/\zeta_{\mathrm{rot}}$ [45]. The steady-state distribution $P_0(\psi)$ from equation (5.37) is just the Boltzmann distribution. Thus there is a formal kinship between the chemoorientation of sperm swimming in a concentration gradient of chemoattractant and the orientation of a polar molecule in an electrical field [26].

5.3.4   Relation to experiments

Already fifty years ago, C. J. Brokaw performed experiments on sperm chemotaxis with bracken fern spermatozoids [26]. These spermatozoids swim along helical paths and are chemotactily responsive to malate ions.[12] The fact that the chemoattractant is charged allows for particular experimental approaches: If a voltage gradient $\mathbf{E}$ is applied to a solution of malate ions, fern spermatozoids swimming in this solution orient along the gradient, probably because the gradient induces a concentration gradient of malate. In a constant electric field $\mathbf{E}$, the steady-state concentration $c(\mathbf{x})$ of malate ions is given by

$$c(\mathbf{x}) \sim \exp\left(-\frac{e\,\mathbf{E}\cdot\mathbf{x}}{k_B T}\right) \tag{5.42}$$

---

[11]For an ensemble of polar molecules, we have the partition function

$$\overline{Z} = \int_0^\pi d\psi\, Z(\psi) = 4\pi\frac{k_B T}{|\mathbf{m}||\mathbf{E}|}\sinh\left(-\frac{|\mathbf{m}||\mathbf{E}|}{k_B T}\right)$$

where $Z(\psi) = 2\pi\sin\psi\,\exp\left(-U(\psi)/(k_B T)\right)$ is the partition function of the sub-ensemble with $\mathbf{m}\cdot\mathbf{E} = |\mathbf{m}||\mathbf{E}|\cos\psi$. Note that $-k_B T\ln(Z(\psi))$ equals the free energy $A(\psi)$ up to a constant.

[12]Ferns and some other lower plants produce motile sperm cells, contrary to immotile pollen grains employed by most plants. The sperm cells of lower plants are called spermatozoids; they differ in morphology from animal sperm cells [96].
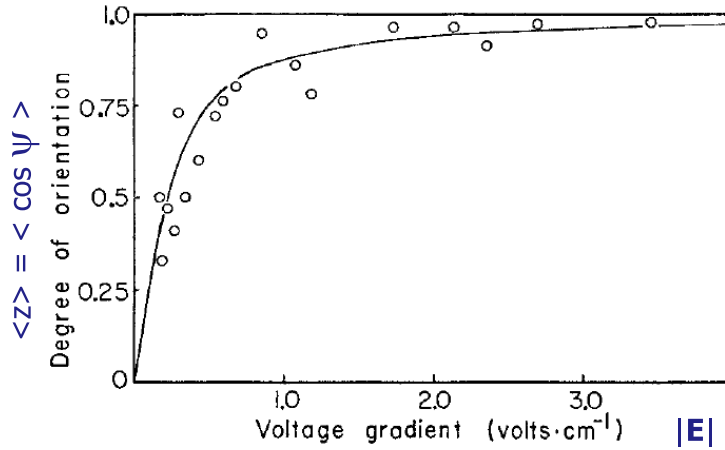
Figure 5.6: Mean orientation $\langle z \rangle = \langle \cos \psi \rangle$ of helical swimming paths of bracken fern spermatozoids as a function of the field strength $|\mathbf{E}|$ of an externally applied electric field $\mathbf{E}$. Sperm cells were swimming in a solution of malate ions which are a chemoattractant for these sperm cells. The angle ψ measures the angle enclosed by the voltage gradient and the helix vector. The experimental data can be well fitted with equation (5.39) if we assume that the angular Peclet number Pe as defined in equation (5.38) is linearly related to the field strength $|\mathbf{E}|$. The figure was taken form [26].

if reactions at the electrodes can be neglected. Here e is the elementary charge. Thus the relative concentration gradient $|\boldsymbol{\nabla} c|/c$ is constant and proportional to electric field strength $|\mathbf{E}|$. For bracken fern spermatozoids swimming in a solution of malate ions with an external electrical field $\mathbf{E}$ applied, the mean orientation $\langle z \rangle = \langle \mathbf{h}_3 \cdot \mathbf{E} \rangle / |\mathbf{E}|$ of the helix vector $\mathbf{h}_3$ with respect to the direction of the electric field was measured as a function of the field strength $|\mathbf{E}|$ [26]. The results can be well fitted with the theoretical result (5.39) for $\langle z \rangle = \langle \cos \psi \rangle$ in steady-state if we assume that the field strength is proportional to the Peclet number $\text{Pe} = \beta / D_\psi$, see figure 5.6.[13] Note that Brokaw did not derive equation (5.39) from a theoretical description of sperm chemotaxis but used this formula as a phenomenological description.

5.4   Rigid body transformations

We will use rigid body transformations in section 5.5 to characterize the dynamics of the full helix frame $\mathcal{H} = (\mathbf{h}_1, \mathbf{h}_2, \mathbf{h}_3, \mathbf{R})$ of the helix disk including the translational motion of the helix disk. In this section, we give a short review of the theory of rigid body transformations [13,14,103], more information on rigid body transformations can be found in appendix D.

Let $\mathcal{L} = (\mathbf{e}_1, \mathbf{e}_2, \mathbf{e}_3, \mathbf{p})$ and $\mathcal{G} = (\mathbf{g}_1, \mathbf{g}_2, \mathbf{g}_3, \mathbf{q})$ be two Cartesian coordinate systems, each

---

[13]It should be noted, however, that the experimental results are somewhat biased because of the finite depth of the observation chamber used in the experiments which restricts sperm swimming and affects the statistics of the helix vector.
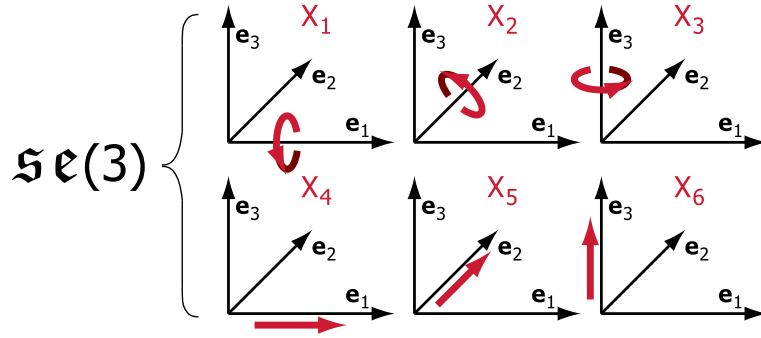
Figure 5.7: Six infinitesimal rigid body transformations span the Lie algebra $\mathfrak{se}(3)$: The infinitesimal rotations X_1, X_2, X_3 and the infinitesimal translations X_4, X_5, X_6.

consisting of an orthonormal set of vectors $\{\mathbf{e}_j\}$ and $\{\mathbf{g}_j\}$, respectively, and a choice origin, $\mathbf{p}$ and $\mathbf{q}$. We represent the rigid body transformation mapping $\mathcal{L}$ onto $\mathcal{G}$ by its coordinate matrix $G = {}^{\mathcal{L}}\mathcal{G}$ (expressed with respect to $\mathcal{L}$). Then G has the block structure

$$G = {}^{\mathcal{L}}\mathcal{G} = \begin{bmatrix} W & V \\ 0 & 1 \end{bmatrix}, \tag{5.43}$$

which comprises a rotation matrix $W \in SO(3)$ with entries $W_{kl} = \mathbf{e}_k \cdot \mathbf{g}_l$, and a translation vector $V \in \mathbb{R}^3$ with $V_j = (\mathbf{q} - \mathbf{p}) \cdot \mathbf{e}_j$.[14] The Lie group of rigid body transformations SE(3) consists of all the matrices of the form (5.43) with $W \in SO(3)$ and $V \in \mathbb{R}^3$. The derivative $g = G^{-1} \cdot \dot{G}$ of a time-dependent rigid body transformation $G(t)$ is an element of the Lie algebra $\mathfrak{se}(3)$ associated to SE(3). The Lie algebra $\mathfrak{se}(3)$ is six-dimensional and spanned by X_j, $j = 1, \ldots, 6$, where for $j = 1, 2, 3$

$$X_j = \begin{bmatrix} E_j & 0 \\ 0 & 0 \end{bmatrix}, \quad (E_j)_{kl} = \epsilon_{kjl}, \quad \text{and} \quad X_{j+3} = \begin{bmatrix} 0 & \mathbf{d}_j \\ 0 & 0 \end{bmatrix}, \quad (\mathbf{d}_j)_k = \delta_{jk}. \tag{5.44}$$

For $j = 1, 2, 3$, X_j generates a rotation around the axis $\mathbf{d}_j$; while X_{j+3} generates a translation along $\mathbf{d}_j$, see figure 5.7.

Consider a moving body frame $\mathcal{G}(t)$ with propagator $G(t) = {}^{\mathcal{G}(0)}\mathcal{G}(t) \in SE(3)$. The propagator $G(t)$ obeys a matrix-valued differential equation

$$\dot{G} = G \cdot g \tag{5.45}$$

for some $g \in \mathfrak{se}(3)$. The formal solution to (5.45) with initial condition $G(0) = \mathbb{1}$ is given by a time-ordered exponential integral $G(t) = \mathbf{T}\exp\int_0^t dt_0\, g(t_0)$, just as in the case of rotation matrices, see equation (5.5). The coefficients of $g = \Omega_1 X_1 + \Omega_2 X_2 + \Omega_3 X_3 + v_1 X_4 + v_2 X_5 + v_3 X_6$ with respect to the basis X_j constitute the instantaneous rotational velocity $\boldsymbol{\Omega} = \Omega_1 \mathbf{g}_1 + \Omega_2 \mathbf{g}_2 + \Omega_3 \mathbf{g}_3$ and the instantaneous translational velocity $\mathbf{v} = v_1 \mathbf{g}_1 + v_2 \mathbf{g}_2 + v_3 \mathbf{g}_3$ of $\mathcal{G} = (\mathbf{g}_1, \mathbf{g}_2, \mathbf{g}_3, \mathbf{q})$. Equation (5.45) also holds in the case

---

[14]Note that the entries of G have different units since the components of W are dimensionless, but the components of V have units of a length. Nevertheless, the product of two matrices of the form (5.43) has again this form.

of a stochastic propagator g. If g contains white noise, the Stratonovich interpretation has to be used.

Any $G \in SE(3)$ can be written as $G = \exp g$ for some $g = \zeta_j X_j \in \mathfrak{se}(3)$, which defines the ζ_j as exponential coordinates of G. If G does not comprise a half-turn, we may require $|(\zeta_1, \zeta_2, \zeta_3)| < \pi$, which fixes a unique choice of exponential coordinates [103]. The ζ_j have a physical interpretation: A body frame $\mathcal{G} = (\mathbf{g}_1, \mathbf{g}_2, \mathbf{g}_3, \mathbf{q})$ moving with rotational velocity $(\zeta_1 \mathbf{g}_1 + \zeta_2 \mathbf{g}_2 + \zeta_3 \mathbf{g}_3)/T$ and translational velocity $(\zeta_4 \mathbf{g}_5 + \zeta_2 \mathbf{g}_6 + \zeta_3 \mathbf{g}_3)/T$ will be propagated by G after a time T.

5.5   Rigid body dynamics of the helix disk

5.5.1   Statistical properties

We can extend the discussion of the rotational dynamics of the helix disk from section 5.3 to account also for translational motion of the disk by using the formalism of rigid body transformations. We derive an effective equation of motion proceeding as in the simpler case studied in section 5.3.1. As an extra step in the coarse-graining procedure, we perform an appropriate average over the helix phase to eliminate anisotropies in the transversal fluctuations of the helix disk. First, we introduce the full Frenet frame $\mathcal{F}$ and the full helix frame $\mathcal{H}$. Note that in this section, we reuse the notation from section 5.3: The symbols F, f, H, h, ... which denoted 3×3-rotation matrices there, now denote the corresponding 4×4-rigid body transformation matrices comprising the same rotation as before, but also a translation.

The full Frenet frame $\mathcal{F}$. The full Frenet frame of a sperm swimming path $\mathbf{r}(t)$ consists of the Frenet vectors $\mathbf{t}, \mathbf{n}, \mathbf{b}$ and the origin $\mathbf{r}$

$$\mathcal{F} = (\mathbf{t}, \mathbf{n}, \mathbf{b}, \mathbf{r}). \tag{5.46}$$

The full Frenet-frame defines a time-dependent rigid body transformation

$$F_{\text{full}}(t) = {}^{\mathcal{F}(0)}\mathcal{F}(t) \in SE(3). \tag{5.47}$$

The full Frenet matrix F_{full} defined in (5.47) is just an extension of the Frenet matrix F introduced in section 5.2; it reads in block matrix notation

$$F_{\text{full}} = \begin{bmatrix} F & \mathbf{r} \\ 0\ 0\ 0 & 1 \end{bmatrix} \in SE(3). \tag{5.48}$$

In the following, we consider only full rigid body transformations. We will therefore omit the subscript of F_{full}. The dynamics of $F(t)$ is given by $\dot{F} = F \cdot f$ with infinitesimal propagator

$$f(t) = v_0 \left(\tau(t) X_1 + \kappa(t) X_3 + X_4 \right) \in \mathfrak{se}(3). \tag{5.49}$$

The full helix frame $\mathcal{H}$. The full helix frame $\mathcal{H}$ consists of the body frame $(\mathbf{h}_1, \mathbf{h}_2, \mathbf{h}_3)$ of the disk as well as its center $\mathbf{R}$

$$\mathcal{H} = (\mathbf{h}_1, \mathbf{h}_2, \mathbf{h}_3, \mathbf{R}). \tag{5.50}$$

The full helix frame is the on-axis-transform of the Frenet-frame [13,14]

$$^{\mathcal{L}}\mathcal{H}(t) = {}^{\mathcal{L}}\mathcal{F}(t) \cdot \mathrm{G}_{\mathrm{ax}} \in \mathrm{SE}(3) \tag{5.51}$$

where $\mathcal{L}$ is an arbitrary lab frame and G_{ax} reads

$$\mathrm{G}_{\mathrm{ax}} = \begin{pmatrix} 0 & \cos\theta & \sin\theta & 0 \\ -1 & 0 & 0 & r_0 \\ 0 & -\sin\theta & \cos\theta & 0 \\ 0 & 0 & 0 & 1 \end{pmatrix} \in \mathrm{SE}(3). \tag{5.52}$$

The on-axis-transform of the Frenet propagator $\mathrm{F}(t)$ gives the propagator $\mathrm{H}(t)$ for the helix frame $\mathcal{H}$

$$\mathrm{H}(t) = {}^{\mathcal{H}(0)}\mathcal{H}(t) = \mathrm{G}_{\mathrm{ax}}^{-1} \cdot \mathrm{F}(t) \cdot \mathrm{G}_{\mathrm{ax}} \in \mathrm{SE}(3). \tag{5.53}$$

Similarly, the infinitesimal propagator $\mathrm{h} = \mathrm{H}^{-1} \cdot \dot{\mathrm{H}}$ satisfies

$$\mathrm{h}(t) = \mathrm{G}_{\mathrm{ax}}^{-1} \cdot \mathrm{f}(t) \cdot \mathrm{G}_{\mathrm{ax}} \in \mathfrak{se}(3). \tag{5.54}$$

Swimming in a homogenous concentration field. In a homogenous concentration field of chemoattractant, $c(\mathbf{x}) = c_0$, sperm cells swim along helical paths with curvature $\kappa(t)$ and torsion $\tau(t)$ that fluctuate around their mean values κ_0 and τ_0 as detailed in equation (5.10). As a consequence, the infinitesimal propagator $\mathrm{h} = \mathrm{H}^{-1} \cdot \dot{\mathrm{H}}$ of the helix frame $\mathcal{H}$ is also stochastic: Analogously to the derivation of (5.12) in section 5.3.1, we find

$$\mathrm{h} = \omega_0 \mathrm{X}_3 + \omega_0 h_0 \mathrm{X}_6 + \xi_j \mathrm{X}_j \tag{5.55}$$

where ξ_1, ξ_2, ξ_3 are given by equation (5.13) and

$$\xi_4 = 0, \quad \xi_5 = -r_0 \xi_3, \quad \xi_6 = r_0 \xi_2. \tag{5.56}$$

The stochastic processes ξ_4 and ξ_5 characterize transversal fluctuations of the helix; while ξ_6 characterizes axial stretching of the helical segment. We introduce complex notation $\mathrm{Z} = \mathrm{X}_4 + i\mathrm{X}_5$ and $\xi_\mathrm{Z} = \xi_4 - i\xi_5$. We redefine $\mathrm{Y} = \mathrm{X}_1 + i\mathrm{X}_2$.

After n helical turns, the helix frame $\mathcal{H}(t)$ is propagated by the rigid body transformation $\mathrm{H}(nT) = {}^{\mathcal{H}(0)}\mathcal{H}(nT)$; $\mathrm{H}(nT)$ reads in exponential coordinates

$$\mathrm{H}(nT) = \exp\left(2\pi h_0 n \mathrm{X}_6 + \Xi_j \mathrm{X}_j\right). \tag{5.57}$$

The fluctuations of $H(nT)$ are characterized by stochastic variables Ξ_j whose expectation values $\langle \Xi_j \rangle$ vanish to linear order in η, i.e. $\langle \Xi_j \rangle = 0 + \mathcal{O}(\eta^2)$. Recall that $\eta = (\lambda c_0 \sigma)^{-1/2}$ characterizes the fluctuation strength of the stochastic chemotactic stimulus, see section 5.3. We can express the Ξ_j in terms of the ξ_j: For Ξ_1, Ξ_2, Ξ_3, we recover equation (5.15); while for Ξ_4, Ξ_5, Ξ_6, we find to leading order in η

$$
\begin{aligned}
\Xi_Z = \Xi_4 - i\,\Xi_5 &= \int_0^{nT} dt\, [\xi_Z(t) - i\omega_0 h_0(t - nT/2)\xi_Y(t)]\, e^{-i\omega_0 t} + \mathcal{O}(\eta^2), \\
\Xi_6 &= \int_0^{nT} dt\, \xi_6(t) + \mathcal{O}(\eta^2).
\end{aligned}
\tag{5.58}
$$

The calculation of the Ξ_j is similar to the derivation of (5.58); the details can be found in appendix M.1. It is interesting to note that bending fluctuations $\xi_Y(t)$ contribute to the total transversal fluctuations Ξ_Z. The reason for this is the coupling of bending and transversal modes: Since the helix disk translates with velocity $\omega_0 h_0 \mathbf{h}_3 + \mathcal{O}(\eta)$, any rotation of the disk around $\mathbf{h}_1$ or $\mathbf{h}_2$ which occurs at a time t_0 changes the helix vector $\mathbf{h}_3$ and thus has an effect on the translational motion of the disk at later times $t > t_0$.

We introduce the correlation matrix C with entries $C_{kl} = \langle \Xi_k \Xi_l \rangle$; below we compute a phase-averaged version $\overline{C}$ of this correlation matrix C.

Averaging over the helix phase. Consider for a moment a rotated helix frame $\mathcal{H}' = (\mathbf{h}'_1, \mathbf{h}'_2, \mathbf{h}_3, \mathbf{R})$ with $\mathbf{h}'_1 = \cos\varphi\, \mathbf{h}_1 + \sin\varphi\, \mathbf{h}_2$ and $\mathbf{h}'_2 = -\sin\varphi\, \mathbf{h}_1 + \cos\varphi\, \mathbf{h}_2$. We find for its propagator

$$
H'(nT) = {}^{\mathcal{H}'(0)}\mathcal{H}'(nT) = X_\varphi^{-1} \cdot H(nT) \cdot X_\varphi
\tag{5.59}
$$

where $X_\varphi = \exp \varphi X_3$. We can write

$$
H'(nT) = \exp\left(2\pi h_0 n\, X_6 + \Xi'_j\, X_j\right)
\tag{5.60}
$$

where the primed coordinates Ξ'_k are related to the unprimed coordinates Ξ_l of $\mathcal{H}(nT)$ as defined in (5.57) by the adjoint action of X_φ

$$
\Xi'_k = \left(\mathrm{Ad}_{X_\varphi}\right)_{kl} \Xi_l
\tag{5.61}
$$

where[15]

$$
X_\varphi = \begin{bmatrix} W & 0 \\ 0 & 1 \end{bmatrix}, \quad
\mathrm{Ad}_{X_\varphi} = \begin{bmatrix} W^T & 0 \\ 0 & W^T \end{bmatrix}, \quad
W = \begin{pmatrix} \cos\varphi & \sin\varphi & 0 \\ -\sin\varphi & \cos\varphi & 0 \\ 0 & 0 & 1 \end{pmatrix}.
\tag{5.62}
$$

The correlation matrix C' with $C'_{kl} = \langle \Xi'_k \Xi'_l \rangle$ is related to the unprimed correlation

---

[15]Recall that if a Lie group element $G = \begin{bmatrix} W & V \\ 0 & 1 \end{bmatrix} \in SE(3)$ acts on an element of the Lie algebra $\mathfrak{g} = \zeta_j X_j$ as $\mathfrak{g}' = G^{-1} \cdot \mathfrak{g} \cdot G$, then the coordinates ζ'_j of $\mathfrak{g}' = \zeta'_j X_j$ are related to ζ_j by the adjoint action of G, i.e. $\zeta'_k = (\mathrm{Ad}_G)_{kl}\zeta_l$ with $\mathrm{Ad}_G^{-1} = \begin{bmatrix} W & 0 \\ \widehat{V}W & W \end{bmatrix}$ where $\widehat{V} = V_1 X_1 + V_2 X_3 + V_3 X_3$.

matrix C by $C' = \text{Ad}_{X_\varphi} \cdot C \cdot \text{Ad}_{X_\varphi}^T$. Interestingly, the correlation matrices C and C' (corresponding to the original helix frame and to the rotated helix frame, respectively) do not agree in general. They differ in exactly those entries which characterize the transversal fluctuations in the plane of the helix disk, see appendix M.2. The anisotropy of these transversal fluctuations is a consequence of the coupling of bending and transversal modes.

We introduce the phase-averaged correlation matrix $\overline{C}$

$$\overline{C} = \frac{1}{2\pi} \int_0^{2\pi} d\varphi \, \text{Ad}_{X_\varphi} \cdot C \cdot \text{Ad}_{X_\varphi}^T. \tag{5.63}$$

The phase-averaged correlation matrix characterizes the statistics of the rotated helix matrix $H'(nT)$ for the case that the phase angle φ itself is a random variable (uniformly distributed)

$$\overline{C}_{kl} = \langle \Xi_k' \, \Xi_l' \rangle_\varphi. \tag{5.64}$$

Here the expectation value $\langle \cdot \rangle_\varphi$ averages both over noise and over the phase angle φ. If n is chosen such that nT is much longer than the correlation time σ of the fluctuations ξ_a of the output variable a, then most entries entries of $\overline{C}$ vanish to leading order except $\overline{C}_{jj}$ for $j = 1, 2, 4, 5$, see appendix M.2. The entries $\overline{C}_{11}$ and $\overline{C}_{22}$ characterize bending fluctuations of the helix and both equal C_{11} given in (5.20); while $\overline{C}_{44}$ and $\overline{C}_{55}$ characterize transversal fluctuations and read

$$\overline{C}_{44} = \overline{C}_{55} \approx \frac{1}{2}\Theta_Z^2 \, nT \, \widetilde{S}_a(\omega_0) + \frac{1}{12}(\omega_0 h_0 \, nT)^2 \, C_{11}, \tag{5.65}$$

where $\Theta_Z = r_0 \Theta_3 = v_0 r_0 (\tau_1 \sin\theta\tau_1 + \kappa_1 \cos\theta)$. This approximation is valid to leading order in η provided nT is much longer than the correlation time σ of ξ_a. Note that $\overline{C}_{11}$ scales linearly with time, $\overline{C}_{11} \sim nT$, but that $\overline{C}_{44}$ has a contribution scaling like $(nT)^3$ due to the coupling of bending and transversal modes.

Swimming in a concentration gradient. We study the set of equations (3.4), (3.20), (3.21), (4.3), (4.4) from section 5.1 in the weak noise limit for a linear concentration field of chemoattractant (5.23). We proceed exactly as in section 5.3.1 and find for the exponential coordinates Ξ_j of the propagator $H(nT) = \exp(\omega_0 h_0 X_6 + \Xi_j X_j)$ of the helix frame $\mathcal{H}$ after n helical turns the identities (5.27) for $\langle \Xi_Y \rangle$ and $\langle \Xi_3 \rangle$, as well as

$$\begin{aligned} \langle \Xi_Z \rangle = \langle \Xi_1 - i\Xi_2 \rangle &= nT \, ic_\perp \, \delta_a \widetilde{\chi}_a(\omega_0) \, e^{-i\varphi_0} &+ \mathcal{O}(\nu^2, \eta^2), \\ \langle \Xi_6 \rangle &= nT \, c_\parallel \, \overline{\delta} &+ \mathcal{O}(\nu^2, \eta^2). \end{aligned} \tag{5.66}$$

Here φ_0 is the phase angle enclosed by $\mathbf{c}_\perp$ and $\mathbf{h}_1(0)$. The coefficients of bending and excess twist of the helix, ε_a and $\overline{\varepsilon}$, respectively, are given below equation (5.27). The coefficient δ_a for helix tilt and the coefficient for axial stretching $\overline{\delta}$ read $\delta_a = \lambda r_0 \Theta_Z/2 = \lambda\omega_0 r_0^2 (r_0\kappa_1 + h_0\tau_1)/2$ and $\overline{\delta} = \mu\omega_0 h_0 r_0 \Theta_Y/c_0$. Note that the tilt coefficient δ_a found here differs from the coefficient $\kappa_1\delta_\kappa + \tau_1\delta_\tau$ stated in chapter 3. The reason for this discrepancy is that a different definition for the helix vector was used in chapter 3: There we used an explicit expression for the helix vector $\mathbf{h}_3$ characterized by the

requirement that $\mathbf{h}_3$ is free of precession with frequency ω_0. We conclude that helix tilt depends in a subtle way on the precise definition used for the helix vector.

For the variances of the exponential coordinates Ξ'_j of the rotated helix frame $\mathcal{H}'$, we find to leading order the same result as in the case of a homogenous concentration field

$$\langle \delta\Xi'_k \, \delta\Xi'_l \rangle_\varphi = \overline{C}_{kl} + \mathcal{O}(\nu\eta^2, \eta^3), \quad k,l = 1,\ldots,6 \tag{5.67}$$

where the expectation value $\langle\cdot\rangle_\varphi$ averages over noise and the phase angle φ.

5.5.2   Effective equation of motion

We can derive an effective equation of motion for the centerline $\mathbf{R}(t)$ in a concentration field of chemoattractant $c(\mathbf{x})$ by performing a continuum limit just as in section 5.3.2. The details of the calculation can be found in appendix M.3; here we present the final result. We obtain the following Stratonovich stochastic differential equation for the centerline $\mathbf{R}(t)$

$$\text{(S)} \quad \dot{\mathbf{R}} \;=\; \omega h \, \mathbf{h}_3 - \delta_a \text{Im} \left(\widetilde{\chi}_a(\omega_0) \, \mathbf{c} \right) + \widehat{\xi}_4 \, \mathbf{h}_1 + \widehat{\xi}_5 \, \mathbf{h}_2, \tag{5.68}$$

while the dynamics of the vectors $\mathbf{h}_j$ characterizing the orientation of the helix disk is given by equation (5.34). As usual, $\mathbf{c}$ denotes the complex gradient vector $\mathbf{c} = \mathbf{c}_\perp + i \, \mathbf{h}_3 \times \mathbf{c}_\perp$. The transversal fluctuations $\widehat{\xi}_4$ and $\widehat{\xi}_5$ are given by uncorrelated Gaussian white noise with $\langle \xi_k(t_1) \, \xi_l(t_2) \rangle = \widehat{C}_{44} \, \delta_{kl} \delta(t_1 - t_2)$, $k,l = 4,5$ where

$$\widehat{C}_{44} = \overline{C}_{44}/\Delta t - (\omega_0 h_0)^2 \Delta t \, \overline{C}_{11}/12 = \Theta_{\text{Z}}^2 \, \widetilde{S}_a(\omega_0)/2. \tag{5.69}$$

We need this special definition for $\widehat{C}_{44}$ because of to the coupling of bending and transversal modes, see appendix M.3. The helix frequency $\omega = \omega_0 + \mathcal{O}(\nu)$, the helix radius $r = r_0 + \mathcal{O}(\nu)$, and the helix pitch $h = h_0 + \mathcal{O}(\nu)$ are perturbed to first order in ν just as in the deterministic case, see equation (K.7) in appendix K.

Effective equation of motion in a radial concentration field. For the case of a radial concentration field $c(\mathbf{x}) = C(|\mathbf{x}|)$, we can use (5.68) to derive an equation of motion for the distance from the origin $R := |\mathbf{R}|$ and the alignment angle ψ enclosed by the helix vector $\mathbf{h}_3$ and the direction of the gradient $\boldsymbol{\nabla} c(\mathbf{R}) \parallel (-\mathbf{R})$

$$\text{(I)} \quad \begin{aligned} \dot{R} &= \quad -\gamma \quad - \Lambda \cos\psi \quad\quad\quad +\xi_4 \sin\psi \quad +A_R, \\ \dot{\psi} &= \quad -\left(\beta - \frac{\Lambda}{R}\right)\sin\psi \quad -\xi_1 \quad +\frac{1}{R}\xi_4 \cos\psi \quad +A_\psi, \end{aligned} \tag{5.70}$$

where $\Lambda = \omega h - \gamma \cos\psi$ and A_R, A_ψ are noise-induced drift terms specified below. The ξ_j denote uncorrelated Gaussian white noise with $\langle \xi_k(t_1) \, \xi_l(t_2) \rangle = \widehat{C}_{kk} \, \delta_{kl} \delta(t_1 - t_2)$, $k,l = 1,4$. For the $\widehat{C}_{kl}$, see equations (5.33) and (5.69). If the stochastic differential equation (5.70) is stated in Itō interpretation, then the noise induced drift-terms read $2A_R = (1 + \cos^2\psi) \, \widehat{C}_{44}/R$ and $2A_\psi = (\widehat{C}_{11} + \cos(2\psi) \, \widehat{C}_{44}/R^2) \cot\psi$. The derivation of
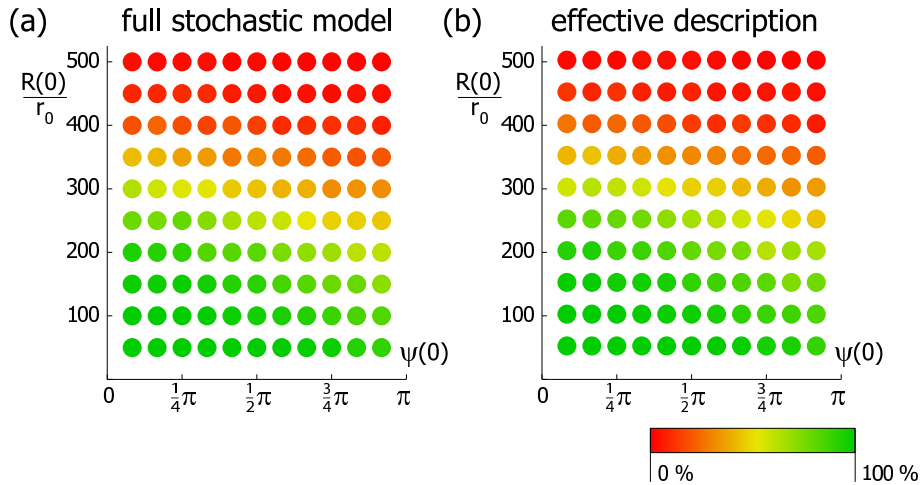
Figure 5.8: Chemotactic success as a function of initial conditions. (a) Same as panel (a) of figure 5.3: An ensemble of helical sperm swimming paths in a radial concentration field of chemoattractant was simulated according to equations (3.4), (3.20), (3.21), (4.3), (4.4) from section 5.1 and the fraction of swimming paths which successfully found a target at the origin of the concentration field was computed. (b) Again chemotactic success as a function of initial conditions is plotted as in panel (a): Instead of simulating the full set of dynamic equations (3.4), (3.20), (3.21), (4.3), (4.4) from section 5.1, the effective equation of motion (5.70) was now used to decide whether a sperm swimming path will find the target. The simulation results from panel (a) and (b) are highly comparable which exemplifies the applicability of our effective description. Parameter values used were as for figure 5.3.

equation (5.70) is analogous to the one of (3.30) given in appendix C.1 if the rules of stochastic calculus are used; see page 131 of section 5.3.2.

In figure 5.3, we presented numeric results for the probability by which a sperm swimming path in a radial concentration field finds a spherical target at the origin of the concentration field. By using the effective equation of motion (5.70) instead of the full set of stochastic equations of motion (3.4), (3.20), (3.21), (4.3), (4.4) from section 5.1, we can speed up such simulations significantly. Figure 5.8 shows again the probability of successfully finding the target as a function of initial conditions; now the probability was computed by simulating both (a) the full set of stochastic equations of sperm swimming, and (b) the effective equation of motion using the same parameters. Results are comparable to a high degree which exemplifies the applicability of our effective description.

The formalism employed in this section is useful also to describe perturbed helices arising in other contexts such as fluctuating DNA molecules [13,14].

Chapter summary

In this chapter, we derived an effective stochastic equation of motion for helical sperm swimming paths in a concentration field of chemoattractant. This equation reveals a formal kinship of sperm chemoorientation in an concentration gradient with the dynamics of a polar molecule in an electric field which is subject to rotational Brownian motion. We find that after a transient alignment period, sperm cells move upward the gradient with an average speed that is comparable to their net swimming speed provided the concentration gradient exceeds a threshold value.

We conclude that sperm chemotaxis along helical swimming paths is a robust strategy for chemotaxis which is functional even in the presence of noise. Noise may even be beneficial for sperm chemotaxis: In the presence of fluctuations, sperm cells might find an egg at the origin of a radial concentration field for initial conditions where they would fail to do so if fluctuations where absent. These particular initial conditions for which sperm cells benefit from noise are characterized by a direction of net swimming pointing initially away from the target; fluctuations may help to correct such an unfavorable initial swimming direction. In the next chapter, we discuss the role of fluctuations on search success for a simple model problem.

Chapter 6
Search along persistent random walks

In this chapter, we ask for optimal search strategies of an active swimmer such as a microorganism to find a target, provided initial target distance R_0 and total search time t_s are specified. This fundamental search problem applies in particular to the hunt of sperm cells for the egg. In this biological context, the search time t_s of the swimmer is set by its life time. A typical target distance R_0 arises, whenever swimmer and target are released in a controlled fashion, such as close-by deposition of egg and sperm spawn in fish and amphibian mating [21]. We find that search success is maximal for a certain level of fluctuations characterized by the persistence length of the swimming path of the swimmer. We derive a scaling law for the optimal persistence length as a function of initial target distance and search time by mapping the search on a polymer physics problem.

6.1   A simple search problem

Persistent random walks.   The motion of an active micro-swimmer, such as a sperm cell, is subject to fluctuations. These fluctuations can be due to (i) translational diffusion, (ii) an interplay of rotational diffusion and the active motion of the swimmer [135], as well as (iii) fluctuations of the propulsion force and torque itself. In general, fluctuations of type (ii) and (iii) do not satisfy an Einstein relation. This is because active swimming is a non-equilibrium phenomenon.

Consider an active swimmer moving with constant speed v_0 along a path $\mathbf{R}(t)$. In the case of helical swimming, $\mathbf{R}$ would denote the centerline of the helical swimming path $\mathbf{r}$. In the presence of fluctuations, the tangent $\mathbf{e} = \dot{\mathbf{R}}/v_0$ of the swimming path will change its direction in a random way which can be effectively described as diffusion on the sphere with an effective rotational diffusion constant D_{rot}. As a consequence, the swimming path $\mathbf{R}(t)$ will be a persistent random walk with persistence length $l_P = v_0/(2D_{\mathrm{rot}})$, see appendix F for a short review on persistent random walks. The persistence length sets the length scale of the decay of the auto-correlation function of the tangent

$$\langle \mathbf{e}(s_0) \cdot \mathbf{e}(s_0 + s) \rangle = \exp(-|s|/l_P), \tag{6.1}$$

where $s = v_0 t$ is arclength. In appendix G, we estimate the persistence length of sperm swimming paths as $l_P \approx 4\,\mathrm{mm}$. If only length scales large compared to the persistence length l_P are of interest, we can describe a persistent random walk effectively as a (non-persistent) random walk with diffusion coefficient $D = l_P v_0/3$ [64].

A simple search problem.   We now ask our main question: What is the probability for a persistent random walker in three-dimensional space to hit a specific target? Let a persistent random walker with persistence length l_P and swimming speed v_0 start at the origin with random initial tangent direction $\mathbf{e}_0$ (uniformly distributed). Additionally, we assume that the persistent random walker swims for a search time t_s before it dies. We then ask for the probability $p(R_0, l_P, t_s)$ that this random walker hits a spherical target of radius R_{target} located at a distance R_0 from the origin during its life-time.
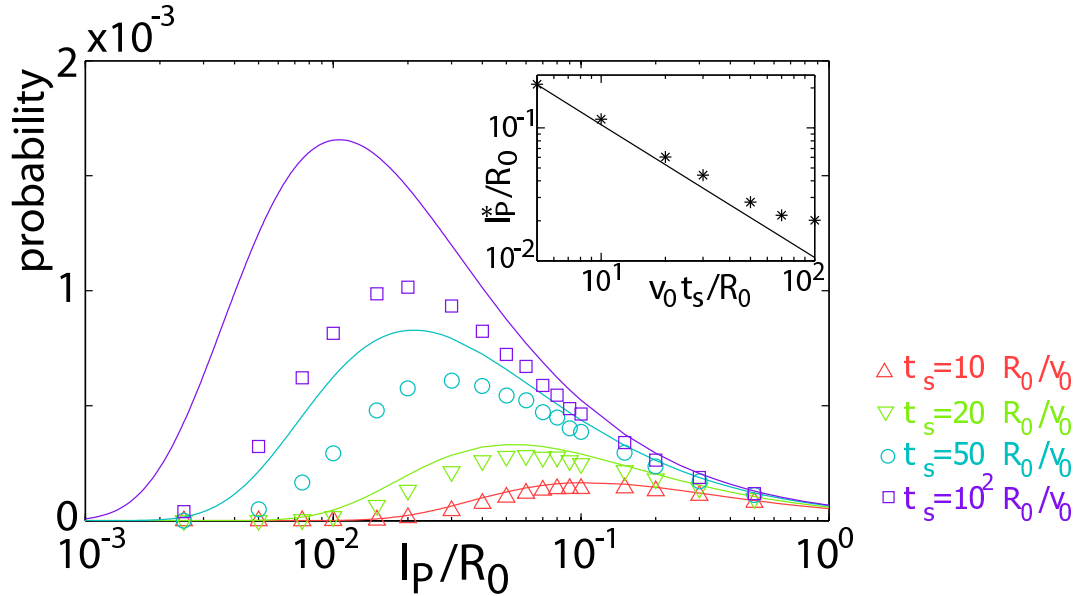
Figure 6.1: Probability $p(R_0, l_P, t_s)$ for a persistent random walker to find a spherical target of radius R_{target} as a function of its persistence length l_P. Simulation results are shown for different search times t_s: red up triangles $t_s = 10\, R_0/v_0$, green down triangles $t_s = 20\, R_0/v_0$, blue circles $t_s = 50\, R_0/v_0$, lilac squares $t_s = 100\, R_0/v_0$. Target size is $R_{\text{target}} = 10^{-2}\, R_0$. Error bars are of the size of the symbols. Also shown is the analytic result (6.9) for the success probability p for search times $t_s = 10, 20, 50, 100\, R_0/v_0$ (solid lines; color: red, green, blue and lilac, respectively). The inset shows the optimal persistence length l_P^* which maximizes p as a function of search time t_s: Stars indicate optimal values for l_P^* obtained by fitting smooth curves to the simulation data and solid lines the analytic approximation (6.10).

Figure 6.1 shows simulation results for the success probability p as a function of persistence length l_P for various search times t_s. Naturally, the success probability increases with search time t_s. Striking is however the existence of pronounced maxima of p for finite l_P. The optimal value $l_P^*(R_0, t_s)$ for the persistence length is a function of initial target distance R_0 and search time t_s.

We can gain more insight into the sperm search problem presented above by relating it to a polymer physics problem:

6.2   A polymer physics problem

The configuration space of persistent random walks $\mathbf{R}(s)$ of length $L = v_0 t_s$ can be mapped one-to-one on the respective space of continuous worm-like chains in the sense of Kratky and Porod [85], i.e. configurations of chains of length L with an elastic energy functional $E = \frac{1}{2} k_B T \, l_P \int_0^L ds \, \kappa(s)^2$, see appendix F. The worm-like chain is a standard model to describe the shape of semiflexible polymers.

Consider now a continuous worm-like chain of length $L = v_0 t_s$ with start point at the origin and random initial tangent direction $\mathbf{e}_0$ (uniformly distributed). How often will this worm-like chain pierce an imaginary sphere of radius R_0 with center at the origin? Let n be the number of piercing events, cf. figure 6.2.

Figure 6.2: Schematic depiction of the polymer physics problem discussed in the text: A continuous worm-like chain of length L with one endpoint at the center of a sphere of radius R_0 will pierce this sphere several times. We can relate the mean number of piercing events to the probability by which a persistent random walker will hit a small target initially at distance R_0, see text for details.

We can find an approximative analytic expression for the success probability p by relating this quantity to the number of piercing events n: A spherical target (of radius R_{target}) at distance R_0 from the origin will intersect the imaginary sphere in a disk. This disk covers a fraction $\alpha \approx \pi R_{\text{target}}^2 / (4\pi R_0^2)$ of the surface of the imaginary sphere. In the limit of small targets, $R_{\text{target}} \ll l_P, R_0$, we can consider the individual piercing events of a worm-like chain of length L starting at the origin as independent trials for hitting the disk. Hence we find for the probability p_{disk} to hit the disk

$$p_{\text{disk}} = \langle 1 - (1 - \alpha)^n \rangle \approx \alpha \langle n \rangle \tag{6.2}$$

if $R_{\text{target}} \ll R_0$. For the probability p to hit the spherical target, we find $p(R_0, l_P, t_s) \approx 2\,p_{\text{disk}}$ by elementary geometry: We can assume an isotropic distribution of endpoint tangent directions in the vicinity of the target. Hence, the probability for a surface patch to be hit is proportional to its area. The surface of the spherical target is twice the area of a two-sided disk of radius R_{target} and the assertion follows.

We give a closed formula for the mean number of piercing events $\langle n \rangle$. First,

$$\langle n \rangle = \int_{R_0}^{L} ds\, J_{\text{in}}(s) + J_{\text{out}}(s), \tag{6.3}$$

where $J_{\text{in}}(s)$ and $J_{\text{out}}(s)$ are the fluxes of worm-like chain piercing the imaginary sphere at arclength position s arriving from the inside or the outside of the sphere, respectively. For our question, the relevant degrees of freedom of a worm-like chain $\mathbf{R}(s)$ are the distance from the origin $R(s) = |\mathbf{R}(s)|$ at each arc-length position s and the 'angle of attack' $\psi(s)$ with $R(s)\cos\psi(s) = \mathbf{R}(s) \cdot \mathbf{e}(s)$. We need the distribution $\Psi(R, \psi; s)$ of worm-like chains in (R, ψ)-space. Let $\Phi(\mathbf{R}, \mathbf{e}; s)$ be the endpoint distribution function for a worm-like chain of length s (with start-point at the origin and random initial tangent direction). Here, $\mathbf{R}$ denotes the end-point and $\mathbf{e}$ the tangent direction at $\mathbf{R}$. We define for $0 < \psi < \pi$

$$\Psi(R, \psi; s) = \int_{|\mathbf{R}|=R} d\mathbf{R} \int_{\mathbf{e}\cdot\mathbf{R}=R\cos\psi} d\mathbf{e}\, \Phi(\mathbf{R}, \mathbf{e}; s). \tag{6.4}$$

A worm-like chain piercing the imaginary sphere inside-out at arclength position s is characterized by $R(s) = R_0$ and $0 < \psi(s) < \pi/2$, whereas the worm-like chain piercing in the reverse direction obeys $R(s_1) = R_0$, $\pi/2 < \psi(s) < \pi$. Since $dR(s)/ds = \cos\psi(s)$, we find for the fluxes

$$
\begin{aligned}
J_{\text{in}}(s) &= \int_0^{\pi/2} d\psi\, \Psi(R_0, \psi; s)\cos\psi, \quad \text{and} \\
J_{\text{out}}(s) &= -\int_{\pi/2}^{\pi} d\psi\, \Psi(R_0, \psi; s)\cos\psi.
\end{aligned}
\tag{6.5}
$$

Thus $\langle n \rangle$ can be expressed in terms of the propagator Φ. Approximation formulas for Φ can be found in the literature [134,161,164]. If lengths much larger than the persistence length are of interest, $s \gg l_P$, we obtain the diffusion limit and can approximate Φ by the propagator of pure diffusion with diffusion coefficient $D = l_P v_0/3$. For $s \gg l_P$, we may assume an isotropic distribution of end-point tangent directions $\mathbf{e}$ and hence find for Ψ

$$\Psi(R, \psi; s) \approx 4\pi R^2 \left(4\pi l_P s/3\right)^{-3/2} \exp\left(-\frac{3R^2}{4l_P s}\right) \frac{\sin\psi}{2}. \tag{6.6}$$

In the limit $R_0 \gg l_P$, we find combining equations (6.3), (6.5), (6.6)

$$\langle n \rangle \approx \frac{3}{2} \frac{R_0}{l_P} \text{Erfc}(R_0/\sqrt{4l_P L/3}). \tag{6.7}$$

Expression (6.7) is maximal for a persistence length

$$l_P^{**} = \frac{3}{4} z_0 \frac{R_0^2}{L}, \tag{6.8}$$

where $z_0 \approx 1.41$ is defined by $0 = \frac{d}{dz}\text{Erfc}(z^{-1/2})/z_{|z=z_0}$. The analytic result (6.7) for $\langle n \rangle$ agrees perfectly with our simulation data in the regime $R_0 \gg l_P$, see figure 6.3.
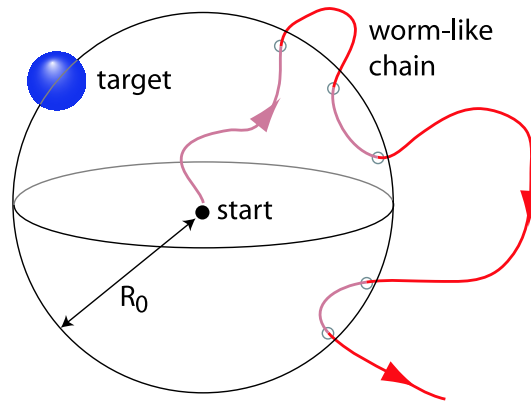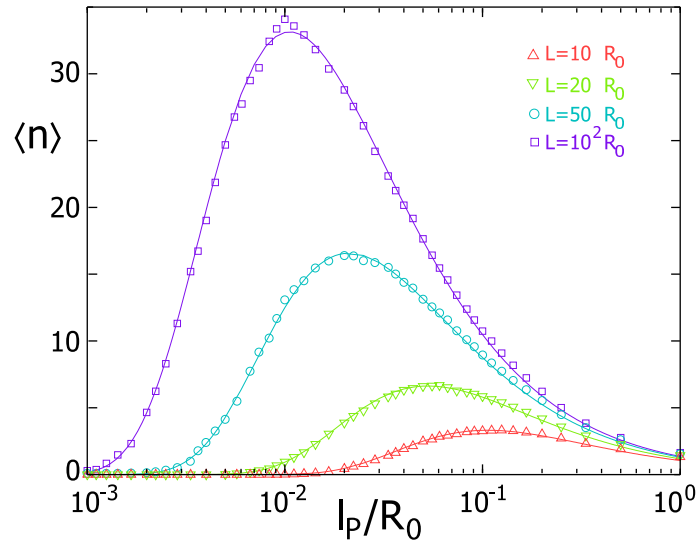
Figure 6.3: The polymer physics problem discussed in the text asks how often a continuous worm-like chain of length L with one endpoint at the center of a sphere of radius R_0 will pierce this sphere. Shown are simulation results for the mean number $\langle n \rangle$ of piercing events as a function of the persistence length l_P of the worm-like chain. Simulations were run for four different lengths of the worm-like chain: red up triangles: $L = 10\,R_0$, green down triangles: $L = 20\,R_0$, blue circles: $L = 50\,R_0$, lilac squares: $L = 100\,R_0$. Error bars are of the size of the symbols. Also shown is the analytic result (6.7) based on a diffusion approximation for chain lengths $L = 10, 20, 50, 100\,R_0$ (solid lines; color: red, green, blue and lilac, respectively)

6.3   Search success is maximal for a finite persistence length

By the correspondence of the sperm search problem and the polymer physics problem, these results can be rephrased as follows: For a persistent random walker, the probability to hit a target as specified above is

$$p(R_0, l_P, t_s) = \frac{3}{4} \frac{R_{\text{target}}^2}{R_0 l_P} \, \text{Erfc}(R_0/\sqrt{4 l_P v_0 t_s/3}), \qquad (6.9)$$

provided $v_0 t_s, R_0 \gg l_P \gg R_{\text{target}}$. This analytic result provides a good semi-quantitative approximation for the simulation data, see figure 6.1. Comparing figures 6.1 and 6.3, we find that the expression for $\langle n \rangle$, equation (6.7), is quite accurate for the parameter values considered in the simulations; while equation (6.2) only provides an approximation. Thus the deviation of our analytic approximation from the simulation data results from the fact that the individual piercing events of the worm-like chain can only approximately be treated as independent events.

The probability $p(R_0, t)$ for a swimmer initially at distance R_0 of the target to find the target after a search time t_s is maximal for a finite persistence length

$$l_P^*(R_0, t_s) \approx l_P^{**}(R_0, v_0 t_s) \approx \frac{3}{4} z_0 \, \frac{R_0^2}{v_0 t_s} \qquad (6.10)$$

with z_0 as above. Thus there exists an optimal level of fluctuations, characterized by the persistence length of the swimming path, for finding the target. The value of the optimal persistence length can be thought of as a trade-off between moving too slowly towards the target $(l_P \ll R_0^2/L)$ and moving away from the target too fast $(l_P \gg R_0^2/L)$. Equation (6.10) corresponds to the matching of two diffusion coefficients $D^* = l_P^* v_0/3 \sim R_0^2/t_s$.

Our result is related to recent research on optimal foraging strategies of water fleas *(Daphnia)* in finite-size food patches where food uptake is maximized for a finite effective diffusion constant [59,135].

Limit of long search times.   It is instructive to study the limit of long search times, $t_s \gg R_0^2/D$. In this limit, we find $p \sim R_{\text{target}}^2/(R_0 l_P)$. This scaling behavior can be easily understood: Consider a neighborhood of the target, bounded by a sphere of radius l_P, concentric with the target. On scales larger than l_P, the swimming path is approximately a random walk. The probability to enter the neighborhood is thus l_P/R_0. Once the swimmer has entered the neighborhood, its swimming path is approximately straight and the conditional probability to hit the target scales as $R_{\text{target}}^2/l_P^2$.

Optimal persistence length in the presence of a chemotactic bias.   A persistent random walk is an effective description of noisy swimming paths in the absence of any external bias. The swimming direction $\mathbf{e}$ of a persistent random walker diffuses on the unit sphere with a diffusion constant $D_{\text{rot}} = v_0/(2l_P)$. In the presence of a chemotactic bias which reorients the swimmer in a concentration field of chemoattractant $c = c(\mathbf{x})$, the swimming direction $\mathbf{e}$ tends to align with the concentration gradient $\boldsymbol{\nabla} c$ while at the same time it is subject to fluctuations. The motion of such a chemotactic swimmer can be described by the following Stratonovich stochastic differential equation for the position $\mathbf{R}$ of the swimmer and its material frame $(\mathbf{e}_1, \mathbf{e}_2, \mathbf{e}_3)$ with $\mathbf{e}_3 = \mathbf{e}$

$$(S) \quad \begin{aligned} \dot{\mathbf{R}} &= v_0\,\mathbf{e}_3, \\ \dot{\mathbf{e}}_3 &= \beta\,\mathbf{c}_\perp/c_\perp + \xi_2\mathbf{e}_1 - \xi_1\mathbf{e}_2, \\ \dot{\mathbf{e}}_j &= -(\dot{\mathbf{e}}_3 \cdot \mathbf{e}_j)\,\mathbf{e}_3, \quad j = 1, 2. \end{aligned} \quad (6.11)$$

Here ξ_j, $j = 1, 2$, is uncorrelated Gaussian white noise satisfying $\langle \xi_k(t_1)\,\xi_l(t_2)\rangle = 2D_{\text{rot}}\,\delta_{kl}\,\delta(t_1 - t_2)$ and $\mathbf{c}_\perp = \boldsymbol{\nabla} c - (\boldsymbol{\nabla} c \cdot \mathbf{e}_3)\,\mathbf{e}_3$ is the component of the concentration gradient perpendicular to $\mathbf{e}_3$ with length $c_\perp = |\mathbf{c}_\perp|$. Equation (6.11) describes the dynamics of a chemotactic swimmer which swims with constant speed v_0 in the direction of its body axis $\mathbf{e}$; the rotational dynamics of the body axis $\mathbf{e}_3$ is characterized by a term $\beta\mathbf{c}_\perp/c_\perp$ which causes alignment of $\mathbf{e}_3$ with the concentration gradient and a stochastic term $\epsilon_{j3k}\xi_j\mathbf{e}_k$ which describes effective rotational diffusion. The bending parameter β characterizes the strength of the chemotactic response; while the parameter $l_P = v_0/(2D_{\text{rot}})$ characterizes the strength of the fluctuations of the swimming direction and generalizes the persistence length. Note that equation (6.11) is a special case of the effective equation of motion (3.2) which we derived as a coarse-grained de-

scription of sperm swimming paths in a concentration field of chemoattractant. The dynamic equation (3.2) contains additional terms which are not required for a minimal model of a chemotactic swimmer and which we did not include in equation (6.11) for simplicity.[16]

We are interested in the probability for chemotactic swimmer to find a small target at the origin of a radial concentration field. We assume that the swimming path $\mathbf{R}(t)$ of the swimmer is described by equation (6.11) and that the bending parameter scales inversely with distance R from the target $\beta = B_0/R$ with a constant B_0. Note that in our theoretical description of sperm chemotaxis, the bending parameter shows exactly such a scaling behavior provided (i) the target releases chemoattractant at a constant rate and the concentration field $c(\mathbf{x})$ is established by diffusion, and (ii) the sensitivity threshold of chemotactic signaling vanishes, $s_b = 0$, see chapter 3. Figure 6.4 shows simulation results for the success probability of finding the target as a function of the generalized persistence length for three values of the chemotactic strength B_0. The swimmer starts at a distance R_0 from the target with random initial swimming direction $\mathbf{e}_3(t)$ (uniformly distributed). The target is spherical with radius R_{target}. For a low value of B_0, diffusion dominates and the success probability of the chemotactic swimmer is only slightly larger than for a persistent random walker with the same persistence length, see panel (a). For an intermediate value, the success probability is significantly enlarged, see panel (b). Nevertheless, the success probability is maximal for a finite value of the persistence length. Finally, we find a success probability close to 1 for a large value of the chemotactic strength. In this case, fluctuations handicap the chemotactic swimmer and success probability is maximal in the absence of fluctuation with $l_P = \infty$. In chapter 5, equation (5.38), we introduced the angular Peclet number $\text{Pe} = \beta/D_{\text{rot}}$ which characterizes the strength of the chemotactic response relative to the effective rotational diffusion of the swimming direction. In our case, the Peclet number is a function of distance to the target and reads $\text{Pe} = 2B_0 l_P/(v_0 R)$. The three panels of figure 6.4 correspond to three different values of the chemotactic strength and are characterized by an angular Peclet number that is in panel (a): much smaller than 1, in panel (b): of order unity in the vicinity of the target, and in panel (c): of order unity in the whole region $R_{\text{target}} < R < R_0$; here we have chosen $l_P = 0.1\,R_0$ as a reference value. The next figure 6.5 displays the value of the persistence length l_P^* that optimizes search success as a function of the chemotactic strength B_0. This optimal persistence length is a monotonously increasing function of B_0: the stronger the chemotactic ability of the swimmer, the lower the optimal level of fluctuations.

Generalizations.   We can generalize the idealistic setting of the 'sperm search problem' to the more realistic case where the swimmer has no *a priori* knowledge of the

---

[16]In equation (3.25), the dynamics of $\dot{\mathbf{R}}$ also includes (i) a chemotactic tilt term $\delta\,\text{Im}\,\widetilde{\chi}\,\mathbf{c}$, and (ii) a noise term $\widehat{\xi}_{j+3}\mathbf{h}_j$ describing transversal fluctuations; the dynamics of $\mathbf{h}_3$ contains a chemotactic bending term which describes bending in a direction $\mathbf{h}_3 \times \mathbf{c}_\perp$ perpendicular to the concentration gradient component $\mathbf{c}_\perp$; and finally, the dynamics of $\mathbf{h}_j$ includes a term which describes rotational fluctuations around $\mathbf{h}_3$.
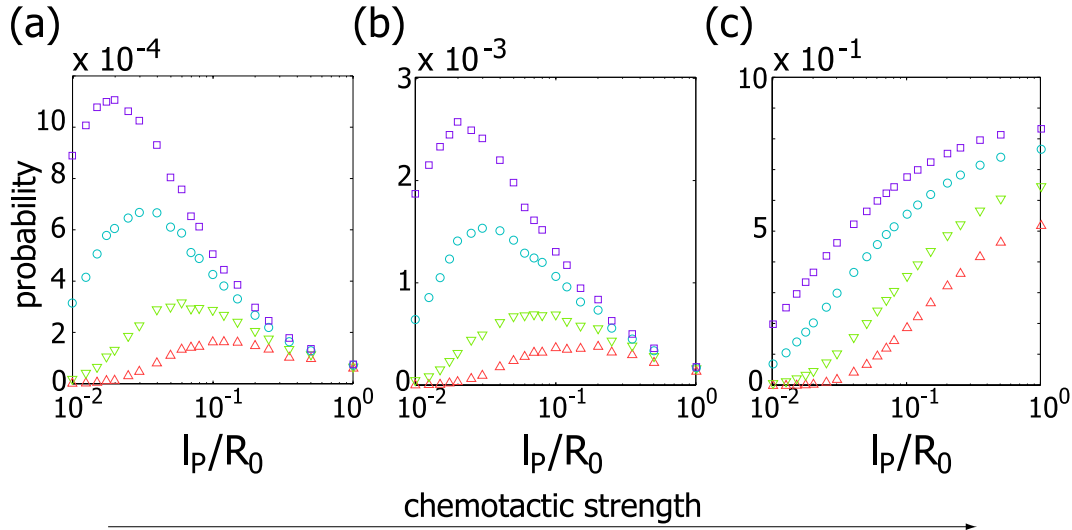
Figure 6.4: Probability p for a chemotactic swimmer to find a small target at the origin of a radial concentration field in a finite time t_s as a function of its generalized persistence length $l_P = v_0/(2D_{\mathrm{rot}})$. The three panels correspond to different strengths of the chemotactic response: (a) $B_0 = 0.01\,v_0$, (b) $B_0 = 0.1\,v_0$, and (c) $B_0 = v_0$, see equation (6.11). Simulation results are shown for different search times t_s: red up triangles $t_s = 10\,R_0/v_0$, green down triangles $t_s = 20\,R_0/v_0$, blue circles $t_s = 50\,R_0/v_0$, lilac squares $t_s = 100\,R_0/v_0$ where R_0 is the initial distance of the swimmer from the target. The target itself is spherical with radius $R_{\mathrm{target}} = 10^{-2}\,R_0$. Errorbars are within the size of the symbols.

precise distance of the target but instead possesses information in form of a probability distribution function $q(R_0)$ of target distance. For example, similar results can be obtained, if $q(R)/(4\pi R^2)$ peaks at a certain $R = R_0$ and if search times t_s follow some distribution. However, a qualitatively different situation occurs, if $q(R)/(4\pi R^2) = d_0$, i.e. if several targets are uniformly distributed with density d_0. In this case the probability of hitting a target scales as $p \sim d_0 R_{\mathrm{target}}^2 v_0 t_s$ independent of l_P. This result dates back to Rothschild [94] and can be restated in the way that success probability p is proportional to "search volume" defined by the volume V_s of a tubular neighborhood of the swimming path of radius R_{target}. If the swimmer is not already in the oversampling regime, $V_s = \pi R_{\mathrm{target}}^2 v_0 t$. We conclude that an optimal persistence length for target search along a persistent random walk only exists if the search problem involves a certain length and time scale.

Planar persistent random walks.   An analogous theory can be developed for planar persistent random walks. In the planar case, we obtain again an analytic approximation for the success probability $p_{2\mathrm{d}}$ for a planar persistent random walker to find a disk-shaped target of radius R_{target} initially located at a distance R_0 within a search time t_s as

$$p_{2\mathrm{d}} = \frac{1}{\pi} \frac{R_{\mathrm{target}}}{l_P} \Gamma\left(0, \frac{R_0^2}{2\,l_P\,v_0\,t_s}\right) \tag{6.12}$$

(a) optimal persistence length

l_P^* / R_0

(b) maximal success probability

p_{max}

chemotactic strength B_0

chemotactic strength B_0
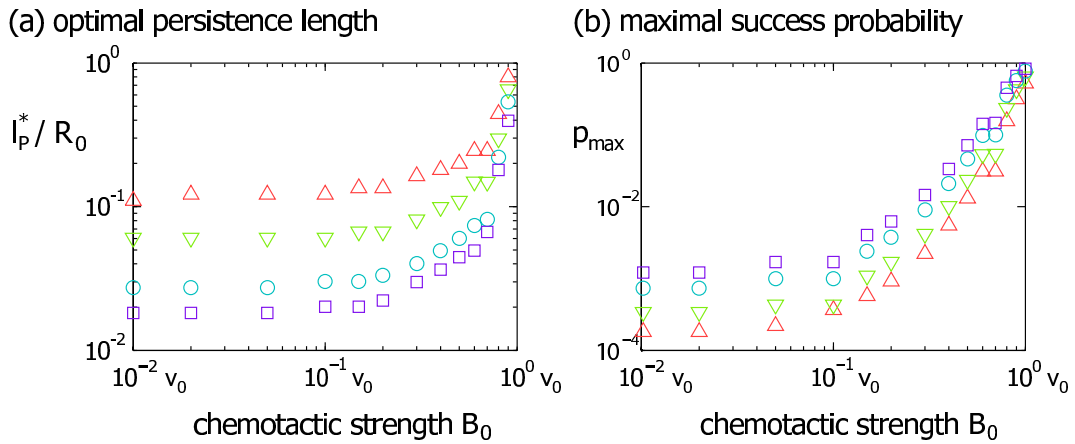
Figure 6.5: The probability for a chemotactic swimmer to find a small target at the origin of a radial concentration field in a finite time t_s is maximal for a finite value of its generalized persistence length $l_P = v_0/(2D_{\mathrm{rot}})$. (a) The optimal value l_P^* depends on the strength of the chemotactic response which is characterized by the parameter B_0, see text for details. (b) The maximal success probability rises with increasing chemotactic strength B_0. Simulation results are shown for different search times t_s: red up triangles $t_s = 10\,R_0/v_0$, green down triangles $t_s = 20\,R_0/v_0$, blue circles $t_s = 50\,R_0/v_0$, lilac squares $t_s = 100\,R_0/v_0$ where R_0 is the initial distance of the swimmer from the target. The target itself is spherical with radius $R_{\mathrm{target}} = 10^{-2}\,R_0$. Maximal success probabilities and optimal values for l_P^* were obtained by fitting smooth curves to simulation data as shown in figure 6.4.

where Γ denotes the Gamma function. Success probability p_{2d} is maximized for a finite persistence length

$$l_{P,\mathrm{2d}}^* = \frac{z_1}{2}\,\frac{R_0^2}{v_0 t_s},\tag{6.13}$$

where $z_1 \approx 2.30$ is defined by $0 = \frac{d}{dz}\Gamma(0, z^{-1})/z_{|z=z_1}$. An example for a planar persistent random walk is given by the motion of a single hunger-state *Dictyostelium discoideum* cell on an agar plate [92,121].

Typical target distance. An important characteristic of our approach is the assumption of a typical initial target distance. One can think of different scenarios where typical target distances occur naturally. (i) The mating of many fish and amphibians is characterized by a close-by deposition of egg and sperm spawn [21]. This controlled release of the swimmers and the target sets a typical initial target distance. (ii) It is known that sperm cells of many species respond to chemical factors released by the egg [58]. While sperm cells of some species show chemotaxis steering upward a concentration gradient of the chemical factor, sperm cells of other species are merely 'activated': they show a prolonged, undirected behavioral response [31]. The absolute concentration of a sperm-activating-factor (SAF) provides information about target distance provided the release rate of SAF is approximately constant. It is possible that the swimming behavior of activated sperm cells is characterized by a persistence length which is optimal for the target distance at which the concentration of SAF attains a

threshold value for activation.

Finite search time.   The search problem studied here assumes a finite search time t_s. The motile lifespan of diluted sperm cells varies significantly among different species with external fertilization and ranges from $20\,\text{s} - 20\,\text{min}$ [89,147].

The search problem studied here highlights one aspect of microswimming and searching, namely the swimming along persistent random walks. The simplified setting considered here cannot be applied one-to-one to the real biological setting without some caution. The search of sperm cells for the egg is a far more complex process than the simplified version studied here. In particular, our considerations only apply for conditions of still water [53,91].

Chapter summary

We studied a new search problem in an unbounded search domain: A population of active swimmers swimming along a persistent random walk with random initial swimming direction is searching for a target initially located at a distance R_0. Since the search domain is unbounded, the population of active swimmers will eventually escape to infinity with probability one after an infinite time. As a consequence, there is no equilibrium distribution of swimmers.

If the swimmers are allowed to search for a finite search time t_s, we find that search success is maximized for a finite level of fluctuations characterized by the persistence length l_P of the swimming paths. By relating the search problem to a problem from polymer physics, we derive an analytic approximation for the probability of finding the target and find a scaling law for the optimal persistence length l_P^* in terms of initial target distance R_0 and search time t_s, $l_P^* \sim R_0^2/(v_0 t_s)$, where v_0 is swimming speed. This result holds in the limit $v_0 t_s, R_0 \gg l_P \gg R_{\text{target}}$.

We also consider a chemotactic swimmer in a radial concentration field of chemoattractant with a target at the origin of the radial field; the swimming direction of the swimmer tends to align with the gradient direction, but is also subject to fluctuations. We find that search succes is again maximal for an intermediate level of fluctuations provided the chemotactic strength does not become too large.

For the length and time scale of a typical search problem of a microorganism, the optimal persistence length of swimming could be hard-wired by evolution into its swimming behavior.

Chapter 7
Conclusion and Outlook

7.1 Summary of our results

Sperm cells are active swimmers which are propelled in a liquid by regular bending waves of their flagellum [23,29,127]. In many species, sperm cells respond to chemical factors released by the egg, so-called chemoattractants [78,99,100]. These sperm cells can navigate in a concentration gradient of such a chemoattractant. This process is called chemotaxis and guides the sperm cells towards the egg. In this thesis, we studied a theoretical description of sperm chemotaxis; our results can be summarized as follows:

1. An asymmetric flagellar beat of the sperm flagellum results in circular and helical sperm swimming paths.

2. Sampling a concentration field of chemoattractant along circular and helical swimming paths is a robust strategy for chemotaxis. It implies that spatial information about the concentration gradient is encoded as temporal information in the form of a periodic modulation of the temporal chemotactic stimulus.

3. Our theoretical description highlights the importance of internal delays of chemotactic signaling for successful navigation in a concentration gradient of chemoattractant. By interfering with chemotactic signaling, it should be experimentally possible to observe chemotactic drift of sperm cells in a direction perpendicular or even anti-parallel to the concentration gradient.

4. The chemotaxis strategy studied is robust with respect to fluctuations. In particular, it is functional if the concentration field can be read out only with limited precision.

5. In a homogenous concentration field of chemoattractant, sperm swimming circles will diffuse with an effective diffusion constant that depends on chemoattractant concentration. This prediction could be tested in experiments.

6. In the presence of fluctuations, a helical sperm swimming path aligns with a concentration gradient, just as a polar molecule subject to rotational diffusion aligns with an electric field. After an alignment period, sperm cells move upward the gradient with an average speed that is comparable to their net swimming speed.

7. The ecological consequences of noisy sperm swimming paths and sperm chemotaxis are a broad field. In this thesis, we studied a simple model problem where target distance and search time are fixed. In this setting, search success is maximal for a finite level of fluctuations of sperm swimming.

Relation to experiments. Our theoretical results are consistent with experimental findings both in two and in three dimensions: When sperm cells swim close to a surface, observed swimming paths in a concentration gradient of chemoattractant resemble drifting circles which drift upwards the concentration gradient [22,100,165]. The local chemoattractant concentration measured along the trajectory of the sperm cell represents a temporal stimulus which is periodically modulated. This stimulus exhibits strong correlations with the time-trace of both the intra-flagellar calcium concentration and the curvature of the swimming path for sperm cells swimming in a concentration gradient, see figure 1.7 on page 11 in the introduction. These observations demonstrate that sperm cells respond to a temporal concentration stimulus, i.e. they employ temporal comparison to detect a concentration gradient instead of comparing concentration at different parts of their cell body. Note that chemotactic signaling in the sea urchin relies on changes in the flagellar membrane potential which effectively averages over different positions of the flagellum and thus makes a spatial comparison mechanism for gradient detection unlikely [148]. First experiments indicate that interfering with the chemotactic signaling network and detuning of its internal timing results in a drift of sperm swimming circles perpendicular or even anti-parallel to the concentration gradient [162] which is in line with our theoretical predictions.

Far from boundary surfaces sperm cells swim along helical paths [25,33,37,38,61]. In a concentration field of chemoattractant, alignment of the helical swimming paths with the concentration gradient was observed [25,26,37]. For plant spermatozoids, experimental data could be well fitted by our theoretical results, see figure 5.6 on page 86.

Helical swimming paths are ubiquitous in nature and are a direct result of an asymmetric propulsion mechanism. In addition to sperm, it has been observed for ascidian larvae [97,98], for eukaryotic flagellates such as *Chlamydomonas* [36,74,166], for flagellated plant spermatozoids [25] and even for some bacteria such as *Thiovulum majus* [152]. There is evidence that these chiral microswimmer exhibit taxis by a mechanism similar to that of sperm chemotaxis. In the case of ascidian larvae both positive and negative phototaxis have been observed in different developmental stages. Such a change in phototactic behavior can be accounted for by our theory by a simple change of the phase shift between the stimulus and the response [98].

7.2   Outlook on future work

Chemotactic signaling. Concerning the chemotactic signaling network of sperm cells, many questions are still open: For example, the mechanism underlying adaptation has not been identified so far. Most probably, the negative cooperativity of chemoattractant binding to the receptor homotrimer contributes to adaption. Additionally, one might think of a modulation of the deactivation time of the receptors, or of the production/degradation rates of the second messenger cGMP to contribute to the adaptation capacity of the chemotactic signaling network.

Another open question is how this network can possibly achieve single-molecule sensitivity. This issue is most likely intimately linked to the fact that the number of chemoattractant receptors is very high and that the binding of chemoattractant molecules is practically irreversible at low concentrations [78].

Finally, the chemotactic signaling of mammalian sperm cells (and maybe even the chemotaxis mechanism) might differ completely from marine invertebrates [47].

Chemoattractant uptake by a beating flagellum. The regular beat of the sperm flagellum stirs the surrounding fluid with consequences for the rate of chemoattractant molecule uptake and for the positional precision of the concentration measurement. Addressing these effects would involve the solution of convection-diffusion problems in the regime of low Reynolds numbers.

Timing of the chemotactic response. In this thesis, we have demonstrated the crucial role of internal delays of chemotactic signaling and the chemotactic response of successful navigation of sperm cells in a concentration gradient of chemoattractant. By analyzing sperm swimming paths and time traces of intraflagellar calcium concentration, we can elucidate the relationship between the chemotactic stimulus, the calcium concentration and the swimming response. In particular, we can test hypothesis on the dynamic dependence of the flagellar beat pattern on the calcium concentration and compare these with models for the generation of the flagellar beat. We are currently collaborating with the group of U. B. Kaupp which conducts single-sperm experiments.

Navigation and search problems. Besides chemotaxis, a full variety of search strategies found in nature: (i) simple random walks are efficient at small length scales [16], (ii) Levy flights are a variant of random search which prevents oversampling [15,44], (iii) chemotaxis can be seen as an implementation of the method of steepest ascent in a concentration field of a chemical factor [18,56], and finally (iv) higher organisms may rely on a cognitive model of the search environment to apply sophisticated search algorithms [157].

One might ask about the evolutionary and ecological constraints which have shaped these strategies. It is an interesting question whether these search strategies are optimal in a particular sense and why some species employ a particular search strategy and not another.

Appendix A
Chemotactic signaling

Sperm chemotaxis relies on signal processing mediated by a biochemical signaling network located in the sperm flagellum. In this appendix, we review the known facts on sea urchin sperm chemotactic signaling and develop some basic physical models for this signaling system.

A.1   The chemotactic signaling cascade in sea urchin sperm

The majority of experiments on sperm chemotactic signaling have been conducted using gametes of the sea urchin *Arbacia punctulata*, the work horse of sperm chemotaxis research. While it is likely, that the chemotactic mechanisms discovered in *A. punctulata* persist also in sperm cells of other marine invertebrates, signaling of mammalian sperm chemotaxis could differ significantly [47]. In the following we will review the known facts about chemotactic signaling in *A. punctulata* sperm cells, see also figure 1.5 from page 6 in the introduction.

Chemoattractant and its receptor. The chemoattractant released by *A. punctulata* eggs is resact, an oligopeptide of 14 aminoascid length and a molecular weight of $1246\,\mathrm{Da}$ [58]. The chemotactic signaling network of the sperm cell is located in the flagellum. A high number of chemoattractant receptors are embedded into the flagellar membrane and can bind with high affinity to resact molecules [78,107]. Recent experiments indicate that there could be as many as 10^6 receptor units with one resact binding site each [78]. This high number of receptors is truly impressive: It implies that roughly half the area of the flagellar membrane is covered by receptors. It has been further proposed that three receptor units assemble to form an oligomeric complex. The binding dynamics of resact to the receptor units exhibits negative cooperativity, which is most likely due interactions between the receptor units within the complex [78].

Cyclic nucleotides open ion channels and trigger a hyperpolarization of the flagellar membrane. The receptor unit is a guanylate cyclase that becomes activated upon binding resact. After a resact molecule has bound to the respective extracellular domain, the catalytic intracellular domain converts guanosine triphosphate (GTP) into 3',5'-cyclic guanine mono-phosphate (cGMP) and pyrophosphate. The energy for this reaction is provided by the GTP molecule, which plays the role of an energy currency in the metabolism of cells. In the time course of about $300\,\mathrm{ms}$ after a binding event, the receptor guanylate cyclase will be deactivated again by sequential dephosphorylization [78], with the ligand possibly still bound to the receptor domain. Due to the small

flagellar volume of just a few femtoliter (μm^3), a small number of cGMP molecules will already result in a local cGMP concentration in the nanomolar range. The next step in the signaling cascade are **c**yclic-**n**ucleotide **g**ated potassium channels (KCNG), whose open probability is greatly enhanced by binding of a cGMP molecule [78,79]. Opening of the KCNG channels results in a potassium efflux which causes a hyperpolarization of the flagellar membrane. The capacitance of the flagellar membrane was measured for mammalian sperm cells and found to be $2.5\,\mathrm{pF}$, which is exceptionally low [106]. The current through a single KCNG is estimated to be about $1\,\mathrm{pA}$. The rest potential of the flagellar membrane is about $-40\,\mathrm{mV}$ [148], upon stimulation hyperpolarizations up to $-75\,\mathrm{mV}$ have been observed [148]. Note that a local change in membrane potential will propagate along the whole length of the flagellum in less than a millisecond. Thus, even if resact binding, cGMP production and opening of KCNG channels have been inhomogenously distributed along the flagellum, the hyperpolarization of the flagellar membrane will be homogenous.

Depolarization of the flagellar membrane and calcium influx. A hyperpolarization of the flagellar membrane will cause **h**yperpolarization-activated (and **c**yclic **n**ucleotide-gated) HCN channels to open which results in a sodium influx and a partial depolarization of the membrane potential. HCN channels are usually found in pace maker cells with rhytmic activity, such as the cells of the sinus node in the heart and the relay neurons of the thalamus [139].

As a consequence to the depolarization of the flagellar membrane, voltage-gated calcium channels will open by a recovery-from-inactivation mechanism. These ion channels are known to have three states: *open*, *closed*, *inactive* with only the *open* state being conductive. At the resting potential, these channels are mostly in the *inactive* state. Upon hyperpolarization, they switch from the *inactive* state to the *closed* state. If a subsequent depolarization occurs, these channels will switch from the *closed* to the *open* state and become conductive. After some time, they relax to the non-conductive *inactive* state again. For the channels found in *A. punctulata* sperm cells, the relaxation time is on the order of $100\,\mathrm{ms}$. It has been argued that sperm cells contain both low- and high-voltage activated calcium channels (LVA, HVA, respectively), which differ in their voltage threshold for opening.

The depolarization current drives the membrane potential back to its resting value. For a strong enough chemotactic stimulation of sperm cells, the depolarization current may even transiently boost the membrane potential above its resting potential. In both natural sea water and in the artifical sea water preparations used in experiments, sodium concentration are higher than calcium concentration by several orders of magnitudes. As a consequence the depolarization current is mainly driven by sodium ions. The main effect of the calcium influx is not so much in charging the membrane but in altering the calcium concentration within the flagellum.

Calcium induced swimming response. The over-all effect of this signaling cascade is a transient increase in the intra-flagellar calcium concentration $[\mathrm{Ca}^{2+}]_i$. It is believed

that calcium is the key regulator for flagellar beating and that the transient rise in $[Ca^{2+}]_i$ is responsible for the observed swimming response after chemotactic stimulation with an increased asymmetry of the flagellar beat. It is known that calcium regulates the activity of the dynein motors which drive the flagellar beat. Since the generation of the flagellar beat is an interplay of the active force generation by the dynein motors and the passive elastic and viscous responses of the flagellum and the surrounding liquid, an increase of the motor activity does not simply change the frequency of the flagellar beat but will most likely change the whole shape of the flagellar bending waves. In an early experiment with demembranated flagella, Brokaw could show that the asymmetry of the flagellar beat pattern is a function of the calcium concentration [27]. In more recent experiments, the time-course of the calcium concentration within in the flagellum of a single free-swimming sperm cell could be recorded after chemotactic stimulation. It was found that both the calcium signal and the curvature of the swimming path of the sperm cell displayed characteristic spikes and that both time series were strongly correlated. It is not clear whether absolute calcium concentration or the temporal change of this concentration trigger the chemotactic swimming response [162].

A.2   Overview of experimental methods

When sperm chemotaxis was first described, only the swimming response of sperm cells after a stimulation with chemoattractant could be studied. With the development of calcium-sensitive fluorescent dyes, it became possible to measure time-resolved calcium concentrations within the flagellum of free-swimming sperm cells by loading the sperm cells with these dyes before the actual experiment. Chemotactic stimulation of these labelled sperm cells elicits characteristic fluorescence signals from the flagellum. In a similar manner, the membrane potential E_m of the flagellar membrane can be recorded in a non-invasive way by incorporating voltage-sensitive dyes into the flagellar membrane.

Two fundamentally different experimental setups can be considered:

1. **Sperm population experiments** with a stopped-flow or quenched-flow setup, where a chemoattractant solution and a suspension of sperm cells are rapidly mixed. This setup accounts for measuring a population average of the calcium or the membrane potential response. The results of these experiments are highly reproducible [148,162]. It was possible to calibrate fluorescene signals of voltage-sensitive dyes, therefore this methods yields absolute numbers for the chemotactic response of the membrane potenital.

2. **Single sperm experiments** where a swimming sperm cell is tracked and simultanously a fluorescence signal is recorded. Although this experimental approach asseses chemotactic signaling most directly, signal-to-noise ratios are in general much lower than in population experiments. [148,162].
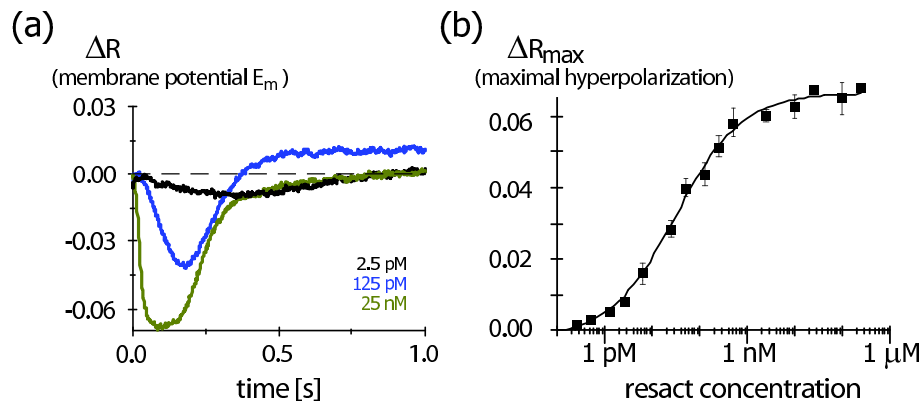
Figure A.1: Voltage response of sperm cells of the sea urchin *A. punctulata* after stimulation with the chemoattractant resact in a stopped-flow setup. The membrane potential is measured indirectly by detecting a shift in the emission spectrum of a voltage-sensitive dye which has been incorporated in to the flagellar membrane before the measurement. A shift of the emission spectrum of the dye is characterized by a quantity ΔR, see [148]. (a) Shown is the time trace of the flagellar membrane potential after stimulation with different concentrations of resact: 2.5 pM (black), 125 pM (light blue), and 25 nM (olive). It can be seen, that the membrane potential quickly hyperpolarizes and subsequently relaxes back to the resting potential on a time-scale of 500 ms. Note that the fluorescence signal was collected from a whole sperm population and hence represents an averaged response. (b) Maximal hyperpolarization of the flagellar membrane as shown in panel (a) as a function of resact concentration. Interestingly, sperm cells respond to a wide range of concentrations ranging over six orders of magnitude from sub-picomolar to micromolar concentrations. Adapted from [148] with permission from Macmillan Publishing Ltd.

Experiments of these two kinds played an important role in revealing the biochemical details of the chemotactic singaling network, see section A.1.

In stopped flow experiments, it was seen that sperm cells respond with a change in flagellar membrane potential to chemoattractant concentrations as low as 625 fM, which correspond to a ratio of one chemoattractant molecule per one sperm cell [148]. A half-maximal response was found for a chemoattractant concentration of 25 pM. The time course of a membrane potential response is shown in figure A.1(a). One can see clearly the rapid hyperpolarization by the potassium efflux and the subsequent rapid depolarization by influx of sodium and calcium which even causes an overshoot of the membrane potential above the resting potential. Finally, the membrane potential relaxes to the resting potential on a timescale of seconds. The typical time scales for hyperpolarization and depolarization are in the range $100\,\mathrm{ms} - 1\,\mathrm{s}$. The maximal hyperpolarization was found to follow a saturation kinetics when the concentration of the chemoattractant stimulation was varied over 6 orders of magnitude starting from picomolar concentrations.

In single sperm experiments, the chemotactic signaling network is stimulated by either (a) a concentration gradient of chemoattractant established by diffusion from a local source (e.g. an egg, a micropipette or a localized UV-flash which uncages a caged

form of the chemoattractant), (b) a sudden homogenous increase in chemoattractant concentration (e.g. by a homogenous UV-illumination of the swimming medium which contains caged chemoattractant), or (c) by uncaging a caged form of cGMP which has been loaded into the sperm's flagellum before the experiment. (Recall that production of cGMP is the next step in the signaling cascade after binding of chemoattractant molecules to the receptors.)

In experiment (a), sperm cells were observed to swim along drifting circles. Form their swimming path, the temporal concentration stimulus $s(t)$ traced from the concentration field of chemoattractant $c(\mathbf{x})$ can be reconstructed. Due to the circular swimming of the sperm cells, the temporal stimulus $s(t)$ includes a periodic component with the frequency ω_0 of circular swimming. Both calcium signal $[\text{Ca}^{2+}]_i$ and curvature of the swimming path showed oscillations with the same frequency and were phase-locked with a characteristic phase shift to the temporal stimulus [22], see also figure 1.7 on page 11 in the introduction.

In experiments (b) and (c), a train of calcium spikes and of curvature spikes was elicited upon stimulation. Calcium and curvature spikes were strongly correlated. The mean inter-spike-interval (mISI) roughly matched the period of circular swimming ω_0.

From a theoretical point of view, one may regard the chemotactic signaling system as a signal transducer that can be viewed independent of its biochemical hardware and is fully characterized by its input-output characteristics. From this point of view, it will be interesting to specify the response of this signaling system to (a) periodic inputs, (b) step inputs, and (c) pulse inputs. These ideal input characteristics are approximately addressed by the respective experiments (a), (b) and (c) mentioned above.

The experiment of choice to investigate the input-output relationship of chemotactic signaling would be to place a sperm cell into a flow chamber with the position of the sperm head fixed and stimulate the sperm cell with well-defined temporal stimuli of chemoattractant while recording its chemotactic response.

A.3 Adaptation in chemotactic signaling

The chemotactic signaling system of sperm cells operates for chemotactic stimuli whose strength varies over several orders of magnitude from picomolar to micromolar concentration [148], see figure A.1(b). It has been even suggested that sperm cells can respond to single chemoattractant molecules [77]. With such an extreme sensitivity, the signaling system should contain some component which prevents it from becoming saturated already for weak stimuli. We expect that the signaling system incorporates an adapation mechanism. We speculate that this adaptation mechanism is (at least partly) located upstream of the electro-physiological signal cascade, since this part of the signaling system is especially vulnerable of becoming saturated: If hyperpolarization of the membrane potential is mainly driven by an efflux of potassium ions, the membrane potential can not fall below the potassium reversal potential. Most likely, the negative

cooperativity of the chemoattractant binding kinetics to the receptors plays some role in adaptation, see section A.6.1. Additionally, chemotactic signaling could adjust the level of cAMP which regulates the opening of the HCN channels [79].

A.4   Excitablity and oscillations in chemotactic signaling

The chemotactic signaling system of sea urchin sperm cells displays characteristics both of an

- excitable system, as well as of an

- relaxation oscillator.

A brief stimulation of sperm cells either with resact of with the second messenger cGMP elicits a characteristic pulse of the flagellar membrane potential with a hyperpolarization and subsequent depolarization on a time-scale of 500 ms, see figure A.1(a). The voltage response is correlated with a temporary rise of the intra-flagellar calcium concentration. Such a pronounced transient response after a brief stimulation is typical for an excitable system. For a sufficiently strong stimulation a whole train of calcium responses could be observed in single sperm experiments. The inter-spike-interval roughly matches the period of circular swimming. For a whole sperm population, both the calcium concentration as well as the membrane potential displayed a train of several pulses after a strong stimulation. The amplitude of the spikes was decreasing with time. It is not clear whether the observed decrease in amplitude is primarily due to an acutal decrease of the spike amplitude in the individual sperm cells or whether a detuning of the oscillatory responses of the different sperm cells in the sperm population is the cause. In a particular experiment, sustained oscillations have been observed after a strong stimulation [162].

A signal transducer which is itself an oscillator will act as a band-pass filter and is well suited to detect and amplify an oscillatory signal with a frequency that matches the eigenfrequency of the transducer. We speculate that the "eigenfrequency" of the sea urchin sperm chemotactic signaling system is tuned for the frequency of circular and helical swimming. In this context, it is interesting to quote the signaling system of *Chlamydomonas*. This unicelluar algae swims by a breast-stroke like beat pattern of its two flagellar and is phototactic, i.e. actively steers towards sources of light [74,132]. Apparently, its phototactic mechanism is very similar to the chemotaxis of sperm cells along helical swimming paths [36]: While swimming forward, the cell body rotates around its axis with a frequency of about 2 Hz. If a light source is present, a light-sensitive cell organelle of *Chlamydomonas* receives a periodic light stimulus due to the cell rotation — at least as long as the swimming direction does not point already towards the light source. A phototactic signaling system transduces this periodic stimulation into a swimming response with an increased asymmetry between the beat patterns of the two flagella which causes a change of the swimming direction. In an intriguing

experiment, a clamped *Chlamydomonas* was exposed to periodic light stimuli of varying frequency and the strength of the flagellar phototactic response was recorded [166]. Interestingly, the amplitude of the flagellar response was maximal exactly at the frequency of body rotation. Thus at least in *Chlamydomonas*, the phototactic signaling system acts as a band-pass filter and is tuned to the stimulus frequency which occurs during real phototaxis.

A.5 Electrophysiology for pedestrians

Cell function requires specific concentrations of various kinds of ions in the cell plasma. The cell membrane enclosing the cell plasma has a small conductance for ions, hence the intracellular ion concentrations have to be maintained actively. This is done by the cell via ion pumps and ion exchangers which use chemical energy in the form of ATP to establish a concentration difference between intracellular and extracellular concentrations. The activity of these ion pumps does not result in a net charge of the cell: As Coulomb forces between two charges scale with the square of their distance, space charge neutrality must hold on a mesoscopic scale. The electrical current carried by the flux of specific ions through selective ion pumps is counterbalanced by a leak current carried by all sorts of ions through the cell membrane. Nevertheless, different concentrations of ions inside and outside the cell result in charge accumulation on a microscopic scale in the vicinity of the membrane which acts as a capacitor. As a consequence, we find a drop of electrical potential E_m across the membrane, the membrane potential. At equilibrium, the membrane potential E_m is given by the Nernst equation in the case of a single kind of (monovalent, positively charged) ions

$$E_m = \frac{k_B T}{e} \ln \frac{c_{\text{out}}}{c_{\text{in}}}. \tag{A.1}$$

Here c_{in} and c_{out} are the concentrations of the ions inside and outside of the cell, respectively. This equilibrium membrane potential is characterized by the balance of two thermodynamic forces

  – an entropic force $k_B T \Delta\mu$ proportional to the difference in chemical potential

$$\Delta\mu = \ln \frac{c_{\text{in}}}{c_{\text{out}}}, \tag{A.2}$$

  – and an electromotive force $-eE_m$ proportional to interior potential relative to the outside.

The Goldman-Hodgkin-Katz equation generalizes to the case of several kinds of ions. If only monovalent ions are present, say cations X_i^+ and anions X_j^-, the steady-state

membrane potential reads

$$E_m = \frac{k_B T}{e} \ln \frac{\sum_i p_{X_i^+}[X_i^+]_{\text{in}} + \sum_j p_{X_j^-}[X_j^-]_{\text{out}}}{\sum_i p_{X_i^+}[X_i^+]_{\text{out}} + \sum_j p_{X_j^-}[X_j^-]_{\text{in}}}. \tag{A.3}$$

Here p_X are membrane permabilities defined as the diffusion constant of the ion divided by the thickness of the membrane and $[X]_{\text{in}}$, $[X]_{\text{out}}$ are the concentrations of ion species X inside and outside the cell, respectively. This equation can be generalized to the case of monovalent ions, see [68].

Note that while the Nernst equation (A.1) describes true thermodynamic equilibrium, the Goldman-Hodgkin-Katz (A.3) equation is a mere steady state of the membrane potential characterized by non-zero ion fluxes. In particular, detailed balance does not hold in the case of several ion species.

The membrane potential E_m is changed by a net current I of ions

$$C_m \dot{E}_m = I, \tag{A.4}$$

where C_m is the capactitance of the membrane. The current I_X carried by ion species X is proportional to the difference between membrane potential E_m and the Nernst potential E_X of this ion

$$I_X = -g_X(E_m - E_X), \tag{A.5}$$

where g_X is the conductance of the membrane for ion X with units of $\text{Si} = \text{A/V}$.

While most cells maintain a stable resting membrane potential, specialized cells such as neurons and apparently sperm cells can rapidly change their membrane potential. The opening and closing of selective ion channels in the membrane change the membrane's permability for these ions resulting in a change of the membrane potential. These ion channels are gated by specific ligands or by voltage. This gives rise to feedback mechanisms which allow these cells to do information processing.

A.6 Physical aspects of chemotactic signaling

A.6.1 Irreversible binding of chemoattractant molecules by 'single-use sperm'

It has been suggested that flagellar receptors bind chemoattractant molecules irreversbily if chemoattractant concentration is sub-picomolar. A sperm cell approaching an egg will first experience such low concentrations and irreversible binding of the chemoattractant may serve to make most of the signal. Note that receptors cannot be internalized and recycled due to the limited metabolism of sperm cells; thus receptors are used up with time. However, a reduction in the number of free receptors does not yet decrease the diffusive flux to the receptors unless their number is decreased below

a critical value $N^* = L/r_r$ which is set by the length L of the flagellar receptor array and the size r_r of the binding site of an individual receptor [16], see appendix H. With $r_r = 10 \, \text{Å}$, we estimate $N^* = 5 \cdot 10^4$ which is much less than the total number of receptors $N = 10^6$ [78]. Once the sperm cell has come closer to the egg, chemoattractant concentration can rise to values in the nanomolar range: If all receptors would bind chemoattractant molecules irreversibly, all receptors would be occupied in short time and the sperm cells would loose its chemotactic sensivity. This, however, is not the case: There is evidence that chemoattractant receptors form trimers that exhibit a strong negative cooperativity in binding chemoattractant [78]. Thus in the case of high ambient chemoattractant concentrations, binding of chemoattractant is probably described by a different dynamic regime. Let us be more precise: For simplicity, we consider the case of N receptor dimers with N_j being the number of dimers having exactly j chemoattractant molecules bound. The total diffusive current to the receptors is not linear in the number of free dimers N_0 since the receptors interferre with each other; thus the diffusive current q is rather described by a saturating function $q = q_0 N_0/(N^* + N_0)$, see appendix H. Hence, we can formulate the following rate equations

$$
\begin{aligned}
\dot{N_0} &= -\lambda_1\, c\, \tfrac{N_0}{N^*+N_0}, & & \\
\dot{N_1} &= \lambda_1\, c\, \tfrac{N_0}{N^*+N_0} & -\lambda_2\, c\, \tfrac{N_1}{N^*+N_1} & +k_2\, N_2, \\
\dot{N_2} &= & \lambda_2\, c\, \tfrac{N_1}{N^*+N_1} & -k_2\, N_2,
\end{aligned}
\tag{A.6}
$$

where c is chemoattractant concentration.[17] A virgin sperm with $N_0(0) = N$ at $t = 0$ will experience a constant rate of receptor activation $\dot{N_1} + \dot{N_2} \approx \lambda_1 c$ for a time $t \ll N/(\lambda_1 c)$ provided $N \gg N^*$. In particular, the system (A.6) is not in steady-state. After this transient period, every dimer will have its first chemoattractant molecule bound, $N_1 \approx N$, and the system will be in steady state with $2N_2 = N + N^* + K - \sqrt{(N - N^* - K)^2 + 4NN^*}$ where $K = \lambda_2 c/k_2$. We can illustrate the dependence of the receptor occupancy N_2 on normalized concentration K by considering two limit cases: We have $N_2 = \min\{N, K\}$ for $N^* \ll N$ and $N_2 = NK/(N^* + K)$ for $N^* \gg N$. Both the transient phase and the steady-state phase might be physiologically relevant and correspond to a sperm cells operating in low and high chemoattractant concentration. We postulate that a sperm cell which has been exposed to a high chemoattractant concentration will loose its ability to detect single molecules if the concentration is lowered again, since every receptor trimer will keep at least one chemoattractant molecule bound and thus has a reduced affinity for binding further molecules. This assertion could be tested in experiments. It would be not surprising if sperm cells were indeed designed for single-use since they are dedicated only for a single purpose: to find the egg.

---

[17]Note that unbinding of chemoattractant molecules from the receptors will locally increase concentration c by an amount on the order of $k_2 N_2/(DL)$ where D is the diffusion constant of the chemoattractant and L the length of the flagellum. However, we will not consider this effect.

A.6.2   Is the chemotactic signaling system a relaxation oscillator?

Motivated by the experiements discussed in section A.4, we expect that the chemotactic signaling system behaves like an oscillator with eigenfrequency close to the frequency ω_0 of circular swimming

$$\ddot{a} + \zeta\,\dot{a} + \omega_0^2\,a = s. \tag{A.7}$$

Here s is the time-dependent stimulus and a is the output variable. A small, positive value of the damping constant ζ will account for strong signal amplification. At $\zeta = 0$ the signaling system undergoes a Hopf bifurcation and oscillates spontaneously for $\zeta < 0$. In general, the damping constant ζ could be function of the stimulus. Using

$$\zeta = (s_c - s)\,(1 - a^2) \tag{A.8}$$

turns (A.7) into the Van-der Pol oscillator, a special case of the familar FitzHugh-Nagumo model used to describe the voltage dynamics of neurons. A periodic stimulus $s = s_0 + s_1 \cos\omega_0 t$ with $s_1 \ll s_0$ can evoke pronounced phase-locked oscillations of a provided the average stimulus level s_0 is close to the critical value s_c. It is possible, that a slow adaptation dynamics tunes s_c accordingly [28].

Appendix B

Linear response function of the curvature

In our theoretical description of sperm chemotaxis from chapter 3, a chemotactic stimulus $s(t)$ is processed a chemotactic signaling system (3.4) whose output modulates the curvature κ of the sperm swimming path. For a time-independent stimulus $s(t) = s_0$, curvature is constant $\kappa(t) = \kappa_0$. The response of the curvature to small variations of the stimulus is characterized by a linear (frequency-domain) response function $\widetilde{\chi}_\kappa(\omega)$: A small periodic variation of the stimulus

$$s(t) = s_0 + s_1 \mathrm{Re}\, e^{i\omega t} \tag{B.1}$$

will evoke curvature oscillations

$$\kappa(t) = \kappa_0 + s_1 \mathrm{Re}\, \widetilde{\chi}_\kappa(\omega) e^{i\omega t} + \mathcal{O}(s_1^2) \tag{B.2}$$

with amplitude gain $|\widetilde{\chi}_\kappa(\omega)|$ and phase shift $\arg \widetilde{\chi}_\kappa(\omega)$. Of particular importance for us is the response coefficient $\widetilde{\chi}_\kappa(\omega_0) = \rho_\kappa e^{i\varphi_\kappa}$ at the frequency of circular swimming ω_0. Below we find that the amplitude gain $\rho_\kappa = |\widetilde{\chi}_\kappa(\omega_0)|$ is concentration dependent; we can write $\rho_\kappa = \overline{\rho}_\kappa/(s_b + s_0)$ with a constant $\overline{\rho}_\kappa$ that represents an amplification strength of the chemotactic signaling system. The response to arbitrary variations of the stimulus $s(t) + s_0 + s_1(t)$ is given to first order by the time-domain response function $\chi_\kappa(t)$

$$\kappa(t_0) = \kappa_0 + \int_{-\infty}^{\infty} dt\, \chi_\kappa(t)\, s_1(t_0 - t) + \mathcal{O}(s_1^2) \tag{B.3}$$

Equation (B.3) is the leading order term of a Volterra expansion of $\kappa(t)$. The time-domain response function $\chi_\kappa(t)$ is simply the inverse Fourier transform of $\widetilde{\chi}_\kappa(\omega)$. Causality implies $\chi_\kappa(t) = 0$ for $t < 0$. Alternative names for the frequency-domain linear response function include susceptibility and impedance; the time-domain linear response function is also called Green's function or fundamental solution. For the signaling system given in equations (3.3-3.4), the linear response function $\widetilde{\chi}_\kappa$ of the curvature is easily found as follows: Linearizing (3.4) around the fixed point $a_0 = 1$, $p_0 = 1/(s_b + s_0)$ yields $\sigma \dot{a}_1 = p_0 s_1 + p_1(s_b + s_0) - a_1$ and $\mu \dot{p}_1 = -a_1$ where $a = a_0 + a_1$, $p = p_0 + p_1$. By taking the Fourier transform and solving for $\widetilde{a}_1$, we obtain a linear relation

$$\kappa_1 \widetilde{a}_1(\omega) = \widetilde{\chi}_\kappa(\omega)\, \widetilde{s}_1(\omega) \tag{B.4}$$

with

$$\widetilde{\chi}_\kappa(\omega) = \frac{\kappa_1}{s_b + s_0} \frac{i\omega\mu}{1 + i\omega\mu - \sigma\mu\omega^2}.$$ (B.5)

The left-hand side of eqauation (B.4) is nothing but the Fourier transform of the curvature response $\kappa(t) - \kappa_0$; hence the factor of proportionality $\widetilde{\chi}_\kappa(\omega)$ is the sought-for response function. Note that $\widetilde{\chi}_\kappa$ is proportional to the linear response function of a damped harmonic oscillator with eigenfrequency $(\sigma\mu)^{-1/2}$ and damping time σ. The inverse Fourier transform $\chi_\kappa(t)$ of $\widetilde{\chi}_\kappa(\omega)$ reads

$$\chi_\kappa(t) = \frac{\kappa_1}{s_b + s_0} \frac{\lambda_1 e^{-\lambda_1 t} - \lambda_2 e^{-\lambda_2 t}}{\sigma(\lambda_1 - \lambda_2)} \theta(t),$$ (B.6)

where $\lambda_{1,2}$ are the roots of $0 = \sigma\mu\lambda^2 - \mu\lambda + 1$, i.e. $2\sigma\lambda_{1,2} = (1 \pm \sqrt{1 - 4\sigma/\mu})$. In the underdamped case $4\sigma > \mu$, we have $\mathrm{Re}\,\lambda_{1,2} = 1/(2\sigma)$.

Appendix C
Radial concentration fields in three dimensions

C.1 Effective equation of motion

In a radial concentration field $c(\mathbf{x}) = C(|\mathbf{x}|)$, we can simplify the effective equation of motion (3.25) of helical sperm swimming paths by exploiting rotational symmetry. We can express the centerline position $\mathbf{R}$ and the helix vector $\mathbf{h}_3$ by five parameters, the distance to the origin $R = |\mathbf{R}|$, the angle ψ between the helix vector $\mathbf{h}_3$ vector and the radial direction of the gradient $\boldsymbol{\nabla}c$, as well as three Euler angles θ, ξ, η, as

$$
\begin{aligned}
\mathbf{R} &= R\,\mathbf{e}_R \\
\mathbf{h}_3 &= -\cos\psi\,\mathbf{e}_R - \sin\psi\,(\cos\eta\,\mathbf{e}_\theta + \sin\eta\,\mathbf{e}_\xi)
\end{aligned}
\tag{C.1}
$$

where

$$
\begin{aligned}
\mathbf{e}_R &= (\cos\theta, \sin\theta\cos\xi, \sin\theta\sin\xi) \\
\mathbf{e}_\theta &= (-\sin\theta, \cos\theta\cos\xi, \cos\theta\sin\xi) \\
\mathbf{e}_\xi &= (0, -\sin\xi, \cos\xi)
\end{aligned}
\tag{C.2}
$$

The vectors $\mathbf{e}_R$, $\mathbf{e}_\theta$, $\mathbf{e}_\xi$ represent a moving frame and obey the dynamic equations

$$
\begin{aligned}
\dot{\mathbf{e}}_R &= \dot\theta\mathbf{e}_\theta + \sin\theta\dot\xi\mathbf{e}_\xi, \\
\dot{\mathbf{e}}_\theta &= -\dot\theta\mathbf{e}_R + \cos\theta\dot\xi\mathbf{e}_\xi, \\
\dot{\mathbf{e}}_\xi &= -\sin\theta\dot\xi\mathbf{e}_R - \cos\theta\dot\xi\mathbf{e}_\theta.
\end{aligned}
\tag{C.3}
$$

From equation (C.1), we find for the following scalar products

$$
\begin{aligned}
\dot{\mathbf{R}}\cdot\mathbf{e}_R &= \dot R, \\
\dot{\mathbf{R}}\cdot\mathbf{e}_\theta &= R\dot\theta, \\
\dot{\mathbf{R}}\cdot\mathbf{e}_\xi &= R\sin\theta\,\dot\xi, \\
\dot{\mathbf{h}}_3\cdot\mathbf{e}_R &= \sin\psi\left(\dot\psi + \cos\eta\,\dot\theta + \sin\eta\sin\theta\,\dot\xi\right), \\
\dot{\mathbf{h}}_3\cdot\mathbf{e}_\theta &= -\cos\psi\,(\cos\eta\dot\psi + \dot\theta) + \sin\psi\sin\eta\,(\dot\eta + \cos\theta\dot\xi).
\end{aligned}
\tag{C.4}
$$

Using equation (3.25), we can express these scalar products alternatively as

$$
\begin{aligned}
\dot{\mathbf{R}} \cdot \mathbf{e}_R &= -\omega h \cos\psi - \gamma \sin^2\psi, \\
\dot{\mathbf{R}} \cdot \mathbf{e}_\theta &= -\omega h \sin\psi \cos\eta + \gamma \sin\psi \cos\psi \cos\eta + \gamma' \sin\psi \sin\eta, \\
\dot{\mathbf{R}} \cdot \mathbf{e}_\xi &= -\omega h \sin\psi \sin\eta + \gamma \sin\psi \cos\psi \sin\eta - \gamma' \sin\psi \cos\eta, \\
\dot{\mathbf{h}}_3 \cdot \mathbf{e}_R &= -\beta \sin^2\psi, \\
\dot{\mathbf{h}}_3 \cdot \mathbf{e}_\theta &= \beta \sin\psi \cos\psi \cos\eta + \beta' \sin\psi \sin\eta
\end{aligned}
\tag{C.5}
$$

where $\beta - i\beta' = |\boldsymbol{\nabla}c|(\varepsilon_\tau\chi_\tau - \varepsilon_\kappa\chi_\kappa)$, and $\gamma' + i\gamma = |\boldsymbol{\nabla}c|(\delta_\tau\chi_\tau - \delta_\kappa\chi_\kappa)$. We can now solve for $\dot{R}$, $\dot{\psi}$, $\dot{\theta}$, $\dot{\xi}$, $\dot{\eta}$ and find

$$
\begin{aligned}
\dot{R} &= -\Lambda\cos\psi - \gamma \\
\dot{\psi} &= -\sin\psi\left(\beta - \frac{\Lambda}{R}\right) \\
\dot{\theta} &= -\frac{\sin\psi}{R}\left(\gamma'\sin\eta + \Lambda\cos\eta\right) \\
\dot{\xi} &= -\frac{\sin\psi}{R\sin\theta}\left(\gamma'\cos\eta - \Lambda\sin\eta\right) \\
\dot{\eta} &= -\beta' - \gamma'\frac{\cos\psi}{R} - \frac{\cot\theta\sin\psi}{R}\left(\gamma'\cos\eta - \Lambda\sin\eta\right)
\end{aligned}
\tag{C.6}
$$

where $\Lambda = \omega h - \gamma\cos\psi$. From this we obtain equation (3.30) with $\dot{R}$, $\dot{\psi}$ independent of θ, ξ, η.

C.2   Linear stability of fixed points

In section 3.2.4, we discuss the dynamical system (3.30) which provides an effective equation of motion for sperm swimming paths in a radial concentration field. There, we assume that the alignment coefficient β and the tilt coefficient γ scale inversely with distance R from the origin

$$
\beta = \frac{B_0}{R}, \quad \gamma = \frac{\Gamma_0}{R}.
\tag{C.7}
$$

Depending on the values of B_0 and Γ_0, this system (3.30) can possess a fixed point (ψ_0, R_0). In this section, we discuss the linear stability of this fixed point.

For $B_0 > \omega_0 h_0$ (which corresponds to regime **A** and **B** in section 3.2.4), the dynamical system (3.30) possesses a unique fixed point (ψ_0, R_0) with

$$
R_0 = \frac{|\Gamma_0|}{\sqrt{(B_0 - \omega_0 h_0)B_0}}, \quad \cos\psi_0 = -\frac{\Gamma_0}{B_0 R_0}.
\tag{C.8}
$$

Linearizing the dynamical system (3.30) around the fixed point (ψ_0, R_0) yields

$$
\frac{d}{dt}\begin{pmatrix} \delta\psi \\ \delta R \end{pmatrix} = \Lambda \begin{pmatrix} \delta\psi \\ \delta R \end{pmatrix},
\tag{C.9}
$$

where

$$\Lambda = \sin\psi_0 \frac{\Gamma_0}{R} \begin{pmatrix} \sin\psi_0/R_0 & \cos\psi_0/R_0^2 \\ -2\cos\psi_0 & \sin\psi_0/R_0 \end{pmatrix}. \tag{C.10}$$

We find

$$\begin{aligned} \operatorname{tr}\Lambda &= 2\sin^2\psi_0\,\Gamma_0/R_0^2, \\ \det\Lambda &= 2\sin^2\psi_0\,\Gamma_0^2/R_0^4 \end{aligned} \tag{C.11}$$

and conclude that the fixed point (ψ_0, R_0) is repulsive in regime **A** with $B_0 > \omega_0 h_0$, $\Gamma_0 > 0$ and and attractive in regime **B** with $B_0 > \omega_0 h_0$, $\Gamma_0 < 0$.

C.3 Criterion for chemotactic success: A second scenario

We analyze under what conditions swimming paths find an egg of radius R_{egg} at the origin by discussing phase space trajectories of the dynamical system (3.30). In general, the alignment rate β and the tilt rate γ depend on the distance R to the target; we discuss the scenario of constant β and γ

$$\beta = \beta_0, \quad \gamma = \gamma_0. \tag{C.12}$$

This scenario corresponds to a situation with

(i) a concentration field of the form $c(\mathbf{x}) \sim \exp(-\lambda|\mathbf{x}|)$, see equation (3.37), where the relative strength of the gradient is constant $|\boldsymbol{\nabla} c|/c = \lambda$, and

(ii) linear response coefficients $\widetilde{\chi}_\kappa$ and $\widetilde{\chi}_\tau$ which scale inversely with local concentration.

Such a concentration field corresponds to the steady state concentration field established by diffusion from a single chemoattractant source with constant chemoattractant release rate if chemoattractant is degraded at a constant rate k_{deg}; in this case $\lambda^2 = k_{\text{deg}}/D$, where D is the diffusion constant. The second condition on the response coefficients is met for the particular signaling system given by equation (3.4), if $s_b = 0$, see equation (3.5). We restrict ourselves to the case $|\gamma_0| < \omega_0 h_0$ relevant to our perturbation calculation in ν by which (3.30) was derived.

Depending on the two parameters β_0 and γ_0, the flow of the dynamical system can exhibit three different regimes:

– regime **A** for $\beta_0 > 0$, $\gamma_0 > 0$,

– regime **B** for $\beta_0 > 0$, $\gamma_0 < 0$, and

– regime **C** for $\beta_0 < 0$,

see figure C.1. In regime **A** and **B** with $\beta_0 > 0$, there exists a fixed point (R_0, ψ_0) where

$$\cos \psi_0 = \frac{\omega_0 h_0 - \sqrt{(\omega_0 h_0)^2 - 4\gamma_0^2}}{2\gamma_0} \tag{C.13}$$

and

$$R_0 = \frac{\omega_0 h_0 - \gamma_0 \cos \psi_0}{\beta_0}. \tag{C.14}$$

This fixed point correspond to swimming paths for which the centerline circles around the origin and R is constant. A linear stability analysis reveals that for regime **A**, these fixed points are repulsive while for regime **B** they are attractive: Linearizing the dynamical system (3.30) around the fixed point (ψ_0, R_0) yields

$$\frac{d}{dt}\begin{pmatrix} \delta\psi \\ \delta R \end{pmatrix} = \Lambda \begin{pmatrix} \delta\psi \\ \delta R \end{pmatrix}, \tag{C.15}$$

where

$$\Lambda = \sin\psi_0 \begin{pmatrix} \gamma_0 \sin\psi_0/R_0 & -\beta_0/R_0 \\ \beta_0 R_0 - \gamma_0 \cos\psi_0 & 0 \end{pmatrix}. \tag{C.16}$$

We find

$$\begin{aligned} \mathrm{tr}\,\Lambda &= \gamma_0 \sin^2\psi_0/R_0, \\ \det\Lambda &= \beta_0^2 \sin^4\psi_0 \end{aligned} \tag{C.17}$$

and conclude that the fixed point (ψ_0, R_0) is repulsive in regime **A** with $B_0 > \omega_0 h_0$, $\Gamma_0 > 0$ and and attractive in regime **B** with $B_0 > \omega_0 h_0$, $\Gamma_0 < 0$. The flow field around the fixed point (ψ_0, R_0) is illustrated in figure C.1. In both regimes (ψ, R)-trajectories of the dynamical system are spirals near the fixed points which correspond to swimming paths that repeatedly

  (i) align with the gradient vector,

 (ii) approach the origin,

(iii) loose alignment when they come near the origin, and

(iv) move away again.

As a consequence, distance R subsequently decreases and increases, with an increasing amplitude of R-changes in regime **A** and a decreasing amplitude in regime **B**. For regime **C** with $\beta_0 < 0$, no fixed points exist, the trajectories are U-shaped and move toward large R at long times, see figure C.1(c).

In the presence of an egg with radius R_{egg}, the centerline of swimming paths reaches the egg for almost all initial conditions in regime **A**, see figure C.2(a). For regime **B**, (R, ψ)-trajectories starting in a finite neighborhood of the fixed points (R_0, ψ_0) correspond to swimming paths that do not reach the egg. Further away from this neighborhood, trajectories can reach the egg before they spiral to the fixed point, see

figure C.2(b). In regime **C** swimming paths are repelled from the egg and chemotaxis acts down the gradient, see figure C.2(c). Therefore, we find again that chemotaxis is a robust property that does not require fine-tuning of parameters. It is most reliably in case **A** for which a sufficient condition is given by

$$\pi < \phi_\kappa < 3\pi/2, \quad 0 < \phi_\tau < \pi/2. \tag{C.18}$$
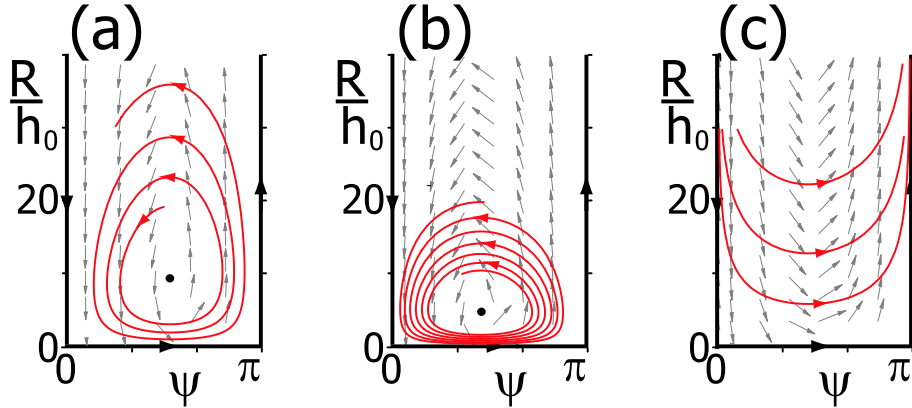
Figure C.1: Flow field and typical trajectories in the (R, ψ)-phase space for the dynamic system given by equation (3.30) which describes chemotaxis in three dimensions in a radial concentration field for $\beta = \beta_0$ and $\gamma = \gamma_0$ (scenario I). Here R is the distance of the centerline to the chemoattractant source and ψ the angle between the helix vector and the gradient direction. Distance R is shown relative to h_0 where $2\pi h_0$ is the pitch of the unperturbed helix. The three panels (a), (b), and (c) are examples for the three regimes **A**, **B**, and **C**, respectively, see text for details. Typical (R, ψ)-trajectories (red lines) as well as the gradient vector field (gray arrows) are shown. (a) In regime **A**, the system possesses a repulsive fixed point (black dot). The (R, ψ)-trajectories are spirals which spiral away from the fixed point. (b) In regime **B**, the fixed point is attractive and (R, ψ)-trajectories spiral toward the fixed point. (c) In regime **C**, no fixed points exist, the (R, ψ)-trajectories are U-shaped and eventually move away from the chemoattractant source. The parameter values used were (a) $\beta_0 = 0.1\,\omega_0$, $\gamma_0 = 0.1\,\omega_0 h_0$, (b) $\beta_0 = 0.2\,\omega_0$, $\gamma_0 = -0.05\,\omega_0 h_0$, (c) $\beta_0 = -0.1\,\omega_0$, $\gamma_0 = -0.1\,\omega_0 h_0$.
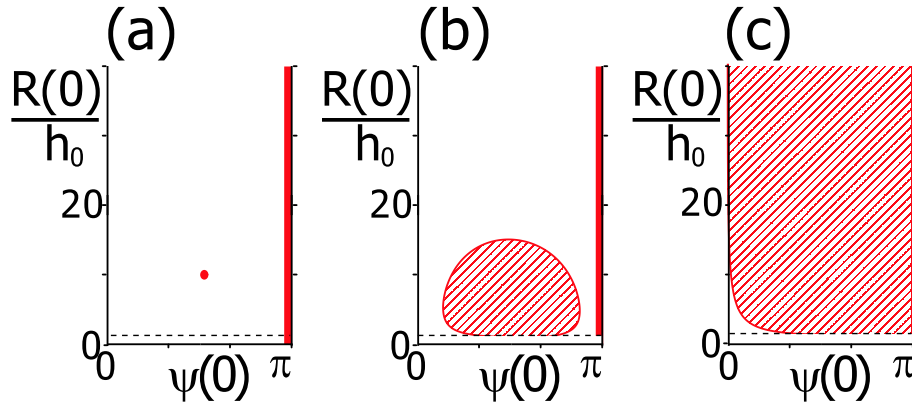
Figure C.2: Chemotactic success as a function of initial conditions of swimming paths according to the dynamic system given by equation (3.30) for $\beta = \beta_0$ and $\gamma = \gamma_0$ constant (scenario I). The initial condition of a path is characterized by the initial distance $R(0)$ of the centerline to the chemoattractant source and the initial angle $\psi(0)$ between the helix axis and the gradient direction. Distance R is shown relative to h_0 where $2\pi h_0$ is the pitch of the unperturbed helix. For a given initial condition, chemotaxis is unsuccessful if the correspondent swimming path has a distance $R(t)$ to the chemoattractant source which is always greater than an egg radius R_{egg}, $R(t) > R_{egg}$. Initial conditions with unsuccessful chemotaxis are shown as red dots, red lines and red hatched regions. The radius of the egg R_{egg} is indicated by a dashed line. The three panels (a), (b), and (c) are examples for the three regimes **A**, **B**, and **C**, respectively, see text for details. (a) In regime **A**, where a repulsive fixed point exists, chemotaxis is robust and fails only at the fixed point and the marginal case $\psi(0) = \pi$, see figure C.1(a). (b) In regime **B**, the fixed point is attractive, see figure C.1(b). Chemotaxis is successful in a large range of initial conditions and fails only in a neighborhood of the fixed point as well as in the marginal case $\psi(0) = \pi$. (c) In regime **C**, no fixed points exist and chemotaxis is repulsive with respect to the chemoattractant source, see figure C.1(c). Chemotaxis is unsuccessful except for those initial conditions where the initial distance to the source is already small and the helix axis is nearly aligned with the gradient direction. The parameter values used were $R_{egg} = h_0$ and (a) $\beta_0 = 0.1\,\omega_0$, $\gamma_0 = 0.1\,\omega_0 h_0$, (b) $\beta_0 = 0.2\,\omega_0$, $\gamma_0 = -0.05\,\omega_0 h_0$, (c) $\beta_0 = -0.1\,\omega_0$, $\gamma_0 = -0.1\,\omega_0 h_0$.

Appendix D
Rigid body transformations

Rigid body transformations are a versatile mathematical tool to relate different coordinate systems. Below, we give a review of their theory, see also [13,14,103].

Homogeneous coordinates. A Cartesian coordinate system $\mathcal{L} = (\mathbf{l}_1, \mathbf{l}_2, \mathbf{l}_3, \mathbf{o})$ of three-dimensional affine space $\mathbb{A}^3$ consists of a choice of origin $\mathbf{o} \in \mathbb{A}^3$ and a right-handed orthonormal set of vectors $\mathbf{l}_j \in T\mathbb{A}^3$, $j = 1, 2, 3$. Note the difference between a genuine point $\mathbf{p} \in \mathbb{A}^3$ denoting a position in space and a vector $\mathbf{v} \in T\mathbb{A}^3$ which merely denotes a direction. It is convenient to represent a point $\mathbf{p}$ of three-dimensional space with respect to a reference frame $\mathcal{L}$ as a 4-tuple

$$^{\mathcal{L}}\mathbf{p} = (^{\mathcal{L}}\mathbf{p}_1, {}^{\mathcal{L}}\mathbf{p}_2, {}^{\mathcal{L}}\mathbf{p}_3, 1)^{\mathrm{T}}, \tag{D.1}$$

where $^{\mathcal{L}}\mathbf{p}_j = (\mathbf{p} - \mathbf{o}) \cdot \mathbf{l}_j$, $j = 1, 2, 3$. For a direction vector $\mathbf{v} \in T\mathbb{A}^3$, we set

$$^{\mathcal{L}}\mathbf{v} = (^{\mathcal{L}}\mathbf{v}_1, {}^{\mathcal{L}}\mathbf{v}_2, {}^{\mathcal{L}}\mathbf{v}_3, 0)^{\mathrm{T}}$$

with fourth entry zero, were $^{\mathcal{L}}\mathbf{v}_j = \mathbf{v} \cdot \mathbf{l}_j$, $j = 1, 2, 3$. Note that the coordinates of a point have the unit of a length; whereas the coordinates of a direction vector are dimensionless. This 4-tuple representation of points and vectors is called homogeneous coordinates.

Rigid body transformations. Rigid body transformations are exactly the special Euclidean transformations $\mathrm{SE}(3)$ of three-dimensional space. These transformations preserve the standard metric as well as handedness. They can be described as the composition of a rotation and a translation. Using homogeneous coordinates, we can represent the action of a rigid body transformation $\mathcal{G}$ on a geometric object $\mathbf{q}$ (either a point or a vector) as a simple matrix multiplication on the coordinate level

$$^{\mathcal{L}}(\mathcal{G} \circ \mathbf{q}) = {}^{\mathcal{L}}\mathcal{G} \cdot {}^{\mathcal{L}}\mathbf{q}, \tag{D.2}$$

where $^{\mathcal{L}}\mathcal{G} \in \mathrm{SE}(3)$ is a rigid body transformation matrix with block structure

$$^{\mathcal{L}}\mathcal{G} = \begin{bmatrix} \mathrm{W} & \mathrm{V} \\ 0 & 1 \end{bmatrix} \tag{D.3}$$

with a rotation matrix $\mathrm{W} \in \mathrm{SO}(3)$ and a translation vector $\mathrm{V} \in \mathbb{R}^3$. Upon the action of $\mathcal{G}$, points get rotated and translated while vectors only get rotated. We will use short-hand notation $^{\mathcal{L}}\mathcal{G} = (\mathrm{W}, \mathrm{V})$ as abbreviation for a block-matrix as shown in equation (D.3).

Why the name "rigid body transformations"? The position and orientation of a rigid (undeformable) body in three-dimensional space can be tracked by a moving body frame $\mathcal{X}(t)$ rigidly attached to the body. Any motion of the body is encoded in the rigid body transformation $\mathcal{G}(t)$ mapping $\mathcal{X}(0)$ onto $\mathcal{X}(t)$.

Frame matrices $^{\mathcal{L}}\mathcal{X}$. Using homogeneous coordinates, we can represent any frame $\mathcal{X} = (\mathbf{e}_1, \mathbf{e}_2, \mathbf{e}_3, \mathbf{p})$ by a frame-matrix $^{\mathcal{L}}\mathcal{X}$ which reads in block-matrix notation $^{\mathcal{L}}\mathcal{X} = [^{\mathcal{L}}\mathbf{e}_1, {}^{\mathcal{L}}\mathbf{e}_2, {}^{\mathcal{L}}\mathbf{e}_3, {}^{\mathcal{L}}\mathbf{p}]$, where $\mathcal{L}$ is a reference frame. This 4×4 matrix is in fact a rigid body transformation matrix.

Coordinate frame gymnastics. Rigid body transformation matrices can be used for various standard tasks related to coordinate frames $\mathcal{L}$, $\mathcal{X}$, $\widetilde{\mathcal{L}}$, $\widetilde{\mathcal{X}}$:

- We can represent a frame $\mathcal{X}$ with respect to a frame of reference $\mathcal{L}$ as $^{\mathcal{L}}\mathcal{X}$

- Changing the reference frame $\mathcal{L} \to \widetilde{\mathcal{L}}$ amounts to **left** multiplication with $^{\widetilde{\mathcal{L}}}\mathcal{L}$

$$^{\widetilde{\mathcal{L}}}\mathcal{X} = {}^{\widetilde{\mathcal{L}}}\mathcal{L} \cdot {}^{\mathcal{L}}\mathcal{X}. \tag{D.4}$$

- Changing the body frame $\mathcal{X} \to \widetilde{\mathcal{X}}$ amounts to **right** multiplication with $^{\mathcal{X}}\widetilde{\mathcal{X}}$

$$^{\mathcal{L}}\widetilde{\mathcal{X}} = {}^{\mathcal{L}}\mathcal{X} \cdot {}^{\mathcal{X}}\widetilde{\mathcal{X}}. \tag{D.5}$$

- The rigid body transformation $\mathcal{G}$ mapping the frame $\mathcal{X}$ on the frame $\mathcal{Y}$ reads in the reference frame $\mathcal{L}$

$$^{\mathcal{L}}\mathcal{G} = {}^{\mathcal{L}}\mathcal{Y} \cdot \left({}^{\mathcal{L}}\mathcal{X} \right)^{-1}. \tag{D.6}$$

- The composition of two rigid body transformations $\mathcal{G}_1$, $\mathcal{G}_2$ is given on the coordinate level by the product of their respective matrices

$$^{\mathcal{L}}(\mathcal{G}_2 \circ \mathcal{G}_1) = {}^{\mathcal{L}}\mathcal{G}_2 \cdot {}^{\mathcal{L}}\mathcal{G}_1. \tag{D.7}$$

Rigid body transformation matrices form a Lie group, the SE(3)**.** The rigid body transformation matrices form a six-dimensional matrix Lie group, the SE(3), with composition being matrix multiplication. The SE(3) is a semi-direct product of the group of rotations SO(3) and the group of translations $\mathbb{R}^3$.

The Lie algebra $\mathfrak{se}(3)$ of infinitesimal rigid body transformations. The Lie algebra $\mathfrak{se}(3)$ associated to the Lie group SE(3) is the tangent space of SE(3) at the identity

$$\mathfrak{se}(3) = \mathrm{T}_{\mathbb{1}}\mathrm{SE}(3). \tag{D.8}$$

Alternatively, one can identify $\mathfrak{se}(3)$ with the left-invariant vector fields of SE(3).

The six-dimensional Lie algebra $\mathfrak{se}(3)$ is spanned by the matrix basis X_j, $j = 1, \ldots, 6$,

where for $j = 1, 2, 3$

$$X_j = \begin{bmatrix} E_j & 0 \\ 0 & 0 \end{bmatrix}, \quad (E_j)_{kl} = \epsilon_{kjl}, \quad \text{and} \quad X_{j+3} = \begin{bmatrix} 0 & \mathbf{d}_j \\ 0 & 0 \end{bmatrix}, \quad (\mathbf{d}_j)_k = \delta_{kj}. \quad (D.9)$$

For $j = 1, 2, 3$, X_j generates a rotation around the axis $\mathbf{d}_j$; while X_{j+3} generates a translation along $\mathbf{d}_j$, see figure 5.7 on page 87. In the sequel, we will use the hat-notation which turns a rotation vector $\boldsymbol{\Omega} = (\Omega_1, \Omega_2, \Omega_3)^{\mathrm{T}}$ into an infinitesimal rotation matrix $\widehat{\boldsymbol{\Omega}} = \Omega_j E_j \in \mathfrak{so}(3)$, i.e. $\widehat{\Omega}_{kl} = \epsilon_{kjl}\Omega_j$. With this notation $E_j = \widehat{\mathbf{d}}_j$, $j = 1, 2, 3$.

The exponential map. For any Lie group, a neighborhood of the identity $\mathbb{1}$ can be parameterized by the associated Lie algebra via the exponential map. In our case, the exponential map is given by the matrix exponential

$$\exp : \mathfrak{se}(3) \to \mathrm{SE}(3), \quad g \mapsto G = \sum_{n=0}^{\infty} \frac{1}{n!} g^n. \quad (D.10)$$

Alternatively, we can define $G = \exp g$ as the solution $G = G(1)$ of the matrix differential equation

$$\dot{G}(t) = G(t) \cdot g, \quad G(0) = \mathbb{1}. \quad (D.11)$$

This differential equation defines $G(t)$ as the integral over the left-invariant vector field $Hg \in T_H \mathrm{SE}(3)$, $H \in \mathrm{SE}(3)$ associated to $g \in \mathfrak{se}(3) = T_{\mathbb{1}}\mathrm{SE}(3)$.

Exponential coordinates. Any $G \in \mathrm{SE}(3)$ can be written as

$$G = \exp g \quad \text{for some } g = \zeta_j X_j \in \mathfrak{se}(3). \quad (D.12)$$

We refer to the ζ_j as the exponential coordinates of G. Are these coordinates well-defined? The inverse of the exponential map, the logarithmic map $\log = \exp^{-1} : \mathrm{SE}(3) \to \mathfrak{se}(3)$, is in general multi-valued. It becomes well-defined, if we restrict ourselves to those $G = (W, V) \in \mathrm{SE}(3)$ which rotate by less than π and pick the branch of the logarithmic map, for which $g = \log G = (\widehat{\boldsymbol{\Omega}}, \mathbf{v})$ has $|\boldsymbol{\Omega}| < \pi$. The rigid body transformations G for which we cannot define the logarithmic map are exactly those which comprise a half-turn. These transformations form a subset of measure zero in $\mathrm{SE}(3)$. We cannot unambiguously define the logarithm $g = (\widehat{\boldsymbol{\Omega}}, \mathbf{v}) = \log G$ for these G, since there is no natural way to fix the sign of the rotation vector $\pm\boldsymbol{\Omega}$ of g in this case. There exists an explicit formula for the logarithmic map of the $\mathrm{SE}(3)$, the Rodrigues formula, see [13].

The adjoint map. Let $^{\mathcal{L}}\mathcal{G} = \exp{}^{\mathcal{L}}g$, $^{\mathcal{L}}g = {}^{\mathcal{L}}\zeta_j X_j$ be the representation of the rigid body transformation $\mathcal{G}$ in exponential coordinates, where $\mathcal{L}$ denotes a frame of reference. Choosing a different reference frame $\widetilde{\mathcal{L}}$ gives

$$^{\widetilde{\mathcal{L}}}\mathcal{G} = {}^{\widetilde{\mathcal{L}}}\mathcal{L} \cdot {}^{\mathcal{L}}\mathcal{G} \cdot {}^{\mathcal{L}}\widetilde{\mathcal{L}} = \exp{}^{\widetilde{\mathcal{L}}}g \quad (D.13)$$

with $^{\widetilde{\mathcal{L}}}g = {}^{\widetilde{\mathcal{L}}}\mathcal{L} \cdot {}^{\mathcal{L}}g \cdot {}^{\mathcal{L}}\widetilde{\mathcal{L}} = {}^{\widetilde{\mathcal{L}}}\zeta_j X_j$. The exponential coordinates $\widetilde{\zeta}_j = {}^{\widetilde{\mathcal{L}}}\zeta_j$ in the new

reference frame $\widetilde{\mathcal{L}}$ are related to the coordinates $\zeta_j = {}^{\mathcal{L}}\zeta_j$ in the old frame $\mathcal{L}$ by the adjoint map

$$
\begin{pmatrix} \widetilde{\zeta}_1 \\ \vdots \\ \widetilde{\zeta}_6 \end{pmatrix} = \mathrm{Ad}_{\widetilde{\mathcal{L}}\mathcal{L}} \cdot \begin{pmatrix} \zeta_1 \\ \vdots \\ \zeta_6 \end{pmatrix} = \begin{bmatrix} \mathrm{W} & 0 \\ \widehat{\mathrm{V}}\,\mathrm{W} & \mathrm{W} \end{bmatrix} \cdot \begin{pmatrix} \zeta_1 \\ \vdots \\ \zeta_6 \end{pmatrix}
\tag{D.14}
$$

where ${}^{\widetilde{\mathcal{L}}}\mathcal{L} = (\mathrm{W}, \mathrm{V})$ and $\widehat{\mathrm{V}}_{kl} = \varepsilon_{kjl}\mathrm{V}_j$.

Moving frames. A moving frame $\mathcal{X}(t)$ defines a rigid body transformation $\mathcal{G}(t)$ which maps $\mathcal{X}(0)$ onto $\mathcal{X}(t)$. The matrix $\mathrm{G}(t) = {}^{\mathcal{X}(t)}\mathcal{X}(0)$ associated to $\mathcal{G}(t)$ acts as a propagator

$$
{}^{\mathcal{L}}\mathcal{X}(t) = {}^{\mathcal{L}}\mathcal{X}(0) \cdot \mathrm{G}(t)
\tag{D.15}
$$

where $\mathcal{L}$ is an arbitrary frame of reference. We define $g(t) \in \mathfrak{se}(3)$ as $g(t) = \mathrm{G}(t)^{-1} \cdot \dot{\mathrm{G}}(t)$. The vectors $\boldsymbol{\Omega}(t)$, $\mathbf{v}(t)$ associated to $g(t) = (\widehat{\boldsymbol{\Omega}}(t), \mathbf{v}(t))$, are nothing but the instantaneous rotational velocity $\boldsymbol{\Omega}(t)$ and the instantaneous translational velocity $\mathbf{v}(t)$ of the moving frame $\mathcal{X}(t)$ expressed in this frame itself. Note that the components Ω_j of $\boldsymbol{\Omega}$ have units of an inverse time; whereas the components $\mathbf{v}_j$ of $\mathbf{v}$ have the units of length over time. From the instantaneous velocities $\boldsymbol{\Omega}(t)$, $\mathbf{v}(t)$ we can recover the rigid body transformation matrix $\mathrm{G}(t)$ by solving the differential equation (D.11): $\dot{\mathrm{G}} = \mathrm{G} \cdot g$.

Time ordered exponentials. The solution of the differential equation (D.11), i.e. $\dot{\mathrm{G}} = G\,g$, can be given as a (reverse) time ordered exponential integral

$$
\mathrm{G}(t) = \mathbf{T}\exp \int_0^t dt_0\, g(t_0) = \sum_{n=0}^{\infty} \int_{0 < t_1 < \ldots < t_n < t} dt_1 \cdots dt_n\, g(t_1) \cdots g(t_n).
\tag{D.16}
$$

For a proof, just differentiate the right-hand side of (D.16) with respect to t and extract a factor of $g(t)$. The time-ordering in (D.16) is necessary, since the infinitesimal transformations $g(t_1)$, $g(t_2)$ at different times t_1, t_2 not necessarily commute. In the special case $g(t) = g_0$ constant, the time-ordered exponential reduces to an ordinary exponential

$$
\mathbf{T}\exp \int_0^{t_0} dt\, g_0 = \exp g_0 t.
\tag{D.17}
$$

Appendix E
Stochastic calculus

The Langevin formulation of Brownian motion was first used to describe the erratic motion of a micrometer-sized particle diffusing in water [45] and has since then been applied to a variety of system which are subject to fluctuations [87]. Langevin theory uses the tools of stochastic calculus for which a detailed discussion can be found in the literature [87,102,111,131]. Here we give an informal introduction and present some basic results for the ease of reference. Note that a Langevin equation with multiplicative noise can be interpreted either in the Stratonovich or the Itō sense; we write (S) in front of Stratonovich stochastic differential equations and likewise (I) in front of Itō stochastic differential equations.

Informal introduction to stochastic calculus. Recall that an ordinary differential equations for a variable $x(t)$ with $x(0) = x_0$

$$\dot{x} = h(x) \tag{E.1}$$

can be solved numerically by employing a simple Euler scheme

$$x_{k+1} = x_k + \Delta t \left[(1 - \alpha) h(x_k) + \alpha h(x_{k+1}) \right]. \tag{E.2}$$

Here $x_k = x(t_k)$ are (approximate) values of $x(t)$ at the discrete times $t_k = k \Delta t$ which are equidistant with time step Δt. Choosing $\alpha = 0$ in equation (E.2) corresponds to an explicit Euler scheme, while the choice $\alpha = 1$ gives an implicit Euler scheme. However, one might think of a more general mixed Euler scheme with $0 \leq \alpha \leq 1$ as well. In the limit of a small time step, $\Delta t \to 0$, the result $x(t_k)$ of the Euler scheme converges to the true solution $x(t)$ of the ordinary differential equation (provided some basic integrability conditions are met), irrespective of the precise value of α chosen. The different Euler schemes are thus equivalent with respect to their limit behavior although they may differ in terms of numeric stability. The situation is quite different for a (non-linear) stochastic differential equation

$$\dot{x} = h(x) + g(x)\xi \tag{E.3}$$

where $\xi(t)$ denotes Gaussian white noise with $\langle \xi(t_1)\,\xi(t_2) \rangle = \delta(t_1 - t_2)$.[18] We can regard the Gaussian white noise term $\xi(t)$ on the right-hand side of (E.3) as a limit

---

[18]Note that treating Gaussian white noise in the sense of a time-dependent function is rather a conceptual tool than a rigorously-defined mathematically quantity. In a mathematically rigorous treatment, one would have to replace the differential equation (E.3) by the corresponding integral equations and consider stochastic integrals which involve Wiener processes.

of a Poissonian spike train $\sum_j \delta(t - t_j)$ where the spike rate tends to infinity while at the same time the spike amplitude is rescaled to preserve the power spectrum of the spike train. In this picture, the term $g(x)\xi(t)$ describes the response of a system characterized by the variable x to a spike; the strength $g(x)$ of this response depends on the state of the system, i.e. the value of x at the instant when the spike occurs. Now the following dilemma arises: Should one use the state x of the system before the spike occurred or the state right after the spike? It turns out that the correct answer depends on the way the Langevin equation (E.3) is derived for the particular physical system under study; the different answers give rise to different interpretations of the stochastic differential equation (E.3). We introduce these different interpretations in terms of a stochastic version of the Euler scheme for the integration of the stochastic differential equation (E.3)

$$
\begin{aligned}
x_{k+1} = x_k &+ \Delta t \left[(1 - \alpha) \, h(x_k) + \alpha \, h(x_{k+1}) \right] \\
&+ \sqrt{\Delta t} \left[(1 - \alpha) \, g(x_k) + \alpha \, g(x_{k+1}) \right] \Xi_k.
\end{aligned}
\tag{E.4}
$$

Here Ξ_k are mutually independent random numbers that are chosen from a Gaussian distribution with zero mean and variance 1. Different choices of α define different solutions of the stochastic differential equation (E.3) in the limit $\Delta t \to 0$ corresponding to the different interpretations of stochastic calculus

- $\alpha = 0$ gives the Itō interpretation,

- $\alpha = 1$ gives the iso-thermal interpretation [87], and finally

- $\alpha = 1/2$ gives the Stratonovich interpretation.

Which interpretation to choose depends on the particular physical problem at hand: Note that a Langevin equation does not capture physical reality in a direct way but provides an effective description. Usually, a Langevin equation is obtained as the limit of a more microscopic description. For example, in many physical considerations, fluctuating forces with a finite albeit small correlation time appear on the right-hand side of a dynamic equation. If one is interested in time-scales much longer than this correlation time, one obtains a Stratonovich stochastic differential equation by the Wong-Zakai theorem. Itō stochastic differential equations are usually used in financial mathematics to describe the stochastic dynamics of stock prices. In the Itō calculus, the value of a function $x(t)$ at time t and the Gaussian white noise term $\xi(t)$ that drives the dynamics of x by a stochastic differential equation of the form (E.3) are independent: The Itō calculus does not "look into the future" [111].

A stochastic differential equation stated in a particular interpretation can be rewritten for any other interpretation; in this case additional noise-induced drift terms appear.

E.1 Rules of stochastic calculus

How to do calculus with functions of time which are actually sample functions of a stochastic process? If the Stratonovich interpretation is employed, the usual rules of calculus can be applied also to stochastic variables. The rules of the Itō stochastic calculus differ from the usual rules of ordinary calculus.

Itō chain rule. Suppose that $x_k(t)$, $k = 1, \ldots, n$, is a solution to the set of Itō stochastic differential equations

$$(I) \quad \dot{x}_k = h_k + g_{kl}\xi_l \tag{E.5}$$

where ξ_l is Gaussian white noise with $\langle \xi_k(t_1)\,\xi_l(t_2) \rangle = \delta_{kl}\,\delta(t_1 - t_2)$ and we use Einstein summation convention. If $y = y(x_k)$ is a function of the x_k, then the Itō chain rule holds [111]

$$(I) \quad \dot{y} = \frac{\partial y}{\partial x_j}\,\dot{x}_j + \frac{1}{2}\frac{\partial^2 y}{\partial x_k \partial x_l}\,g_{km}g_{ml}. \tag{E.6}$$

Switching between Itō and Stratonovich stochastic differential equations. Consider a set of Stratonovich stochastic differential equation

$$(S) \quad \dot{x}_k = h_k + g_{kl}\xi_l \tag{E.7}$$

driven by uncorrelated Gaussian white noise ξ_j with $\langle \xi_k(t_1)\xi_l(t_2) \rangle = \delta_{kl}\,\delta(t_1 - t_2)$. This Stratonovich stochastic differential equation is equivalent to an Itō stochastic differential equation of the form [87]

$$(I) \quad \dot{x}_k = h_k + g_{kl}\xi_l + \frac{1}{2}\frac{\partial g_{kl}}{\partial x_m}g_{ml}. \tag{E.8}$$

Thus one can switch the interpretation at will and work with the interpretation most suitable for the application at hand irrespective of the interpretation of the original Langevin equation (which is given by the physics of the underlying microscopic model).

Fokker-Planck equation associated to a Langevin equation. Consider a stochastic trajectory which is characterized by time-dependent coordinates $x_j(t)$ whose stochastic dynamics is governed by a set of stochastic differential equations in α-interpretation (with $\alpha = 0$ corresponding to Itō and $\alpha = 1/2$ to Stratonovich interpretation)

$$(\alpha) \quad \dot{x}_k = h_k + g_{kl}\xi_l. \tag{E.9}$$

Here ξ_j denotes uncorrelated Gaussian white noise ξ_j with $\langle \xi_k(t_1)\xi_l(t_2) \rangle = \delta_{kl}\,\delta(t_1 - t_2)$. The Fokker-Planck equation for the time-dependent probability density P of a whole ensemble of such stochastic trajectories is given by [87]

$$\frac{\partial}{\partial t}P = \frac{\partial}{\partial x_k}\left[-\left(h_k + \alpha\frac{\partial g_{kl}}{\partial x_m}g_{ml} \right) P + \frac{1}{2}\frac{\partial}{\partial x_m}\left(g_{kl}g_{ml}P \right) \right]. \tag{E.10}$$

E.2   Example: Effective dynamics of helical swimming paths

For noisy helical swimming paths in a linear concentration field $c(\mathbf{x}) = c_0 + \mathbf{c}_1 \cdot \mathbf{x}$, we can exploit symmetries and derive an effective equation for the stochastic dynamics of the alignment angle ψ enclosed by the helix vector $\mathbf{h}_3$ and the gradient direction $\mathbf{c}_1$ by rewriting the stochastic differential equation (5.34) in spherical coordinates. The symmetries of the problem imply that the dynamics of ψ decouples from the other degrees of freedom. For simplicity, we assume that the concentration gradient $\mathbf{c}_1$ is parallel to the x-axis of a fixed lab frame; with respect to this lab frame, we can write

$$
\begin{aligned}
\mathbf{h}_3 &= (\cos\psi, \sin\psi\cos\theta, \sin\psi\sin\theta), \\
\mathbf{h}_1 &= \cos\varphi\,\mathbf{s}_1 + \sin\varphi\,\mathbf{s}_2, \\
\mathbf{h}_2 &= \mathbf{h}_3 \times \mathbf{h}_1
\end{aligned}
\tag{E.11}
$$

where $\mathbf{s}_1 = \mathbf{c}_\perp/c_\perp = -\frac{\partial}{\partial\psi}\mathbf{h}_3$ and $\mathbf{s}_2 = \mathbf{h}_3 \times \mathbf{c}_\perp/c_\perp = -\frac{\partial}{\partial\theta}\mathbf{h}_3/\sin\psi$. In the Stratonovich stochastic calculus, the rules of ordinary calculus apply: thus we find from (E.11)

$$
\text{(S)} \quad
\begin{aligned}
\dot{\mathbf{h}}_3 \cdot \mathbf{s}_1 &= -\dot\psi, \\
\dot{\mathbf{h}}_3 \cdot \mathbf{s}_2 &= -\dot\theta\sin\psi, \\
\dot{\mathbf{h}}_1 \cdot \mathbf{h}_2 &= \dot\varphi + \dot\theta\cos\psi.
\end{aligned}
\tag{E.12}
$$

Using equation (5.34), we can express these scalar products alternatively as

$$
\text{(S)} \quad
\begin{aligned}
\dot{\mathbf{h}}_3 \cdot \mathbf{s}_1 &= \beta\sin\psi - \xi_1\sin\varphi - \xi_2\cos\varphi, \\
\dot{\mathbf{h}}_3 \cdot \mathbf{s}_2 &= \beta'\sin\psi + \xi_1\cos\varphi - \xi_2\sin\varphi, \\
\dot{\mathbf{h}}_1 \cdot \mathbf{h}_2 &= \omega
\end{aligned}
\tag{E.13}
$$

where $\beta - i\beta' = |\boldsymbol{\nabla}c|\,\varepsilon_a\widetilde{\chi}_a$. Comparing (E.12) and (E.13), we obtain two Stratonovich stochastic differential equations for the angles ψ and φ

$$
\text{(S)} \quad
\begin{aligned}
\dot\psi &= -\beta\cos\psi + \sin\varphi\,\xi_1 + \cos\varphi\,\xi_2, \\
\dot\varphi &= -\cot\psi\,(-\cos\varphi\,\xi_1 + \sin\varphi\,\xi_2)
\end{aligned}
\tag{E.14}
$$

We can decouple the dynamics of ψ from φ by using a simple trick: First, we rewrite this equation as an Itō stochastic differential equation

$$
\text{(I)} \quad \dot\psi = -\beta\cos\psi + \sin\varphi\,\xi_1 + \cos\varphi\,\xi_2 + D_\psi\cot\psi,
\tag{E.15}
$$

and $\dot\varphi$ as above. Note the noise-induced drift term $D_\psi\cot\psi$ in the equation for $\dot\psi$ with $2D_\psi = \widehat{C}_{11}$. In the Itō calculus, $\sin\varphi\,\xi_1 + \cos\varphi\,\xi_2$ is equivalent to a Gaussian white noise term ξ with $\langle\xi(t_1)\,\xi(t_2)\rangle = 2D_\psi\,\delta(t_1 - t_2)$ since $\varphi(t)$ and $\xi_j(t)$ are independent. Thus, we have an equivalent Langevin equation for the dynamics of ψ

$$
\dot\psi = -\beta\sin\psi + \xi + D_\psi\cot\psi. \qquad\qquad \text{cf. eqn. (5.35)}
$$

We discuss the properties of this dynamic equation in section 5.3.2.

Appendix F
Persistent random walks

We define a persistent random walk $\mathbf{R}(t)$ with speed v_0 as a path whose tangent $\mathbf{e} = \dot{\mathbf{R}}/v_0 \in \mathrm{S}^2$ performs a random walk on the unit sphere S^2. See [151] for a related approach.

We review some facts concerning diffusion on a sphere: A physical example of a random walk on the sphere is provided by the trajectory of a unit vector $\mathbf{e}$ parallel to the axis of symmetry of a spheroid subject to rotational Brownian motion [118]. If $\mathbf{e}_j$, $j = 1, 2, 3$ is a full body frame of the spheroid with $\mathbf{e}_3 = \mathbf{e}$, rotational diffusion of the spheroid is described by the following Langevin equation in Stratonovich interpretation

$$\text{(S)} \quad \dot{\mathbf{e}}_j = \epsilon_{kjl}\, \xi_k\, \mathbf{e}_l \tag{F.1}$$

where the $\xi_j(t)$ denote uncorrelated Gaussian white noise with variance $2D_k$, i.e. $\langle \xi_k(t_1)\, \xi_l(t_2) \rangle = 2D_k\, \delta_{kl}\, \delta(t_1 - t_2)$. By writing (S) in front of (F.1), we highlight the fact that (F.1) is to be interpreted in the Stratonovich sense. Likewise, we will write (I) in front of Itō stochastic differential equations. See appendix E for a discussion of Itō and Stratonovich stochastic differential equations. The symmetry of the spheroid implies $D_1 = D_2$; we write $D_{\mathrm{rot}} = D_1$. By the equipartition theorem, one can conclude Einstein relations for the rotational diffusion coefficient $D_j = k_B T/\zeta_j$, where the ζ_j are the frictional drag coefficients for rotations around axis $\mathbf{e}_j$ [16,118].

We now leave this particular example and merely regard diffusion on the sphere as an abstract process given by (F.1). We rewrite (F.1) in Itō interpretation [87,111]:

$$\text{(I)} \quad \dot{\mathbf{e}}_j = \epsilon_{kjl}\, \xi_k \mathbf{e}_l - \sum_{k=1}^{3}(1 - \delta_{kj})D_k\, \mathbf{e}_j \tag{F.2}$$

where ξ_j denotes Gaussian white noise as above. Taking the scalar product with $\mathbf{e}(0)$ on both sides and averaging with respect to noise yields an ordinary differential equation for the autocorrelation function

$$\frac{d}{dt}\langle \mathbf{e}(0) \cdot \mathbf{e}(t) \rangle = -2D_{\mathrm{rot}}\, \langle \mathbf{e}(0) \cdot \mathbf{e}(t) \rangle \tag{F.3}$$

from which we conclude equation (6.1) with $l_P = v_0/(2D_{\mathrm{rot}})$

$$\langle \mathbf{e}(0) \cdot \mathbf{e}(t) \rangle = \exp{-2D_1|t|}. \tag{F.4}$$

Note that in deriving (F.3) we have made essential use of the fact that $\mathbf{e}_i(t)$ and $\Omega_j(t)$ are independent for the Itō interpretation [111].

There is a full equivalence in the sense of statistical mechanics between persistent random walks of length L and configurations of worm-like chains in the sense of Kratky and Porod [85], i.e. configurations of chains of length L with an energy functional $E = \frac{1}{2}k_B T l_P \int_0^L ds\,\kappa^2$, where $\kappa = |\dot{\mathbf{e}}|/v_0$ is local curvature. In short, this equivalence stems from the fact that both persistent random walks $\mathbf{R}(t_0) = v_0 \int_0^{t_0} dt\,\mathbf{e}(t)$ and the configurations of worm-like chains $\mathbf{R}(v_0 t_0) = \int_0^{v_0 t_0} ds\,\mathbf{e}(s)$ integrate over a unit vector $\mathbf{e} \in S^2$ which diffuses on the sphere [134]. The correspondence can be made more formal by noting that the probability density $P(\mathbf{R}, \mathbf{e}, s)$ of both persistent random walks and worm-like chains obey the same Fokker-Planck equation [24,133]

$$\frac{\partial}{\partial s}P = -\mathbf{e}\cdot\frac{\partial}{\partial \mathbf{R}}P + D_{\text{rot}}/v_0\,\Delta_{\mathbf{e}}P. \tag{F.5}$$

Here $\Delta_{\mathbf{e}}$ is the spherical Laplacian

$$\Delta_{\mathbf{e}} = \frac{1}{\sin\theta}\frac{\partial}{\partial\theta}\left(\sin\theta\frac{\partial}{\partial\theta}\right) + \frac{1}{\sin^2\theta}\frac{\partial^2}{\partial\phi^2}, \tag{F.6}$$

where θ and ϕ are the spherical coordinates of $\mathbf{e}$, i.e. $\mathbf{e} = (\cos\theta, \sin\theta\cos\phi, \sin\theta\sin\phi)$.

Appendix G
Persistence length of sperm swimming paths

We give an estimate for the persistence length l_P of the centerline of helical sea urchin sperm swimming paths as $l_P \sim 4\,\mathrm{mm}$. It is the centerline $\mathbf{R}$ of the helical swimming path $\mathbf{r}$ of a sperm cell which matters when we ask whether the sperm cell will hit the egg, since the radius $r_0 \approx 15\,\mu\mathrm{m}$ of the helical path is smaller than the egg radius $R_{\mathrm{target}} \approx 100\,\mu\mathrm{m}$ [37].

Sperm cells of many species swim on helical paths $\mathbf{r}(t)$ with net motion along the centerline $\mathbf{R}(t)$ of the helix. Near boundary surfaces, the sperm cells become localized to the surface and swim in circles. In an experiment with sea urchin sperm in a shallow observation chamber [126], single sperm cells swam in circles of radius $r_0 \approx 40\,\mu\mathrm{m}$ with a speed of $v_0 \approx 100\,\mu\mathrm{m}/s$. The center-point $\mathbf{R}(t)$ of the swimming circles was diffusing with a diffusion constant of

$$D_{\mathrm{2d}} \approx 9 \pm 2\,\mu\mathrm{m}^2/s. \tag{G.1}$$

The diffusion of the swimming circles is due to fluctuations $\eta(t)$ of the curvature $\kappa(t) = 1/r_0 + \eta$ of the swimming path $\mathbf{r}(t)$. Since the correlation time of curvature fluctuations is on the order of the period of the flagellar beat which is much smaller than the period of circular swimming, we can model $\eta(t)$ as Gaussian white noise with $\langle \eta(t)\eta(t') \rangle = 2D_{\kappa,\mathrm{2d}}\delta(t - t')$. A short calculation shows that the noise strength $D_{\kappa,\mathrm{2d}}$ is related to the diffusion constant D_{2d} by

$$D_{\mathrm{2d}} = \frac{1}{2}\left(v_0 r_0\right)^2 D_{\kappa,\mathrm{2d}}, \tag{G.2}$$

see equation (4.19). As a simple model case for noisy helical swimming, we assume for curvature and torsion of the path $\mathbf{r}(t)$

$$
\begin{aligned}
\kappa(t) &= \kappa_0 + \xi_\kappa, \\
\tau(t) &= \tau_0 + \xi_\tau,
\end{aligned}
\tag{G.3}
$$

where $\xi_\kappa(t)$, $\xi_\tau(t)$ denote Gaussian white noise with $\langle \xi_\kappa(t_1)\,\xi_\kappa(t_2) \rangle = 2D_{\kappa,\mathrm{3d}}\delta(t_1 - t_2)$, $\langle \xi_\tau(t_1)\,\xi_\tau(t_2) \rangle = 2D_{\tau,\mathrm{3d}}\delta(t_1 - t_2)$, $\langle \xi_\kappa(t_1)\,\xi_\tau(t_2) \rangle = 0$. Using the theory presented in chapter 5, for noisy helices, we find for the persistence time t_P and persistence length

l_P of the centerline of helical sperm swimming path

$$
t_p = \frac{1}{\omega_0^2} \frac{1}{h_0^2 D_{\kappa,\mathrm{3d}} + r_0^2 D_{\tau,\mathrm{3d}}}, \quad \text{and}
$$

$$
l_P = \omega_0 h_0 \, t_P,
$$

(G.4)

see equation (5.22). For sea urchin sperm, radius and pitch of helical swimming paths are $r_0 \approx 15\,\mu\mathrm{m}$, and $2\pi h_0 \approx 50\,\mu\mathrm{m}$, respectively [37]. Assuming that the curvature and torsion fluctuations in the helix case are of the same order of magnitude as in the planar case, i.e. $D_{\kappa,\mathrm{3d}} \approx D_{\kappa,\mathrm{2d}}$, $D_{\tau,\mathrm{3d}} \approx D_{\kappa,\mathrm{2d}}$, we obtain the order of magnitude estimates $t_P \approx 90\,\mathrm{s}$ and

$$
l_P \approx 4\,\mathrm{mm}.
$$

(G.5)

This estimate of the persistence length l_P of three-dimensional sperm swimming paths is rather high. It would be desirable to measure this quantity in a direct way. To the author's knowledge, the only such experiment was performed by Brokaw for bracken fern spermatozoids and yielded the value $l_P \approx 1\,\mathrm{mm}$ [26].

Appendix H
Diffusion to capture

H.1 Success probability of a single random walker

What is the probability p_0 for a random walker to hit a target in three-dimensional space after sufficiently long time? We assume that the target is spherical with radius R_s and that the random walker starts at a distance R_0 of the target at time $t = 0$. In one and two space dimensions, a classic result of Pólya states $p_0 = 1$ [120]. In three-dimensional space, the answer is

$$p_0 = R_s/R_0. \tag{H.1}$$

To prove this result, note that we can rephrase the problem in a radially symmetric form: Place the target at the origin and replace the single random walker by a population of diffusing particles that is evenly distributed on a spherical shell of radius R_0 with its center at the origin at time $t = 0$. We introduce the density P of particles with units of an inverse volume and consider $P = P(R, t)$ as a function of distance R from the origin and time t. The density P satisfies the radial diffusion equation

$$\frac{\partial}{\partial t} P = D \, R^{-1} \, \partial_R^2 \, (R \, P). \tag{H.2}$$

At $t = 0$, we have $P(R, 0) = c_0 \, \delta(R - R_0)$. Here c_0 is the initial surface concentration on the sphere. At the surface of the target, we impose absorbing boundary conditions $P(R_s, t) = 0$. Using the method of images, we can solve this boundary value problem

$$P(R, t) = \frac{c_0}{\sqrt{4\pi D t}} \frac{R_0}{R} \left[\exp\left(-\frac{(R - R_0)^2}{4Dt} \right) - \exp\left(-\frac{(R + R_0 - 2R_s)^2}{4Dt} \right) \right].$$

The time-dependent rate of random walker arriving at the target is $q(t) = -4\pi R_s^2 D \, \partial_R P(R, t)_{|R = R_s}$. By integrating the flux over time, we find the fraction $p(t)$ of particles that will be absorbed within a time t

$$p(t) = \int_0^t dt_1 \, k(t_1)/(4\pi R_0^2 c_0) = \frac{R_s}{R_0} \left[1 - \text{Erf}\left(\frac{R_0 - R_s}{2\sqrt{Dt}} \right) \right]. \tag{H.3}$$

Thus, equation (H.1) follows. Note that the conditional mean first passage time $\int_0^\infty dt \, t \, k(t) / \int_0^\infty dt \, k(t)$ diverges. However, the majority of particles predestinated to hit the target will have done so within a time $t \gg (R_0 - R_s)^2/D$.

H.2 Diffusive current to an absorbing target

Diffusion to a sphere. *Now let us consider a spherical target of radius R_s in a solution of suspended particles with concentration $c(\mathbf{x}, t)$. What will the current of particles absorbed by the target?* The particles diffuse with a diffusion constant D and the concentration field $c(\mathbf{x}, t)$ obeys the diffusion equation $\dot{c} = D\Delta c$. We assume that any particle that hits the surface of the target will be absorbed immediately, i.e. we impose an absorbing boundary condition $c(\mathbf{x}, t) = 0$ for $|\mathbf{x}| = R_s$. If c_0 is the concentration of particles far from the sphere, we find for the steady-state concentration profile $c(\mathbf{x}) = c_0 \left(1 - R_s/|\mathbf{x}|\right)$. The diffusive current q_0 to the sphere at steady state is

$$q_0 = 4\pi \, R_s \, D \, c_0. \tag{H.4}$$

Note that the diffusive current is not proportional to the surface of the absorber but to its linear dimension as is typical for diffusion-to-capture problems [16].

Diffusion to a partially absorbing sphere. We consider an impenetrable non-absorbing sphere of radius R_s covered by N disk-like absorbers of radius R_b in an infinite medium containing these molecules at an initial concentration c_0. The steady-state current q to the absorbing disks is estimated as [16,19].

$$q = q_0 \frac{N}{N^* + N}, \qquad N^* = \pi R_s/R_b \tag{H.5}$$

where $q_0 = 4\pi D r_s c_0$ would have been the flux to a fully absorbing sphere, see equation (H.4). In particular, we find $q \approx q_0$ for $N \gg N^*$.

Diffusion to a moving sphere. How will the absorption current to a receptor-coated cell or the flagellar membrane of a sperm cell if the fluid is stirred by an active motion of the cell? We discuss the case of an absorbing sphere with radius R_s immersed in a solution of particles that moves uniformly with speed v_0. We stick to the case of low Reynolds number hydrodynamics relevant for the swimming of microorganisms [122]. Let q be the current to the moving sphere, q_0 is the respective current for a stationary sphere. The increase of diffusive uptake $q/q_0 - 1$ is related to the power dissipated in the stirring and found to scale quadratically with the Peclet number $\mathrm{Pe} = v_0 R_s/D$ as long as $\mathrm{Pe} \lesssim 1$ [19,123]. For a large Peclet number, we have [1]

$$q \approx 0.991 \, q_0 \, \mathrm{Pe}^{1/3}. \tag{H.6}$$

Since q/q_0 scales only with the 1/3 power of the Peclet number, even a considerably high speed v_0 of the sphere results only in a moderate increase of the diffusive current.

Appendix J
Some aspects of sperm swimming

J.1 Instantaneous swimming velocities from the beat pattern

The instantaneous swimming velocities $\mathbf{v}(t)$, $\Omega(t)$ of an internally driven filament such as a flagellum can be determined from force and torque balance (2.19). The expression for the force and torque, equation (2.18), involves the temporal change of the flagellar shape $\dot{\mathbf{B}}$. With (2.4) and (2.5), we have

$$
\begin{aligned}
\dot{\mathbf{B}} &= \dot{\mathbf{r}} + b_j \dot{\mathbf{e}}_j + \dot{b}_j \mathbf{e}_j, \\
&= \mathbf{v} + b_j \mathbf{\Omega} \times \mathbf{e}_j + \dot{b}_j \mathbf{e}_j.
\end{aligned}
\tag{J.1}
$$

Now we can derive a linear equation for $\mathbf{v}$ and $\mathbf{\Omega}$

$$
\begin{bmatrix} \Gamma_{\mathbf{F},\mathbf{v}} & \Gamma_{\mathbf{F},\mathbf{\Omega}} \\ \Gamma_{\mathbf{M},\mathbf{v}} & \Gamma_{\mathbf{M},\mathbf{\Omega}} \end{bmatrix} \cdot \begin{bmatrix} \mathbf{v} \\ \mathbf{\Omega} \end{bmatrix} = - \begin{bmatrix} \mathbf{F}_1 \\ \mathbf{M}_1 \end{bmatrix} \qquad \text{cf. eqns. (2.20), (2.21)}
$$

with

$$
\begin{aligned}
(\mathbf{F}_1)_j &= -\int_0^L ds\, \zeta_\perp \dot{b}_j + \zeta \dot{b}_k b_k' b_j', \\
(\mathbf{M}_1)_j &= -\int_0^L ds\, \zeta_\perp \epsilon_{jkl} \dot{b}_k b_l + \zeta \epsilon_{jkl} \dot{b}_m b_m' b_k' b_l
\end{aligned}
\tag{J.2}
$$

and

$$
\begin{aligned}
(\Gamma_{\mathbf{F},\mathbf{v}})_{kl} &= -\zeta_\perp \delta_{kl} & -\zeta b_k' b_l', \\
(\Gamma_{\mathbf{F},\mathbf{\Omega}})_{kl} &= -\zeta_\perp \epsilon_{klj} b_j & -\zeta \epsilon_{jlm} b_j' b_k' b_m, \\
(\Gamma_{\mathbf{M},\mathbf{v}})_{kl} &= -\zeta_\perp \epsilon_{klm} b_m & -\zeta \epsilon_{kjm} b_l' b_j' b_m, \\
(\Gamma_{\mathbf{M},\mathbf{\Omega}})_{kl} &= -\zeta_\perp \epsilon_{kjm} \epsilon_{jln} b_n b_m & -\zeta \epsilon_{kjm} \epsilon_{nlp} b_m' b_j' b_m b_p.
\end{aligned}
\tag{J.3}
$$

Here the dot denotes time derivatives and the prime denotes derivatives with respect to arclength. We used the abbreviation $\zeta = \zeta_\parallel - \zeta_\perp$.

J.2 Averaged swimming velocities for planar swimming

Equation (2.11) relates the net motion after one full flagellar beat cycle with the average swimming velocities. In the case of planar swimming, we can make this relationship

more explicite. Let

$$
\mathrm{G}(T_f) = \begin{bmatrix} \mathrm{W} & \mathrm{V} \\ 0 & 1 \end{bmatrix} \text{ with } \mathrm{W} = \begin{pmatrix} \cos\varphi & \sin\varphi & 0 \\ -\sin\varphi & \cos\varphi & 0 \\ 0 & 0 & 1 \end{pmatrix}, \quad \mathrm{V} = \begin{pmatrix} V_1 \\ V_2 \\ 0 \end{pmatrix}. \tag{J.4}
$$

Then we have for the averaged velocities

$$
\begin{array}{ll}
\bar{v}_1 = \frac{\varphi}{2}\left(\cot\left(\frac{\varphi}{2}\right)V_1 - V_2\right)/T_f, & \\
\bar{v}_2 = \frac{\varphi}{2}\left(V_1 + \cot\left(\frac{\varphi}{2}\right)V_2\right)/T_f, & \overline{\Omega}_1 = \overline{\Omega}_2 = 0, \\
\bar{v}_3 = 0, & \overline{\Omega}_3 = \varphi/T_f.
\end{array} \tag{J.5}
$$

These velocities are expressed in the body frame of the swimmer at time $t = 0$, hence their coordinate representation depends on the choice of the beginning of the beat period. Note that in general $\bar{v}_j$ does not equal the mean of v_j since the sperm head rotates.

J.3 Drag coefficients

To compute the hydrodynamic drag force of a flagellum, we approximate the flagellum as a sequence of cylinders. The hydrodynamic drag acting on a cylinder of length L and radius r_f moving in a viscous liquid is given by equation (2.16); The perpendicular and parallel drag coefficients $\zeta_\perp$ and $\zeta_\parallel$ are given by [23]

$$
\zeta_\perp = \frac{4\pi\eta}{\ln(2L/r_f) - \frac{1}{2}}, \quad \zeta_\parallel = \frac{2\pi\eta}{\ln(2L/r_f) - \frac{3}{2}}. \tag{J.6}
$$

Here η is the dynamic viscosity of the liquid. These formulas are valid in the zero Reynolds number limit and are exact up to corrections of order $\ln(L/r_f)^{-3}$.

Perpendicular and parallel hydrodynamic drag coefficients for a spheroid with semi-axes r_1 and $r_2 = r_3 < r_1$ were derived by Perrin [83,119]

$$
\zeta_\perp = 32\pi\eta\frac{r_1^2 - r_2^2}{(2r_1^2 - 3r_2^2)S + 2r_1}, \quad \zeta_\parallel = 16\pi\eta\frac{r_1^2 - r_2^2}{(2r_1^2 - r_2^2)S - 2r_1}. \tag{J.7}
$$

where $S = 2(r_1^2 - r_2^2)^{-1/2}\ln[(r_1 + \sqrt{r_1^2 - r_2^2})/r_2]$. In the limit $r_1 \gg r_2$, one finds [16]

$$
\zeta_\perp = \frac{4\pi\eta}{\ln(r_1/r_2) + \frac{1}{2}}, \quad \zeta_\parallel = \frac{2\pi\eta}{\ln(r_1/r_2) - \frac{1}{2}}. \tag{J.8}
$$

Appendix K
Helical swimming paths in a weak concentration gradient

As in the planar case studied in section 3.1.3, the chemotactic feedback loop for three space dimensions given in equations (3.2), (3.4), (3.20) and (3.21) can be studied in the limit of weak gradients by a perturbation calculation in the small parameter $\nu = r_0|\boldsymbol{\nabla}c|/c$. Again we assume that the nonlinearities of the concentration field $c(\mathbf{x})$ are small on the length-scale r_0, $|\boldsymbol{\nabla}^2 c| \ll |\boldsymbol{\nabla}c|/r_0$, which implies that during a few helical turns of the swimming path we can approximate the concentration field linearly as

$$c(\mathbf{x}) = c_0 + \mathbf{c}_1 \cdot \mathbf{x}. \tag{K.1}$$

Recall that such a helical swimming path can be described as the trajectory of a point on the circumference of an imagined solid disk of radius r_0 that rotates in its plane with rotation rate Ω_3 and whose center moves along the centerline $\mathbf{R}(t)$, see figure 3.6. The orientation of the disk is characterized by its material frame $(\mathbf{h}_1, \mathbf{h}_2, \mathbf{h}_3)$ where $\mathbf{h}_3$ is the helix vector normal to the disk. The deformed helical swimming path $\mathbf{r}(t)$ can now be written as

$$\mathbf{r}(t) = \mathbf{R}(t) + r\,\mathbf{h}_1(t), \tag{K.2}$$

where the radius $r = r_0 + \mathcal{O}(\nu)$ may change only on a slow time-scale. The time dependence of the frame $\mathbf{h}_j$ is given by pure rotations $\dot{\mathbf{h}}_j = \epsilon_{kjl}\,\Omega_k\,\mathbf{h}_l$, where the Ω_k denote rotation rates. The concentration gradient $\boldsymbol{\nabla}c = \mathbf{c}_1$ can be expressed as the sum of

(i) a component $\mathbf{c}_{\parallel} = c_{\parallel}\mathbf{h}_3$ with $c_{\parallel} = \boldsymbol{\nabla}c \cdot \mathbf{h}_3$ parallel to $\mathbf{h}_3$, and

(ii) a component $\mathbf{c}_{\perp} = \boldsymbol{\nabla}c - \mathbf{c}_{\parallel}$ perpendicular to $\mathbf{h}_3$ of length $\mathbf{c}_{\perp} = |\mathbf{c}_{\perp}|$.

We anticipate that the swimming path $\mathbf{r}(t)$ is a perfect helix whose shape is perturbed to first order in ν

$$\mathbf{r}(t) = r\cos\varphi(t)\,\mathbf{h}_1(0) + r\sin\varphi(t)\,\mathbf{h}_2(0) + \omega h\,t\,\mathbf{h}_3(0) + \mathcal{O}(\nu), \tag{K.3}$$

with an angular frequency $\omega = \omega_0 + \mathcal{O}(\nu)$, a radius $r = r_0 + \mathcal{O}(\nu)$, a pitch $2\pi h = 2\pi h_0 + \mathcal{O}(\nu)$, and a rotation rate $\dot{\varphi} = \Omega_3 = \omega + \mathcal{O}(\nu)$. For simplicity, we assumed $\mathbf{R}(0) = 0$ in equation (K.3). The swimming path $\mathbf{r}(t)$ samples a temporal stimulus from the locally linear concentration field which to first order in ν and for $t \ll (\nu\omega_0)^{-1}$

reads

$$s(t) = c(\mathbf{r}(t)) = c_0 + \omega_0 h_0 c_\parallel t + r_0 c_\perp \cos(\omega_0 t + \varphi_0) + \mathcal{O}(\nu^2) \tag{K.4}$$

where φ_0 is the angle enclosed by the projection $\mathbf{c}_\perp$ of the concentration gradient on the disk and the vector $\mathbf{h}_1$ such that $\mathbf{h}_1(0) + i\,\mathbf{h}_2(0) = \mathbf{c}\,e^{-i\,\varphi_0}/c_\perp$. Recall that the complex gradient vector $\mathbf{c}$ is defined as $\mathbf{c} = \mathbf{c}_\perp + i\,\mathbf{h}_3 \times \mathbf{c}_\perp$. The stimulus (K.4) combines a linear ramp and a periodic component. To first order in ν the signaling network generates the output $a(t) = 1 + a_1 + \rho_a r_0 c_x \cos(\omega t + \varphi_0 + \varphi_a) + \mathcal{O}(\nu^2)$ where $a_1 = \mu \omega_0 h_0 c_\parallel / c_0$ and $\widetilde{\chi}_a(\omega_0) = \rho_a \exp(i\varphi_a)$ is the linear response coefficient of equation (3.4) at the helix frequency ω_0. This output elicits curvature and torsion oscillations

$$
\begin{aligned}
\kappa(t) &= \kappa_0 + \kappa_1 a_1 + \rho_\kappa c_\perp r_0 \cos(\omega t + \varphi_0 + \varphi_\kappa) + \mathcal{O}(\nu^2), \\
\tau(t) &= \tau_0 + \tau_1 a_1 + \rho_\tau c_\perp r_0 \cos(\omega t + \varphi_0 + \varphi_\tau) + \mathcal{O}(\nu^2).
\end{aligned}
\tag{K.5}
$$

Curvature $\kappa(t)$ and torsion $\tau(t)$ determine the swimming path by the Frenet-Serret equations (3.20). If we express the swimming path in the form of equation (K.2), the centerline $\mathbf{R}(t)$ and the vectors $\mathbf{h}_j(t)$ have to change according to equation (3.25) for the time dependent curvature and torsion to satisfy equation (K.5)

$$
\begin{aligned}
\dot{\mathbf{R}} &= \omega h\,\mathbf{h}_3 - \delta_\kappa \operatorname{Im}\left(\widetilde{\chi}_\kappa(\omega_0)\,\mathbf{c}\right) + \delta_\tau \operatorname{Im}\left(\widetilde{\chi}_\tau(\omega_0)\,\mathbf{c}\right) + \mathcal{O}(\nu^2), \\
\dot{\mathbf{h}}_3 &= \qquad - \varepsilon_\kappa \operatorname{Re}\left(\widetilde{\chi}_\kappa(\omega_0)\,\mathbf{c}\right) + \varepsilon_\tau \operatorname{Re}\left(\widetilde{\chi}_\tau(\omega_0)\,\mathbf{c}\right) + \mathcal{O}(\nu^2), \\
\dot{\mathbf{h}}_1 &= \ \ \Omega_3\,\mathbf{h}_2 - (\dot{\mathbf{h}}_3 \cdot \mathbf{h}_1)\mathbf{h}_3, \\
\dot{\mathbf{h}}_2 &= -\Omega_3\,\mathbf{h}_1 - (\dot{\mathbf{h}}_3 \cdot \mathbf{h}_2)\mathbf{h}_3.
\end{aligned}
\qquad \text{cf. eqn. (3.25)}
$$

Here the coefficients read

$$
\begin{array}{llll}
\delta_\kappa &= \omega_0 r_0 (2r_0^2 + 3h_0^2)/4, & \varepsilon_\kappa &= \omega_0 r_0 h_0/2, \\
\delta_\tau &= \omega_0 r_0^2 h_0/4, & \varepsilon_\tau &= \omega_0 r_0^2/2.
\end{array}
\tag{K.6}
$$

A special case of the corresponding calculation is presented in horry-gorry detail below. The helix frequency $\omega = \omega_0 + \mathcal{O}(\nu)$, the helix radius $r = r_0 + \mathcal{O}(\nu)$, and the helix pitch $2\pi h = 2\pi h_0 + \mathcal{O}(\nu)$ are perturbed to first order in ν: We have

$$\omega = v_0 \sqrt{\overline{\kappa}^2 + \overline{\tau}^2}, \quad r = \overline{\kappa}\, v_0^2/\omega^2, \quad h = \overline{\tau}\, v_0^2/\omega^2 \tag{K.7}$$

where $\overline{\kappa}$ and $\overline{\tau}$ equal the mean of $\kappa(t)$ and $\tau(t)$ averaged over a helix period, respectively. From (K.5), we have $\overline{\kappa} = \kappa_0 + \kappa_1 a_1 + \mathcal{O}(\nu^2)$, $\overline{\tau} = \tau_0 + \tau_1 a_1 + \mathcal{O}(\nu^2)$ with $a_1 = \mu \omega_0 h_0\, c_\parallel / c_0$. We thus have $\omega = \omega_0 + \omega_0 (h_0 \tau_1 + r_0 \kappa_1)\, a_1 + \mathcal{O}(\nu^2)$ and $\omega h = \omega_0 h_0 + \omega_0 r_0 (r_0 \tau_1 - h_0 \kappa_1)\, a_1 + \mathcal{O}(\nu^2)$ in accordance with equations (5.27) and (5.66).

The rotation rate $\Omega_3(t)$ is given by the helix frequency ω plus a periodic modulation

$$
\begin{aligned}
\Omega_3 = \omega + \frac{\omega_0 c_\perp}{4} \Big[&(2r_0^2 + h_0^2)\rho_\kappa \cos(\omega_0 t + \varphi_0 + \varphi_\kappa) \\
&+ r_0 h_0 \rho_\tau \cos(\omega_0 t + \varphi_0 + \varphi_\tau) \Big] + \mathcal{O}(\nu^2).
\end{aligned}
\tag{K.8}
$$

From equation (3.25), we see that two fundamental perturbations of a perfect helix are important in the presence of a gradient. The helix can bend for $\dot{\mathbf{h}}_3 \neq 0$ or it can tilt if $\dot{\mathbf{R}}$ and $\mathbf{h}_3$ do not align, see figure K.1.

fundamental perturbations of a helix
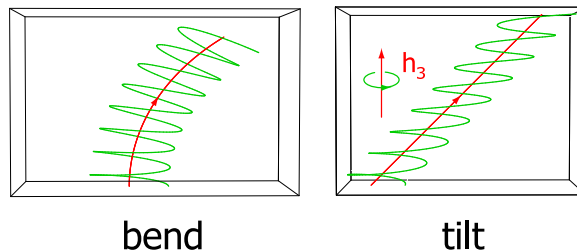
Figure K.1: The symmetry of a perfect helix can be broken in two fundamental ways as it can bend (left panel) and tilt (right panel), see text for details.

Note that this calculation is general and applies to any signaling system which shows adaptation and is characterized by linear response coefficients $\widetilde{\chi}_\kappa$ and $\widetilde{\chi}_\tau$ for curvature and torsion.

Example calculation for the special case where only the curvature is modulated by chemotactic signaling. We present the deviation of (3.25) in full detail for the special case $\tau_1 = 0$, where the torsion of the sperm swimming path $\mathbf{r}(t)$ is not affected by chemotactic signaling. We calculate the centerline $\mathbf{R}$ and the helix vector $\mathbf{h}$ for a space curve $\mathbf{r}(t)$ with periodically modulated curvature and constant torsion

$$\kappa(t) = \overline{\kappa} + \widetilde{\kappa}_1 \cos \omega t, \quad \tau(t) = \tau_0. \tag{K.9}$$

where $\overline{\kappa} = \kappa_0 + \kappa_1 a_1$ and $\widetilde{\kappa}_1 = \rho_\kappa c_\perp r_0$, see equation (K.5). Note that $\widetilde{\kappa}_1 = \mathcal{O}(\nu)$. For equation (K.9) to hold, we have chosen time zero $t = 0$ such that $\varphi_0 = -\varphi_\kappa$; this ensures that the periodic modulation of the curvature can be written without any phase shift. By the Frenet-Serret equations, curvature and torsion determine a space curve $\mathbf{r}(t)$ which is unique up to a rigid body transformation $\mathcal{G}$ which itself depends on the initial conditions imposed. We express this space curve $\mathbf{r}(t)$ with respect to its Frenet frame $(\mathbf{t}(0), \mathbf{n}(0), \mathbf{b}(0))$ at time $t = 0$, thus postponing the issue of choosing initial conditions for a moment. As short-hand notation, we introduce the time-independent vectors

$$\begin{aligned}
\mathbf{e}_1 &= -\mathbf{n}(0) \\
\mathbf{e}_2 &= \cos \theta \, \mathbf{t}(0) - \sin \theta \, \mathbf{b}(0) \\
\mathbf{e}_3 &= \sin \theta \, \mathbf{t}(0) + \cos \theta \, \mathbf{b}(0)
\end{aligned} \tag{K.10}$$

where θ is the helix angle of the unperturbed helix with $\tan\theta = \tau_0/\kappa_0$. Solving the Frenet-Serret equations yields for $\mathbf{r}(t)$ to first order in ν

$$
\begin{aligned}
\mathbf{r}(t) = \mathbf{r}(0) &+ \left[r(\cos\omega t - 1) - \frac{\widetilde{\kappa}_1}{4}\omega^2 h^2 t^2 + \frac{\widetilde{\kappa}_1}{8}(2r^2 + h^2)(\cos 2\omega t - 1) \right] \mathbf{e}_1 \\
&+ \left[r\sin\omega t - \frac{\widetilde{\kappa}_1}{4}\omega(2r^2 + h^2)t + \frac{\widetilde{\kappa}_1}{8}(2r^2 + h^2)\sin 2\omega t \right] \mathbf{e}_2 \\
&+ \left[\omega h t + \frac{\widetilde{\kappa}_1}{2}rh\,(\omega t\cos\omega t - \sin\omega t) \right] \mathbf{e}_3 + \mathcal{O}(\nu^2)
\end{aligned}
\tag{K.11}
$$

The expression (K.11) for $\mathbf{r}$ can be rewritten nicely as $\mathbf{r} = \mathbf{R} + r\mathbf{h}_1$ with a centerline $\mathbf{R}$ that is free of oscillations

$$
\mathbf{R}(t) = \mathbf{R}(0) - \frac{\widetilde{\kappa}_1}{4}\omega^2 h^2\,t^2\,\mathbf{e}_1 - \frac{\widetilde{\kappa}_1}{4}\omega(2r^2 + h^2)\,t\,\mathbf{e}_2 + \omega h\,t\,\mathbf{e}_3(0) + \mathcal{O}(\nu^2),
\tag{K.12}
$$

and a rotating vector $\mathbf{h}_1$

$$
\mathbf{h}_1(t) = \cos\varphi(t)\,\mathbf{s}_1(t) + \sin\varphi(t)\,\mathbf{s}_2(t) + \mathcal{O}(\nu^2).
\tag{K.13}
$$

Here we introduced for notational convenience the time-dependent vectors $\mathbf{s}_1(t)$, $\mathbf{s}_2(t)$

$$
\mathbf{s}_1(t) = \mathbf{e}_1 + \frac{\widetilde{\kappa}_1}{2}\,\omega h\,t\,\mathbf{e}_3, \qquad \mathbf{s}_2(t) = \mathbf{e}_2 - \frac{\widetilde{\kappa}_1}{2}\,h\,\mathbf{e}_3.
\tag{K.14}
$$

The helix phase $\varphi(t)$ which characterizes the rotation of $\mathbf{h}_1$ obeys

$$
\dot\varphi = \Omega_3, \quad \varphi(0) = 0
\tag{K.15}
$$

with rotation rate

$$
\Omega_3(t) = \omega + \omega\widetilde{\kappa}_1\,\frac{r^2 + h^2}{4r}\cos\omega t + \mathcal{O}(\nu^2).
\tag{K.16}
$$

For the vectors $\mathbf{h}_2$ and $\mathbf{h}_3$, we have

$$
\begin{aligned}
\mathbf{h}_2(t) &= -\sin\varphi(t)\,\mathbf{s}_1(t) + \cos\varphi(t)\,\mathbf{s}_2(t) + \mathcal{O}(\nu^2), \\
\mathbf{h}_3(t) &= \mathbf{s}_1(t)\times\mathbf{s}_2(t) + \mathcal{O}(\nu^2) \\
&= \mathbf{e}_3 - \frac{\widetilde{\kappa}_1}{2}\omega h t\,\mathbf{e}_1 + \frac{\widetilde{\kappa}_1}{2}h\,\mathbf{e}_2 + \mathcal{O}(\nu^2)
\end{aligned}
\tag{K.17}
$$

The space curve $\mathbf{r}(t)$ is a perturbed helix which bends and tilts; bend and tilt of the helix is characterized by

$$
\begin{aligned}
\dot{\mathbf{h}}_3 \cdot \mathbf{s}_1 &= -\varepsilon_\kappa c_\perp \rho_\kappa + \mathcal{O}(\nu^2), & \left(\dot{\mathbf{R}} - \omega h\,\mathbf{h}_3\right)\cdot\mathbf{s}_1 &= 0 + \mathcal{O}(\nu^2), \\
\dot{\mathbf{h}}_3 \cdot \mathbf{s}_2 &= 0 + \mathcal{O}(\nu^2), & \left(\dot{\mathbf{R}} - \omega h\,\mathbf{h}_3\right)\cdot\mathbf{s}_2 &= -\delta_\kappa \rho_\kappa c_\perp + \mathcal{O}(\nu^2).
\end{aligned}
\tag{K.18}
$$

From the correspondence $\mathbf{s}_1(t) + i\,\mathbf{s}_2(t) = \mathbf{c}(t)\,e^{i\varphi_\kappa}/c_\perp + \mathcal{O}(\nu^2)$ we conclude (3.25) for the special case $\tau_1 = 0$.

Appendix L
Noisy trochoids:
Planar swimming paths in the weak noise limit

We study the stochastic equations (4.1-4.5) of planar sperm motion for a linear concentration field of chemoattractant $c(\underline{x}) = c_0 + c_1 \operatorname{Re} \underline{x}$ in the limit of

(i) a shallow concentration gradient with $\nu = c_1 r_0/(2c_0) \ll 1$, and

(ii) weak fluctuations of the effective stimulus $s_b + s(t)$ with $\eta = (s_b \sigma + \lambda c_0 \sigma)^{-1/2} \ll 1$.

Under these conditions, sperm swimming paths are noisy trochoids. Below we derive the expressions (4.32) and (4.33) for $\langle \underline{R} \rangle$ and $\langle |\delta \underline{R}|^2 \rangle$. To leading order, we anticipate a circular swimming path

$$\underline{r}(t) = \underline{R}(t) - i r_0 \, e^{i\omega_0 t + i\varphi_0} + \mathcal{O}(\nu, \eta) \tag{L.1}$$

which results in a periodic modulation of the binding rate $q(t)$ as in equation (4.26). Thus the stochastic stimulus can be written as

$$s(t) = \lambda c(\underline{R}(t)) + \lambda c_1 r_0 \sin(\omega_0 t + \varphi_0) + \xi_s + \mathcal{O}(\nu^2) \tag{L.2}$$

where ξ_s has zero mean and characterizes the fluctuations of $s(t)$. The autocorrelation function $S_s(t, \tau) = \langle \xi_s(t) \, \xi_s(t + \tau) \rangle$ of ξ_s changes with time t due to the presence of the concentration gradient. The Fourier transform of $S_\kappa(t, \tau)$ with respect to the time lag τ is given to leading order by $\widetilde{S}_\kappa(\omega_0) = \lambda c_0 + \mathcal{O}(\nu)$. In the following, we treat ξ_s as stationary with power spectrum $\widetilde{S}_s(\omega) = \lambda c_0$. The stimulus $s(t)$ determines a curvature

$$\kappa(t) = \kappa_0 + \rho_\kappa \lambda c_1 r_0 \sin(\omega_0 t + \varphi_0 + \varphi_\kappa) + \xi_\kappa + \mathcal{O}(\nu^2) \tag{L.3}$$

where ξ_κ is a stochastic process with zero mean representing the fluctuations of the curvature. Approximately, ξ_κ is stationary with power spectrum $\widetilde{S}_\kappa(\omega_0) = \rho_\kappa^2 \widetilde{S}_s(\omega_0) + \mathcal{O}(\nu)$. We compute the first and second moment of $\underline{R}$: In analogy to equation (4.13), we have

$$\text{(S)} \quad \dot{\underline{R}} = -r_0 v_0 \, (\kappa - \kappa_0) \, e^{i\varphi}. \tag{L.4}$$

Using (L.3), we find

$$\text{(S)} \quad \langle \dot{\underline{R}} \rangle = -r_0 v_0 \, \rho_\kappa \lambda c_1 r_0 \langle \sin(\omega_0 t + \varphi_0 + \varphi_\kappa) \, e^{i\omega_0 t + \varphi_0} \rangle + \mathcal{O}(\nu\eta^2, \nu^3) \tag{L.5}$$

and we conclude equation (4.32) for the chemotactic drift of the centerline. For the variance $\langle |\delta \underline{R}|^2 \rangle$, we proceed as in the case of a homogenous concentration field and find

$$\langle |\delta \underline{R}|^2 \rangle = \int_0^t dt_1 \int_0^t dt_2 \, \langle \delta \dot{\underline{R}} \, \delta \dot{\underline{R}}^* \rangle \tag{L.6}$$

with $\delta \dot{\underline{R}} = \dot{\underline{R}} - \langle \dot{\underline{R}} \rangle = -r_0 v_0 \, \xi_\kappa \, e^{i\varphi} + \mathcal{O}(\eta^2)$. From this, we conclude equation (4.33) for $\langle |\delta \underline{R}|^2 \rangle$. This result holds for times $t \ll c_0/(c_1 v_d)$, where $c_0/(c_1 v_d) = \mathcal{O}(\nu^2)$ is the time-scale on which $c(\underline{R}(t))$ changes.

Appendix M
Rigid body motion of the helix disk

M.1   The exponential coordinates of the helix matrix

In chapter 5, we introduced the helix matrix $H(t)$: The helix matrix characterizes the rigid body motion of the helix disk of helical sperm swimming paths in a concentration field of chemoattractant, see equation (5.53). In a homogenous concentration field, the helix matrix $H(nT)$ at time $t = nT$ can be expressed using exponential coordinates Ξ_j, see equation (5.14). Here, we derive the equations (5.15) and (5.58) for these exponential coordinates. Let $h_u = \omega_0 X_3 + \omega_0 h_0 X_6$ denote the **u**nperturbed infinitesimal propagator of $\mathcal{H}$. While the generators X_3 and X_6 of $\mathfrak{se}(3)$ commute with h_u, the complex generators Y and Z do not. Instead, we have the following relations which can be proved by induction

$$
\begin{aligned}
h_u^k \cdot Y &= Y \cdot (h_u - i\omega_0\, \mathbb{1})^k - i\omega_0 h_0\, k\, Z \cdot (h_u - i\omega_0\, \mathbb{1})^{k-1}, \quad \text{and} \\
h_u^k \cdot Z &= Z \cdot (h_u - i\omega_0\, \mathbb{1})^k.
\end{aligned}
\tag{M.1}
$$

Similarly, X_6 commutes with X_3, X_6, Z, but not with Y; we have the relation

$$
X_6^k \cdot Y = Y \cdot X_6^k - ik\, Z \cdot X_6^{k-1}.
\tag{M.2}
$$

Using these relations, we can compute the time-ordered exponential integral $H(nT) = \mathbf{T}\exp \int_0^{nT} dt\, h_u + \xi_j X_j$ to leading order in η proceeding exactly as in (5.17). We do not give the full calculation, but rather present three example cases below which convey the central idea. In the calculations, terms of the form $(\mathbb{1} + \zeta_j X_j) \cdot \exp(2\pi nh_0 X_6)$ appear where the ζ_j are some coefficients of order $\mathcal{O}(\eta)$. We state the useful identity

$$
(\mathbb{1} + \zeta_j X_j) \cdot \exp\left(2\pi nh_0 X_6\right) = \exp\left(2\pi nh_0 X_6 + \zeta_j X_j + \Psi\right) + \mathcal{O}(\eta^2)
\tag{M.3}
$$

with $\Psi = \pi nh_0(\zeta_1 X_5 - \zeta_2 X_4)$. We prove (M.3) in a special case

$$
\begin{aligned}
&\exp(2\pi nh_0 X_6 + \zeta_Y Y) \\
&= \exp(2\pi nh_0 X_6) + \sum_{k=0}^{\infty} \frac{(2\pi nh_0)^k}{(k+1)!}\, \zeta_Y \sum_{l=0}^{k} X_6^l \cdot Y \cdot X_6^{k-l} + \mathcal{O}(\eta^2) \\
&= \exp(2\pi nh_0 X_6) + \sum_{k=0}^{\infty} \frac{(2\pi nh_0)^k}{(k+1)!}\, \zeta_Y \sum_{l=0}^{k} Y \cdot X_6^k - i\,l\, Z \cdot X_6^{k-1} + \mathcal{O}(\eta^2) \\
&= (\mathbb{1} + \zeta_Y Y - i\pi nh_0\, \zeta_Y Z) \cdot \exp(2\pi nh_0 X_6) + \mathcal{O}(\eta^2).
\end{aligned}
\tag{M.4}
$$

We introduce short-hand notation for the terms which appear on the right-hand side of equations (5.15) and (5.58)

$$
\begin{aligned}
\Xi_{\mathrm{Y}}^{(0)} &= \int_0^{nT} dt\, \xi_{\mathrm{Y}}(t)\, e^{-i\omega_0 t}, \\
\Xi_{\mathrm{Z}}^{(0)} &= \int_0^{nT} dt\, \xi_{\mathrm{Z}}(t)\, e^{-i\omega_0 t}, \\
\Xi_{\mathrm{Z}}^{(1)} &= -i\omega_0 h_0 \int_0^{nT} dt\, t\, \xi_{\mathrm{Y}}(t)\, e^{-i\omega_0 t}, \\
\Xi_{j}^{(0)} &= \int_0^{nT} dt\, \xi_j(t), \quad j = 3, 6.
\end{aligned}
\tag{M.5}
$$

Now we have all the prerequisites to study the three examples announced above.

First example: complex bending fluctuations. Bending fluctuations of the helical swimming path are characterized by the complex stochastic process $\xi_{\mathrm{Y}} = \xi_1 - i\xi_2$. For the time integral of the infinitesimal propagator $\mathrm{h}_u + \xi_{\mathrm{Y}}\mathrm{Y}$, we find

$$
\begin{aligned}
\mathbf{T}\exp &\int_0^{nT} dt\, \mathrm{h}_u + \xi_{\mathrm{Y}}(t)\mathrm{Y} \\
&= \sum_{k=-1}^{\infty} \int_{0<t_1<\cdots<t_{k+1}<nT} dt_1 \cdots dt_{k+1} \prod_{l=1}^{k+1} (\mathrm{h}_u + \xi_{\mathrm{Y}}(t_l)\,\mathrm{Y}) \\
&= \exp(nT\,\mathrm{h}_u) + \sum_{k=0}^{\infty} \frac{1}{k!} \int_0^{nT} dt \sum_{l=0}^{k} \binom{k}{l} t^l\, (nT - t)^{k-l}\, \xi_{\mathrm{Y}}(t)\, \mathrm{h}_u^l \cdot \mathrm{Y} \cdot \mathrm{h}_u^{k-l} + \mathcal{O}(\eta^2) \\
&\overset{(*)}{=} \exp(nT\,\mathrm{h}_u) + \sum_{k=0}^{\infty} \frac{1}{k!} \int_0^{nT} dt \sum_{l=0}^{k} \binom{k}{l} t^l (nT - t)^{k-l} \\
&\qquad\qquad \xi_{\mathrm{Y}}(t) \left[\mathrm{Y} \cdot (\mathrm{h}_u - i\omega_0\,\mathbb{1})^l - i\omega_0 h_0\, l\, \mathrm{Z} \cdot (\mathrm{h}_u - i\omega_0\,\mathbb{1})^{l-1} \right] \mathrm{h}_u^{k-l} + \mathcal{O}(\eta^2) \\
&= \exp(2\pi n h_0\, \mathrm{X}_6) + \sum_{k=0}^{\infty} \frac{1}{k!} \int_0^{nT} dt\, \xi_{\mathrm{Y}}(t)\, \mathrm{Y} \cdot (nT\,\mathrm{h}_u - i\omega_0 t\,\mathbb{1})^k \\
&\qquad\qquad - i\omega_0 h_0\, k\, t\, \xi_{\mathrm{Y}}(t)\, \mathrm{Z} \cdot (nT\,\mathrm{h}_u - i\omega_0 t\,\mathbb{1})^{k-1} + \mathcal{O}(\eta^2) \\
&= \left(\mathbb{1} + \Xi_{\mathrm{Y}}^{(0)}\mathrm{Y} + \Xi_{\mathrm{Z}}^{(1)}\mathrm{Z} \right) \cdot \exp(2\pi n h_0 \mathrm{X}_6) + \mathcal{O}(\eta^2) \\
&\overset{(**)}{=} \exp\left(2\pi n h_0\, \mathrm{X}_6 + \Xi_{\mathrm{Y}}^{(0)}\mathrm{Y} + \Xi_{\mathrm{Z}}^{(1)}\mathrm{Z} + i\pi n h_0\, \Xi_{\mathrm{Y}}^{(0)}\mathrm{Z} \right) + \mathcal{O}(\eta^2).
\end{aligned}
\tag{M.6}
$$

Here we used the commutator relation (M.1) at $(*)$ and the matrix exponential formula (M.3) at $(**)$.

Second example: Complex transversal fluctuations. The complex stochastic process $\xi_{\mathrm{Z}} = \xi_4 - i\xi_5$ characterizes transversal fluctuations of the helical swimming

path; for $\mathbf{T}\exp \int dt\, \mathrm{h}_u + \xi_{\mathrm{Z}}\mathrm{Z}$, we have

$$
\mathbf{T}\exp \int_0^{nT} dt\, \mathrm{h}_u + \xi_{\mathrm{Z}}(t)\mathrm{Z}
$$

$$
= (\mathbb{1} + \Xi_{\mathrm{Z}}^{(0)}\mathrm{Z}) \cdot \exp(2\pi h_0 n \mathrm{X}_6) + \mathcal{O}(\eta^2) \tag{M.7}
$$

$$
= \exp\left(2\pi h_0 n \mathrm{X}_6 + \Xi_{\mathrm{Z}}^{(0)}\mathrm{Z}\right) + \mathcal{O}(\eta^2).
$$

Third example: Twist fluctuations. Finally, ξ_3 represents excess twist of the helical path; we obtain for $\mathbf{T}\exp \int dt\, \mathrm{h}_u + \xi_3 \mathrm{X}_3$

$$
\mathbf{T}\exp \int_0^{nT} dt\, \mathrm{h}_u + \xi_3(t)\mathrm{X}_3
$$

$$
= (\mathbb{1} + \Xi_3^{(0)}\mathrm{X}_3) \cdot \exp(2\pi h_0 n \mathrm{X}_6) + \mathcal{O}(\eta^2) \tag{M.8}
$$

$$
= \exp\left(2\pi h_0 n \mathrm{X}_6 + \Xi_3^{(0)}\mathrm{X}_3\right) + \mathcal{O}(\eta^2).
$$

The case of axial stretching characterized by ξ_6 can be dealt with analogously.

The computation of $\mathrm{H}(nT)$ combines all these examples and gives

$$
\mathrm{H}(nT) = \mathbf{T}\exp \int_0^{nT} dt\, \mathrm{h}_u + \xi_j \mathrm{X}_j
$$

$$
= \mathrm{Re}\left(\mathbb{1} + \Xi_{\mathrm{Y}}^{(0)}\mathrm{Y} + \Xi_{\mathrm{Z}}^{(0)}\mathrm{Z} + \Xi_{\mathrm{Z}}^{(1)}\mathrm{Z} + \Xi_3^{(0)}\mathrm{X}_3 + \Xi_6^{(0)}\mathrm{X}_6\right) \cdot \exp(2\pi h_0 n \mathrm{X}_6) + \mathcal{O}(\eta^2)
$$

$$
= \exp\Big(2\pi h_0 n \mathrm{X}_6 + \mathrm{Re}\, \Xi_{\mathrm{Y}}^{(0)}\mathrm{Y} + \Xi_{\mathrm{Z}}^{(0)}\mathrm{Z} + \Xi_{\mathrm{Z}}^{(1)}\mathrm{Z} - i\omega_0 h_0 nT\, \Xi_{\mathrm{Y}}^{(0)}\mathrm{Z}
$$

$$
\qquad\qquad\qquad\qquad + \Xi_3^{(0)}\mathrm{X}_3 + \Xi_6^{(0)}\mathrm{X}_6\Big) + \mathcal{O}(\eta^2). \tag{M.9}
$$

M.2 The correlation matrix

In section 5.5, we introduced the phase-averaged correlation matrix $\overline{\mathrm{C}}$, see equation (5.63). For an arbitrary symmetric matrix C, we find that its phase-averaged version $\overline{\mathrm{C}}$ is symmetric with 7 independent entries (entries not shown are zero)

$$
\overline{\mathrm{C}} = \begin{pmatrix}
\overline{C}_{11} & & & \overline{C}_{14} & \overline{C}_{15} & \\
& \overline{C}_{11} & & -\overline{C}_{15} & \overline{C}_{14} & \\
& & \overline{C}_{33} & & & \overline{C}_{36} \\
\overline{C}_{14} & -\overline{C}_{15} & & \overline{C}_{44} & & \\
\overline{C}_{15} & \overline{C}_{14} & & & \overline{C}_{44} & \\
& & \overline{C}_{36} & & & \overline{C}_{66}
\end{pmatrix} \tag{M.10}
$$

where the $\overline{C}_{kl}$ relate to the C_{kl} as follows

$$
\begin{aligned}
2\,\overline{C}_{jj} &= C_{jj} + C_{j+1,j+1}, \quad j = 1, 4 \\
2\,\overline{C}_{14} &= C_{14} + C_{25}, \\
2\,\overline{C}_{15} &= C_{15} - C_{24}, \\
\overline{C}_{kl} &= C_{kl}, \quad k, l = 3, 6.
\end{aligned}
\tag{M.11}
$$

We now consider the particular case of the correlation matrix C introduced in section 5.5 with entries $C_{kl} = \langle \Xi_k \Xi_l \rangle$. Here the Ξ_j are the exponential coordinates of the propagator $\mathrm{H}(nT)$ of the helix frame $\mathcal{H}$ of a helical sperm swimming path in a homogenous concentration field. To compute the entries $\overline{C}_{kl}$ of the phase-averaged correlation matrix $\overline{\mathrm{C}}$, we can proceed as in (5.21). With equation (M.11), we obtain to leading order in η

$$
\begin{aligned}
2\,\overline{C}_{11} &= \langle |\Xi_{\mathrm{Y}}|^2 \rangle &&= \Theta_{\mathrm{Y}}^2\, nT\, \widetilde{S}_a(\omega_0) && +\mathcal{O}(\eta^3), \\
2\,\overline{C}_{44} &= \langle |\Xi_{\mathrm{Z}}|^2 \rangle &&= \Theta_{\mathrm{Z}}^2\, nT\, \widetilde{S}_a(\omega_0) + \tfrac{1}{6}(\omega_0 h_0\, nT)^2\, \overline{C}_{11} && +\mathcal{O}(\eta^3), \\
2\,\overline{C}_{14} + 2i\,\overline{C}_{15} &= \langle \Xi_{\mathrm{Y}} \Xi_{\mathrm{Z}}^* \rangle &&= 0 && +\mathcal{O}(\eta^3), \\
\overline{C}_{kl} &= \langle \Xi_k \Xi_l \rangle &&= 0 && +\mathcal{O}(\eta^3)
\end{aligned}
\tag{M.12}
$$

where $\Theta_{\mathrm{Y}} = v_0(\tau_1 \cos\theta - \kappa_1 \sin\theta)$ and $\Theta_{\mathrm{Z}} = v_0 r_0(\tau_1 \sin\theta + \kappa_1 \cos\theta)$. These results hold provided nT is much larger than the correlation time σ of the fluctuations ξ_a of the output variable a. Note that all entries of the correlation matrix scale linearly with time, $\overline{C}_{kl} \sim nT$, except for $\overline{C}_{44}$. This entry has a contribution scaling like $(nT)^3$ due to the coupling of bending and transversal modes.

The phase-averaged correlation matrix $\overline{\mathrm{C}}$ is by definition invariant with respect to the adjoint action of $\mathrm{X}_\varphi = \exp \varphi \mathrm{X}_3$. The original correlation matrix C, however, lacks this property. The non-invariance of C with respect to the adjoint action of X_φ is a result of the non-phase-invariance of the bending and transversal fluctuations ξ_{Y} and ξ_{Z}, respectively. The quantity $\Phi = C_{14} - C_{25} - iC_{24} - iC_{15}$ is one (of several) measures for the non-phase-invariance of a correlation matrix. It is obviously zero for the phase-averaged matrix $\overline{\mathrm{C}}$. For the original correlation matrix, we compute

$$
\begin{aligned}
\Phi &= C_{14} - C_{25} - iC_{24} - iC_{15} \\
&= \langle \Xi_{\mathrm{Y}} \Xi_{\mathrm{Z}} \rangle \\
&= -\omega_0 h_0 \int_0^{nT} dt_1\, (t_1 - nT/2)\, e^{2i\omega_0 t_1} \int_0^{nT} dt_2\, \langle \xi_{\mathrm{Y}}(t_1)\, \xi_{\mathrm{Y}}(t_2) \rangle\, e^{-i\omega_0(t_1 - t_2)} + \mathcal{O}(\nu\eta^2, \eta^3) \\
&\approx -i\omega_0 h_0 \int_0^{nT} dt_1\, (t_1 - nT/2)\, e^{2i\omega_0 t_1} \Theta_{\mathrm{Y}}^2 \widetilde{S}_a(\omega_0) \\
&= -\frac{h_0\, nT}{2} \Theta^2\, \widetilde{S}_a(\omega_0)
\end{aligned}
\tag{M.13}
$$

which obviously is not zero.

M.3   Effective equation of motion

Continuum limit. We perform a continuum limit to derive an effective equation of motion for the centerline $\mathbf{R}(t)$ in a linear concentration field (5.23), proceeding essentially as in section 5.3.2.

We introduce an intermediate time-scale $\Delta t = nT$ which is much longer than the correlation time of total curvature and torsion fluctuations ξ_κ and ξ_τ, but as the same time much shorter than the time-scale on which $c(\mathbf{R}(t))$ changes. We design a stochastic trajectory $\widehat{\mathrm{H}}(t)$ in SE(3) which reproduces to leading order the second-order statistics of H(t) at the discrete times $t_m = m\,\Delta t$. More formally, we express $\widehat{\mathrm{H}}$ in terms of exponential coordinates $\widehat{\Xi}_j$

$$\widehat{\mathrm{H}}(t_{m+1}) \cdot \widehat{\mathrm{H}}(t_m)^{-1} = \exp\left(\omega_0\Delta t\mathrm{X}_3 + \omega_0 h_0\Delta t\mathrm{X}_6 + \widehat{\Xi}_j\mathrm{X}_j\right) \tag{M.14}$$

and require for the statistics of the $\widehat{\Xi}_j$ in view of (5.66) and (5.28)

$$\begin{aligned}
\langle\widehat{\Xi}_{\mathrm{Y}}\rangle = \langle\widehat{\Xi}_1 - i\widehat{\Xi}_2\rangle &= -nT\,c_\perp\,i\varepsilon_a\widetilde{\chi}_a(\omega_0)\,e^{-i\varphi_0} &+\mathcal{O}(\nu^2,\eta^2), \\
\langle\widehat{\Xi}_{\mathrm{Z}}\rangle = \langle\widehat{\Xi}_4 - i\widehat{\Xi}_5\rangle &= nT\,c_\perp\,i\delta_a\widetilde{\chi}_a(\omega_0)\,e^{-i\varphi_0} &+\mathcal{O}(\nu^2,\eta^2), \\
\langle\widehat{\Xi}_3\rangle &= nT\,c_\parallel\,\overline{\varepsilon} &+\mathcal{O}(\nu^2,\eta^2), \\
\langle\widehat{\Xi}_6\rangle &= nT\,c_\parallel\,\overline{\delta} &+\mathcal{O}(\nu^2,\eta^2)
\end{aligned} \tag{M.15}$$

as well as

$$\langle\delta\widehat{\Xi}_k\,\delta\widehat{\Xi}_l\rangle = \overline{C}_{kl} \quad + \mathcal{O}(\nu\eta^2,\eta^3). \tag{M.16}$$

Here φ_0 is the angle enclosed by $\mathbf{c}_\perp$ and $\mathbf{h}_1$ and $\delta\widehat{\Xi}_j = \widehat{\Xi}_j - \langle\widehat{\Xi}_j\rangle$. As usual, $c_\perp$ and $c_\parallel$ denote the lengths of the components of the concentration gradient $\boldsymbol{\nabla}c = \mathbf{c}_1$ perpendicular and parallel to $\mathbf{h}_3$, respectively; here the helix vector $\mathbf{h}_3(t_m)$ has to be evaluated at time t_m.

For the dynamics of $\widehat{\mathrm{H}}$, we anticipate a Stratonovich stochastic differential equation of the form

$$(\mathrm{S}) \quad \frac{d}{dt}\widehat{\mathrm{H}} = \widehat{\mathrm{H}} \cdot \widehat{\mathrm{h}}. \tag{M.17}$$

To fulfill equations (M.15) and (M.15), we choose $\widehat{\mathrm{h}}$ as

$$\widehat{\mathrm{h}} = \omega_0\mathrm{X}_3 + \omega_0 h_0\mathrm{X}_6 + \frac{1}{\Delta t}\langle\widehat{\Xi}_j\rangle\mathrm{X}_j + \widehat{\xi}_j\mathrm{X}_j \tag{M.18}$$

where $\widehat{\xi}_j$ is Gaussian white noise with $\langle\widehat{\xi}_k(t_1)\,\widehat{\xi}_l(t_2)\rangle = \widehat{C}_{kl}\,\delta(t_1 - t_2)$. The entries of the correlation matrix $\widehat{\mathrm{C}}$ satisfy

$$\begin{aligned}
\widehat{C}_{kl} &= \overline{C}_{kl}/\Delta t, \quad \text{unless } k = l = 4, 5, \text{ and} \\
\widehat{C}_{jj} &= \overline{C}_{44}/\Delta t - (\omega_0 h_0)^2\Delta t^2\,\overline{C}_{11}/12, \quad \text{for } j = 4, 5
\end{aligned} \tag{M.19}$$

We need a special definition for $\widehat{C}_{44}$ and $\widehat{C}_{55}$ due to the coupling of bending and transversal modes. Analogously to the computation in section M.1, one shows that

(M.16) is indeed fulfilled for our choice of noise terms given in equations (M.18) and (M.19). Note that $\check{C}_{kl} = \langle \delta \widehat{\Xi}_k \, \delta \widehat{\Xi}_l \rangle$ is already phase-invariant, i.e. $\check{C} = \mathrm{Ad}_{X_\varphi} \, \check{C} \, \mathrm{Ad}_{X_\varphi}^{\mathrm{T}}$. This is a consequence of the phase-invariance of the bending and transversal fluctuations $\widehat{\xi}_Y = \widehat{\xi}_1 - i\widehat{\xi}_2$ and $\widehat{\xi}_Z = \widehat{\xi}_4 - i\widehat{\xi}_5$, respectively. Equation (M.17) provides a coarse-grained description of helical sperm swimming path on time-scales larger than Δt. This result can be generalized to the case of a nonlinear concentration field provided that the local gradient is weak $\nu \ll 1$, and the nonlinearities are small on the length-scale $\omega_0 h_0 nT$.

Effective equation of motion. Rewriting (M.17) explicitly yields a Stratonovich stochastic differential equation for the centerline $\mathbf{R}(t)$ and the helix vector $\mathbf{h}(t)$

$$
\text{(S)} \quad
\begin{aligned}
\dot{\mathbf{R}} &= \omega h \, \mathbf{h}_3 - \delta_a \mathrm{Im} \left(\widetilde{\chi}_a(\omega_0) \, \mathbf{c} \right) + \widehat{\xi}_4 \, \mathbf{h}_1 + \widehat{\xi}_5 \, \mathbf{h}_2, \\
\dot{\mathbf{h}}_3 &= \phantom{\omega h \, \mathbf{h}_3} + \varepsilon_a \mathrm{Re} \left(\widetilde{\chi}_a(\omega_0) \, \mathbf{c} \right) + \varepsilon_{j3k} \, \widehat{\xi}_j \, \mathbf{h}_k, \\
\dot{\mathbf{h}}_1 &= -(\dot{\mathbf{h}}_3 \cdot \mathbf{h}_1) \, \mathbf{h}_3 \quad + \omega \, \mathbf{h}_2, \\
\dot{\mathbf{h}}_2 &= -(\dot{\mathbf{h}}_3 \cdot \mathbf{h}_2) \, \mathbf{h}_3 \quad - \omega \, \mathbf{h}_1,
\end{aligned}
\tag{M.20}
$$

where $\mathbf{c}$ is the complex gradient vector $\mathbf{c} = \mathbf{c}_\perp + i \, \mathbf{h}_3 \times \mathbf{c}_\perp$. The helix frequency $\omega = v_0 \sqrt{\overline{\kappa}^2 + \overline{\tau}^2}$, the helix radius $r = \overline{\kappa} \, v_0^2 / \omega^2$, and the helix pitch $h = \overline{\tau} \, v_0^2 / \omega^2$ are perturbed to first order in ν; here $\overline{\kappa}$ and $\overline{\tau}$ equal the mean of κ and τ averaged over a helix period, respectively. As in the deterministic case, we have $\overline{\kappa} = \kappa_0 + \kappa_1 a_1 + \mathcal{O}(\nu^2, \nu\eta, \eta^2)$ and $\overline{\tau} = \tau_0 + \tau_1 a_1 + \mathcal{O}(\nu^2, \nu\eta, \eta^2)$ with $a_1 = \mu\omega_0 h_0 \, c_\parallel / c_0$, see below equation (K.7).

Appendix N
List of symbols

Short list

a	answer variable of chemotactic signaling system 3.4
c	chemoattractant concentration
h_0	pitch of a helix is $2\pi\, h_0$
p	adaptation variable of the chemotactic signaling system (3.4)
r_0	radius of swimming circle or helix
$\mathbf{r}$	sperm swimming path
$\mathbf{R}$	centerline of circular or helical sperm swimming path $\mathbf{r}$
α	drift angle of sperm swimming circles w.r.t. to gradient direction
β	bending rate in eqn. (3.25): $\beta = |\boldsymbol{\nabla} c|\,\mathrm{Re}\left[\varepsilon_\tau \widetilde{\chi}_\tau(\omega_0) - \varepsilon_\kappa \widetilde{\chi}_\kappa(\omega_0)\right]$
κ	curvature of swimming path $\mathbf{r}$
τ	torsion of swimming path $\mathbf{r}$
χ	linear response function of chemotactic signaling system (3.4)
ψ	alignment angle of helical paths w.r.t. to gradient direction
ω_0	frequency of circular and helical swimming

The comprehensive symbol list

A	free energy
a	answer variable of chemotactic signaling system (3.4)
$\mathbf{b}$	binormal vector
c	chemoattractant concentration
$\mathbf{c}$	complex gradient vector $c = \mathbf{c}_\perp + i\,\mathbf{h}_3 \times \mathbf{c}_\perp$
C	correlation matrix
D	diffusion constant, fluctuation strength
$\mathbf{e}$	unit vector
E	Hamiltonian
$\mathbf{E}$	electric field
E_j	generator of $\mathfrak{so}(3)$: $(\mathrm{E}_j)_{kl} = \epsilon_{kjl}$
$\mathcal{F}$, F, f	Frenet frame, Frenet matrix (either $\in$ SO(3) or $\in$ SE(3)) and its infinitesimal propagator
$\mathbf{F}$	force
g	infinitesimal rigid body transformation
G	rigid body transformation

h_0	pitch of a helix is $2\pi\, h_0$
h	$h = h_0 + \mathcal{O}(\nu)$, see eqn. (K.7)
$\mathbf{h}_3$	helix vector
$\mathcal{H}$, H, h	helix frame, helix matrix and its infinitesimal propagator
h_u	infinitesimal propagator of **u**nperturbed helix $\mathrm{h}_u = \omega_0 \mathrm{X}_3 + \omega_0 h_0 \mathrm{X}_6$
i	imaginary unit
(I)	Itō stochastic differential equation
j, k, l, m, n	indices
k	a rate
J	probability flux
k_B	Boltzmann constant
l_P	persistence length
$\mathcal{L}$	lab frame; Fokker-Planck operator (chapter 4)
$\mathbf{M}$	angular momentum
$\mathbf{n}$	normal vector
$\underline{\mathrm{n}}$	normal vector in complex notation (chapter 4)
N	number of receptors
$\mathcal{O}(\varepsilon^n)$	big-O notation for terms of order ε^n with $\varepsilon \ll 1$
p	adaptation variable of the chemotactic signaling system (3.4); a probability
$\mathbf{p}$	point
P	probability density function
q	a rate of chemoattractant binding by the respective receptors
$\mathbf{q}$	a 4-vector representing either a point $\mathbf{p} \in \mathbb{A}^3$ or a vector $\mathbf{v} \in \mathrm{T}\mathbb{A}^3$
Q	rate of chemoattractant release by the egg
r_0	radius of swimming circle or helix
r	$r = r_0 + \mathcal{O}(\nu)$, see eqn. (K.7)
$\mathbf{r}$	sperm swimming path
$\underline{\mathrm{r}}$	planar sperm swimming path in complex notation (chapter 4)
R	distance from target $R = |\mathbf{R}|$
$\mathbf{R}$	centerline of circular or helical sperm swimming path $\mathbf{r}$
$\underline{\mathrm{R}}$	centerline of circular swimming path $\underline{\mathrm{r}}$ in complex notation (chapter 4)
s	chemoattractant stimulus; arclength (chapter 6)
S	autocorrelation function; entropy
$\widetilde{S}$	power spectrum
(S)	Stratonovich stochastic differential equation
t	time
$\mathbf{t}$	tangent vector $\mathbf{t} = \dot{\mathbf{r}}/v$
$\underline{\mathrm{t}}$	tangent vector in complex notation (chapter 4)
T	period of helical turn $T = 2\pi/\omega_0$; temperature
U	internal energy
$\mathbf{u}$	swimming response unit
v	swimming speed
$\mathbf{v}$	vector

V	translation vector
W	rotation matrix
x, y, z	Cartesian coordinates
X_j	generator of $\mathfrak{se}(3)$: X_1, X_2, X_3 for rotations, X_1, X_2, X_3 for translations
Y	complex bending mode: $Y = X_1 + iX_2 \in \mathfrak{se}(3) \times \mathbb{C}$
Z	complex tilting mode: $Z = X_4 + iX_5 \in \mathfrak{se}(3) \times \mathbb{C}$
α	drift angle of sperm swimming circles w.r.t. to gradient direction
β	bending rate in eqn. (3.25): $\beta = \lvert \boldsymbol{\nabla} c \rvert \operatorname{Re} \left[\varepsilon_\tau \widetilde{\chi}_\tau(\omega_0) - \varepsilon_\kappa \widetilde{\chi}_\kappa(\omega_0) \right]$
γ	tilt coefficient in eqn. (3.25): $\gamma = \lvert \boldsymbol{\nabla} c \rvert \operatorname{Im} \left[\delta_\tau \widetilde{\chi}_\tau(\omega_0) - \delta_\kappa \widetilde{\chi}_\kappa(\omega_0) \right]$
δ	Dirac δ-function
δ_κ, δ_τ	coupling coefficients for helix tilt: $\delta_\kappa = \omega_0 r_0 (2r_0^2 + 3h_0^2)/4$, $\delta_\tau = \omega_0 r_0^2 h_0/4$
δ_a	$\delta_a = \lambda \omega_0 r_0^2 (r_0 \kappa_1 + h_0 \tau_1)/2$
$\overline{\delta}$	coefficient for axial stretching: $\overline{\delta} = \mu \omega_0 h_0 r_0 \Theta_Y / c_0$
ε	perturbation parameter
ε_κ, ε_τ	coupling coefficients for helix bending: $\varepsilon_\kappa = \omega_0 r_0 h_0/2$, $\varepsilon_\tau = \omega_0 r_0^2/2$
ε_a	$\varepsilon_a = \lambda (\varepsilon_\tau \tau_1 - \varepsilon_\kappa \kappa_1)$
$\overline{\varepsilon}$	coefficient for excess axial twisting: $\overline{\varepsilon} = \mu \omega_0 h_0 \Theta_3 / c_0$
ζ	friction coefficient
η	a spherical coordinate, dynamical viscosity of water
θ	helix angle $\tan^{-1}(h_0/r_0)$, a spherical coordinate, Heaviside function
ι	not used ☺
κ	curvature of swimming path $\mathbf{r}$
κ_0	mean torsion
κ_1	coupling coefficient for the curvature response, see eqn. (3.3)
λ	normalized chemoattractant binding rate: $\langle s \rangle = \lambda c$
μ	adaptation time scale of chemotactic signaling, see eqn. (3.4)
ν	characterizes weak concentration gradients: $\nu = r_0 \lvert \boldsymbol{\nabla} c \rvert / c$
$\xi(t)$	random process
π	the circle number
ρ	amplitude gain of chemotactic signaling; a density
$\overline{\rho}_\kappa$	amplification strength of chemotactic signaling $\rho_\kappa = \overline{\rho}_\kappa / (s_b + \lambda c)$
σ	relaxation time scale of chemotactic signaling, see eqn. (3.4)
τ	torsion of swimming path $\mathbf{r}$; time interval (chapter 4)
τ_0	mean torsion
τ_1	coupling coefficient for the torsion response, see eqn. (3.21)
υ	an exponent: $\upsilon = \Gamma_0 / D_0$
φ	phase angle
χ_κ, χ_τ, χ_a	linear response function of chemotactic signaling system (3.4) for κ, τ, a
ψ	alignment angle of helical paths w.r.t. to gradient direction
ω_0	angular frequency of circular and helical swimming
ω	$\omega = \omega_0 + \mathcal{O}(\nu)$, see eqn. (K.7)
ω_f	angular frequency of the flagellar beat

Γ_0	in chapter 3: $\gamma = \Gamma_0/R$; in chapter 5: $v_d \sin \varphi_\kappa = \Gamma_0/R$
Δ	finite difference; Laplace operator
Θ	a coefficient in chapter 4: $\Theta = \bar{\rho}_\kappa r_0^2 v_0 / 2$
$\Theta_Y, \Theta_Z, \Theta_3$	$\Theta_Y = v_0(\tau_1 \cos \theta - \kappa_1 \sin \theta)$, $\Theta_Z = r_0 \Theta_3$,
	$\Theta_3 = v_0(\tau_1 \sin \theta + \kappa_1 \cos \theta)$, see chapter 5
Λ	a coefficient in (3.30): $\Lambda = \omega h - \gamma \cos \psi$
Ξ	random variable
Φ	radial distribution function of persistent random walks, see chapter 6
Ψ	an integral of Φ
Π	product
Ω	rotation rate
$\boldsymbol{\Omega}$	rotational velocity
$\mathbb{1}$	Identity matrix
$\mathbf{T}\exp$	time ordered exponential integral
Re	real part
Im	imaginary part

Bibliography

[1] A. Acrivos and T. D. Taylor. Heat and mass transfer from single spheres in Stokes flow. *The Phys. of Fluids*, 5(4):387–394, 1962.

[2] B. A. Afzelius. Asymmetry of cilia and flagella of mice and men. *Int. J. Dev. Biol.*, 43(4):2283–286, 1999.

[3] B. A. Afzelius, S. L. R. Dallai, and P. L. Bellon. Flagellar structure in normal human spermatozoa and in spermatozoa that lack dynein arms. *Tissue and Cell*, 27(3):241–247, 1995.

[4] B. Alberts, D. Bray, K. Hopkins, A. Johnson, J. Lewis, M. Raff, K. Roberts, and P. Walter. *Essential Cell Biology*. Garland Science, second edition, 2004.

[5] B. Alberts, D. Bray, J. Lewis, M. Raff, K. Roberts, and J. D. Watson. *Molecular Biology of the Cell*. Garland Publ. Inc., third edition, 1994.

[6] U. Alon, M. Surette, N. Barkai, and S. Leibler. Robustness in chemical networks. *Nature*, 397:168–171, 1999.

[7] W. Alt and R. Schaaf. Chemotaxis of gametes: A diffusion approximation. *IMA J. Math. Appl. in Med. & Biol.*, 2:109–129, 1985.

[8] S. Asakura. Polymerization of flagellin and polymorphism of flagella. *Adv. Biophys.*, 1:99–155, 1970.

[9] R. C. Babcock, C. N. Mundy, and D. Whitehead. Sperm diffusion models and in situ confirmation of long-distance fertilization in the free-spawning asteroid *Acanthaster planci*. *Biol. Bull.*, 186:17–28, 1994.

[10] A. Bahat and M. Eisenbach. Sperm thermotaxis. *Mol. and Cell. Endocrin.*, 252(1):115–119, 2006.

[11] N. Barkai and S. Leibler. Robustness in simple biochemical networks. *Nature*, 387:913–917, 1997.

[12] L. E. Becker, S. A. Koehler, and H. A. Stone. On self-propulsion of micromachines at low Reynolds number: Purchell's three-link swimmer. *J. Fluid Mech.*, 490:15–35, 2003.

[13] N. B. Becker. *Sequence Dependent Elasticity of DNA*. PhD thesis, MPI PKS and TU Dresden, 2007. Supervisor: R. Everaers.

[14] N. B. Becker and R. Everaers. From rigid base pairs to semiflexible polymers: Coarse-graining DNA. *Phys. Rev. E*, 76:021923, 2007.

[15] O. Bénichou, C. Loverdo, and R. Voiturez. A minimal model of intermittent search in dimension two. *J. Phys.: Condens. Matter*, 19:065141–065158, 2007.

[16] H. C. Berg. *Random Walks in Biology.* Princeton UP, 1993.

[17] H. C. Berg. E. coli *in Motion.* Springer, 2004.

[18] H. C. Berg and D. A. Brown. Chemotaxis in *Escherichia coli* analysed by three-dimensional tracking. *Nature*, 239:500–504, 1972.

[19] H. C. Berg and E. M. Purchell. Physics of chemoreception. *Biophys. J.*, 20:193–219, 1977.

[20] W. Bialek and S. Setayeshgar. Physical limits to biochemical signaling. *Proc. Natl. Acad. Sci. U.S.A.*, 102(29):10040–10045, 2007.

[21] T. R. Birkhead and A. P. Møller, editors. *Sperm competition and sperm selection.* Academic Press, 1998.

[22] M. Böhmer, Q. Van, I. Weyand, V. Hagen, M. Beyermann, M. Matsumoto, M. Hoshi, E. Hildebrand, and U. B. Kaupp. Ca^{2+}-spikes in the flagellum control chemotactic behaviour of sperm. *EMBO J.*, 24(15):2741–2752, 2005.

[23] C. Brennen and H. Winet. Fluid mechanics of propulsion by cilia and flagella. *Ann. Rev. Fluid Mech.*, 9:339–398, 1977.

[24] D. R. Brillinger. A particle migrating randomly on a sphere. *J. theoret. Prob.*, 10(2):429–443, 1997.

[25] C. J. Brokaw. Chemotaxis of bracken spermatozoids. *J. exp. Biol.*, 35(1):197–212, 1958.

[26] C. J. Brokaw. Random and oriented movements of bracken spermatozoids. *J. Cell. Comp. Physiol.*, 54:95–101, 1959.

[27] C. J. Brokaw. Calcium-induced asymmetrical beating of triton-demembranated sea urchin sperm flagella. *J. Cell Biol.*, 82(2):401–411, 1979.

[28] S. Camalet, T. Duke, F. Jülicher, and J. Prost. Auditory sensitivity provided by self-tuned critical oscillations of hair cells. *Proc. Natl. Acad. Sci. U.S.A.*, 97(7):3183–3188, 2000.

[29] S. Camalet and F. Jülicher. Self-organized beating and swimming of internally driven filaments. *Phys. Rev. Lett.*, 82(7):1590–1593, 1999.

[30] S. Camalet and F. Jülicher. Generic aspects of axonemal beating. *New J. of Phys.*, 2:24.1–24.23, 2000.

[31] D. L. Clapper and G. G. Brown. Sperm motility in the horseshoe crab *Limulus polyphemus L. Dev. Biol.*, 76:341–349, 1980.

[32] C. A. Condat, G. J. Sibona, and C. E. Budde. Steady state in two-dimensional diffusion-controlled reations. *J. Stat. Phys.*, 89(1):369–377, 1997.

[33] G. Corkidi, B. Taboada, C. D. Wood, A. Guerrero, and A. Darszon. Tracking sperm in three-dimensions. *Biochem. & Biophys. Res. Comm.*, 373(1):125–129, 2008.

[34] H. C. Crenshaw. Orientation by helical motion i. Kinematics of the helical motion of organisms with up to 6 degrees of freedom. *Bull. Math. Biol.*, 55(1):197 – 212, 1993.

[35] H. C. Crenshaw. Orientation by helical motion iii. Microorganisms can orient to stiumuli by changing the direction of their rotational velocity. *Bull. Math. Biol.*, 55(1):231 – 255, 1993.

[36] H. C. Crenshaw. Negative phototaxis in *Chlamydomonas* is via helical klinotaxis - A new paradigm for phototaxis. *Mol. Biol. Cell.*, 7:279 – 279, 1996.

[37] H. C. Crenshaw. A new look at locomotion in microorganisms: Rotating and translating. *Americ. Zool.*, 36(6):608 – 618, 1996.

[38] H. C. Crenshaw, C. N. Ciampaglio, and M. McHenry. Analysis of the three-dimensional trajectories of organisms: Estimates of velocity, curvature and torsion from positional information. *J. exp. Biol.*, 203(6):961 – 982, 2000.

[39] H. C. Crenshaw and L. Edelstein-Keshet. Orientation by helical motion ii. Changing the direction of the axis of motion. *Bull. Math. Biol.*, 55(1):213 – 230, 1993.

[40] P. J. W. Debye. *Polar molecules.* Dover, 1929.

[41] T. Dertinger and U. B. Kaupp. Diffusion constant of *resact-Alexa647* obtained by fluorescence correlation spectroscopy. Unpublished result.

[42] R. Dreyfus, J. Baudry, and H. A. Stone. Purcell's rotator: mechanical rotation at low Reynolds number. *Eur. Phys. J. B*, 47:161–164, 2005.

[43] S. K. Dutcher. Elucidation of basal body and centriole functions in *Chlamydomonas reinhardtii. Traffic*, 4(7):443–451, 2003.

[44] A. M. Edwards, R. A. Phillips, N. W. Watkins, M. P. Freeman, E. J. Murphy, V. Afanasyev, S. V. Buldyrev, M. G. E. da Luz, E. P. Raposo, E. H. Stanley, and G. M. Viswanathan. Revisiting Lévy flight search patterns of wandering albatrosses, bumblebees and deer. *Nature*, 449(7165):1044–1048, 2007.

[45] A. Einstein. Über die von der molekularkinetischen Theorie der Wärme geforderte Bewegung von in ruhenden Flüssigkeiten suspendierten Teilchen. *Annal. Phys.*, 322(8):549–560, 1905.

[46] M. Eisenbach. Sperm chemotaxis. *Rev. Reprod.*, 4(1):56 – 66, 1999.

[47] M. Eisenbach. Towards understanding the molecular mechanism of sperm chemotaxis. *J. of Gen. Physol.*, 124(2):105 – 108, 2004.

[48] M. Eisenbach and L. C. Giojalas. Sperm guidance in mammals – an unpaved road to the egg. *Nature Rev. Mol. Cell Biol.*, 7:276–285, 2006.

[49] J. Elgeti and G. Gompper. Hydrodynamics of active mesoscopic systems. In G. Münster, D. Wolf, and M. Kremer, editors, *NIC Symposium 2008*, volume 39, pages 53–62. John von Neumann Institute for Computing, Jülich, 2008.

[50] G. Fabro, R. A. Rovasio, S. Civalero, A. Frenkel, S. R. Caplan, M. Eisenbach, and L. C. Giojalas. Chemotaxis of capacitated rabbit spermatozoa to follicular fluid revealed by a novel directionality-based assay. *Biol. of Reprod.*, 67(5):1565 – 1571, 2002.

[51] G. S. Farley. Helical nature of sperm swimming affects the fit of fertilization-kinetics to empirical data. *Biol. Bull.*, 203:51–57, 2001.

[52] G. S. Farley and D. R. Levitan. The role of jelly coats in sperm-egg encounters, fertilization success, and selection on egg size in broadcast spawners. *Americ. Naturalist*, 157(6):626–636, 2001.

[53] T. Fenchel. Microbial behavior in a heterogeneous world. *Science*, 296:1068–1071, 2002.

[54] H. Fischer and A. F. Craievich. Average protein density is a molecular-weight-dependent function. *Prot. Science*, 13:2825–2828, 2004.

[55] B. M. Friedrich. A mesoscopic model for helical bacterial flagella. *J. Math. Biol.*, 53(1):162–178, 2006.

[56] B. M. Friedrich and F. Jülicher. Chemotaxis of sperm cells. *Proc. Natl. Acad. Sci. U.S.A.*, 104(33):13256–13261, 2007.

[56a] B. M. Friedrich. Search along persistent random walks. *Phys. Biol.*, 5:026007, 2008.

[56b] B. M. Friedrich and F. Jülicher. The stochastic dance of circling sperm cells: sperm chemotaxis in the plane. *New J. of Phys.*, 10:123025, 2008.

[57] A. Gakamsky. *Gradient sensing mechanism and behavioral response of mammalian sperm chemotaxis.* PhD thesis, Weizmann Institute of Science, Rehovot, Israel, 2006. Supervisor: M. Eisenbach.

[58] D. L. Garbers. Molecular basis of fertilization. *Annu. Rev. Biochem.*, 58:719–742, 1989.

[59] R. Garcia, F. Moss, A. Nihongi, J. R. Strickler, S. Göller, U. Erdmann, L. Schimansky-Geier, and I. M. Sokolov. Optimal foraging by zooplankton within patches: The case of *Daphnia. Math. Biosci.*, 207:165–188, 2007.

[60] L. C. Giojalas and R. A. Rovasio. Mouse spermatozoa modify their dynamic parameters and chemotactic response to factors from the oocyte microenvironment. *Int. J. Androl.*, 21:201–206, 1998.

[61] J. Gray. The movement of sea-urchin spermatozoa. *J. Exp. Biol.*, 32:775–801, 1955.

[62] S. Grill, K. Kruse, and F. Jülicher. Theory of mitotic spindle oscillations. *Phys. Rev. Lett.*, 94:108104–108107, 2005.

[63] S. Hecht, S. Shlaer, and M. H. Pirenne. Energy, quanta and vision. *J. Gen. Physiol.*, 25:819–840, 1942.

[64] J. J. Hermans and R. Ullman. The statistics of stiff chains, with applications to light scattering. *Physica*, 18(11):951–971, 1952.

[65] P. Herzmark, K. Campbell, F. Wang, K. Wong, H. El-Samad, A. Groisman, and H. R. Bourne. Bound attractant at the leading vs. the trailing edge determines chemotactic prowess. *Proc. Natl. Acad. Sci. U.S.A.*, 104(33):13349–13354, 2007.

[66] A. Hilfinger. *Dynamics of Cilia and Flagella.* PhD thesis, MPI PKS and TU Dresden, 2005. Supervisor: Frank Jülicher.

[67] A. Hilfinger and F. Jülicher. The chirality of ciliary beats. *Phys. Biol.*, 5:1–12, 2008.

[68] B. Hille. *Ion Channels of Excitable Membranes*. Sinauer, 2001.

[69] J. Howard. *Mechanics of Motor Proteins and the Cytoskeleton*. Sinauer, 2001.

[70] K. Inaba. Molecular architecture of the sperm flagella: Molecules for motility and signaling. *Zool. Sci.*, 20:1043–1056, 2003.

[71] S. Ishijima, S. Oshio, and H. Mohri. Flagellar movement of human spermatozoa. *Gamete Research*, 13:185–197, 1986.

[72] M. Ishikawa, H. Tsutsui, J. Cosson, Y. Oka, and M. Morisawa. Strategies for sperm chemotaxis in the siphonophores and ascidians: A numerical simulation study. *Biol. Bull.*, 206(2):95 – 102, 2004.

[73] R. E. Johnson and C. J. Brokaw. Flagellar hydrodynamics. *Biophys. J.*, 25:113–127, 1979.

[74] K. Josef, J. Saranak, and K. W. Foster. Ciliary behaviour of a negatively phototactic *Chlamydomonas reinhardtii*. *Cell Mot. Cytoskel.*, 61:97–111, 2005.

[75] F. Jülicher and J. Prost. Spontaneous oscillations of collective molecular motors. *Phys. Rev. Lett.*, 78(23):4510–4513, 1997.

[76] U. B. Kaupp. Personal communication.

[77] U. B. Kaupp, E. Hildebrand, and I. Weyand. Sperm chemotaxis in marine invertebrates – Molecules and mechanisms. *J. Cell. Phys.*, 208:487–494, 2006.

[78] U. B. Kaupp, N. D. Kashikar, and I. Weyand. Mechanisms of sperm chemotaxis. *Annu. Rev. Physiol.*, 70:93–117, 2008.

[79] U. B. Kaupp, J. Solzin, E. Hildebrand, J. E. Brown, A. Helbig, V. Hagen, M. Beyermann, F. Pampaloni, and I. Weyand. The signal flow and motor response controling chemotaxis of sea urchin sperm. *Nature Cell Biol.*, 5(2):109 – 117, 2003.

[80] E. F. Keller and L. A. Segel. Model for chemotaxis. *J. theoret. Biol.*, 30:225–234, 1971.

[81] J. B. Keller and S. I. Rubinow. Swimming of flagellated microorganisms. *Biophys. J.*, 16:151–170, 1976.

[82] M. Kemp. MicroAUVs II: Control. In *Proc. 12th Unmanned, Untethered Submersible Technology*, Lee, NH, 2001. Autonomous Undersea Systems Institute.

[83] S. H. Koenig. Brownian motion of an ellipsoid. A correction to Perrin's results. *Biopolymers*, 14:2421–2423, 1975.

[84] J. Koiller, K. Ehlers, and R. Montgomery. Problems and progress in microswimming. *J. Nonlinear Sci.*, 6:507–541, 1996.

[85] O. Kratky and G. Porod. Röntgenuntersuchung gelöster Fadenmoleküle. *Rec. Trav. Chim. Pays-Bas*, 68:1106–1123, 1949.

[86] L. D. Landau and E. M. Lifschitz. *Hydrodynamik*. Akademie Verlag, 1991.

[87] A. W. C. Lau and T. C. Lubensky. State-dependent diffusion: Thermodynamic consistency and its path integral formulation. *Phys. Rev. E*, 76:011123(17), 2007.

[88] H. Levine, D. A. Kessler, and W. Rappel. Directional sensing in eukaryotic chemotaxis: A balanced inactivation model. *Proc. Natl. Acad. Sci. U.S.A.*, 103(26):9761–9766, 2006.

[89] D. Levitan, M. Sewell, and F. Chia. Kinetics of fertilization in the sea urchin *Strongylocentrus franciscanus*: Interaction of gamete dilution, age and contact time. *Biol. Bull.*, 181:371–378, 1991.

[90] D. R. Levitan. Sperm velocity and longevity trade off each other and influence fertilization in the sea urchin. *Proc. R. Soc. Lond. B*, 533, 2000.

[91] D. R. Levitan and C. Petersen. Sperm limitation in the sea. *Trends in Ecology & Evolution*, 10(6):228–231, 1995.

[92] L. Li, S. F. Nørrelykke, and E. C. Cox. Persistent cell motion in the absence of external signals: A search strategy for eukaryotic cells. *PLOS One*, 3(5):e2093, 2008.

[93] J. H. Long, A. C. Lammert, C. A. Pell, M. Kemp, J. A. Strother, H. C. Crenshaw, and M. J. McHenry. A navigational primitive: Biorobotic implementation of cycloptic helical klinotaxis in planar motion. *IEEE J. Oceanic Engineering*, 29(3):795 – 806, 2004.

[94] Lord Rothschild and M. M. Swann. The fertilization reaction in the sea-urchin egg. A propagated response to sperm attachment. *J. exp. Biol.*, 26:164–176, 1949.

[95] H. Machemer. Ciliary activity and the origin of metachrony in *Paramecium*: Effects of increased viscosity. *J. exp. Biol.*, 57:239–259, 1972.

[96] I. Manton. Observations on the microanatomy of the spermatozoid of the bracken fern (*Pteridium aquilinum*). *J. Biophys. and Biochem. Cytol.*, 6:413–418, 1959.

[97] M. J. McHenry. The morphology, behaviour, and biomechanics of swimming in ascidian larvae. *Can. J. Zool.*, 83:62–74, 2005.

[98] M. J. McHenry and J. A. Strother. The kinematics of phototaxis in larvae of the ascidian *Aplidium constellatum*. *Marine Biol.*, 142:173–184, 2003.

[99] R. L. Miller. Sperm chemotaxis in ascidians. *Americ. Zool.*, 22(4):827 – 840, 1982.

[100] R. L. Miller. Sperm chemo-orientation in the metazoa. In C. B. Metz and A. Manory, editors, *Biology of Fertilization. Biology of the Sperm*, volume 2, pages 275–337. Academic, 1985.

[101] P. Moore and J. Crimaldi. Odor landscapes and animal behavior: tracking odor plumes in different physical worlds. *J. of Marine Systems*, 49:55–64, 2004.

[102] R. E. Mortensen. Modeling stochastic nonlinear dynamic systems. *J. Stat. Phys.*, 2:271–296, 1969.

[103] R. M. Murray, Z. Li, and S. S. Sastry. *A Mathematical Introduction to Robotic Manipulation*. CRC Press, 1996.

[104] A. Najafi and R. Golestanian. Simple swimmer at low Reynolds number: Three linked spheres. *Phys. Rev. E*, 69(6):062901–4, 2004.

[105] K. Namba and F. Vonderviszt. Molecular architecture of bacterial flagellum. *Quart. Rev. of Biophys.*, 30(1):1–65, 1997.

[106] B. Navarro, Y. Kirichok, and D. E. Clapham. KSper, a pH-sensitive K^+ current that controls sperm membrane potential. *Proc. Natl. Acad. Sci. U.S.A.*, 104(18):7688–7692, 2007.

[107] T. Nishigaki and A. Darszon. Real-time measurements of the interactions between fluorescent speract and its sperm receptor. *Develop. Biol.*, 233:17–26, 2000.

[108] T. Nishigaki, C. D. Wood, Y. Tatsu, N. Yumoto, T. Furuta, D. Elias, K. Shiba, S. A. Baba, and A. Darszon. A sea urchin egg jelly peptide induces a cGMP-mediated decrease in sperm intracellular Ca^{2+} before its increase. *Develop. Biol.*, 272(2):376 – 388, 2004.

[109] S. Nonaka, H. Shiratori, Y. Saijoh, and H. Hamada. Determination of left-right patterning of the mouse embryo by artificial nodal flow. *Nature*, 418(6893):96–99, 2002.

[110] S. Nonaka, Y. Tanaka, S. Takeda, A. Hareda, Y. Kanai, M. Kino, and N. Hirokawa. Randomization of left-right asymmetry due to loss of nodal cilia generating leftward flow of extraembryonic fluid in mice lacking kif3b motor protein. *Cell*, 95(6):829, 1998.

[111] B. Øksendal. *Stochastic differential equations.* Springer, 2000.

[112] A. Okubo and S. A. Levin. *Diffusion and Ecological Problems.* Springer, 1980.

[113] R. G. Oliveira, L. Tomasi, R. A. Rovasio, and L. C. Giojalas. Increased velocity and induction of chemotactic response in mouse spermatozoa by follicular and oviductal fluids. *J. Reprod. Fertil.*, 115:23–27, 1999.

[114] J. H. Olson, X. Y. Xiang, T. Ziegert, A. Kittelson, A. Rawls, A. L. Bieber, and D. E. Chandler. Allurin, a 21-kDa sperm chemoattractant from *Xenopus* egg jelly, is related to mammalian sperm-binding proteins. *Proc. Natl. Acad. Sci. U.S.A.*, 98(20):11205 – 11210, 2001.

[115] J. Pan, Q. Wang, and W. J. Snell. Cilium generated signalling and cilia-related disorders. *Lab. Invest.*, 85:452–463, 2005.

[116] G. J. Pazour and G. B. Witman. The vertebrate primary cilium is a sensory organelle. *Current Opinion*, 15:105–110, 2003.

[117] J. T. Pennington. The ecology of fertilization of *Echinoid* eggs: The consequences of sperm dilution, adult aggregation, and synchronous spawning. *Biol. Bull.*, 169:417–430, 1985.

[118] F. Perrin. Etude mathematique du mouvement Brownien de rotation. *Ann. Sci. de l'ENS*, 3(45):1–51, 1928.

[119] F. Perrin. Mouvement Brownien d'un ellipsoide (I). Dispersion dièlectrique pour des molécules ellipsoidales. *Le Journal de Physique et le Radium*, 7(5):497–511, 1934.

[120] G. Pólya. Über eine Aufgabe der Wahrscheinlichkeitsrechnung betreffend die Irrfahrt im Straßennetz. *Math. Ann.*, 84:149–160, 1921.

[121] M. J. Potel and S. A. MacKay. Preaggregative cell motion in *Dictyostelium. J. Cell Sci.*, 36:281–309, 1979.

[122] E. M. Purcell. Life at low Reynolds numbers. *Am. J. Phys.*, 45(1):1–11, 1977.

[123] E. M. Purcell. The effect of fluid motion of the absorption of molecules by suspended particles. *J. Fluid. Mech.*, 84(3):551–559, 1978.

[124] D. Ralt, M. Manor, A. Cohen-Dayag, I. Tur-Kaspa, I. Makler, I. Yuli, J. Dor, S. Blumberg, S. Mashiach, and M. Eisenbach. Chemotaxis and chemokinesis of human spermatozoa to follicular factors. *Biol. Reprod.*, 50:774–785, 1994.

[125] I. H. Riedel. *Mechanics of the axoneme: Self-organized beating patterns and vortex arrays of spermatozoa.* PhD thesis, TU Dresden, 2005. Supervisor: Jonathon Howard.

[126] I. H. Riedel, K. Kruse, and J. Howard. A self-organized vortex array of hydrodynamically entrained sperm cells. *Science*, 309(5732):300–303, 2005.

[127] I. H. Riedel-Kruse, A. Hilfinger, J. Howard, and F. Jülicher. How molecular motors shape the flagellar beat. *HFSP*, 1(3):192–208, 2007.

[128] J. A. Riffell and P. J. Krug. The ecological and evolutionary consequences of sperm chemoattraction. *Proc. Natl. Acad. Sci. U.S.A.*, 101(13):4501–4506, 2004.

[129] J. A. Riffell, P. J. Krug, and R. K. Zimmer. Fertilization in the sea : The chemical identity of an abalone sperm attractant. *J. exp. Biol.*, 205:1439–1450, 2002.

[130] J. A. Riffell and R. K. Zimmer. Sex and flow: The consequences of fluid shear for sperm-egg interactions. *J. exp. Biol.*, 210:3644–3660, 2007.

[131] H. Risken. *The Fokker-Planck Equation.* Springer, 1996.

[132] U. Rüffer and W. Nultsch. High-speed cinematographic analysis of the movement of *Chlamydomonas. Cell Motility*, 5:251–263, 1985.

[133] N. Saito, K. Takahashi, and Y. Yunoki. The statistical mechanics of stiff chains. *J. Phys. Soc. Japan*, 22(1):219–226, 1967.

[134] J. Samuel and S. Sinha. Elasticity of semiflexible polymers. *Phys. Rev. E*, 66:050801–050804, 2002.

[135] L. Schimansky-Geier, U. Erdmann, and N. Komin. Advantages of hopping on a zig-zag course. *Physica A*, 351:51–59, 2005.

[136] K. A. Schmitz, D. L. Holocomb-Wygle, D. J. Oberski, and C. B. Lindemann. Measurement of the force produced by an intact bull sperm flagellum in isometric arrest and estimation of the dynein stall force. *Biophys. J.*, 79:468–478, 2000.

[137] M. J. Schnitzer. Theory of continuum random walks and applications to chemotaxis. *Phys. Rev. E*, 48(4):2553–2568, 1993.

[138] J. E. Segall, S. M. Block, and H. C. Berg. Temporal comparisons in bacterial chemotaxis. *Proc. Natl. Acad. Sci. U.S.A.*, 83:8987–8991, 1986.

[139] R. Seifert, A. Scholten, R. Gauss, A. Mincheva, P. Lichter, and U. B. Kaupp. Molecular characterization of a slowly gating human hyperpolarization-activated channel predominantly expressed in thalamus, heart, and testis. *Proc. Natl. Acad. Sci. U.S.A.*, 96(16):9391–9396, 1999.

[140] I. Sendiña-Nadal, S. Alonso, V. Pérez-Muñuzuri, M. Gómez-Gesteira, . V. Pérez-Villar, L. Ramírez-Piscina, J. Casademunt, J. M. Sancho, and F. Sagués. Brownian motion of spiral waves driven by spatiotemporal structured noise. *Phys. Rev. Lett.*, 84(12):2734–2737, 2000.

[141] W. J. Shack, C. S. Fray, and T. J. Lardner. Observations on the hydrodynamics and swimming motions of mammalian spermatozoa. *Bull. Math. Biol.*, 36:555–565, 1974.

[142] A. Shapere and F. Wilczek. Self-propulsion at low Reynolds number. *Phys. Rev. Lett.*, 58(20):2051–2054, 1987.

[143] V. Singla and J. F. Reiter. The primary cilium as the cell's antenna: Signaling at a sensory organelle. *Science*, 313:629–633, 2006.

[144] Sir G. I. Taylor. The action of waving cylindrical tails in propelling microscopic organisms. *Proc. Roy. Soc. London Ser. A*, 211:225–239, 1952.

[145] M. A. Sleigh, editor. *Cilia and Flagella*. Academic Press, New York, 1974.

[146] C. A. Solari, S. Ganguly, J. O. Kessler, R. E. Michod, and R. E. Goldstein. Multicellularity and the functional interdependence of motility and molecular transport. *Proc. Natl. Acad. Sci. U.S.A.*, 103(5):1353–1358, 2006.

[147] P. Stockley, M. J. G. Gage, G. A. Parker, and A. P. Møller. Female reproductive biology and the coevolution of ejaculate characteristics in fish. *Proc.: Biol. Sci.*, 263(1369):451–458, 1996.

[148] T. Strünker, I. Weyand, W. Bönigk, Q. Van, A. Loogen, J. E. Brown, N. Kashikar, V. Hagen, E. Krause, and U. B. Kaupp. A K^+-selective cGMP-gated ion channel controls chemosensation of sperm. *Nat. Cell Biol.*, 8(10):1149 – 1154, 2006.

[149] S. S. Suarez and A. A. Pacey. Sperm transport in the female reproductive tract. *Human Reprod. Update*, 12(1):23–37, 2006.

[150] F. Sun, L. C. Giojalas, R. A. Rovasio, I. Tur-Kaspa, R. Sanchez, and M. Eisenbach. Lack of species-specificity in mammalian sperm chemotaxis. *Devel. Biol.*, 255(2):423 – 427, 2003.

[151] G. I. Taylor. Diffusion by continous movements. *Proc. Roy. Soc. A*, 20:196–212, 1920.

[152] R. Thar and T. Fenchel. True chemotaxis in oxygen gradients of the sulfur-oxidizing bacterium *Thiovolum majus*. *Appl. Env. Microbiol.*, 67(7):3299–3303, 2001.

[153] J. S. Trimmer and V. D. Vacquier. Activation of sea urchin gametes. *Ann. Rev. Cell Biol.*, 2:1–26, 1986.

[154] H. Tsutsui, M. Ishikawa, J. Cosson, Y. Oka, and M. Morisawa. Two strategies for sperm chemotaxis in ciona and siphonophores: Numerical simulation study. *Zool. Sci.*, 17, 2000.

[155] N. G. van Kampen. *Stochastic Processes in Physics and Chemistry*. North Holland, 1992.

[156] S. van Teeffelen and H. Löwen. Dynamics of a Brownian circle swimmer. *Phys. Rev. E*, 78:020101, 2008.

[157] M. Vergassola, E. Villermaux, and B. I. Shraiman. 'Infotaxis' as a strategy for searching without gradients. *Nature*, 445:406–409, 2007.

[158] G. Vogel. Betting on cilia. *Nature*, 310(5746):216–218, 2005.

[159] C. R. Ward and G. S. Kopf. Molecular events mediating sperm activation. *Dev. Biol.*, 158:9–34, 1993.

[160] D. N. Wheatley, A. M. Wang, and G. E. Strugnell. Expression of primary cilia in mammalian cells. *Cell Bio. Int.*, 20(1):73–81, 1996.

[161] J. Wilhelm and E. Frey. Radial distribution function of semiflexible polymers. *Phys. Rev. Lett.*, 77(12):2581–2584, 1996.

[162] C. D. Wood, T. Nishigaki, T. Furuta, A. S. Baba, and A. Darszon. Real-time analysis of the role of Ca^{2+} in flagellar movement and motility in single sea urchin sperm. *J. Cell. Biol.*, 169(5):725–731, 2005.

[163] X. Y. Xiang, A. Kittelson, J. Olson, A. Bieber, and D. Chandler. Allurin, a 21 kDa sperm chemoattractant, is rapidly released from the outermost jelly layer of the *Xenopus* egg by diffusion and medium convection. *Mol. Reprod. Devel.*, 70(3):344 – 360, 2005.

[164] H. Yamakawa. *Helical Wormlike Chains in Polymer Solutions*. Springer, 1997.

[165] M. Yoshida, H. Izumi, R. Desantis, and M. Morisawa. Capacitative calcium entry controls sperm chemotaxis in the ascidian ciona intestinalis. *Zool. Sci.*, 19(12), 2002.

[166] K. Yoshimura and R. Kamiya. The sensitivity of *Chlamydomonas* photoreceptor is optimized for the frequency of cell body rotation. *Plant Cell Physiol.*, 42(6):665–672, 2001.

[167] P. O. Yund. How severe is sperm limitation in natural populations of marine free-spawners? *Trends Ecol. Evol.*, 15:10–13, 2000.

[168] A. P. Yundt, W. J. Shack, and T. J. Lardner. Applicability of hydrodynamic analyses of spermatozoan motion. *J. exp. Biol.*, 62:27–41, 1975.

[169] S. H. Zigmond. Mechanisms of sensing chemical gradients by polymorphonuclear leukocytes. *Nature*, 249:450–452, 1974.

Eigenständigkeitserklärung

Hiermit erkläre ich die vorliegende Arbeit ohne unzulässige Hilfe Dritter und ohne Benutzung anderer als der angegebenen Hilfsmittel angefertigt zu haben; die aus fremden Quellen direkt oder indirekt übernommenen Gedanken sind als solche kenntlich gemacht. Die Arbeit wurde bisher weder im Inland noch im Ausland in gleicher oder ähnlicher Form einer anderen Prüfungsbehörde vorgelegt. Die vorliegende Arbeit und die darin präsentierten Ergebnisse wurden vom 01.08.2005 bis 31.10.2008 unter Betreuung von Prof. Dr. Frank Jülicher am Max-Planck-Institut für Physik komplexer Systeme in Dresden erarbeitet.

Ich versichere, dass ich bisher keine erfolglosen Promotionsverfahren unternommen habe. Ich erkenne die Promotionsordnung der Fakultät Mathematik und Naturwissenschaften der Technischen Universität Dresden an.

Dresden, im Oktober 2008, Benjamin M. Friedrich